

**University of Alberta**

**Effects of Material Anisotropy on the Buckling Resistance  
of High Strength Steel Pipelines**

by

**Ali Fathi**

A thesis submitted to the Faculty of Graduate Studies and Research  
in partial fulfilment of the requirements for the degree of

**Doctor of Philosophy**

in

**Structural Engineering**

Department of Civil and Environmental Engineering

©Ali Fathi

Fall 2012

Edmonton, Alberta

Permission is hereby granted to the University of Alberta Libraries to reproduce single copies of this thesis and to lend or sell such copies for private, scholarly or scientific research purposes only. Where the thesis is converted to, or otherwise made available in digital form, the University of Alberta will advise potential users of the thesis of these terms.

The author reserves all other publication and other rights in association with the copyright in the thesis and, except as herein before provided, neither the thesis nor any substantial portion thereof may be printed or otherwise reproduced in any material form whatsoever without the author's prior written permission.

## **ABSTRACT**

This research investigates the buckling response of high strength steel (HSS) pipes with anisotropic material properties. The stress-strain responses of eight material types of grades X80 and X100 pipes were studied focusing on the elastic, yielding, and early plastic regions that affect the pipe's buckling. Based on the observed hardening patterns in longitudinal and transverse directions, a combined hardening material model was introduced with linear isotropic and Armstrong-Frederick kinematic hardening rules. A simple method for model calibration was also introduced using longitudinal and transverse tensile stress-strain responses.

After validation with experimental stress-strain data, the anisotropic material model was used in the buckling analyses of HSS pipes to improve the accuracy of finite element simulations. Fifteen finite element models were developed for buckling analyses of HSS pipes previously tested under different load combinations. The results showed that using the anisotropic material model results in more precise simulations of the actual behaviour of HSS pipes compared to isotropic models.

The anisotropic model was employed in a parametric study to investigate the effects of material anisotropy and five other parameters on the critical buckling strain of HSS pipes. Finite element models were developed and analyzed with different values of diameter to thickness ratio, internal pressure, initial imperfection, material grade, strain hardening rate, and level of anisotropy. The results provide a better understanding of the effects of material properties on the buckling resistance of HSS pipes when there is a significant level of anisotropy.

## **ACKNOWLEDGEMENTS**

Throughout this work I was surrounded by a spectacular group of people and privileged to have their generous help and support.

First I sincerely express my gratitude to my supervisor, Dr. J.J. Roger Cheng, who has supported me throughout my thesis with his patience and knowledge whilst providing me with the freedom to work in my own way.

Special thanks to Dr. Samer Adeb, who shared the material test results of high strength steel pipes with me.

Many thanks to all my graduate friends, for sharing their resources and thoughts.

Thanks to the University of Alberta, Faculty of Engineering for providing the financial means to complete this project.

I would also like to extend my gratitude to my mother and my brothers in Iran, who have done their best to help me in my endeavors.

Last, but not least, I would like to thank my dear wife, Salma whose love and support were unconditional during the past few years despite her tight schedule. This thesis is sincerely dedicated to her.

# TABLE OF CONTENTS

<b>1</b>	<b>INTRODUCTION.....</b>	<b>1</b>
1.1	Background .....	1
1.2	Parameters Employed in CBS Criteria.....	5
1.3	High Strength Steel Pipes .....	12
1.4	Problem Statement.....	15
1.5	Objectives and Methodology .....	17
1.6	Thesis Layout .....	18
<b>2</b>	<b>ANISOTROPIC MATERIAL MODELING METHOD FOR HSS PIPES USING COMBINED HARDENING CONCEPT .....</b>	<b>27</b>
2.1	HSS Pipes' Material Database.....	29
2.2	Major Features of HSS Pipes Material Responses.....	32
2.3	Combined Hardening Material Modeling Concept .....	37
2.4	Idealizations and Postulations of HSS Pipe Material Responses.....	41
2.5	Calibration of the Combined Hardening Material Model .....	47
2.6	Results and Discussion.....	52
2.7	Summary.....	55
<b>3</b>	<b>BUCKLING ANALYSIS OF HSS PIPES WITH ANISOTROPIC MATERIAL MODELING .....</b>	<b>84</b>
3.1	The Database of HSS Pipes Buckling Tests.....	85
3.1.1	HSS Pipe Specimens .....	85
3.1.2	Buckling Tests .....	86
3.1.3	Initial Imperfection Measurements.....	88
3.2	Finite Element Modeling of HSS Pipes Bending Tests .....	89

3.2.1	Finite Element Method .....	89
3.2.2	Features of the HSS Pipe Models .....	93
3.2.3	Material Modeling .....	99
3.2.4	Mesh Study .....	103
3.2.5	Initial Imperfection Modeling .....	105
3.2.6	Loading Scheme .....	109
<b>3.3</b>	<b>Results and Discussion.....</b>	<b>110</b>
3.3.1	Preliminary Results.....	111
3.3.2	Results of All 15 HSS Pipes .....	116
<b>3.4</b>	<b>Summary.....</b>	<b>120</b>
<b>4</b>	<b>PARAMETRIC STUDY .....</b>	<b>145</b>
<b>4.1</b>	<b>Response Surface Methodology.....</b>	<b>146</b>
<b>4.2</b>	<b>Parameters to Investigate.....</b>	<b>147</b>
4.2.1	Material Parameters .....	150
4.2.2	Pipe's Diameter and Thickness .....	153
4.2.3	Internal Pressures.....	154
4.2.4	Initial Imperfections .....	155
<b>4.3</b>	<b>Dimensional analysis.....</b>	<b>156</b>
4.3.1	Ranges of $\pi$ -Parameters to Investigate .....	160
4.3.2	Geometry and Loading Scheme of the Pipe Models .....	169
4.3.3	Screening Study .....	171
4.3.4	Cases Analyzed.....	179
<b>4.4</b>	<b>Results of the Parametric Study .....</b>	<b>181</b>
4.4.1	Effects of Anisotropy on CBS of HSS Pipes with $D/t=50$ .....	181
4.4.2	Effects of Anisotropy on the CBS of HSS Pipes with $D/t=70$ .....	184
4.4.3	Effects of Anisotropy on CBS of HSS Pipes with $D/t=90$ .....	186
<b>4.5</b>	<b>Summary.....</b>	<b>188</b>
<b>5</b>	<b>BUCKLING SENSITIVITY OF HSS TO PIPES DIFFERENT MATERIAL RESPONSES.....</b>	<b>220</b>

5.1	<b>Tested Cases Studied .....</b>	<b>221</b>
5.1.1	Different Material Models .....	222
5.1.2	Extensions to the Selected Models .....	225
5.2	<b>Cases Analyzed.....</b>	<b>230</b>
5.3	<b>Results and Discussion.....</b>	<b>231</b>
5.3.1	Effects of Directional Material Responses on HSS Pipes Buckling...	231
5.3.2	Effects of Cross-sectional Distribution of Normal Strain on HSS Pipes Buckling.....	234
5.4	<b>Summary.....</b>	<b>237</b>
6	<b>MODELING THE ANISOTROPIC MATERIAL RESPONSE OF THERMALLY COATED HSS PIPES .....</b>	<b>251</b>
6.1	<b>Effects of Thermal Coating on the HSS Pipes' Material.....</b>	<b>252</b>
6.2	<b>Experimental Data .....</b>	<b>255</b>
6.2.1	Material Tests .....	255
6.2.2	Full-scale Buckling Tests .....	256
6.3	<b>Anisotropic Material Modeling.....</b>	<b>257</b>
6.3.1	Material Anisotropy Features of Thermally Coated HSSP .....	257
6.3.2	Modified Combined Hardening Material Models .....	259
6.4	<b>Buckling Analyses .....</b>	<b>262</b>
6.5	<b>Results and Discussions .....</b>	<b>264</b>
6.6	<b>Summary.....</b>	<b>266</b>
7	<b>SUMMARY, CONCLUSION, AND RECOMMENDATIONS .....</b>	<b>277</b>
7.1	<b>Summary.....</b>	<b>277</b>
7.2	<b>Conclusion .....</b>	<b>279</b>
7.3	<b>Recommendations .....</b>	<b>284</b>

## LIST OF TABLES

Table 2-1 Steel grades and dimensions of the HSS pipes and number of different coupons for each material type.....	60
Table 2-2 Longitudinal and transverse values for different material parameters .....	60
Table 2-3 Material parameters used to define the combined hardening model .....	61
Table 3-1 HSS pipe specimens' grade, dimensions and testing conditions.....	125
Table 3-2 Specimens' initial imperfections.....	126
Table 3-3 Comparison of experimental CBS with predicted values by isotropic and anisotropic models.....	127
Table 4-1 Distribution of non-dimensional material variables in the available (HSS pipe) material database.....	191
Table 4-2 Parameters' values used in the finite element models of the screening study.....	191
Table 4-3 CBS corresponding to different levels of each variable in the screening study .....	192
Table 4-4 Combination matrix of $PL_L/\sigma_{y(T)}$ and $\gamma$ and the resultant $\sigma_{y(L)}/\sigma_{y(T)}$ ratio .....	192
Table 6-1 Specimens' grade, dimensions, and testing conditions .....	269
Table 6-2 Specimens' initial imperfections.....	269
Table 6-3 Material properties in both directions from tensions tests.....	269
Table 6-4 Material properties used in anisotropic models.....	269
Table 6-5 Material simulation error by combined hardening models.....	270

# LIST OF FIGURES

Figure 1-1 Stress-based design concept .....	26
Figure 1-2 Strain-based design concept .....	26
Figure 2-1 Longitudinal and transverse tension stress-strain curves for the material type A - entire range.....	62
Figure 2-2 Longitudinal and transverse tensile stress-strain curves for the material type B - entire range.....	62
Figure 2-3 Longitudinal and transverse tensile stress-strain curves for the material type C - entire range.....	63
Figure 2-4 Longitudinal and transverse tensile stress-strain curves for the material type D - entire range.....	63
Figure 2-5 Longitudinal and transverse tensile stress-strain curves for the material type E - entire range.....	64
Figure 2-6 Longitudinal and transverse tensile stress-strain curves for the material type F - entire range.....	64
Figure 2-7 Longitudinal and transverse tensile stress-strain curves for the material type G - entire range.....	65
Figure 2-8 Longitudinal and transverse tensile stress-strain curves for the material type H - entire range.....	65
Figure 2-9 Schematic shape of the stress-strain curves of HSS pipe materials .....	66
Figure 2-10 Longitudinal and transverse tensile stress-strain curves for the material type A – 0.0% to 3.0% total strain .....	66
Figure 2-11 Longitudinal and transverse tensile stress-strain curves for the material type B – 0.0% to 3.0% total strain .....	67
Figure 2-12 Longitudinal and transverse tensile stress-strain curves for the material type C – 0.0% to 3.0% total strain .....	67
Figure 2-13 Longitudinal and transverse tensile stress-strain curves for the material type D – 0.0% to 3.0% total strain .....	68
Figure 2-14 Longitudinal and transverse tensile stress-strain curves for the material type E – 0.0% to 3.0% total strain .....	68
Figure 2-15 Longitudinal and transverse tensile stress-strain curves for the material type F – 0.0% to 3.0% total strain .....	69
Figure 2-16 Longitudinal and transverse tensile stress-strain curves for the material type G – 0.0% to 3.0% total strain .....	69
Figure 2-17 Longitudinal and transverse tensile stress-strain curves for the material type H – 0.0% to 3.0% total strain .....	70
Figure 2-18 Longitudinal and transverse tensile yield strength for material A to H .....	70
Figure 2-19 Schematic shape of the longitudinal tensile stress-strain curve of HSS pipes' materials – 0.0% to 3.0% total strain .....	71

Figure 2-20 Schematic shape of the transversal tensile stress-strain curve of HSS pipes' materials – 0.0% to 3.0% total strain .....	71
Figure 2-21 Evolution of back-stress according to Armstrong-Fredrick kinematic hardening law.	72
Figure 2-22 Evolution of the yield surface in the stress space when combined hardening is used .	72
Figure 2-23 Distribution and average of $E_T/E_L$ ratio in the material database .....	73
Figure 2-24 Distribution and average of $E_{sh(T)}/E_{sh(L)}$ ratio in the material database .....	73
Figure 2-25 Distribution and average of $\sigma_{y(nom/T)}/\sigma_{y(nom/L)}$ ratio in the material database.....	74
Figure 2-26 Idealized stress-strain curves in the longitudinal and transverse directions of HSS pipes .....	74
Figure 2-27 Shifted yield surface in stress space (for plane stress).....	75
Figure 2-28 Evolution of back-stress, yield stress, and total stress of the proposed material model (linear isotropic and Armstrong-Fredrick kinematic hardening).....	75
Figure 2-29 A material with combined hardening changes behaviour in two perpendicular directions after applying initial back-stress .....	76
Figure 2-30 Tensile stress-strain data from the material model and average experimental results for material types A .....	76
Figure 2-31 Tensile stress-strain data from the material model and average experimental results for material types B .....	77
Figure 2-32 Tensile stress-strain data from the material model and average experimental results for material types C .....	77
Figure 2-33 Tensile stress-strain data from the material model and average experimental results for material types D .....	78
Figure 2-34 Tensile stress-strain data from the material model and average experimental results for material types E.....	78
Figure 2-35 Tensile stress-strain data from the material model and average experimental results for material types F .....	79
Figure 2-36 Tensile stress-strain data from the material model and average experimental results for material types G .....	79
Figure 2-37 Tensile stress-strain data from the material model and average experimental results for material types H .....	80
Figure 2-38 MAE in predicting tensile stress-strain relationship by the material model in the longitudinal and transverse directions.....	80
Figure 2-39 Longitudinal tensile and compressive experimental stress-strain curves for the material type B .....	81
Figure 2-40 Longitudinal tensile and compressive experimental stress-strain curves for the material type F .....	81
Figure 2-41 Longitudinal tensile and compressive experimental stress-strain curves for the material type G.....	82
Figure 2-42 Modeled material behaviour under longitudinal compression and average longitudinal stress-strain data from tests for material type B .....	82
Figure 2-43 Modeled material behaviour under longitudinal compression and average longitudinal stress-strain data from tests for material type F .....	83

Figure 2-44 Modeled material behaviour under longitudinal compression and average longitudinal stress-strain data from tests for material type G .....	83
Figure 3-1 The set-up used for the buckling test on HSS pipes .....	128
Figure 3-2 Typical load-displacement response of shell structures.....	129
Figure 3-3 General attribute of the finite element model of HSS pipe specimens developed in ABAQUS .....	129
Figure 3-4 Bulge-type imperfection used for pressurized pipes.....	130
Figure 3-5 Dent-type imperfection used for pressurized pipes.....	130
Figure 3-6 Results of mesh study on the isotropic model of HSSP#11 .....	131
Figure 3-7 Results of mesh study on the anisotropic model of HSSP#11 .....	131
Figure 3-8 Results of mesh study on the isotropic model of HSSP#14.....	132
Figure 3-9 Results of mesh study on the anisotropic model of HSSP#14 .....	132
Figure 3-10 Deformed shape of the pipe HSSP #11 (unpressurized).....	133
Figure 3-11 Deformed shape of the pipe HSSP #14 (pressurized).....	133
Figure 3-12 Effects of imperfection magnitudes on the buckling response of HSSP#11 - isotropic model .....	134
Figure 3-13 Effects of imperfection magnitudes on the buckling response of HSSP#11 - anisotropic model.....	134
Figure 3-14 Effects of imperfection magnitudes on the buckling response of HSSP#14 - isotropic model .....	135
Figure 3-15 Effects of imperfection magnitudes on the buckling response of HSSP#14 - anisotropic model.....	135
Figure 3-16 Global moment versus $2D$ average compressive strain of the buckling zone – from experimental measurements and isotropic and anisotropic models of HSSP#01 .....	136
Figure 3-17 Global moment versus $2D$ average compressive strain of the buckling zone – from experimental measurements and isotropic and anisotropic models of HSSP#02 .....	136
Figure 3-18 Global moment versus $2D$ average compressive strain of the buckling zone – from experimental measurements and isotropic and anisotropic models of HSSP#03 .....	137
Figure 3-19 Global moment versus $2D$ average compressive strain of the buckling zone – from experimental measurements and isotropic and anisotropic models of HSSP#04 .....	137
Figure 3-20 Global moment versus $2D$ average compressive strain of the buckling zone – from experimental measurements and isotropic and anisotropic models of HSSP#05 .....	138
Figure 3-21 Global moment versus $2D$ average compressive strain of the buckling zone – from experimental measurements and isotropic and anisotropic models of HSSP#06 .....	138
Figure 3-22 Global moment versus $2D$ average compressive strain of the buckling zone – from experimental measurements and isotropic and anisotropic models of HSSP#07 .....	139
Figure 3-23 Global moment versus $2D$ average compressive strain of the buckling zone – from experimental measurements and isotropic and anisotropic models of HSSP#08 .....	139
Figure 3-24 Global moment versus $2D$ average compressive strain of the buckling zone – from experimental measurements and isotropic and anisotropic models of HSSP#09 .....	140
Figure 3-25 Global moment versus $2D$ average compressive strain of the buckling zone – from experimental measurements and isotropic and anisotropic models of HSSP#10 .....	140

Figure 3-26 Global moment versus $2D$ average compressive strain of the buckling zone – from experimental measurements and isotropic and anisotropic models of HSSP#11 .....	141
Figure 3-27 Global moment versus $2D$ average compressive strain of the buckling zone – from experimental measurements and isotropic and anisotropic models of HSSP#12 .....	141
Figure 3-28 Global moment versus $2D$ average compressive strain of the buckling zone – from experimental measurements and isotropic and anisotropic models of HSSP#13 .....	142
Figure 3-29 Global moment versus $2D$ average compressive strain of the buckling zone – from experimental measurements and isotropic and anisotropic models of HSSP#14 .....	142
Figure 3-30 Global moment versus $2D$ average compressive strain of the buckling zone – from experimental measurements and isotropic and anisotropic models of HSSP#15 .....	143
Figure 3-31 Stress paths for tension and compression elements of an unpressurized pipe under bending moment.....	143
Figure 3-32 Stress paths for tension and compression elements of a pressurized pipe under bending moment.....	144
Figure 4-1 General format of longitudinal and transverse material (tension) responses of the proposed combined hardening model .....	193
Figure 4-2 Different levels of $\sigma_{y(T)}/E$ considered for the screening study .....	194
Figure 4-3 Different levels of $PL_L/\sigma_{y(T)}$ considered for the screening study .....	194
Figure 4-4 Different levels of $\gamma$ considered for the screening study .....	195
Figure 4-5 Different levels of $E_{sh}/E$ considered for the screening study .....	195
Figure 4-6 Effects of $\sigma_{y(T)}/E$ on the buckling response of the finite element used in the screening study .....	196
Figure 4-7 Effects of $PL_L/\sigma_{y(T)}$ on the buckling response of the finite element used in the screening study .....	196
Figure 4-8 Effects of $\gamma$ on the buckling response of the finite element used in the screening study	197
Figure 4-9 Effects of $E_{sh}/E$ on the buckling response of the finite element used in the screening study .....	197
Figure 4-10 Effects of $D/t$ on the buckling response of the finite element used in the screening study .....	198
Figure 4-11 Effects of $\sigma_h/\sigma_{y(T)}$ on the buckling response of the finite element used in the screening study .....	198
Figure 4-12 Effects of $II_{max}/D$ on the buckling response of the finite element used in the screening study .....	199
Figure 4-13 Effects of the variation of $\sigma_{y(T)}$ .....	199
Figure 4-14 Effects of the variation of $PL_L/\sigma_{y(T)}$ .....	200
Figure 4-15 Effects of the variation of $\gamma$ .....	200
Figure 4-16 Effects of the variation of $E_{sh}/E$ .....	201
Figure 4-17 Effects of the variation of $D/t$ .....	201
Figure 4-18 Effects of the variation of $\sigma_h/\sigma_{y(T)}$ .....	202
Figure 4-19 Effects of the variation of $II_{max}/D$ .....	202

Figure 4-20 Distribution of $\gamma$ versus $PL_L/\sigma_{y(T)}$ in the experimental database compared to 25 combinations used in the screening study .....	203
Figure 4-21 Stress-strain curves for 25 combinations of $PL_L/\sigma_{y(T)}$ and $\gamma$ .....	203
Figure 4-22 Variation of the CBS with $\sigma_{y(L)}/\sigma_{y(T)}$ .....	204
Figure 4-23 Stress-strain curves for minimum, intermediate, and maximum $\sigma_{y(L)}/\sigma_{y(T)}$ .....	204
Figure 4-24 Effects of $\sigma_{y(L)}/\sigma_{y(T)}$ on the buckling response of the finite element used in the screening study .....	205
Figure 4-25 Effects of the variation of $\sigma_{y(L)}/\sigma_{y(T)}$ .....	205
Figure 4-26 Variation of the CBS versus $\sigma_{y(L)}/\sigma_{y(T)}$ for $D/t=50$ , $\sigma_H/\sigma_{y(T)}=0.0$ , $II_{max}/D=0.05\%$ .....	206
Figure 4-27 Variation of the CBS versus $\sigma_{y(L)}/\sigma_{y(T)}$ for $D/t=50$ , $\sigma_H/\sigma_{y(T)}=0.0$ , $II_{max}/D=0.25\%$ .....	206
Figure 4-28 Variation of the CBS versus $\sigma_{y(L)}/\sigma_{y(T)}$ for $D/t=50$ , $\sigma_H/\sigma_{y(T)}=0.0$ , $II_{max}/D=0.50\%$ .....	207
Figure 4-29 Variation of the CBS versus $\sigma_{y(L)}/\sigma_{y(T)}$ for $D/t=50$ , $\sigma_H/\sigma_{y(T)}=0.4$ , $II_{max}/D=0.05\%$ .....	207
Figure 4-30 Variation of the CBS versus $\sigma_{y(L)}/\sigma_{y(T)}$ for $D/t=50$ , $\sigma_H/\sigma_{y(T)}=0.4$ , $II_{max}/D=0.25\%$ .....	208
Figure 4-31 Variation of the CBS versus $\sigma_{y(L)}/\sigma_{y(T)}$ for $D/t=50$ , $\sigma_H/\sigma_{y(T)}=0.4$ , $II_{max}/D=0.50\%$ .....	208
Figure 4-32 Variation of the CBS versus $\sigma_{y(L)}/\sigma_{y(T)}$ for $D/t=50$ , $\sigma_H/\sigma_{y(T)}=0.8$ , $II_{max}/D=0.05\%$ .....	209
Figure 4-33 Variation of the CBS versus $\sigma_{y(L)}/\sigma_{y(T)}$ for $D/t=50$ , $\sigma_H/\sigma_{y(T)}=0.8$ , $II_{max}/D=0.25\%$ .....	209
Figure 4-34 Variation of the CBS versus $\sigma_{y(L)}/\sigma_{y(T)}$ for $D/t=50$ , $\sigma_H/\sigma_{y(T)}=0.8$ , $II_{max}/D=0.50\%$ .....	210
Figure 4-35 Variation of the CBS versus $\sigma_{y(L)}/\sigma_{y(T)}$ for $D/t=70$ , $\sigma_H/\sigma_{y(T)}=0.0$ , $II_{max}/D=0.05\%$ .....	210
Figure 4-36 Variation of the CBS versus $\sigma_{y(L)}/\sigma_{y(T)}$ for $D/t=70$ , $\sigma_H/\sigma_{y(T)}=0.0$ , $II_{max}/D=0.25\%$ .....	211
Figure 4-37 Variation of the CBS versus $\sigma_{y(L)}/\sigma_{y(T)}$ for $D/t=70$ , $\sigma_H/\sigma_{y(T)}=0.0$ , $II_{max}/D=0.50\%$ .....	211
Figure 4-38 Variation of the CBS versus $\sigma_{y(L)}/\sigma_{y(T)}$ for $D/t=70$ , $\sigma_H/\sigma_{y(T)}=0.4$ , $II_{max}/D=0.05\%$ .....	212
Figure 4-39 Variation of the CBS versus $\sigma_{y(L)}/\sigma_{y(T)}$ for $D/t=70$ , $\sigma_H/\sigma_{y(T)}=0.4$ , $II_{max}/D=0.25\%$ .....	212
Figure 4-40 Variation of the CBS versus $\sigma_{y(L)}/\sigma_{y(T)}$ for $D/t=70$ , $\sigma_H/\sigma_{y(T)}=0.4$ , $II_{max}/D=0.50\%$ .....	213
Figure 4-41 Variation of the CBS versus $\sigma_{y(L)}/\sigma_{y(T)}$ for $D/t=70$ , $\sigma_H/\sigma_{y(T)}=0.8$ , $II_{max}/D=0.05\%$ .....	213
Figure 4-42 Variation of the CBS versus $\sigma_{y(L)}/\sigma_{y(T)}$ for $D/t=70$ , $\sigma_H/\sigma_{y(T)}=0.8$ , $II_{max}/D=0.25\%$ .....	214
Figure 4-43 Variation of the CBS versus $\sigma_{y(L)}/\sigma_{y(T)}$ for $D/t=70$ , $\sigma_H/\sigma_{y(T)}=0.8$ , $II_{max}/D=0.50\%$ .....	214
Figure 4-44 Variation of the CBS versus $\sigma_{y(L)}/\sigma_{y(T)}$ for $D/t=90$ , $\sigma_H/\sigma_{y(T)}=0.0$ , $II_{max}/D=0.05\%$ .....	215
Figure 4-45 Variation of the CBS versus $\sigma_{y(L)}/\sigma_{y(T)}$ for $D/t=90$ , $\sigma_H/\sigma_{y(T)}=0.0$ , $II_{max}/D=0.25\%$ .....	215
Figure 4-46 Variation of the CBS versus $\sigma_{y(L)}/\sigma_{y(T)}$ for $D/t=90$ , $\sigma_H/\sigma_{y(T)}=0.0$ , $II_{max}/D=0.50\%$ .....	216
Figure 4-47 Variation of the CBS versus $\sigma_{y(L)}/\sigma_{y(T)}$ for $D/t=90$ , $\sigma_H/\sigma_{y(T)}=0.4$ , $II_{max}/D=0.05\%$ .....	216
Figure 4-48 Variation of the CBS versus $\sigma_{y(L)}/\sigma_{y(T)}$ for $D/t=90$ , $\sigma_H/\sigma_{y(T)}=0.4$ , $II_{max}/D=0.25\%$ .....	217
Figure 4-49 Variation of the CBS versus $\sigma_{y(L)}/\sigma_{y(T)}$ for $D/t=90$ , $\sigma_H/\sigma_{y(T)}=0.4$ , $II_{max}/D=0.50\%$ .....	217
Figure 4-50 Variation of the CBS versus $\sigma_{y(L)}/\sigma_{y(T)}$ for $D/t=90$ , $\sigma_H/\sigma_{y(T)}=0.8$ , $II_{max}/D=0.05\%$ .....	218
Figure 4-51 Variation of the CBS versus $\sigma_{y(L)}/\sigma_{y(T)}$ for $D/t=90$ , $\sigma_H/\sigma_{y(T)}=0.8$ , $II_{max}/D=0.25\%$ .....	218
Figure 4-52 Variation of the CBS versus $\sigma_{y(L)}/\sigma_{y(T)}$ for $D/t=90$ , $\sigma_H/\sigma_{y(T)}=0.8$ , $II_{max}/D=0.50\%$ .....	219
Figure 5-1 Longitudinal stress-strain data from the material tension test and the average curve used in the LT isotropic models .....	240

Figure 5-2 Transverse stress-strain data from the material tension test and the average curve used in the TT isotropic models .....	240
Figure 5-3 Longitudinal stress-strain data from the material compression test and the extended average curve used in the LC isotropic models.....	241
Figure 5-4 Buckling responses from finite element models with different material models compared with the experimental result for HSSP#11 .....	241
Figure 5-5 Buckling responses from finite element models with different material models compared with the experimental result for HSSP#12 .....	242
Figure 5-6 Buckling responses from finite element models with different material models compared with the experimental result for HSSP#13 .....	242
Figure 5-7 Buckling responses from finite element models with different material models compared with the experimental result for HSSP#14 .....	243
Figure 5-8 Buckling responses from finite element models with different material models compared with the experimental result for HSSP#15 .....	243
Figure 5-9 Different initial (linear-elastic) strain distributions as indicators of different ratio of applied axial compressive force-to-bending moments .....	244
Figure 5-10 Different imperfection patterns used in pipe models .....	245
Figure 5-11 Variation of the CBS with the $y/D$ ratio for the unpressurized pipe with a blister-type imperfection pattern and different material modeling methods .....	246
Figure 5-12 Variation of the CBS with the $y/D$ ratio for the unpressurized pipe with a half-ring type imperfection pattern and different material modeling methods .....	246
Figure 5-13 Variation of the CBS with the $y/D$ ratio for the unpressurized pipe with a full-ring type imperfection pattern and different material modeling methods .....	247
Figure 5-14 Variation of the CBS with the $y/D$ ratio for the pressurized pipe with a blister-type imperfection pattern and different material modeling methods .....	247
Figure 5-15 Variation of the CBS with the $y/D$ ratio for the pressurized pipe with a half-ring type imperfection pattern and different material modeling methods .....	248
Figure 5-16 Variation of the CBS with the $y/D$ ratio for the pressurized pipe with a full-ring type imperfection pattern and different material modeling methods .....	248
Figure 5-17 Stress path of unpressurized pipe elements under longitudinal compression .....	249
Figure 5-18 Stress path of pressurized pipe elements under longitudinal compression .....	249
Figure 5-19 E Constrained and constraining area in the critical cross-section of a pipe under compression and bending.....	250
Figure 5-20 Typical buckling modes of unpressurized (a) and pressurized (b) models under compression and bending.....	250
Figure 6-1 Effects of thermal coating on the tension stress-strain response of HSSP (grade X100) - transverse tension coupon and ring expansion test results .....	271
Figure 6-2 Longitudinal and transverse stress-strain data from the material tension test for material type "I" – entire range.....	271
Figure 6-3 Longitudinal and transverse stress-strain data from the material tension test for material type "I" – elastic and early plastic response.....	272
Figure 6-4 Average experimental and combined hardening material model results for material type "I" – longitudinal and transverse tension responses.....	272

Figure 6-5 Average experimental and combined hardening material model results for material type “I” – longitudinal compression responses .....	273
Figure 6-6 Average experimental and modified combined hardening material model results for material type “I” – longitudinal and transverse tension responses .....	273
Figure 6-7 Average experimental and modified combined hardening material model results for material type “I” – longitudinal compression responses .....	274
Figure 6-8 Average experimental stress-plastic strain points and the smoothed curve used in the isotropic TT pipe model - transverse tension response .....	274
Figure 6-9 Variation of global moment versus $2D$ compressive strain from isotropic FE models and experimental result of HSSP#16 .....	275
Figure 6-10 Variation of global moment versus $2.25D$ compressive strain from isotropic FE models and experimental result of HSSP#17 .....	275
Figure 6-11 Variation of global moment versus $2D$ compressive strain from anisotropic FE models and experimental result of HSSP#16 .....	276
Figure 6-12 Variation of global moment versus $2.25D$ compressive strain from anisotropic FE models and experimental result of HSSP#17 .....	276

## LIST OF SYMBOLS AND ABBREVIATIONS

API	American Petroleum Institute
$c$	Kinematic hardening material constant
CBS	Critical buckling strength
cos	Cosine function
CSA	Canadian Standard Association
°C	Degrees Celsius
$C^e$	Elastic tangent modulus
$C^{ep}$	Elasto-plastic tangent modulus
$D$	Outside diameter of the linepipe
$D_{average}$	Average outside diameter of the linepipe in each cross-section
$D_{max}$	Maximum local outside diameter of the linepipe in each cross-section
$D_{min}$	Minimum local outside diameter of the linepipe in each cross-section
$E$	Modulus of elasticity
$E_s$	CAN/CSA-Z662-07 modulus of elasticity
$E_{sh}$	Strain hardening modulus
$f_y$	DNV-OS-F101 yield strength of the pipe material
$F_u$	Ultimate strength of the pipe material
$F_y$	Yield strength of the pipe material
HSS	High strength steel
$imp$	Blister-type imperfection expressed as a percentage of the wall thickness
$I$	Moment of inertia
$II_{max}$	Maximum magnitude of out-of-roundness
$J_2$	Second invariant of the deviatoric stress tensors
$L_e$	Effective length of the column
$L_{II}$	Gauge length of the imperfect section of the linepipe
$m$	Units of meter
$mm$	Units of millimeter

MPa	Units of megapascals (N/mm <sup>2</sup> )
MN	Mega newton
n	Number of regression coefficients
$p$	Internal pressure
$p_i$	CAN/CSA-Z662-07 internal pressure
$p_e$	CAN/CSA-Z662-07 external pressure
$p_y$	Internal pressure that causes yielding in the transverse (hoop) direction
$PL_{L(com)}$	Compressive proportional limit in longitudinal direction
$r$	Radius of gyration
$R$	Distance of the imperfect grid point to the pipe axis in finite element models
$R^o$	Original radius of the pipe in finite element models
$R^2$	Coefficient of multiple determination
$s$	Deviatoric stress tensor
S4R	Four-node, quadrilateral element from ABAQUS library
SMYS	Specified minimum yield strength
STR13	Three-node, triangular element from ABAQUS library
$t$	Pipe wall thickness
$t_{average}$	Average wall thickness in each cross-section of pipe specimens
$WT$	Pipe wall thickness
$x$	Longitudinal distance of the grid point from the cross-section where imperfection begins
$y$	Distances of the neutral axes to the pipe's longitudinal axis

### **Greek Symbols**

$\alpha$	Magnitude of back-stress
$\alpha^{dev}$	Deviatoric part of the back-stress tensor
$\alpha_{gw}$	DNV-OS-F101 correction factor if girth weld is present
$\alpha_h$	DNV-OS-F101 maximum allowed yield-to-tensile stress ratio
$\dot{\alpha}$	Back-stress rate
$\beta$	Angular distance between the grid point and the point of extreme compression fiber

$\gamma$	Kinematic hardening material constant
$\eta$	True response function
$\varepsilon^e$	Elastic strain
$\varepsilon_c$	Average compressive strain in the specified gauge length in the buckled zone
$\varepsilon_{cr}$	Buckling strain
$\varepsilon_{eng}$	Engineering strain
$\varepsilon_i$	Total strain associated with $\sigma_i$
$\varepsilon_t$	Tensile strain of the extreme tension fiber located at the buckled section of the linepipe
$\varepsilon_{true}$	True strain
$\dot{\varepsilon}_{eq}$	Equivalent plastic strain-rate
$\dot{\varepsilon}^e$	Elastic part of strain rate tensor
$\varepsilon_i^p$	Plastic strain tensor
$\dot{\varepsilon}^p$	Plastic part of strain rate tensor
$\kappa$	Pipe's curvature for the given gauge length
$\dot{\lambda}$	Plastic multiplier
$\nu$	Poisson's ratio
$\pi_1$	Preliminary Pi-parameter 1, $(\frac{\sigma_{y(T)}}{E})$
$\pi_2$	Preliminary Pi-parameter 2, $(\frac{PL_L}{\sigma_{y(T)}})$
$\pi_3$	Preliminary Pi-parameter 3, $(\gamma)$
$\pi_4$	Preliminary Pi-parameter 4, $(\frac{E_{sh}}{E})$
$\pi_5$	Preliminary Pi-parameter 5, $(\frac{D}{t})$
$\pi_6$	Preliminary Pi-parameter 6, $(\frac{\sigma_h}{\sigma_{y(T)}})$
$\pi_7$	Preliminary Pi-parameter 7, $(\frac{H_{max}}{D})$

$\Pi_1$	Pi-parameter 1, $(\frac{\sigma_{y(T)}}{E})$
$\Pi_2$	Pi-parameter 2, $(\frac{\sigma_{y(L)}}{\sigma_{y(T)}})$
$\Pi_3$	Pi-parameter 3, $(\frac{E_{sh}}{E})$
$\Pi_4$	Pi-parameter 4, $(\frac{D}{t})$
$\Pi_5$	Pi-parameter 5, $(\frac{\sigma_h}{\sigma_{y(T)}})$
$\Pi_6$	Pi-parameter 6, $(\frac{H_{max}}{D})$
$\sigma$	Stress
$\sigma_{0.5}$	Stress at 0.5% total strain
$\sigma_{1.5}$	Stress at 1.5% total strain
$\sigma_{eng}$	Engineering stress
$\sigma_h$	DNV-OS-F101 characteristic transverse stress
$\sigma_{true}$	True stress
$\sigma_{y(nom)}$	Nominal yield stress
$\sigma_{y(T)}$	Transverse yield stress that replaces $\sigma_{y(nom)}$ as discussed in section 4.2.1.2
$\sigma^o$	Size of yield surface
$\sigma_o^o$	Size of yield surface at zero plastic strain
$\dot{\sigma}^o$	Yield stress rate

### Subscripts

$L$	Longitudinal
$T$	Transversal

# 1 INTRODUCTION

## 1.1 Background

The increase in oil price, significant increase in natural gas supply, and environmental concerns about global warming in the beginning of the 21<sup>st</sup> century brought natural gas to the attention of the energy market. Natural gas extraction and production was started in many remote fields, specifically the Arctic and sub-Arctic regions, leading to a need for transportation from the extraction fields to industrial or urban areas. Buried pipelines are the most efficient way to transport natural gas. While the ever-increasing exploration of natural gas resources has resulted in larger number of long pipelines, some of which are exposed to harsh environment, the major concern is to keep the transportation process safe and economical.

It is proven that for long pipelines transporting a high volume of natural gas, higher operational pressure makes the transportation more cost-effective (Corbett et al., 2003). It reduces the integrated project cost, operational cost, and the transportation cost per unit volume of gas. To withstand higher internal pressures, pipelines need to have higher strength to resist the hoop stress. Therefore, with a certain steel grade, the wall thickness of a highly pressurized pipeline will increase compared to a pipeline with a lower operating pressure. The increase in a pipeline's wall thickness boosts the capital cost of the pipeline project dramatically, because in addition to increasing the material cost, it increases the project's construction time and cost. This is particularly important because constructing pipeline projects in remote area requires transporting and accommodating large numbers of personnel, materials, and equipment far from established infrastructures.

Another way of dealing with high operating pressures is to use steel grades with higher strength. This solution is more advantageous, yet challenging. Using high strength steel (HSS) pipes makes it possible to operate pipelines with higher pressure, which makes it possible to transport larger quantities of gas and results in fewer compressor stations. In addition, it reduces the pipe diameter<sup>1</sup> and wall thickness, thus saves on the costs of materials, transportation, installation and welding. Consequently, using HSS pipes reduces the total construction time, which is critical for projects of this nature.

Some of the pipelines are crossing areas with hostile environment such as regions with seismic risks, permafrost areas, and mountains. Under severe and complex environmental loading conditions and hoop stresses up to 80% of the specified minimum yielding stress (SMYS), failure of large-diameter HSS pipes can be catastrophic. Safe implementation of HSS pipes requires complying with various and specific demands that challenge all parties involved in the pipeline projects.

Linepipe producers have to face the challenges of making pipe products with all desired material properties such as strength, ductility, weldability, acceptable defect size, good dimension tolerance, and resistance to fracture initiation and crack propagation. Pipeline contractors need to be able to work with pipes with thinner walls, which are highly susceptible to mechanical damage during construction. And, finally, pipeline designers have to ensure that highly

---

<sup>1</sup> Using HSS pipes facilitates applying higher internal pressure which results in higher flow rate. Therefore, with a constant target flow rate using HSS pipes for pipeline project results in reduction of pipe diameter (Corbett et al., 2003).

pressurized HSS pipes will safely operate in all scenarios which might occur during the project life.

The safe design of highly pressurized pipes made of HSS requires dealing with all limit states due to different operational and environmental loads. Appendix C of the current Canadian Standard – CAN/CSA Z662-07 (2007) defines and addresses the ultimate and serviceability limit states of energy pipelines. The ultimate limit states are those concerning burst or collapse and include:

- Rupture
- Yielding caused by primary loads
- Buckling resulting in collapse or rupture
- Fatigue.

The serviceability limit states are those that restrict normal operations or affect durability and include:

- Yielding caused by secondary loads
- Buckling not resulting in collapse.

Although the required pipe grade and thickness are usually determined primarily by the pipe wall's resistance against hoop stress caused by operating pressure, designers should also check the adequacy of designed pipelines for all above limit states. The last serviceability limit state (i.e., buckling not resulting in collapse) is quite common for the pipelines crossing harsh environment which imposes excessive longitudinal displacements. Longitudinal strain may be caused by the construction-operation temperature differential, ground motions caused by earthquakes, slope instability, permafrost thaw subsidence, frost heaves, etc. Excessive longitudinal compressive deformations eventually cause pipes to buckle.

When external compressive deformations are imposed on a pipeline segment, internal axial load and/or bending moment develop in that segment. Under excessive compressive deformations, the internal load/moment of the pipe increases to a peak load. Subsequently, the resistance force decreases while the deformation continues to rise. This phenomenon is referred to as wrinkling or local buckling. Depending on different conditions, buckling may occur before or after a pipe develops a fully plastic local cross section. If the applied compressive load/deformation becomes sufficiently large, plastic strains concentrate at a critical location and the structure develops a local buckle of large amplitude. This is known as a wrinkle, defined by Souza and Murray (1996) as: “a local buckle of large amplitude that is clearly visible to the naked eye and possesses the following attributes:

- I. its wave form is localized and restricted to approximately a single half-wave, or similar primitive shape,
- II. it is formed from plastic deformation, and
- III. the amplification (and growth) of the single primitive wave-form occurs coincidentally with softening.”

The effective initiation point of the wrinkle formation is the limit point of the pipe response. In other words, the point of incipient buckling is the same as the point of wrinkle initiation. The wrinkle formation continues in the post-buckling range (Yoosef-Ghodsi et al., 1995). Although the beginning of a wrinkle development in the pipe wall does not highly affect the flow of products or cause a leak, it shows the onset of the pipe’s degraded capacity to resist against excessive deformations. Excessive deformations may cause flow problems, disable the cleaning and inspection tools to operate inside the pipeline, and might act as an initiation point for ultimate limit states, e.g. fracture of pipe walls. In fact, the onset of buckling is a warning sign of other imminent ultimate limit states that may cause more catastrophic failures.

The maximum compressive strain that a pipe can resist before buckling is known as the critical buckling strain (CBS). It is one of the key limiting values in pipeline design. The CBS is expressed as a global strain with a gauge length usually twice the pipe's diameter (Dorey et al., 2001). Placing limits on the strain in lieu of stress is based on a design method called strain-based design. Strain-based design is a limit-state design method which is suitable for dealing with pipeline buckling. This method allows selected extensions to the stress-based design to benefit from the steel's well-known ability to deform plastically and preserve stability at the same time. Strain-based design is applicable under two conditions: first, the situation must be displacement controlled or at least partly displacement-controlled (this means that the pipe deformation will be completed when a given displacement is reached); second, plastic deformation must be part of the design condition. These two conditions are present once displacements are imposed to a pipeline from the aforementioned sources.

It is very difficult, if not impossible, to estimate the limiting axial (longitudinal) strain in any particular geologic condition. Researchers tend to give the maximum expected values for general design, based on parameters which naturally have less uncertainty. These parameters have been discovered by a variety of theoretical and experimental studies generating knowledge in this field.

Through reviewing a group of equations developed for CBS predictions, the next section of this chapter briefly describes the parameters affecting the longitudinal strain capacity of a pipeline under compression.

## **1.2 Parameters Employed in CBS Criteria**

Several research projects have been conducted in the past 60 years on how pipelines behave when they are subjected to either single or combined loadings. These studies have been trying to investigate the parameters affecting the

buckling resistance of pipelines and to identify their relationship to the CBS by introducing design equations. These equations use different combinations of parameters to estimate the CBS of pipelines.

A wide range of previously introduced equations for predicting CBS have been summarized by Dorey et al. (2001). Clear classification of available equations and the involved parameters makes it possible to realize if new studies are required when any aspect of pipeline buckling changes. This section describes a selected range of criteria for CBS predictions. These criteria are selected in an order representing the evolution of knowledge about the pipeline buckling phenomenon and the implementation of different parameters.

In earlier equations developed for the buckling resistance of pipelines, the CBS was only a function of a pipe's geometry. One of the simplest and earliest equations is the classical elastic equation for tubular shell structures introduced by the Column Research Council in 1966.

$$\varepsilon_{cr} = \left( \frac{1}{\sqrt{3(1-\nu^2)}} \right) \frac{t}{D} \approx 1.2 \frac{t}{D} \quad (1-1)$$

where

$\varepsilon_{cr}$ : buckling compressive strain

$\nu$ : Poisson's ratio

$t$ : wall thickness

$D$ : pipe outside diameter.

This linear equation usually gives unconservative results for the CBS. It was developed solely based on the material's elastic behaviour (Liu and Wang, 2007).

Stephens et al. (1991) developed an equation based on pipe diameter and thickness which was derived from test data compiled by a number of researchers.

The equation shows a nonlinear relationship between the  $t/D$  ratio and the critical strain,  $\varepsilon_{cr}$ , as

$$\varepsilon_{cr} = 2.42 \left( \frac{t}{D} \right)^{1.59} \quad (1-2)$$

In more advanced equations, the effect of internal pressure is also considered in the estimations. The current Canadian standard for oil and gas pipeline systems (CAN/CSA Z662-07, 2007) has an equation for determining the compressive strain limit which takes into account the differential pressure across the pipeline segment wall. This equation is recommended for pipelines under combined axial force and bending moment.

$$\varepsilon_{cr} = 0.5 \frac{t}{D} - 0.0025 + 3000 \left[ \frac{(p_i - p_e)D}{2tE_s} \right]^2 \quad (1-3)$$

where

$E_s$ : modulus of elasticity of steel pipe

$p_i$ : internal pressure

$p_e$ : external pressure.

In addition to the  $D/t$  ratio and internal pressure, a material property parameter (i.e., modulus of elasticity) is also included in this equation. However, since the variation of the modulus of elasticity is very limited in pipeline steels, the CBS predicted by this equation does not significantly fluctuate from one steel type to another.

Since the local buckling in pipelines is an inelastic phenomenon, some standards include plastic material properties in their equations. The CBS equation developed by the Det Norske Veritas Offshore Standard (DNV-OS-F101, 2007) includes a factor of maximum allowed yield-to-tensile stress ratio as an indicator

of the steel's plastic work hardening capacity. A higher yield-to-tensile strength ratio indicates lower plastic work hardening capacity and vice versa. The DNV equation is recommended for submarine pipeline systems under bending moment,

$$\varepsilon_{cr} = 0.78 \left( \frac{t}{D} - 0.01 \right) \left( 1 + 5 \frac{\sigma_h}{f_y} \right) \alpha_h^{-1.5} \alpha_{gw} \quad (1-4)$$

where

$\sigma_h$ : characteristic transverse stress

$f_y$ : yield strength of the pipe material

$\alpha_h$ : maximum allowed yield-to-tensile stress ratio

$\alpha_{gw}$ : correction factor if girth weld is present (linear function of D/t ; equals 1 if no welds).

Another factor that DNV included in the CBS estimation is the girth weld effect, i.e.  $\alpha_{gw}$ . It is well established that due to the material and geometrical disturbance induced by the girth weld, segments of pipeline with girth weld show a lower buckling resistance compared to plain segments.

Dorey et al. (2002) studied the effects of material properties on the buckling response of linepipes and showed that the CBS is affected by the material response in yielding region. They concluded that the CBS is affected by both steel grade (steel pipes with higher yield strength have a lower CBS) and the shape of the stress-strain curve in the yielding and early plastic regions. Pipe specimens that show a distinct yield plateau in the material tests have a lower CBS compared to pipe specimens with a continuous yield region (rounded material yield curves).

Initial imperfections also affect the CBS. Initial imperfections of pipelines essentially originate from different sources, such as production tolerances, transportation and construction. Pipeline imperfections include out-of-straightness, out-of-roundness, thickness and radius changes. Although initial imperfections might not change the magnitude of a pipe buckling strength, they

can reduce the compressive strain capacity quite significantly (Limam et al., 2010; Dorey et al., 2006a).

Dorey et al. (2006b) proposed four equations to estimate the CBS in pipelines subjected to combined axial force and bending moment. Depending on the material behaviour (rounded stress-strain curve or with distinct yield plateau) and whether the pipe segment is plain or has a girth weld, one of four Dorey's equations can be applied. For instance, the following equation estimates the CBS for plain pipe sections (without girth weld) with a typical rounded material property curve:

$$\epsilon_{cr} = \left( \frac{2.94}{D/t} \right)^{1.59} \left( \frac{1}{1 - 0.868 \left( \frac{p}{p_y} \right)} \right) \left( \frac{E}{F_y} \right)^{0.854} \left( 1.27 - \left( \frac{imp}{100} \right)^{0.150} \right) \quad (1-5)$$

where

$p$ : internal pressure

$p_y$ : internal pressure that causes yielding in the transverse (hoop) direction

$F_y$ : yield strength of the pipe material

$imp$ : initial imperfection expressed as a percentage of the wall thickness for a blister-type initial imperfection pattern.

This set of four equations introduced by Dorey et al. (2006b) is the most comprehensive equation in terms of taking all affecting parameters into account. Based on these equations, the CBS of steel pipes is a function of:

- diameter to thickness ratio
- internal pressure
- initial imperfections
- presence or absence of girth weld

- material properties.

All aforementioned equations have been developed based on experimental and/or numerical studies on normal-strength steel pipes. Since the major differences between normal-strength steel pipes and the HSS line are the material properties, this study focuses on the material properties.

As indicated by Ishikawa et al. (2007 and 2009), the key material property affecting the buckling resistance of steel pipelines is deformability. A higher deformability of the pipe material results in a larger compressive strain before buckling. If a pipe is made of a steel material with poor deformability, compressive strain (due to externally induced deformations) can easily localize to reach a level enough for wrinkling.

Although the main factors that influence the deformability of linepipe steel are not fully understood, it is generally known that the deformability is closely related to the yield-to-tensile strength ratio, the amount of uniform elongation, the strain hardening exponent, and the shape of the stress-strain curve (Seo et al., 2008).

As material strength is important for load control conditions, deformability is the desired material property for displacement control situations. The stress-based design method is a suitable approach for load control conditions in which the structure is designed to resist a certain level of applied loads. Based on this design method, the stress level in the structure should be less than the allowable design stress, with a certain design margin below the yield strength. Figure 1-1 shows the concept of the stress-based design with respect to the material properties and applied stress. Two types of material properties, A and B, are shown in this figure. While both types have similar elastic stiffness and ultimate strength, material type A shows a higher strength in the yielding region compared to material type B. Therefore, material type A can carry larger loads without any plastic

deformations; or, under a similar load, the safety margin for material type A will be larger compared to material type B.

In displacement control conditions, especially when the plastic deformation is part of the design condition, the allowable strain limit provides a safe margin to the ultimate strain limit. This approach, which is the basis of the strain-based design method, is illustrated in Figure 1-2. The schematic material types A and B are similar to those in Figure 1-1. As this figure shows, both material types underwent plastic deformations and have margins similar to the ultimate strain limit. However, material type B develops a lower stress level under the applied deformation compared to material type A. Therefore, a structure made of material type B has greater reserved strength after applying the deformation and is more stable compared to a similar structure made of material type A. Consequently, any structure made of material type B has a higher degree of deformability compared to material type A.

Highly pressurized pipelines crossing harsh environments (e.g. permafrost or seismic regions, or areas susceptible to ground movement or slope instability) are under both load-control and displacement-control conditions. The hoop stress due to the operating pressure has a load control nature. Therefore, the pipe steel should provide high yield strength in the transverse direction to resist these pressures. On the other hand, axial loads and bending moments built up due to environmentally induced deformations have a displacement control nature, i.e. the development of internal loads stops when a certain deformation is achieved (Macia et al., 2010). As a result, a desirable material for highly pressurized pipelines in hostile environments should have different properties in longitudinal and transverse directions. The primary feature for the steel material is to have enough strength to resist the extreme operating pressures that cause high hoop stress. The secondary desired material property is having the capacity to accommodate externally induced longitudinal strains from a variety of sources.

Pipeline producers try to address these dual demands on the material by producing a new generation of HSS pipes. The next section describes the main material properties of HSS pipelines as presented in current literature.

### **1.3 High Strength Steel Pipes**

In the field of engineering, the definition of the term “high strength” is rather time-dependent. Currently, pipes made of grades X80, X100, and X120 (having SMYS of 550, 690 and 825 MPa, respectively) are considered HSS pipes. Pipe producers came up with specific chemical compositions as well as rolling and thermal treatments to satisfy all demands on the final product. The final steel products are produced as plates with different thicknesses that possess the required properties in terms of yield and ultimate strengths, weldability, toughness, corrosion, strain aging, etc. (for more details on the production of HSS plates see Shinohara et al., 2007; Seo et al., 2008; and Muraoka et al., 2010).

The final stage in steel linepipe production is forming the flat plates into pipes. There are two methods of making pipes from steel plates: the spiral forming (helical welding) and the UOE process. In the spiral pipe formation, plates are spirally bent and the forming process is finished by welding the spiral seam along the pipe segment. The UOE pipe-making process has three sequential formation steps. In the U stage, a punch with an adapted radius is pushed into the plate’s mid-section, making a U-shape of the plate’s cross section. Then, an O press completes the process of forming an almost round, open-seam tube. After welding the longitudinal seam, the last step is the mechanical expansion, the E stage, which makes the pipes rounder and straighter.

These two pipe-making processes apply different plastic deformations to the pipe body. In the spiral-welded pipes, the plastic deformation has components in the pipe’s longitudinal and transverse directions. In this method, pipe’s wall only

experiences plastic deformation due to bending; i.e., the inner parts of the pipe deform in a compressive mode while the outer parts deform in a tensile mode. As a result, the average plastic deformation through the thickness of the pipe due to the pipe formation is zero. In UOE pipes, however, all deformations are applied in the transverse direction in forms of bending and uniform plastic strains. During the U and O stages, the pipe body experiences bending stresses. In the E stage, the pipe expansion results in circumferential tensile plastic strains that are uniform throughout the entire thickness of the pipe's wall.

Due to the Bauschinger's effect, plastic deformations applied to the pipe body during the pipe formation process result in special material properties in the final products of HSS pipes. Since the histories of plastic deformations are different in spiral-welded pipes and UOE pipes, they show different features of material responses in the longitudinal and transverse directions. Numerical and experimental models have been developed in the literature to predict the final products' properties based on the formation processes (See Lui and Wang, 2007; Thibaux and Adeele, 2010; and Hilgert et al., 2010).

In a study about forming plastic strains and their influence on the yielding behaviour of HSS pipes' materials, Walsh and Preston (2010) explained the difference between UOE and spiral-welded HSS pipes. They concluded that forming operations that load the entire cross section in a single direction tend to leave a stronger Bauschinger's effect. Therefore, the Bauschinger's effect is insignificant when the forming operation involves bending only, because the tensile and compressive contributions tend to cancel each other out. On the other hand, the Bauschinger's effect is more significant in expansion and sizing operations because the entire cross section is loaded in a single direction.

The results of a study by Bian et al. (2011) on the material properties of spiral-welded and UOE HSS pipes agree with above conclusions. They showed that

since the spiral-welded HSS pipes only experienced bending plastic strains during the spiral-forming process, the overall applied work hardening was small. Therefore, the difference between the longitudinal and transversal yield strengths is not significant. In UOE pipes, however, the expansion stage applies a uniform tensile strain in the transverse direction of the pipes, typically in the range of 1.0% – 1.5%. This work hardening due to the expansion enhances the material strength and consumes the material ductility in the transversal direction. This phenomenon leaves a significant level of plastic anisotropy in the material response of HSS pipes made by the UOE process. Anisotropic material responses have been highlighted in several papers and technical reports about HSS pipes formed by the UOE process.

Generally, the anisotropy is manifested by a higher proportional limit and yield strength in the transverse direction compared to the longitudinal direction of HSS pipes formed by the UOE process. This translates to higher yield strength in the transverse direction along with higher deformability in the longitudinal direction. These features perfectly fit to the load and deformation demands on the material in the longitudinal and transverse directions of a buried linepipe, i.e. high yield strength in the transverse direction to resist the high internal pressures and high deformability in the longitudinal direction to resist externally induced deformations. This suitability might explain why the majority of HSS pipe productions reported in the literature are UOE pipes.

The available knowledge on the structural behaviour of energy linepipes has been generally developed through studies of normal-strength steel pipes in which the level of anisotropy was not significant enough to draw much attention. Conventionally, these studies have employed isotropic material models using tensile stress–strain data from longitudinal coupon tests. This conventional material modeling method is incapable of simulating the anisotropic properties of

HSS pipes' material and may provide inaccurate results if used to simulate these pipes' structural behaviour.

Since the HSS pipes came to the market, there have been a few attempts to deal with the anisotropic material properties of HSS pipes. Two types of anisotropic material models for metals have been used for HSS pipes: the Hill's non-quadratic model, and the combined (isotropic and kinematic) hardening model. Liu and Wang (2006) suggested that the combined hardening model is more appropriate for material modeling of HSS pipes because it incorporates the Bauschinger's effect and can simulate different tensile and compressive responses.

Based on the above discussions, it seems worthwhile to develop an accurate anisotropic material model for HSS pipes based on a comprehensive study of material properties. This material model should be capable of accurately simulating the material responses under all stress paths that an onshore energy pipelines might undergo. This model should also have a straightforward calibration process. Such a model can serve as a useful tool to understand the effects of different material properties on the structural behaviour of HSS pipes when anisotropy is present.

## **1.4 Problem Statement**

Numerous advancements have been made in the production of HSS pipes in recent years and HSS pipes have been used in some pipeline projects. The safe use of HSS linepipes requires a comprehensive understanding of their performance in all possible limit states. Local buckling due to externally induced deformations is one of the complex and yet challenging limit states of energy pipelines that is affected by different factors, including the material properties. Based on previous studies, one of the material properties affecting the CBS of pipelines is the steel grade. Therefore, the potential resistance of HSS against

applied deformations is expected to be different from that of normal-strength steel pipes. Besides, the unique anisotropic material properties of HSS pipes make them substantially different from normal-strength steel pipes. Therefore, considering the unique HSS pipe material properties, the current knowledge about linepipes' buckling behaviour should be updated.

Comprehensive studies of this subject should include finite element studies, because it is impossible to test HSS linepipes with all conceivable combinations of material, geometry, and operation conditions. Previous research on normal-strength steel pipes has resulted in abundant developments in the finite element modeling of steel linepipes in terms of appropriate mesh generation, element type, solution strategies, etc. The main difficulty in finite element analyses of HSS linepipes is anisotropic materials modeling. The isotropic method of material modeling that has been used by research projects dealing with normal-strength steel pipes and -despite the significant anisotropy- even HSS pipes, is unable to simulate the material response under all possible stress paths. The primary requirement for accurate finite element modeling of HSS pipes is a suitable anisotropic material model. This model should be able to simulate the material response in all possible stress paths and the range associated with the considered limit state.

The next subject that needs to be explored is the pattern through which the material properties of HSS pipes affect the pipes' behaviour in different conditions. Due to the anisotropy, the number of parameters required to define the material response in longitudinal and transverse directions is higher compared to that of isotropic material models. Correlating these parameters to the pipe response in a simple and comprehensible manner is a worthwhile research. Once this study is accomplished, the results can be used in other investigations about the desired material properties of HSS linepipes for strain-based design. This will

help pipeline companies to select products suitable for their needs and pipeline producers to better target the necessary properties for their final products.

## **1.5 Objectives and Methodology**

This research project is designed to address the concerns stated in section 1.4. The primary objective of the proposed research project is to understand how the significant difference between the HSS pipes' longitudinal and transversal material properties affect the pipes' capacity for longitudinal compressive strains.

The study results will be used to introduce guidelines for efficient material modeling, which will use a practical and precise technique to capture the material's anisotropic behaviour. This modeling method will be used to acquire a better understanding of how other parameters affect the CBS of HSS pipes when the difference between the longitudinal and transverse deformability is accounted for. Therefore, to achieve the objectives stated above, the following specific steps were considered:

1. Carry out a quantitative study of the similarities and differences in elastic and plastic behaviour of HSS pipes material in longitudinal and transverse directions, based on available experimental stress-strain curves.
2. Find the most suitable metal plasticity model that can potentially represent observed material response patterns in longitudinal and transverse directions of HSS pipes.
3. Introduce an anisotropic material model, based on the observations made in the study of longitudinal and transverse stress-strain curves, which can be easily calibrated and used by pipeline designers.
4. Verify the proposed material model by using experimental stress-strain data of longitudinal and transverse directions.

5. Incorporate the proposed material model in the finite element modeling and analysis of HSS pipes.
6. Validate the finite element models of HSS pipes with the proposed anisotropic model by using results of full-scaled buckling tests on HSS pipes.
7. Perform a comprehensive parametric study using the validated finite element and material models on the key parameters that influence linepipe buckling.
8. Investigate how the material anisotropy affects the buckling resistance of HSS pipes under different combinations of geometry, operation, material properties, etc.
9. Use the proposed material model to study the buckling mechanism and the effects of material properties on the buckling response when anisotropy is present.
10. Use the proposed material model to understand what features of material properties in different directions of HSS pipes are important for the buckling resistance.

## **1.6 Thesis Layout**

This report consists of seven chapters, including this chapter. Chapter 2 describes all elements of a study conducted to develop a practical model (in terms of accuracy and simplicity) for anisotropic materials of HSS pipes. It describes general patterns of the HSS pipes' material response in longitudinal and transverse directions. Then it focuses on the regions of the material response that are more important for the buckling response. The material database of HSS pipes used in Chapter 2 consists of 152 material coupon test results conducted on the materials of eight different HSS pipes. The remainder of this chapter is allocated to the development of an anisotropic material model for HSS pipes with typical

anisotropic materials. This includes finding a general pattern applicable for all material types in the database, developing a hypothesis, introducing a novel model, calibrating a model and, finally, validating the model's performance.

Chapter 3 outlines the details of finite element models and analyses developed for 15 HSS pipes. These pipes had been tested for buckling under different load combinations and were made of materials studied in Chapter 2. A brief introduction and review of the concept of the finite element method is presented, followed by a detailed discussion of the specific features implemented in this research project. Two types of material modeling methods were used for the finite element models developed in Chapter 3: the conventionally used isotropic model and the anisotropic model developed in Chapter 2. The results of buckling analyses of both models are compared with experimental measurements. The advantages of using the anisotropic material modeling are discussed later in this chapter.

Chapter 4 presents a parametric study on 486 cases of HSS linepipe models with different values of parameters that are important for pipe buckling. The Buckingham-Pi Theorem was used to develop a set of six non-dimensional parameters to study the effects of all factors on the CBS of HSS pipes. The effects of operating pressure, diameter-to-thickness ratio, initial imperfection magnitude, material grade, plastic work hardening, and the ratio of longitudinal-to-transversal yield strength were taken into account. The finite element models were analyzed under a pure bending moment condition and the CBS was examined under different combinations of affecting parameters. As per this research project's objectives, this chapter's results were used to develop an insight into the material properties' effects on the buckling resistance of HSS pipes with anisotropic materials. The CBS of HSS pipes with different geometry, material, and operation conditions versus the level of material anisotropy are presented in several graphs.

Despite the evident material anisotropy of HSS pipes, many researchers have been using the isotropic material model in their finite element analyses. The neglect of this effect is partly due to the lack of understanding of the mechanism through which the material properties affect the pipeline's buckling response. The anisotropic material model developed in Chapter 2 was used in Chapter 5 to explore the effects of mechanical properties of material on CBS of HSS pipes under a more generalized buckling condition. Chapter 5 presents the results of a finite element study on one unpressurized and one pressurized pipe under different combinations of bending moment and compressive axial load. Four material modeling methods were used in these finite element models: the anisotropic material model, and three isotropic models using material responses for longitudinal tension, longitudinal compression, and transverse tension. The results of this chapter demonstrate how the material properties affect the buckling response of HSS pipes. In addition, this chapter shows which aspect of the material response has the most important role in strain-based design.

Chapter 6 describes a case study on the material properties and buckling response of thermally coated HSS pipes. This includes a literature review about changes to material properties due to the thermal aging and typical anisotropy aspects of thermally coated HSS pipes. This is followed by a finite element study on two HSS pipes (one unpressurized and one pressurized) that had been tested for buckling after being thermally coated. Intact and modified forms of the anisotropic material model (developed in Chapter 2 for uncoated HSS pipes) were used in the finite element models. The modifications applied to the anisotropic model were based on the results of Chapter 4 and Chapter 5. The final results show that with minor modifications, the anisotropic material model developed in this research project is also useful for thermally coated HSS pipes.

Chapter 7 presents an overall summary of the research project, and a conclusion of the findings that outlines the expected improvement that HSS pipes can bring

to the pipeline industry regarding strain-based design. This chapter also provides recommendations that can be used in future studies, especially for developing design criteria for HSS pipes with anisotropic materials.

## References

Bian Y., Penniston C., Collins L. and Mackenzie R., (2011), "Evaluation of UOE and Spiral-welded Line Pipe for Strain-based Design", 2010 ASME International Pipeline Conference, IPC 2010, September 21, 2010 - October 1, American Society of Mechanical Engineers, Calgary, AB, Canada, v4, pp 139-148.

Canadian Standard Association, (2007), "Z662-07 Oil and Gas Pipeline Systems", Canadian Standard Association, Etobicoke, Ontario.

Corbett K.T., Bowen R.R. and Petersen C.W., (2003), "High Strength Steel Pipeline Economics", Proceedings of the Thirteenth International Offshore and Polar Engineering Conference, May 25, 2002 - May 30, International Society of Offshore and Polar Engineers, Honolulu, HI, United states, pp. 2355-2362.

Det Norske Veritas, (2007), "Offshore Standard, DNV-OS-F101, Submarine Pipeline Systems," Det Norske Veritas, Norway.

Dorey A.B., Cheng J.J.R. and Murray D.W., (2001), "Critical Buckling Strain in Energy Pipelines", Structural Engineering Report No. 237, Department of Civil and Environmental Engineering, University of Alberta, Edmonton, Alberta, 346 pages.

Dorey A.B., Murray D.W. and Cheng J.J.R., (2002), "Material property effects on critical buckling strains in energy pipelines", Proceedings of the 4th International Pipeline Conference, September 30, 2002 - October 3, American Society of Mechanical Engineers, Calgary, Alta., Canada, A, pp. 475-484.

Dorey A.B., Murray D.W and Cheng J.J.R., (2006a), "Initial Imperfection Models for Segments of Line Pipe", Journal of Offshore Mechanics and Arctic Engineering, 128(4) pp. 322-329.

Dorey A.B., Murray D.W., and Cheng J.J.R. (2006b), “Critical Buckling Strain Equations for Energy Pipelines – A Parametric Study”, *Journal of Offshore Mechanics and Arctic Engineering*, 128(3), pp. 248-255.

Hilgert O., Höhler S., Zimmermann S. and Kalwa, C., (2011) ,”Numerical Modeling of Plastic Deformations in UOE Line Pipe”, 2010 ASME International Pipeline Conference, IPC 2010, September 21, 2010 - October 1, American Society of Mechanical Engineers, Calgary, AB, Canada, v4, pp 375-383.

Ishikawa N., Okatsu M. and Endo S., (2007), “Design concept and production of high deformability linepipe”, 2006 6th International Pipeline Conference, IPC 2006, September 25, 2006 - September 29, American Society of Mechanical Engineers, Calgary, AB, Canada, v3 Part A, pp. 215-222.

Ishikawa N., Okatsu M. and Shimamura J., (2009), “Material development and strain capacity of grade X100 high strain linepipe produced by heat treatment online process”, 2008 ASME International Pipeline Conference, IPC 2008, September 29, 2008 - October 3, American Society of Mechanical Engineers, Calgary, AB, Canada, v3, pp. 713-720.

Johnston B.G., (1966), “Column Research Council Guide to Design Criteria for Metal Compression Members”, John Wiley and Sons, New York, NY.

Limam A., Lee, L.H. and Kyriakides S., (2011), “Effects of Local Imperfections on the Collapse of Tubes Under Bending and Internal Pressure”, 2010 ASME International Pipeline Conference, IPC 2010, September 21, 2010 - October 1, American Society of Mechanical Engineers, Calgary, AB, Canada, v4, pp 313-320.

Liu M. and Wang Y., (2007), “Modeling of Anisotropy of TMCP and UOE Linepipes”, *International Journal of Offshore and Polar Engineering*, 17(4) pp. 288-293.

Liu M. and Wang Y., (2007), “Advanced Modeling of Plasticity of Linepipe Steel with Anisotropic Texture and Complex Loading History”, 17th 2007 International Offshore and Polar Engineering Conference, ISOPE 2007, July 1, 2007 - July 6, International Society of Offshore and Polar Engineers, Lisbon, Portugal, pp 3093-3100.

Macia M.L., Kibey, S.A. and Arslan, H., (2011), ”Approaches to Qualify Strain-Based Designed Pipelines”, 2010 ASME International Pipeline Conference, IPC 2010, September 21, 2010 - October 1, American Society of Mechanical Engineers, Calgary, AB, Canada, v4, pp 365-374.

Muraoka R. and Kondo J., (2011), “Production of Grade X80 High Strain Linepipes for Seismic Regions Application”, 2010 ASME International Pipeline Conference, IPC 2010, September 21, 2010 - October 1, American Society of Mechanical Engineers, Calgary, AB, Canada, v4, pp 287-292.

Seo , D.H, Yoo, J.Y., Song, W.H. and Kang, K.B., (2008), “Development of X100 Linepipe Steel with High Deformation Capacity”, 2008 ASME International Pipeline Conference, IPC 2008, September 29, 2008 - October 3, American Society of Mechanical Engineers, Calgary, AB, Canada, v3, pp 585-592.

Shinohara Y., Hara T., Tsuru E. and Asahi H., (2007), “Development of High Strength Steel Line Pipe for Strain-Based Design Applications”, 17th International Offshore and Polar Engineering Conference, ISOPE 2007, July 1, 2007 - July 6, International Society of Offshore and Polar Engineers, Lisbon, Portugal, v18, n 3, pp 220-225.

Souza L.T. and Murray D.W., (1994), “Prediction of Wrinkling Behaviour of Girth Welded Line Pipe”, Structural Engineering Report No. 197, Department of Civil and Environmental Engineering, University of Alberta, Edmonton, Alberta, 134 pages.

Stephens, D.R., Olson, R.J. and Rosenfeld, M.J., (1991), “Topical report on pipeline monitoring – Limit state criteria”, Battelle, NG-18 Report No. 188, Columbus, OH.

Thibaux P. and Adeele F.V., (2011), “Influence of the Forming Operations on the Yield Stress Measured on Pipe”, 2010 ASME International Pipeline Conference, IPC 2010, September 21, 2010 - October 1, American Society of Mechanical Engineers, Calgary, AB, Canada, v2, pp 399-407.

Walsh W.J. and Preston D., (2011), “Yield Strength of Line Pipe – Analysis Of Forming Operations and Flattened Straps”, 2010 ASME International Pipeline Conference, IPC 2010, September 21, 2010 - October 1, American Society of Mechanical Engineers, Calgary, AB, Canada, v2, pp 891-905.

Yoosef-Ghodsi N., Kulak G.L. and Murray D.W., (1995), “Some Test Results for Wrinkling of Girth Welded Linepipes”, Proceedings of the 14th International Conference on Offshore Mechanics and Arctic Engineering (OMAE95) vol. V- Pipeline Technology, ASME. pp. 379-388.

## Figures

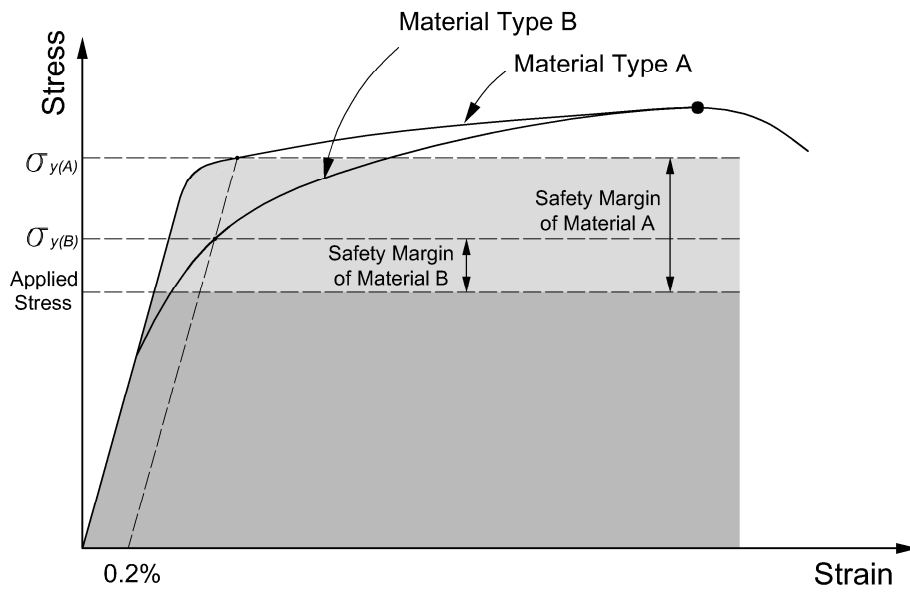


Figure 1-1 Stress-based design concept

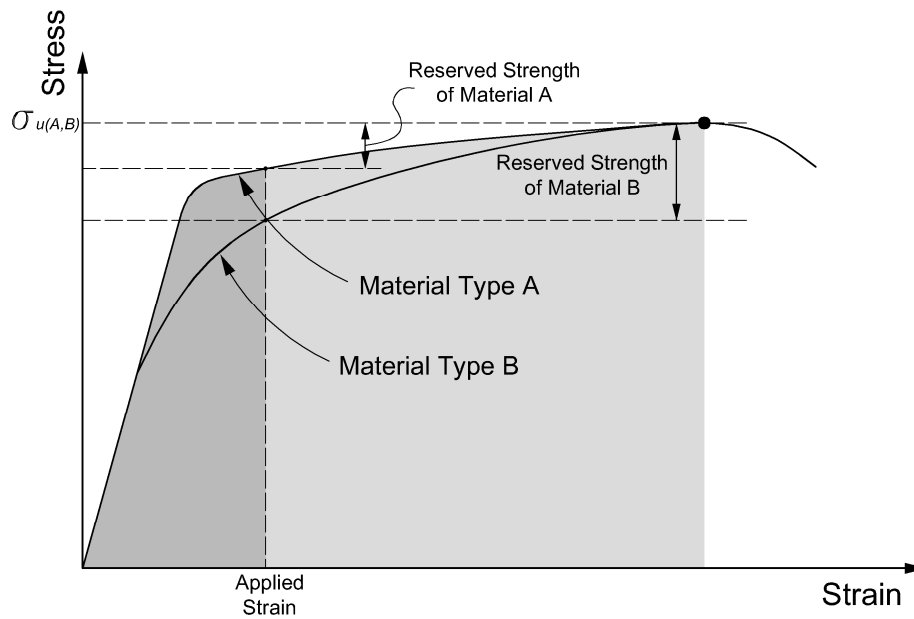


Figure 1-2 Strain-based design concept

## **2 ANISOTROPIC MATERIAL MODELING METHOD FOR HSS PIPES USING COMBINED HARDENING CONCEPT**

The primary quality for the material properties of a highly pressurized pipeline is the ability to resist high internal pressures that cause hoop (transverse) stresses. If the pipeline is crossing a hostile environment, it should also have the capacity to accommodate extensive (externally induced) deformations in the longitudinal direction. In other words, the pipe should have enough strength in the transverse direction and, at the same time, it should have adequate deformability in the longitudinal direction. Although the main factors that influence the deformability of pipeline steel are not fully defined, it is generally known that these factors are closely related to the yield-to-tensile stress ratio, the amount of uniform elongation, the strain hardening exponent, and the shape of the stress-strain curve (Seo et al., 2008).

This dual demand has led pipeline producers to come up with pipeline products that have a high proportional limit and yield strength in the transverse direction as well as a low proportional limit and yield-to-tensile stress ratio in the longitudinal direction. Hence, although the anisotropy observed in high strength steel (HSS) pipes' material is essentially a result of the plastic deformations applied to the pipes in the pipe-making process, it is somehow inspired by the different demands on a pipeline in the field. Therefore, anisotropy more or less, exists in all new generations of HSS pipes (i.e. grade X80, X100 and X120) as the producers try to maintain the deformability in the longitudinal direction while trying to enhance the strength in the transverse direction.

Although it seems that anisotropy does not have any significant effect on the pipe's response to internal pressure, for more complicated limit states such as

local buckling, it might change the pipe's response compared to cases with no anisotropy. The effects of the material anisotropy on the buckling response of HSS pipes is a legitimate engineering question because one of the main factors that changes the longitudinal deformation capacity of pipelines is material deformability, and in HSS pipes, the level of deformability is different in longitudinal and transverse directions due to anisotropy.

The majority of studies on the buckling response and CBS predictions of energy pipelines have been performed on normal-strength pipes. Since previous works did not account for the effects of material anisotropy on the pipe's behaviour, current understanding about pipeline buckling should be updated and the available criteria for the CBS should be reassessed (or probably modified) before they are used for HSS pipes.

Most of the numerical and analytical research on the buckling response of HSS pipes has ignored the anisotropy and used isotropic material properties. Meanwhile, there have been few attempts to address the material anisotropy of the pipe when the critical buckling strain (CBS) is being studied. A limited number of researchers showed that the stress-strain behaviour in the transverse direction may have an appreciable impact on the pipeline buckling strain capacity (Adeeb et al., 2007; and Liu et al., 2007), but a comprehensive study on the material anisotropy of HSS pipes and a guideline for modeling the material anisotropy are still lacking.

Careful study of the effects of anisotropy on the buckling response of HSS pipes requires a powerful material model, capable of simulating the material responses in different directions of the pipe and under all possible stress paths during the buckling process. In this chapter, the material responses of HSS pipes were studied using a comprehensive database of material test results performed on 15 pipes made of eight different HSS materials. Based on the observations made on

different material responses of HSS pipes, an anisotropic material model was developed for studying the CBS of HSS pipes. This material model was intended to capture all aspects of anisotropy that are important for the buckling response and it can be easily calibrated by routine material test results of pipeline.

## **2.1 HSS Pipes' Material Database**

A database containing 152 stress-strain curves from eight different types of HSS pipes' material was used in this chapter for developing the anisotropic material model. Strap and round-bar tension coupons that had been used for material tests were cut from longitudinal and transverse directions of HSS pipes. The HSS pipes' materials that are called types A to H in this chapter were from different mills of X80 and X100 steel grades with three different outer diameter and two different wall thicknesses. Table 2-1 shows the material grade and nominal dimensions of the parent HSS pipes as well as the number of different tension coupons tested for each material type. As this table shows, there are few compression test results in the database for three types of the HSS pipes' materials which belong to longitudinal round-bar coupons.

All eight pipes were formed from steel plates through the UOE pipe-making process. For material types A, C, D, E, and H, all specimens were taken from two positions around the pipe circumference: 3 o'clock and 9 o'clock (when the seam-weld is located at 12 o'clock). For material types B, F, and G, the specimens were taken from 6 o'clock, 7 o'clock and 9 o'clock. Tsuru et al. (2007) showed that the UOE pipe-making process changes the distribution of yield strength around the pipe's circumference; therefore the specimen might show a different yield-to-tensile strength ratio in material tests depending on the distance of the sampling location to the seam weld. This phenomenon, which is also reported by Li et al. (2010), might have significant effects on the assessment of the pipe's longitudinal

strain capacity because it might affect the perceived level of material ductility. Nevertheless, all above material data were considered good representatives for the material properties of each pipe. However, based on the above discussion, the specimens from the second group of material types (B, F, and G) represent a more comprehensive picture of the pipes' material response.

The tension stress-strain data fall under four different groups based on the shape and orientation of the tension coupon specimens:

- Round-bar coupons in the longitudinal direction
- Strap coupons in the longitudinal direction
- Round-bar coupons in the transverse direction
- Flattened strap coupons in the transverse direction.

Recent research on pipeline materials showed a number of advantages and drawbacks regarding different material testing methods, specimen shape, and size for longitudinal and transverse directions.

The main challenge in the material testing of pipelines is to obtain the material response in the transverse direction. Saikaly et al. (1996) recommended using a ring expansion test to obtain a true measure of a pipe's transversal yield strength. However, according to Crone et al. (2010), the ring expansion test has its own limitations. Not only it is impossible to evaluate the ultimate tensile strength, it is even difficult to extend the test past 0.6% strain due to the limitations of the test specimen. Alternatively, tension coupon tests can provide the full stress-strain response of the material but their major limitation is that they require straight specimens. There are two ways to prepare a straight specimen from the transverse direction of a pipe: flattening a circumferential arched strap cut from the pipe, or machining a straight round-bar specimen through the pipe's thickness.

The flattened strap has been the most common method for qualifying pipeline products. Its major drawback is that the preparation methods, specifically the flattening procedures, can have a significant effect on the measured yielding behavior. As a result, flattened straps measure significantly lower yield strength in the transverse direction compared to ring expansion results. This loss of yield strength is due to the Bauschinger effects during the flattening process (Klein et al., 2008 and Li et al., 2010).

On the other hand, round-bar tensile specimens have their own drawbacks in testing and preparation (due to the pipe's circumferential curvature). Sampling round-bar specimens requires extra care, especially for smaller pipe diameters. As the specimen must be prepared out of a non-flattened formed pipe, part of the thickness should be machined off. In some cases, some steel parts need to be welded to the grip section to ease the machining of the specimens' reduced gauge area. Removing part of the thickness in order to make a straight specimen makes it impossible to test the entire pipe thickness by a round-bar sample. In some cases only half of the thickness is tested due to the geometric restrictions (depending on the diameter-to-thickness ratio). It is reported that removing the fine-grained surface material during preparation of round-bars may result in reduction of yield strength (see Klein et al., 2008 and Li et al., 2010).

Despite all the aforementioned difficulties and drawbacks, several researchers believe that round-bar specimens provide more reliable results compared to flattened straps, because the yield strength reported by round-bar specimens is very close to the ring expansion results (Klein et al., 2008). However, the more conservative results of yield strength measured by flattened straps can be used to qualify the products' grade (Crone et al., 2010).

Unlike the transversal yield strength, which is quite sensitive to the testing method, it is reported that the ultimate tensile strength is not significantly affected

by the testing method or the sample's geometry (Li et al., 2010). Consequently, for strain-based design concerns, lower yield strength results in a lower estimation of the yield-to-tensile strength ratio (which is an indicator of material work hardening) and an overestimation of the pipe products' longitudinal strain capacity. Therefore, it was decided to use only the round-bar tension test results in the present study and discard the results of the flattened straps for transverse directions.

In the longitudinal direction of steel pipes, however, no significant difference between the results of strap and round-bar coupons has been reported, and using round coupons results in the same outcome as using strap coupons (Lessem et al., 2008 and Klein et al., 2008). Therefore, it was decided to maintain both longitudinal round-bar and strap tensile specimens in the study of material behaviour.

As a result, from all 152 coupon tests, 113 stress-strain data from eight material types were used in the material study.

## **2.2 Major Features of HSS Pipes Material Responses**

The material properties obtained from the coupon tests were expressed in terms of engineering stress versus engineering strain. In this form of material data, the stress and strain are functions of the undeformed cross sectional dimensions. This form of input should be converted to the true stress-true strain data based on the updated cross sectional dimensions before they can be used for any material studies.

The following equations were used to convert the engineering stress, and engineering strain, to the true stress and true strain, as

$$\sigma_{true} = \sigma_{eng} (1 + \varepsilon_{eng}) \quad (2-1)$$

$$\varepsilon_{true} = \ln(1 + \varepsilon_{eng}) \quad (2-2)$$

where

$\sigma_{true}$ : true stress

$\sigma_{eng}$ : engineering stress

$\varepsilon_{true}$ : true strain

$\varepsilon_{eng}$ : engineering strain.

Hereafter, the terms stress and strain refer to the true stress and true strain, respectively. Figure 2-1 to Figure 2-8 show the longitudinal and transverse (tensile) stress-strain curves of material types A to H. In these figures, the longitudinal stress-strain curves are shown by a solid black line and the transverse stress-strain curves are shown by gray lines.

Several material properties can be extracted from different parts of a complete stress-strain curve. Hart et al. (1996) divided the entire range of stress-strain response of a pipeline material in five major sections. Figure 2-9 shows these five sections on a schematic stress-strain curve. These regions are:

- The linear-elastic region. The behaviour of the steel material is linear and elastic and this region ends in the proportional limit point. Additional loading beyond this point leaves permanent deformations.
- The yielding region, which starts after the linear-elastic region. The tangent modulus becomes progressively smaller in this region.
- The strain hardening region, which starts after the yielding process is complete. The specimen continues to strain-harden in this essentially linear region.
- The constant strength region. In this rather long region, the stress-strain curve becomes flat and the material reaches its ultimate tensile strength.

- The strain softening and fracture region. In this region the strength reduces, the cross section necks, and the specimen ultimately fractures.

Not all these regions affect the CBS of pipelines. The buckling onset associates with the localization of the longitudinal strain in the buckling location. Before the incipient buckling, the longitudinal strain is distributed quite uniformly along the pipe. The CBS in HSS pipes hardly exceeds 3.0%; therefore, it is only affected by elastic and early plastic material properties (Hart et al., 1996). Hence, to study the pipe's response up to the buckling point, the focus of the material study could be placed on these regions (i.e., the elastic and early plastic responses). The intended material modeling method for studying the pipe's response up to the incipient buckling should adequately simulate the material response in this region.

Figure 2-10 to Figure 2-17 show tensile stress-strain curves of material types A to H, up to 3.0% total strain. The longitudinal curves contain both round-bar and strap coupon test results and the transverse curves contain only round-bar coupon results. These stress-strain curves contain the first three regions (i.e., linear elastic, yielding region, and linear strain hardening regions) of the five illustrated in Figure 2-9.

As Figure 2-10 to Figure 2-17 show, the stress-strain curves of longitudinal and transverse directions have some differences and similarities. Up to 3.0% total strain, the HSS pipes' material behaviour in both directions can be summarized as follows:

- Both longitudinal and transverse curves start with similar linear-elastic responses. In the longitudinal direction, the linear-elastic responses end at the longitudinal proportional limit ( $PL_L$ ), which is significantly smaller compared to the transverse direction.
- The yielding region in the longitudinal direction starts after a comparatively low proportional limit, continues in a curvilinear form, and

finally ends approximately at 1.5% total strain. On the other hand, the yielding region is relatively smaller in the transverse direction and it can be neglected. The material behaviour can be considered bilinear in the transverse direction.

- Both longitudinal and transverse responses merge to a linear strain hardening behaviour. For the longitudinal direction, this linear behaviour starts after approximately 1.5% of total strain, while in the transverse direction, it is approximately right after yielding.

In a nutshell, the material elastic and strain hardening responses are quite similar. The significant difference in the longitudinal and transverse behaviour is the yielding region. The yielding region is believed to have important effects on the pipe deformability. In other words, the amount of hardening that a material shows during yielding (the area between the start of plastic deformation and linear strain hardening region) plays an important role in the longitudinal strain capacity of pipelines. Ishikawa et al. (2008) introduced a material property parameter called stress ratio  $\sigma_r$ , to correlate the material yielding response to the buckling resistance of HSS pipes.

$$\sigma_r = \frac{\sigma_{1.5}}{\sigma_{0.5}} \quad (2-3)$$

where

$\sigma_{0.5}$ : the stress at 0.5% total strain

$\sigma_{1.5}$ : the stress at 1.5% total strain.

Here,  $\sigma_{0.5}$  can be an indicator of the yield strength and  $\sigma_{1.5}$  can represent the material strength after the yielding process is complete. A higher value of  $\sigma_r$  indicates higher material work hardening in the yielding region and eventually higher longitudinal strain capacity before buckling. Looking back at Figure 2-10 to Figure 2-17, for each material type, the transversal  $\sigma_{0.5}$  is higher than the

longitudinal one, while  $\sigma_{1.5}$  is about the same in both directions. This results in a lower  $\sigma_r$  in longitudinal direction compared to the transverse direction.

The difference between yielding regions in longitudinal and transverse directions leads to different yield strength in these two directions. There are two widely used methods to define the yield strength of steel materials: 0.5% EUL method (material strength at 0.5% total strain) and 0.2% offset method (material strength at 0.2% plastic strain). Klein et al. (2008) and Li et al. (2010) recommended that for pipe with a yield strength above 550 MPa (grade X80), the 0.5% EUL method is not appropriate for determining the yield strength, so the 0.2% offset method should be used.

Figure 2-18 shows the longitudinal and transverse yield stresses for all eight material types. The yield strength in this figure is defined as the tension stress at 0.2% plastic strain. For all material types, yield stress in the transverse direction is higher compared to the longitudinal direction. The average of the difference between longitudinal and transverse yield stress is 25% throughout all material types.

Introducing a simple and accurate material model requires using a behavioural pattern that can be applied to all stress-strain curves and can be defined using reasonably few parameters. Figure 2-19 and Figure 2-20 show a schematic shape of stress-strain curves in the longitudinal and transverse directions, respectively. In the longitudinal direction, the stress-strain curve can be defined by the modulus of elasticity ( $E_L$ ), the proportional limit ( $PL_L$ ), the nominal yield stress ( $\sigma_{y(nom/L)}$ ), the strain hardening modulus ( $E_{sh(L)}$ ), and an exponential factor that defines the curvilinear yielding region. The nominal yield stress,  $\sigma_{y(nom)}$  is defined as the point at which linear-elastic and linear isotropic strain hardening curves intersect. In the transverse direction, as shown in Figure 2-20, the stress-strain curve can be defined by the modulus of elasticity ( $E_T$ ), nominal yield stress ( $\sigma_{y(nom/T)}$ ), and the

strain hardening modulus ( $E_{sh(T)}$ ) (ignoring the small yielding region and assuming a bilinear response).

## 2.3 Combined Hardening Material Modeling Concept

Mechanical response of a material is characterized by a constitutive equation which defines stress as a function of deformation. Constitutive models used to describe the inelastic behavior of steel are based on the existence of a yield surface. Yield surface plasticity models include a criterion for yielding, a loading criterion, a plastic flow equation, and a hardening rule. In a general state of stress, the yield criterion establishes the limit of elastic behavior during the loading history. The loading criterion determines whether elastic or inelastic strain will result when the stress state reaches the limit of elastic behavior. The flow equation, relates the plastic strain increment tensor to the stress state and loading increment. And, the hardening rule is utilized for predicting alterations in yield criterion and flow equation caused by inelastic straining (Chakrabarty, 2006).

In the general form of von Mises plastic theory which included both isotropic and kinematic hardening effects, the plasticity criterion is defined in the following form

$$f = J_2(\sigma - \alpha) - \sigma_y \leq 0 \quad (2-4)$$

where

$\sigma$ : stress tensor

$\sigma_y$ : size of the yield surface

$\alpha$ : back-stress tensor

$J_2$ : the second invariant and provides the following expression for deviatoric tensors

$$J_2(\boldsymbol{\sigma} - \boldsymbol{\alpha}) = \sqrt{\frac{3}{2}(\boldsymbol{s} - \boldsymbol{\alpha}^{dev}) : (\boldsymbol{s} - \boldsymbol{\alpha}^{dev})} \quad (2-5)$$

where

$\boldsymbol{s}$ : deviatoric stress tensor

$\boldsymbol{\alpha}^{dev}$ : deviatoric part of the back-stress tensor; it can be verified that  $\boldsymbol{\alpha}^{dev} = \boldsymbol{\alpha}$ .

For a hardening material, loading occurs when the current stress state is on the yield surface and an additional stress increment,  $d\boldsymbol{\sigma}$ , produces plastic strain. During loading, the yield surface will change in a way that the stress state will remain on the yield surface.

$$f = (\boldsymbol{\sigma}, \boldsymbol{\alpha}, \boldsymbol{\sigma}_y) = 0 \quad \frac{\partial f}{\partial \boldsymbol{\sigma}} : \dot{\boldsymbol{\sigma}} > 0 \quad (2-6)$$

In the incremental plastic theory, by decomposition of the strain rate tensor we have

$$\dot{\boldsymbol{\epsilon}} = \dot{\boldsymbol{\epsilon}}^e + \dot{\boldsymbol{\epsilon}}^p \quad (2-7)$$

where

$\dot{\boldsymbol{\epsilon}}^e$ : elastic part of strain rate tensor

$\dot{\boldsymbol{\epsilon}}^p$ : plastic part of strain rate tensor

Classical normality hypothesis requires that the plastic strain-rate tensor to be proportional to the derivative of the von Mises yield function with respect to the stress tensor

$$\dot{\boldsymbol{\epsilon}}^p = \dot{\lambda} \frac{\partial f}{\partial \boldsymbol{\sigma}} \quad (2-8)$$

where

$\dot{\lambda}$ : plastic multiplier

Equation (2-8) is also referred to as the plastic flow equation or the plastic flow rule which requires that the representative point of stress state stays on the yield surface (i.e.  $f > 0$  is impossible). This is referred to as the consistency condition in plasticity. To determine the plastic multiplier,  $\dot{\lambda}$ , the consistency condition is used as:

$$\dot{f} = \frac{\partial f}{\partial \sigma} : \dot{\sigma} + \frac{\partial f}{\partial \alpha} : \dot{\alpha} + \frac{\partial f}{\partial \sigma_y} \dot{\sigma}_y = 0 \quad (2-9)$$

von Mises plastic theory assumes that the plastic multiplier is equal to the equivalent plastic strain-rate,  $\dot{\epsilon}_{eq}$

$$\dot{\lambda} = \dot{\epsilon}_{eq} = \sqrt{\frac{2}{3} \dot{\epsilon}^p : \dot{\epsilon}^p} \quad (2-10)$$

Finally, a tangent material modulus  $C^{ep}$ , a fourth order tensor, can be defined which relate the stress increment to the total strain increment. This tangent material modulus is used to compute the tangent stiffness matrix. The constitutive relation for an elasto-plastic material is

$$\dot{\sigma} = C^e : (\dot{\epsilon} - \dot{\epsilon}^p) \quad (2-11)$$

and by substituting Equation (2-8), we have

$$\dot{\sigma} = C^e : \left( \dot{\epsilon} - \dot{\lambda} \frac{\partial f}{\partial \sigma} \right) \quad (2-12)$$

Equation (2-12) can be rewritten as follows

$$\dot{\sigma} = C^{ep} : \dot{\epsilon} \quad (2-13)$$

and the current stress  $\sigma$  can be obtained by integration of (2-13). During the plastic deformations, the tangent material tensor changes from point to point in a body, depending on the location and the applied loads. The variation of the tangent material modulus with respect to plastic strain depends on the isotropic and kinematic hardening laws that define the expansion and translation of the yield surface within the stress space.

There are different forms of kinematic hardening. Their difference is in how the evolution law of the kinematic hardening model describes the translation of the yield surface in stress space through the back-stress tensor, and what is the evolution rate of  $\alpha$  as a function of the plastic strain. One of the most widely and successfully used kinematic evolution laws is the Armstrong-Fredrick non-linear kinematic hardening law (Armstrong and Frederick, 1966). In its uniaxial form, the back-stress rate,  $\dot{\alpha}$  is given by:

$$\dot{\alpha} = c \dot{\epsilon}^p - \gamma \alpha \dot{\epsilon}^p \quad (2-14)$$

where

$c$ : material constant

$\gamma$ : material constant

$\dot{\epsilon}^p$ : plastic strain rate.

Equation (2-14) can be integrated, taking  $\alpha$  to be zero at  $\epsilon^p=0$ , to give

$$\alpha = \frac{c}{\gamma} (1 - e^{-\gamma \epsilon^p}) \quad (2-15)$$

The resulting uniaxial form of the back-stress-strain curve for the Armstrong-Fredrick hardening is shown in Figure 2-21. As the plastic strain increases, the back-stress,  $\alpha$ , saturates to the limiting value,  $c/\gamma$ .

Using the kinematic hardening model provides the possibility of moving the yield surface in the stress space. As a result, the kinematic hardening can be used alone or along with the isotropic hardening law (combined hardening) to simulate a response of materials with particular anisotropic properties under monotonic loadings.

Figure 2-22 shows the yield surface of the combined isotropic-kinematic hardening model. The evolution law of the combined hardening model consists of two components: a kinematic hardening component, which describes the translation of the yield surface in stress space through the back-stress tensor; and an isotropic hardening component, which describes the changes of the yield stress by defining the size of the yield surface,  $\sigma^o$ , as a function of plastic strain.

If the Armstrong-Fredrick kinematic hardening law is used in the combined hardening, the centre of the von Mises circle stays in a limiting circle. When the back-stress saturates and reaches the limiting value,  $c/\gamma$ , under a state of proportionally increased loading, any further hardening will be only isotropic hardening.

## **2.4 Idealizations and Postulations of HSS Pipe Material Responses**

Looking back at Figure 2-10 to Figure 2-17, among three different regions of material behaviour, HSS pipes' materials show almost similar linear-elastic and strain hardening responses in longitudinal and transverse directions. On the other hand, the yielding region is quite different in the longitudinal and transverse directions. The divergence of the longitudinal and transverse stress-strain curves starts at  $PL_L$  and both curves converge to a linear strain hardening curve after 1.5% total strain. Based on this observation, the material behaviour pattern, shown in Figure 2-19 and Figure 2-20, can be idealized one step further by

assuming exactly the same behaviour for both directions in the linear-elastic and linear strain hardening regions. These regions are defined by the modulus of elasticity, nominal yield stress, and the strain hardening modulus. Having exactly the same behaviour in these regions requires  $E$ ,  $\sigma_{y(nom)}$ , and  $E_{sh}$  to be equal in both directions. The magnitudes of the difference between these parameters in the longitudinal and transverse directions are discussed in the next paragraphs.

### **Longitudinal and Transverse Modulus of Elasticity, $E_L$ , and $E_T$**

Figure 2-23 shows the distribution of  $E_T/E_L$  for all HSS pipe material types. Generally, the modulus of elasticity in the transverse direction was slightly higher than in the longitudinal direction. Throughout eight material types the average and standard deviation of  $E_T/E_L$  were 1.05 and 5.5%, respectively.

### **Longitudinal and Transverse Strain Hardening Moduli, $E_{sh(L)}$ , and $E_{sh(T)}$**

Most of the HSS pipe material types showed a lower strain hardening modulus in the transverse direction compared to the longitudinal direction. Figure 2-24 shows the distribution of  $E_{sh(T)}/E_{sh(L)}$  for all HSS pipes in the database. The average and standard deviations of  $E_{sh(T)}/E_{sh(L)}$  were 0.83 and 11.6%, respectively.

### **Longitudinal and Transverse Nominal Yield Stress, $\sigma_{y(nom/L)}$ and $\sigma_{y(nom/T)}$**

The nominal yield stress was slightly higher in the transverse direction for all HSS pipes' material types. Figure 2-25 shows the distribution of  $\sigma_{y(nom/T)}/\sigma_{y(nom/L)}$  for all HSS pipes in the database. The average of this difference was 5.3% and the corresponding standard deviation was 2.8%.

If the differences between  $E$ ,  $\sigma_{y(nom)}$  and  $E_{sh}$  in both directions are neglected and these values are considered equal for both directions, the simplified shape of the longitudinal and transverse behaviour would be similar to the stress-strain curves

illustrated in Figure 2-26. This idealized behaviour can be simulated by a combined hardening model.

In Figure 2-26, the slope of the linear-elastic response is similar for both the longitudinal and transverse directions. Therefore for normal stress

$$\sigma = \varepsilon^e \times E \quad (2-16)$$

where

$\sigma$ : uniaxial stress on the true stress-strain curve

$\varepsilon^e$ : elastic strain

$E$ : modulus of elasticity.

Therefore, the Hook's isotropic elastic law applies to any point inside the yielding surface regardless of the direction.

$$\begin{bmatrix} \sigma_{xx} \\ \sigma_{yy} \\ \sigma_{xy} \end{bmatrix} = \frac{E}{1-\nu^2} \begin{bmatrix} 1 & \nu & 0 \\ \nu & 1 & 0 \\ 0 & 0 & 1-\nu \end{bmatrix} \begin{bmatrix} \varepsilon_{xx} \\ \varepsilon_{yy} \\ \varepsilon_{xy} \end{bmatrix} \quad (2-17)$$

The second parameter that should be defined to complete the isotropic elastic constitutive law is the Poisson's ratio,  $\nu$ . The widely accepted value for the Poisson's ratio of steel materials is 0.3. Here, the same value was assumed for all material types of HSS pipes.

The plastic response can be modeled by combining isotropic and kinematic hardening components. According to the combined hardening model, in the plastic range the evolution of total stress is a combination of yield stress and back-stress evolutions which can be defined by isotropic and kinematic hardening rules, respectively.

$$\sigma = \sigma^o + \alpha \quad (2-18)$$

where

$\sigma$ : combined stress

$\sigma^o$ : size of yield surface (yield stress)

$\alpha$ : magnitude of back-stress for any point on the stress-strain curve.

The next step is to define the evolution laws for isotropic and kinematic hardenings. In Figure 2-26, the longitudinal and transverse curves converge to a linear hardening region after almost 1.5% total strain. It can be hypothesized that a linear hardening component exists in both directions. Therefore, it was decided to use a linear isotropic component of hardening with a constant isotropic strain hardening modulus,  $E_{sh}$ . The evolution of yield stress can be defined as

$$\dot{\sigma}^o = E_{sh} \times \dot{\epsilon}^p \quad (2-19)$$

where

$\dot{\sigma}^o$ : yield stress rate

$\dot{\epsilon}^p$ : plastic strain rate

$E_{sh}$ : slope of linear hardening part of the stress-plastic strain curve.

As Figure 2-26 shows, the stress-strain curve in the transverse direction is bilinear and the isotropic component adequately defines the hardening behaviour. If the Armstrong-Fredrick law is used, the kinematic hardening can be assumed to become saturated in the transverse direction during the pipe-making process. In the longitudinal direction however, the curvilinear behaviour is the result of combining the Armstrong-Fredrick kinematic hardening and linear isotropic hardening components.

For the plane stress condition, this state of the back-stress and yield surface is shown in Figure 2-27. The original yield surface is shifted in the transverse direction by an initial back-stress equal to  $c/\gamma$ , i.e., the ultimate magnitude of

back-stress. The yield circle intersects the longitudinal and transverse axes at the longitudinal proportional limit,  $PL_L$ , and the nominal yield stress,  $\sigma_{y(nom)}$ , respectively. Introducing the limiting back-stress,  $c/\gamma$ , applies the effects of the residual plastic strain and the Bauschinger effects due to the expansion stage of the UOE pipe-making process. In the expansion stage, the pre-straining and consequently the initial back-stress are applied to the entire thickness of the pipe in the transverse direction; hence, the centre of the yield circle in Figure 2-27 essentially moves on the transverse axis.

As Figure 2-27 shows, the longitudinal and transverse yield stresses of the proposed material model are different not only in tensile loading but also under compressive loads. In this model, depending on the direction (longitudinal versus transverse) and type of load (tensile versus compressive) the material shows four different yield strengths. The transversal tensile yield strength is the highest yield strength, the second highest is the longitudinal compression yield strength, the third highest is the longitudinal tension yield strength, and the lowest is the transversal yield strength under the compressive load.

This phenomenon completely agrees with the observation made by researchers on the Bauschinger effects on the HSS pipes' material due to the transverse expansions during the pipe forming stage. Tsuru et al. (2005) reported that for anisotropic HSS pipes, the maximum and minimum yield strengths are the transversal tension and the transversal compression, respectively. Moreover, the longitudinal yield strengths are in between them and the longitudinal yield strength is higher under compression compared to tension. Similar observations were reported by Liessem et al. (2008).

Knowing  $PL_L$  and  $\sigma_{y(nom)}$  and the fact that the centre of the yield circle is on the transverse axis is sufficient for finding the location and size of the yield surface in

the stress space. The radius of this circle which equals the original size of the yield circle,  $\sigma_o^o$ , can be calculated as:

$$\sigma_o^o = \left( \frac{PL_L / 2 + \sigma_{y(nom)}}{2} \right) \left( 1 + \left( \frac{\sqrt{3} / 2 PL_L}{PL_L / 2 + \sigma_{y(nom)}} \right)^2 \right) \quad (2-20)$$

And the distance between the yield circle's centre to the centre of the coordination system which equals the limiting value of the back-stress,  $c/\gamma$ , can be calculated as:

$$\frac{c}{\gamma} = \sigma_{y(nom)} - \sigma_o^o \quad (2-21)$$

The yield circle's radius,  $\sigma_o^o$ , represents the hypothetical initial yield stress of the parent plate material before the UOE process, and the distance of its centre to the centre of the coordinate system represents the hypothetical imposed back-stress during the UOE process.

The general form of the Armstrong-Fredrick kinematic hardening law for two- and three-dimensional stress states can be used to define the relationship between the equivalent plastic strain and back-stress rates as

$$\dot{\alpha} = c \frac{1}{\sigma_0} (\sigma - \alpha) \dot{\epsilon}^p - \gamma \alpha \dot{\epsilon}^p \quad (2-22)$$

where

$\dot{\alpha}$  : back-stress rate.

For the proposed material model, the material constants  $c$  and  $\gamma$  can be defined based on the longitudinal stress-strain data which contain the kinematic hardening component.

Figure 2-28 shows the patterns of the kinematic, isotropic and combined hardening for the proposed material model. The evolutions of the back-stress, yield surface and the total stress can be defined using Equations (2-22), (2-19) and (2-18), respectively. As Figure 2-28 shows, the plastic constitutive law of the material is fully defined once values of  $\sigma_o^o$ ,  $\gamma$ ,  $E_{sh}$  and  $c$  are known ( $\sigma_{y(nom)}$  is not an independent value and equals  $\sigma_o^o + c/\gamma$ ).

As shown in Figure 2-28, the kinematic component hardens non-linearly and eventually saturates after certain plastic stress, and remains constant to  $c/\gamma$ , while the isotropic component continues linear hardening. The combined stress, however, starts non-linear hardening. After a certain amount of strain, it smoothly converts to a linear hardening pattern.

Any loading beyond the elastic range of the material with combined hardening similar to Figure 2-28, results in translation and expansion of the yield surface in the stress space. This translation causes the material to show different yield stress and plastic responses where it is reloaded in different directions. Therefore, if a material with combined hardening is already calibrated by applying an appropriate initial back-stress tensor, it can adequately simulate anisotropic responses.

## **2.5 Calibration of the Combined Hardening Material Model**

After defining the pattern for each hardening type of the material model, the next step is to calibrate the model with material test data so the model can reproduce outputs similar to actual test results for different stress paths. As the tension coupon test is the easiest and most routine method for qualifying the mechanical properties of pipelines' material, the material model development and calibration

focused on the tension test data. The compression test results were used later in this chapter to verify the model. This approach makes the proposed material modeling method easier to use and calibrate.

Basically, the model calibration is building an idealized longitudinal and transverse tension stress-strain relationship between 0.0% and 3.0% total strain for each material type, similar to the curves shown in Figure 2-26. These idealized curves can be built by extracting five material constants (i.e.  $E$ ,  $PL_L$ ,  $E_{sh}$ ,  $\sigma_{y(nom)}$ ) and kinematic material exponent,  $\gamma$ ) from the longitudinal and transverse tension stress-strain curves.

For each group of longitudinal and transverse stress-strain curves of each material type, the average experimental stress and strain were calculated for equally spaced 0.05% strain intervals. This resulted in a uniform distribution of stress-strain points between 0.0% to 3.0% total strains. The next step was to combine all uniformly distributed longitudinal stress-strain curves belonging to each material type into one average longitudinal curve, and to repeat this process for the transverse stress-strain curves. The combination of the curves was performed by using the average value of all stress-strain curves in the same category for equally spaced 0.05% strain intervals between 0.0% to 3.0% total strains. As a result, one longitudinal and one transverse curve represented the response of each material type, which consists of 60 stress-strain points uniformly distributed between 0.0% and 3.0% total strain. Hereafter, these curves are called average experimental curves.

### **Modulus of Elasticity, E**

The modulus of elasticity was calculated using a linear regression on the linear region of the longitudinal and transverse average stress-strain curves. Therefore, for each material type, the longitudinal modulus of elasticity,  $E_L$ , was the average

of this value among all the longitudinal curves; and the transverse modulus of elasticity,  $E_T$ , was the average value in transverse curves.

The average of the longitudinal and transversal modulus of elasticity was used to define the model's modulus of elasticity,  $E$ .

$$E = \frac{(E_T + E_L)}{2} \quad (2-23)$$

### **Linear Strain Hardening Modulus, $E_{sh}$**

For each pair of stress-strain data on an average curve ( $\sigma_i, \varepsilon_i$ ), the plastic strain was calculated as:

$$\varepsilon_i^p = \varepsilon_i - \sigma_i / E \quad (2-24)$$

where

$\varepsilon_i^p$ : plastic strain

$\varepsilon_i$ : total strain associated with  $\sigma_i$ .

The longitudinal and transverse strain hardening moduli are the slope of the line drawn by the linear regression on the pairs of stress-plastic strain data, ( $\sigma_i, \varepsilon_i^p$ ) which belong to the range between 1.5% and 3.0% total strain (where both curves converge to a linear strain hardening response).

For each material type, the strain hardening modulus used in the model was the average of  $E_{sh}$  in the transverse and longitudinal directions,

$$E_{sh} = \frac{(E_{sh(T)} + E_{sh(L)})}{2} \quad (2-25)$$

### **Nominal Yield Stress, $\sigma_{y(nom)}$**

The nominal yielding stress is the intercept of the line drawn by the linear regression on the pairs of stress-plastic strain data within 1.5% and 3.0% total strain range (same line of which slope was used as  $E_{sh}$ ). The nominal yield stress used in the material models was calculated as the average of this value in the longitudinal and transverse directions for each HSS pipe material type,

$$\sigma_{y(nom)} = \frac{(\sigma_{y(nom/T)} + \sigma_{y(nom/L)})}{2} \quad (2-26)$$

### **Longitudinal proportional Limit, $PL_L$**

For each material type, the  $PL_L$  was defined as the stress at the onset of plastic deformation on the longitudinal average curve. Knowing the  $PL_L$  and  $\sigma_{y(nom)}$ , the hypothetical initial yield stress,  $\sigma_o^o$ , can be defined using Equation (2-20). The limiting value of the back-stress,  $c/\gamma$ , can also be defined knowing  $\sigma_{y(nom)}$  and  $\sigma_o^o$ , using Equation (2-21). Introducing initial back-stress equal to  $c/\gamma$  to the back-stress tensor in the axis associated with the pipe transverse direction, results in an anisotropic behaviour similar to tension coupon test results in both directions.

So far, the only parameter left is  $\gamma$ , which defines the evolution rate of back-stress in the kinematic hardening component.

### **Kinematic Hardening Constant, $\gamma$**

This model assumes that the kinematic hardening is saturated in the transverse direction and the transverse hardening only has the isotropic component. Therefore, only the longitudinal stress-strain curves can be used to define  $\gamma$ .

Equations (2-22), (2-19), and (2-18) and the  $\gamma$  value can be used to estimate the stress corresponding to each total strain on the longitudinal stress-strain curves with certain error. The most accurate value for  $\gamma$  was defined for each material

type by finding the best fit of  $(\sigma_i, \varepsilon_i)$  data pairs to the longitudinal stress-strain data. The criterion used here was the least sum of squared errors in predicting  $\sigma_i$  for all given  $\varepsilon_i$ .

The kinematic hardening constant,  $\gamma$ , is the last material property that should be extracted from the experimental data. Table 2-2 illustrates all longitudinal and transverse values for different material parameters required for the calibration of the combined hardening model.

After obtaining  $\gamma$ , the other kinematic material parameter,  $c$ , can be defined using Equation (2-21) knowing  $\sigma_{y(nom)}$  and  $\sigma_o^o$ . Finding all of the above five main parameters can define the elastic and plastic behaviour of the material under any stress path. The modulus of elasticity,  $E$  and the Poisson's ratio, ( $\nu=0.3$ ) define the elastic response. Having  $\sigma_o^o$ ,  $\gamma$ ,  $c$ , and  $E_{sh}$  calibrated by the experimental data, and using Equations (2-22), (2-19), and (2-18), the combined hardening plastic behaviour of the parent plate can be calculated.

In order to simulate the effects of the UOE pipe-making process and generate the desired anisotropy in the material response, the next and final step is to move the centre of the yield circle to the limiting back-stress in the transverse axis. In a plane-stress state, the initial back-stress tensor should be applied to the material as follows:

$$\begin{bmatrix} \alpha_{LL} = 0 & \alpha_{LT} = 0 \\ \alpha_{TL} = 0 & \alpha_{TT} = c/\gamma \end{bmatrix}$$

Figure 2-29 schematically shows the hypothetical behaviour of the parent plate material before applying the initial back-stress, as well as the longitudinal and transverse material behaviour after applying the initial back-stress.

After applying the initial back-stress, the tensile stress-strain response becomes bilinear in the transverse direction; the material yields at  $\sigma_{y(nom)}$  and continues linear hardening with slope of  $E_{sh}$ . Under tensile loads in the longitudinal direction, the material yields at  $PL_L$ ; after a curvilinear yield, the curve merges to a linear hardening similar to the transverse direction with a slope of  $E_{sh}$ .

## 2.6 Results and Discussion

The proposed material modeling and calibration methods were used for eight available HSS pipes' material data in this study. Sixty uniformly distributed stress-strain data points between 0.0% to 3.0% total strain were used for calibrating the material model for each material type. The five independent parameters of  $E$ ,  $PL_L$ ,  $E_{sh}$ ,  $\sigma_{y(nom)}$ , and  $\gamma$  were extracted from the experimental data according to the procedures explained in the previous section.  $E$ ,  $E_{sh}$ , and  $\sigma_{y(nom)}$  were extracted from both longitudinal and transverse stress-strain curves and average values were used for each material type.  $E$  and  $\nu=0.3$  were used to define the elastic constitutive law which is essentially isotropic.  $PL_L$  and  $\gamma$  were defined based on the longitudinal stress-strain data. The size and location of the yielding circle were calculated using  $\sigma_{y(nom)}$  and  $PL_L$  to obtain  $\sigma_o^o$  and limiting back-stress,  $c/\gamma$ . Subsequently, the kinematic parameter  $\gamma$  was defined by using combined hardening equations and curve-fitting to the longitudinal stress-strain data. Finally,  $\sigma_o^o$ ,  $\gamma$ ,  $E_{sh}$ , and  $c$  were used to build the combined hardening model for each material type. All parameters defining the combined hardening model for each material type are shown in Table 2-3.

Figure 2-30 to Figure 2-37 show the simulated stress-strain data by the proposed model, as well as the average experimental stress-strain data in longitudinal and transverse directions for the material types A to H. These average values consist

of 60 stress-strain data each of which calculated as the average of stress and strain in all similar curves located in the same range of total strain with 0.05% width.

Figure 2-30 to Figure 2-37 show that the model adequately captures the differences in the material behaviour in longitudinal and transverse directions. The mean absolute error (MAE) of the model predictions of corresponding stress to each of 60 strain points in the average curves is illustrated in Figure 2-38 for the longitudinal and transverse directions of all material types. The average MAE among all material types in the longitudinal and transverse directions was 2.2 and 2.1, respectively. The maximum MAE among all material types in both directions did not exceed 3.3%. These errors are in an acceptable range considering that the average test data contain the data noise existing in the test results. Despite the simplicity of the proposed model and the easy calibration method, this model adequately simulates the tension behaviour of HSS pipes' material in longitudinal and transverse directions.

Pipeline materials are usually under tension stresses in the transverse direction; however, in the longitudinal direction, pipeline materials might be under either tension or compression. As discussed before, HSS pipe materials show higher strength under compressive deformations compared to tensile deformations in the longitudinal direction. Liessem et al. (2008) suggested that this might be related to the plastic deformations in the expansion stage of UOE pipe-making process. They hypothesized that since the pipe contracts in the longitudinal direction when it is expanded in the circumferential direction, it shows higher strength in compression tests because the specimen is loaded in the same direction. A tensile specimen on the other hand shows lower strength because it is loaded in the opposite direction.

A proper material model for HSS linepipes should also simulate the longitudinal compression stress-strain curves adequately. Compression tests have been

performed on material types B, F and G. Figure 2-39 to Figure 2-41 show the difference between the average longitudinal compression and tension stress-strain data for material types B, F, and G, respectively. These figures also illustrate the higher longitudinal strength when the material is loaded under compressive loads compared to tensile loads. Other studies have reported the same observations (see Tsuru et al., 2005 and Fatemi et al., 2009). These tests have been performed on round bar coupons machined from the pipe specimens in the longitudinal direction. Due to the specimen buckling, compression tests on coupons have more limitations compared to the tension tests; therefore, the results were available only up to around 1.0% total strain.

Looking back to the proposed model, once the yield circle is shifted by the initial back-stress in the transverse direction (as Figure 2-27 shows), the elastic range becomes larger in longitudinal compression compared to longitudinal tension. Based on the combined hardening material model and after shifting the yield surface by  $c/\gamma$  in the transverse direction, the compressive longitudinal proportional limit can be found as

$$PL_{L(com)} = \left( \frac{\sigma_{y(nom)} - \sigma_o^o}{2} \right) + \sqrt{\sigma_o^o{}^2 - \frac{3(\sigma_{y(nom)} - \sigma_o^o)^2}{4}} \quad (2-27)$$

where

$PL_{L(com)}$ : compressive proportional limit in longitudinal direction.

In the plastic range, with exactly similar equivalent plastic strain, the combined stresses will be larger in compression compared to tension. Therefore, using the combined hardening model developed in this chapter eventually results in higher strength in longitudinal compression compared to tension.

In order to verify the accuracy of the model in simulating the longitudinal compression behaviour, the results were compared with the average experimental compression stress-strain data for material types B, F, and G. Figure 2-42 to

Figure 2-44 show comparisons between compressive stress-strain curves from the model and average values from experiments for material types B, F, and G, respectively. The average longitudinal tension test results are also shown in these figures (longitudinal tension results would be similar to the compression behaviour if an isotropic material model were used).

Among all experimental longitudinal compressive data points of material B, F, and G, the difference between the experimental and predicted stress values for a given strain point did not exceed 6.0%. The average MAE in model predictions for the longitudinal compression points was 3.5%, 3.3% and 2.1% for material types B, F, and G, respectively. This small range of error shows that the combined hardening model and the von Mises yielding criterion are competent for predicting the material response. This is an advantage for the proposed model because it is calibrated by tension coupon test results which are more common and convenient for material testing, but it can also predict the compression response with an acceptable error.

## **2.7 Summary**

When transversal plastic deformations are applied to the HSS pipes during the expansion stage of the UOE pipe-making process the resulting Bauschinger's effects lead to material anisotropy. The HSS pipe material responses are not only different in the longitudinal and transverse directions, but also different under tension and compression in the same direction. Conventional isotropic material modeling is unable to address the anisotropy of the HSS pipes' materials, since it uses one stress-strain response under any stress path.

In order to capture the anisotropic behaviour of the HSS pipe material, this chapter introduces a combined hardening material model consisting of a linear isotropic, and Armstrong-Frederick kinematic hardening components. This model

can be easily calibrated with longitudinal and transverse stress-strain data from tension tests. The material model results agree adequately with the actual behaviour of HSS pipe material responses in longitudinal and transverse directions. The assumptions and simplifications made to develop the model and its calibration method do not adversely affect the model's performance.

The next chapter shows how using this material model in HSS pipes' buckling analyses improves the adequacy of the models and helps promote a better understanding of the effects of the material anisotropy on the structural behaviour of HSS pipes.

## References

Adeeb S., Zhou J. and Horsley D., (2007), “Investigating the effect of UOE forming process on the buckling of line pipes using finite element modeling”, 6th International Pipeline Conference, IPC 2006, September 25, 2006 - September 29, American Society of Mechanical Engineers, Calgary, AB, Canada, 1, pp. 169-174.

Armstrong P.J. and Frederick C.O., (1966), “A Mathematical Representation of Multiaxial Bauschinger Effect”, Report RD/B/N731, CEGB, Central Electricity Generating Board, Berkeley, UK.

Berisha B., (2010), “Computational Modeling of Combined Hardening Phenomena Based on Dislocation Density Theory”, Diss. ETH No. 19172, Institute of Virtual Manufacturing, ETH Zurich, Zurich, Switzerland, 146 pages.

Chakrabarty J., (2006), “Theory of Plasticity (3<sup>rd</sup> Edition)”, Butterworth-Heinemann, Burlington, MA, USA, 895 pages.

Crone D.G., Collins L.E., Bian Y. and Weber, P., (2010), “The Effect of Sample Flattening on Yield Strength Measurement in Line Pipe”, Proceeding of the International Pipeline Conference, American Society of Mechanical Engineers, Calgary, Alberta, v2, pp 477-482.

Fatemi A., Zhou J., Kenny S., (2009), “Investigations on the local buckling response of high strength linepipe”, 2008 ASME International Pipeline Conference, IPC 2008, September 29, 2008 - October 3, American Society of Mechanical Engineers, Calgary, AB, Canada, v3, pp. 649-656.

Hart J.D., Powell G.H. and Zulficar N., (1996), “A Material Model for Pipeline Steels”, International Pipeline Conference, IPC, ASME, 1996, v 2, pp 613-627.

Ishikawa N., Okatsu M., Shimamura J., Endo, S., Shikanai, N., Muraoka, R., Kondo, J. and Suzuki, N., (2009), "Material development and strain capacity of grade X100 high strain linepipe produced by heat treatment online process", 2008 ASME International Pipeline Conference, IPC 2008, September 29, 2008 - October 3, American Society of Mechanical Engineers, Calgary, AB, Canada, v3, pp 713-720.

Klein R., Collins L., Hamad F., (2009), "Determination of mechanical properties of high strength linepipe", 2008 ASME International Pipeline Conference, IPC 2008, September 29, 2008 - October 3, American Society of Mechanical Engineers, Calgary, AB, Canada, v3, pp. 577-583.

Li Y., Zhang W., Gong S., Ji L., Huo C. and Feng Y., (2010), "Study on Tensile Property and Strain Ageing Behavior of X100 Linepipe", Proceeding of the International Pipeline Conference, American Society of Mechanical Engineers, Calgary, Alberta, v2, pp 351-357.

Liessem A., Schroder J., Pant M., Knauf G., Zimmermann S., Stallybrass C. and Erdelen-Peppler M., (2009), "Investigation of the stress-strain behaviour of large-diameter X100 linepipe in view of strain-based design requirements", 2008 ASME International Pipeline Conference, IPC 2008, September 29, 2008 - October 3, American Society of Mechanical Engineers, Calgary, AB, Canada, v3, pp 755-762.

Liu M. and Wang, Y., (2007), "Modeling of Anisotropy of TMCP and UOE Linepipes", International Journal of Offshore and Polar Engineering, v17, n 4, pp 288-293.

Saikaly W.E., Bailey W.D. and Collins L.E., (1996), "Comparison of ring expansion vs flat tensile testing for determining linepipe yield strength", Part 1 (of 2), June 9, 1996 - June 13, Calgary, AB, Canada, v1, pp 209-213.

Seo , D.H, Yoo, J.Y., Song, W.H. and Kang, K.B., (2008), “Development of X100 Linepipe Steel with High Deformation Capacity”, 2008 ASME International Pipeline Conference, IPC 2008, September 29, 2008 - October 3, American Society of Mechanical Engineers, Calgary, AB, Canada, v3, pp 585-592.

Tsuru E., Shinohara Y., and Asahi H., (2008), “Evaluation precept for buckling resistance of high-strength UOE line pipes used in strain based design (SBD) applications”, *Int. J. Offshore Polar Eng.*, v18, n 3, pp 176-182.

Tsuru E., Shinohara Y., Asahi H. and Terada, Y., (2005),”Strain capacity of line pipe with yield point elongation”, 15th International Offshore and Polar Engineering Conference, ISOPE-2005, June 19, 2005 - June 24, International Society of Offshore and Polar Engineers, Seoul, Korea, pp 177-184.

## Tables

Table 2-1 Steel grades and dimensions of the HSS pipes and number of different coupons for each material type

Material Type	A	B	C	D	E	F	G	H
Steel Grade	X80	X80	X80	X100	X100	X100	X100	X100
Nominal Outside Diameter (mm)	762	762	610	914	762	762	762	610
Nominal Wall Thickness (mm)	12.7	12.7	15.2	12.7	12.7	12.7	12.8	15.2
D/t ratio	60	60	40	72	60	60	60	40
Tension coupon tests								
Longitudinal Round Coupon	8	4	4	2	7	4	4	8
Longitudinal Strap Coupon	8	1	4	2	6	1	1	8
Transverse Round Coupon	8	4	3	2	8	4	4	8
Transverse Flattened Strap	8	1	1	2	8	1	1	8
Compression coupon tests								
Longitudinal Round Coupon	-	3	-	-	-	3	3	-

Table 2-2 Longitudinal and transverse values for different material parameters

Material Property	Material Type							
	A	B	C	D	E	F	G	H
$E_L$ (MPa)	197888	195552	207521	181800	203787	203376	203114	201290
$E_T$ (MPa)	221942	216858	217799	203458	205877	201524	203225	207993
$PL_L$ (MPa)	286	400	288	405	367	368	404	379
$E_{sh(L)}$ (MPa)	2989	1761	2847	3284	3222	2222	2753	2842
$E_{sh(T)}$ (MPa)	2689	1459	2372	2158	2588	1928	1999	2968
$\sigma_{y(nom/L)}$ (MPa)	604	687	631	807	795	764	777	760
$\sigma_{y(nom/T)}$ (MPa)	629	695	666	881	823	807	847	784
$\gamma$	394	709	421	465	479	581	582	522

Table 2-3 Material parameters used to define the combined hardening model

<b>Material Property</b>	<b>Material Type</b>							
	<b>A</b>	<b>B</b>	<b>C</b>	<b>D</b>	<b>E</b>	<b>F</b>	<b>G</b>	<b>H</b>
$E$ (MPa)	209915	206205	212660	192629	204832	202450	203169	204642
$E_{sh}$ (MPa)	2839	1610	2610	2721	2905	2075	2376	2905
$\sigma_0^0$ (MPa)	420	513	435	582	547	537	567	537
$\gamma$	394	709	421	465	479	581	582	522
$c$ (MPa)	77519	126427	89778	121706	125493	144495	142361	122513

## Figures

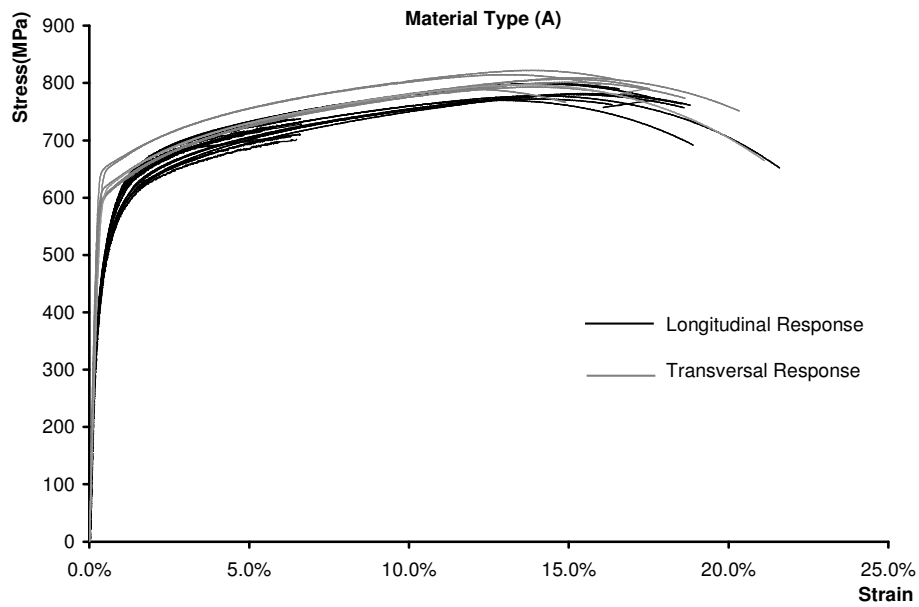


Figure 2-1 Longitudinal and transverse tension stress-strain curves for the material type A - entire range

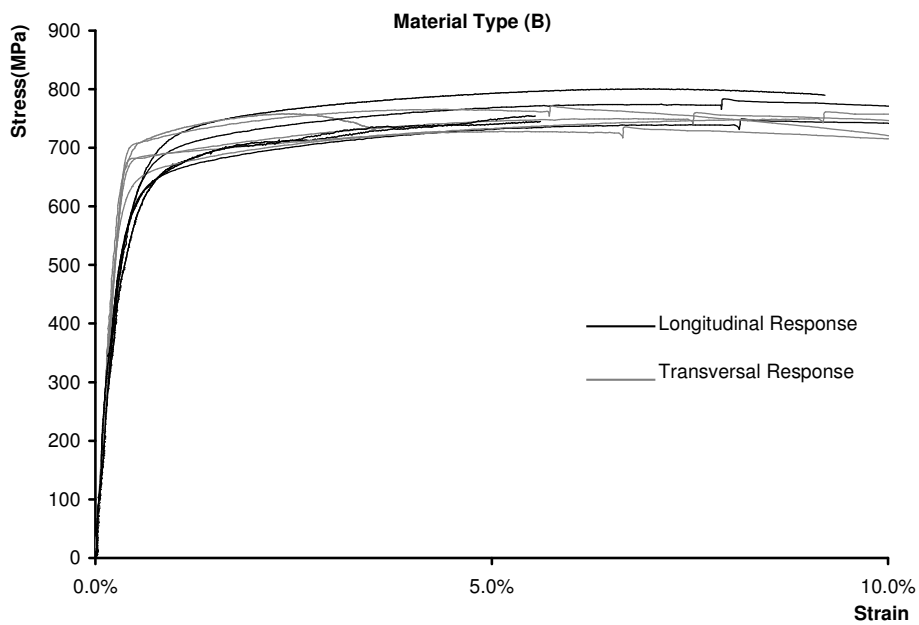


Figure 2-2 Longitudinal and transverse tensile stress-strain curves for the material type B - entire range

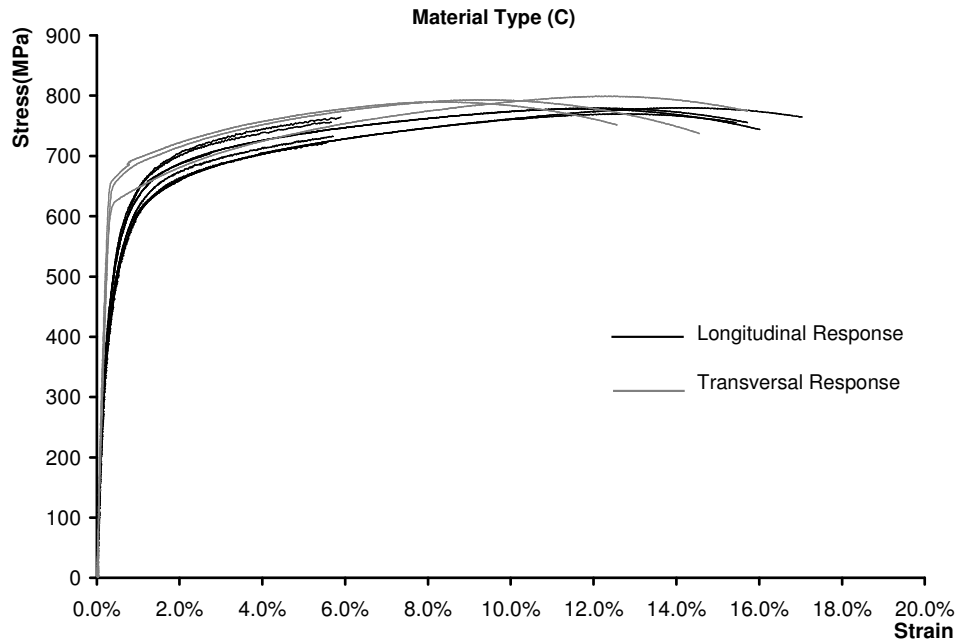


Figure 2-3 Longitudinal and transverse tensile stress-strain curves for the material type C - entire range

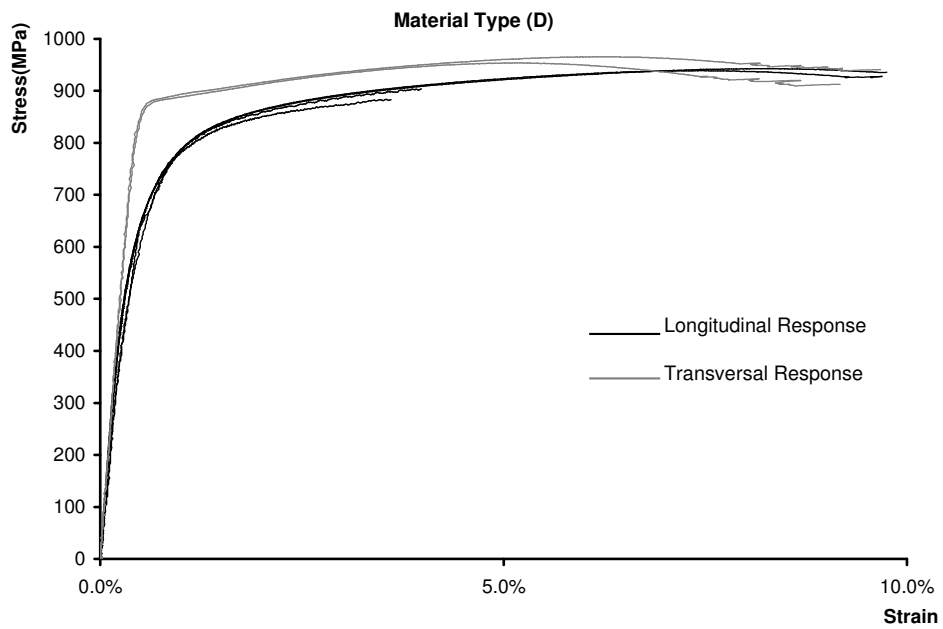


Figure 2-4 Longitudinal and transverse tensile stress-strain curves for the material type D - entire range

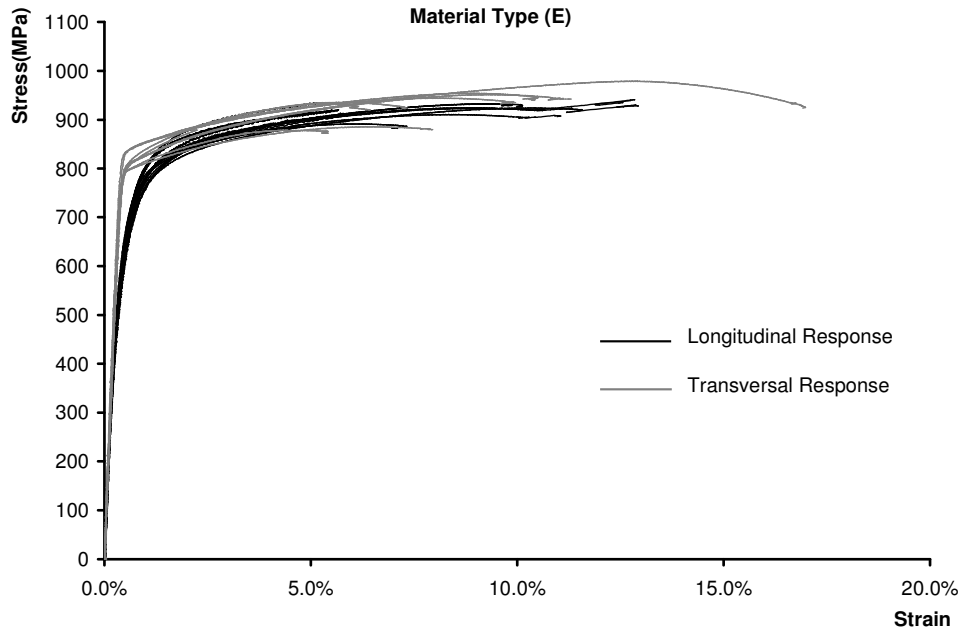


Figure 2-5 Longitudinal and transverse tensile stress-strain curves for the material type E - entire range

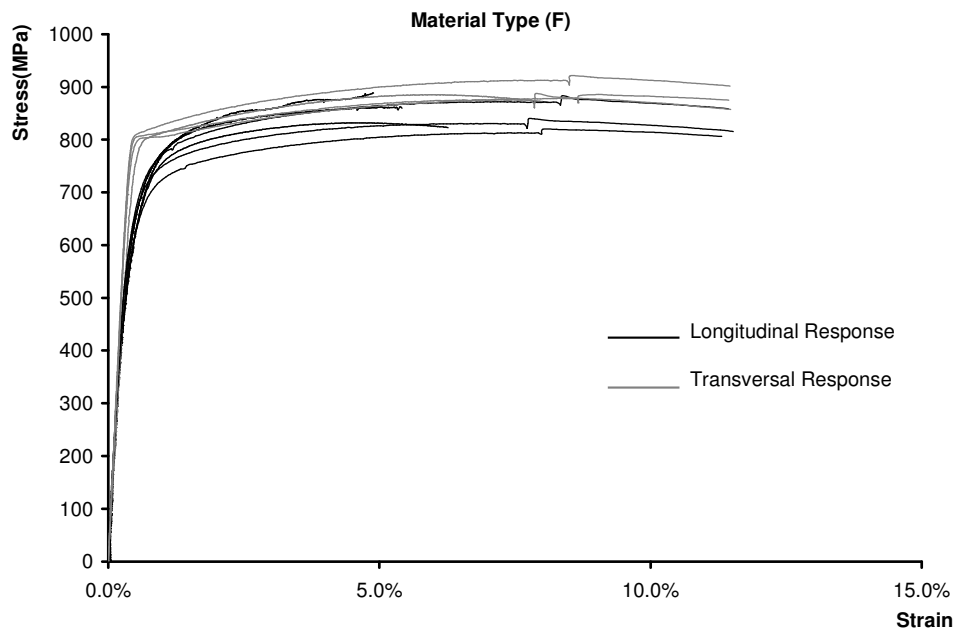


Figure 2-6 Longitudinal and transverse tensile stress-strain curves for the material type F - entire range

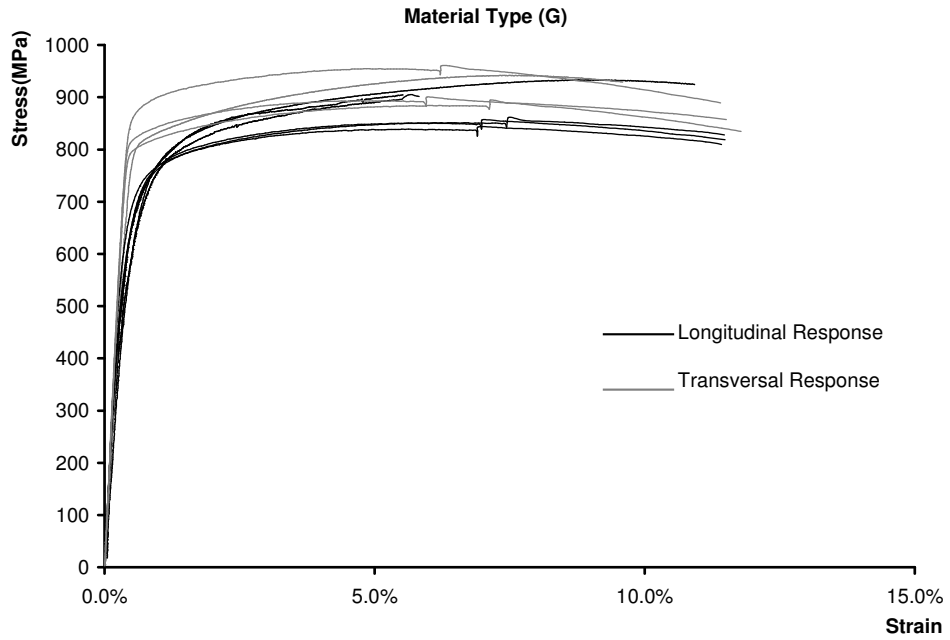


Figure 2-7 Longitudinal and transverse tensile stress-strain curves for the material type G - entire range

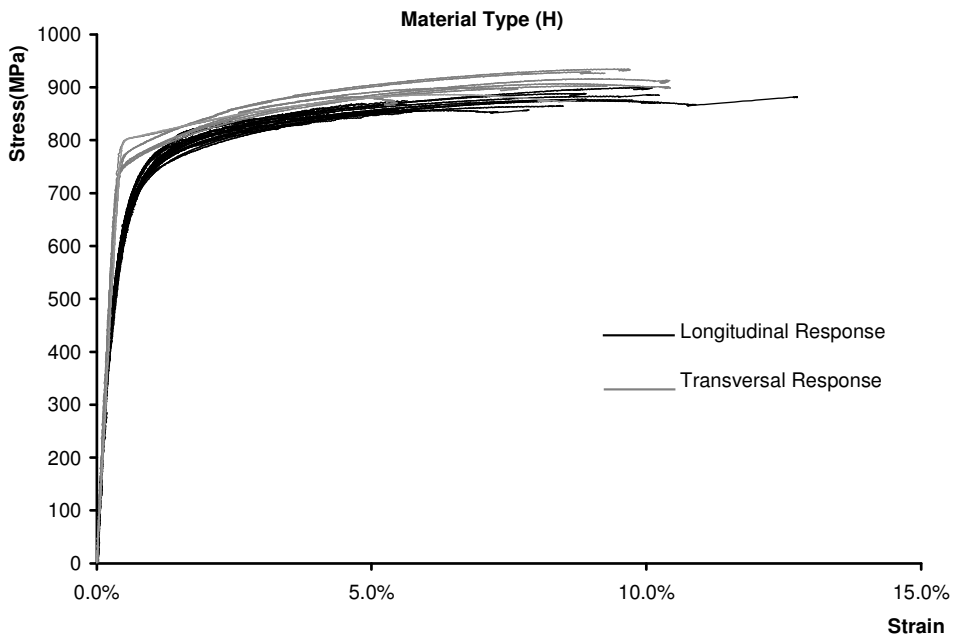


Figure 2-8 Longitudinal and transverse tensile stress-strain curves for the material type H - entire range

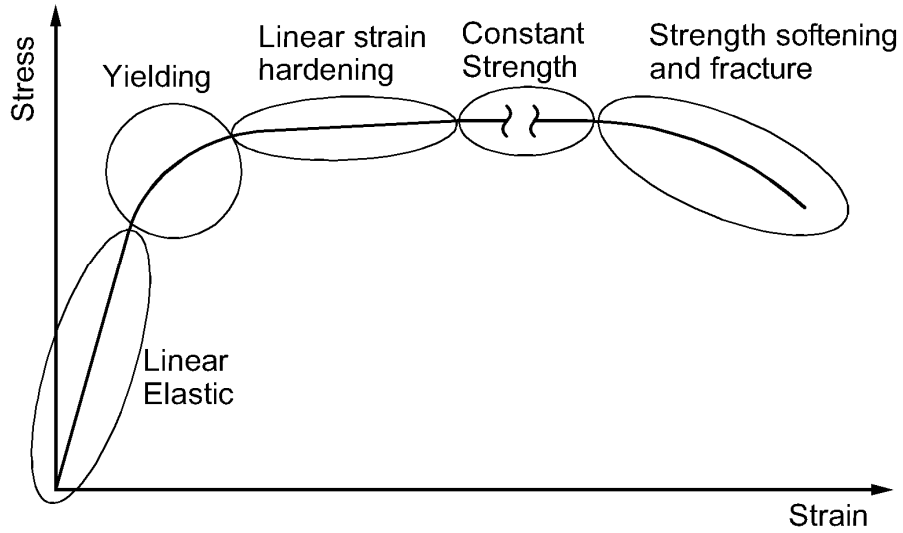


Figure 2-9 Schematic shape of the stress-strain curves of HSS pipe materials

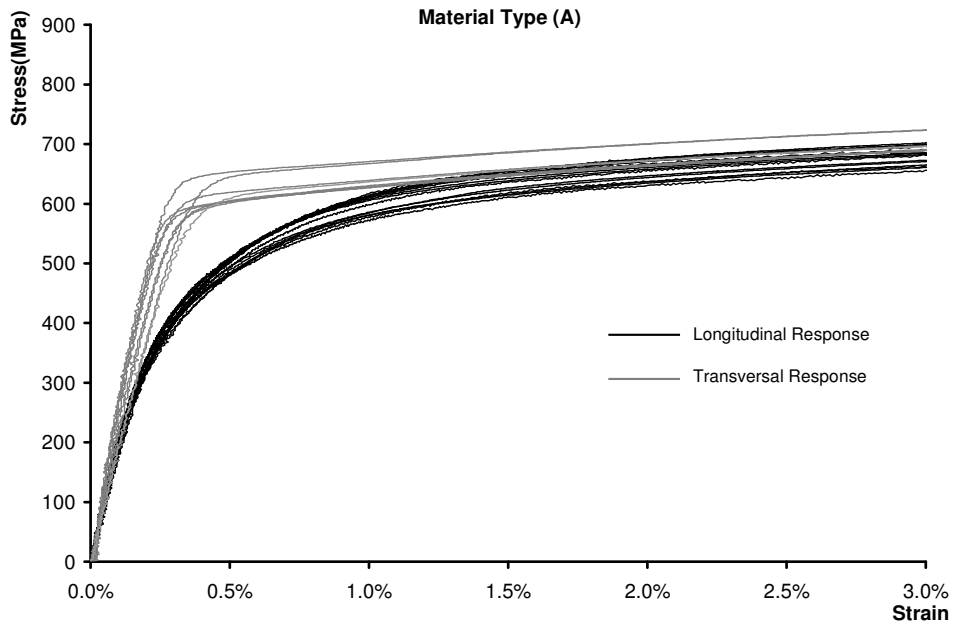


Figure 2-10 Longitudinal and transverse tensile stress-strain curves for the material type A – 0.0% to 3.0% total strain

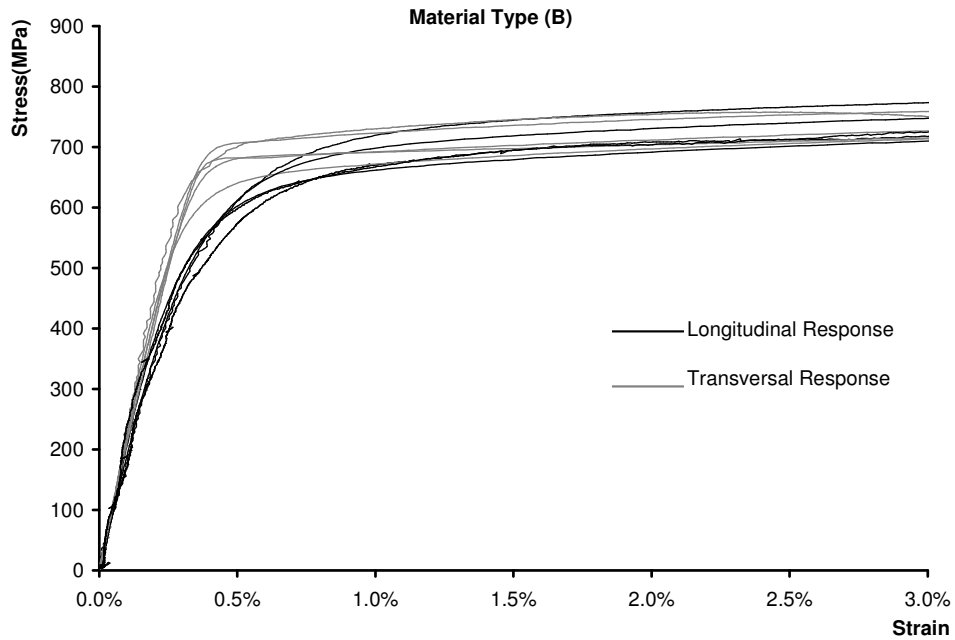


Figure 2-11 Longitudinal and transverse tensile stress-strain curves for the material type B – 0.0% to 3.0% total strain

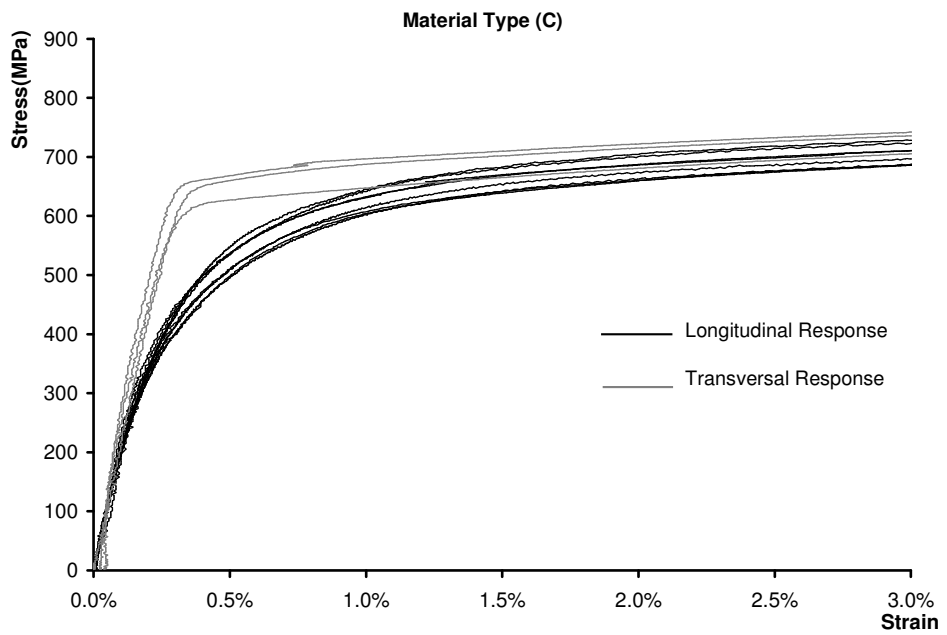


Figure 2-12 Longitudinal and transverse tensile stress-strain curves for the material type C – 0.0% to 3.0% total strain

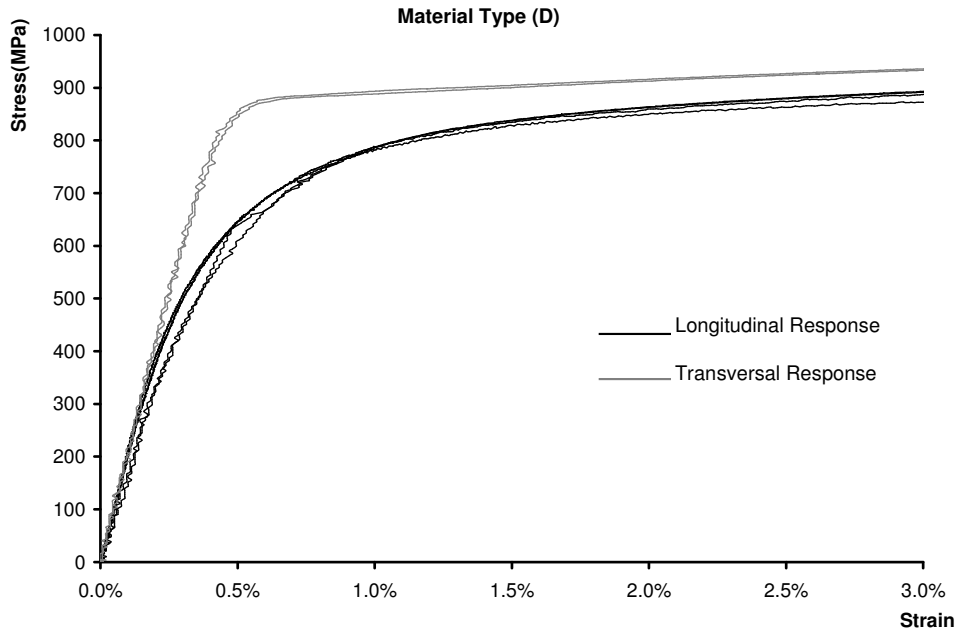


Figure 2-13 Longitudinal and transverse tensile stress-strain curves for the material type D – 0.0% to 3.0% total strain

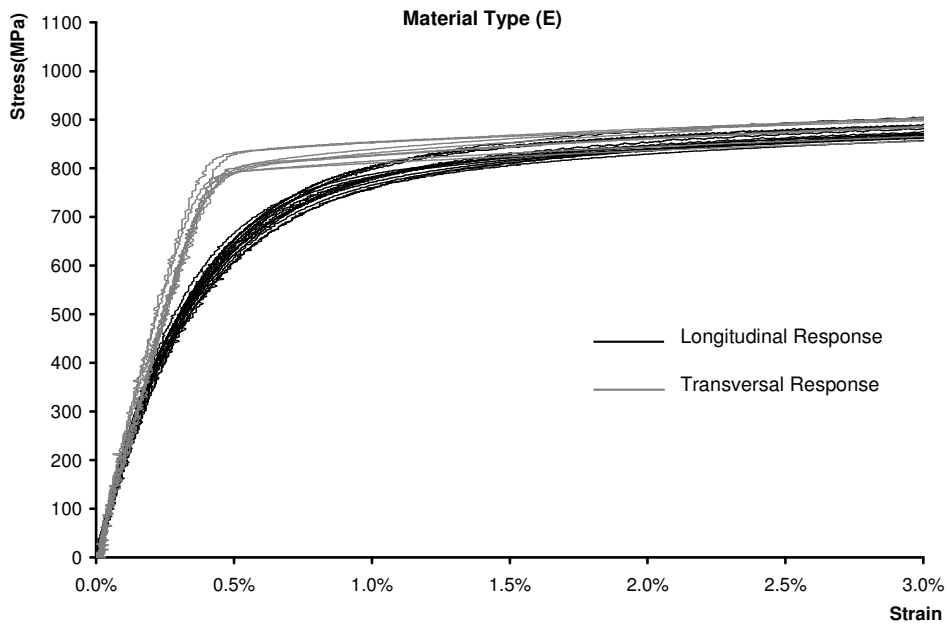


Figure 2-14 Longitudinal and transverse tensile stress-strain curves for the material type E – 0.0% to 3.0% total strain

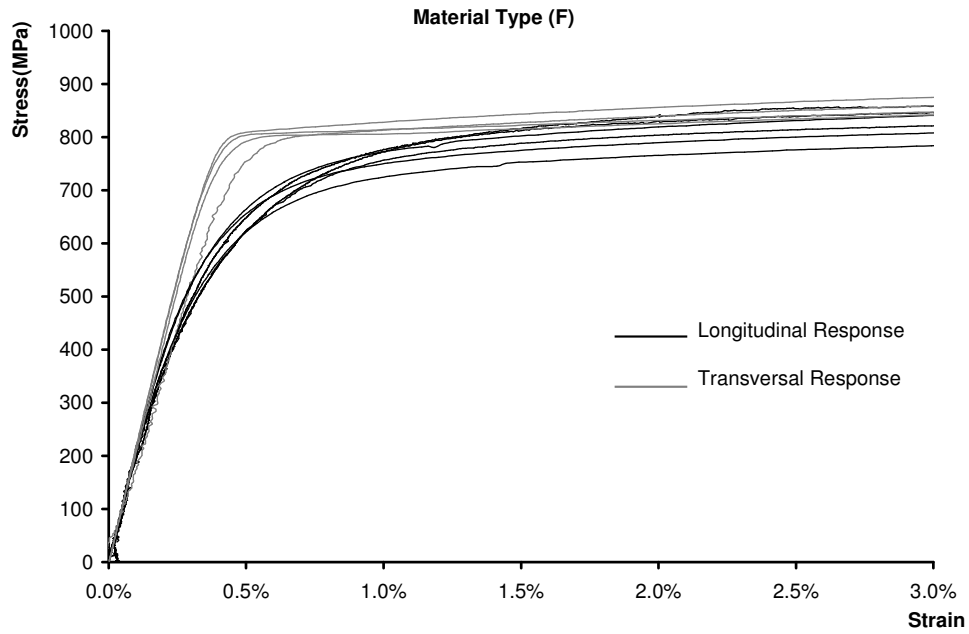


Figure 2-15 Longitudinal and transverse tensile stress-strain curves for the material type F – 0.0% to 3.0% total strain

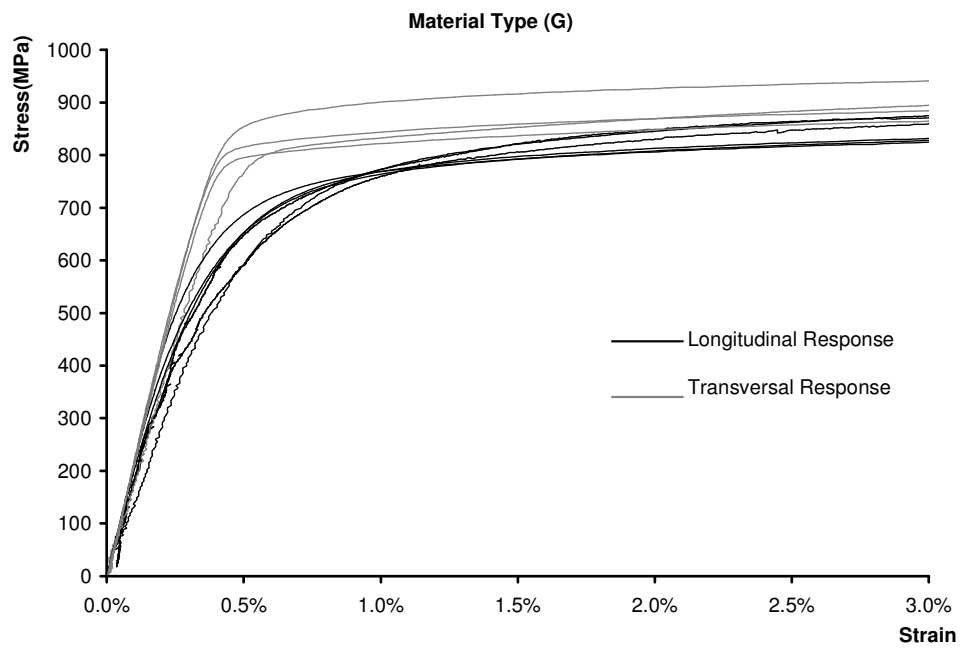


Figure 2-16 Longitudinal and transverse tensile stress-strain curves for the material type G – 0.0% to 3.0% total strain

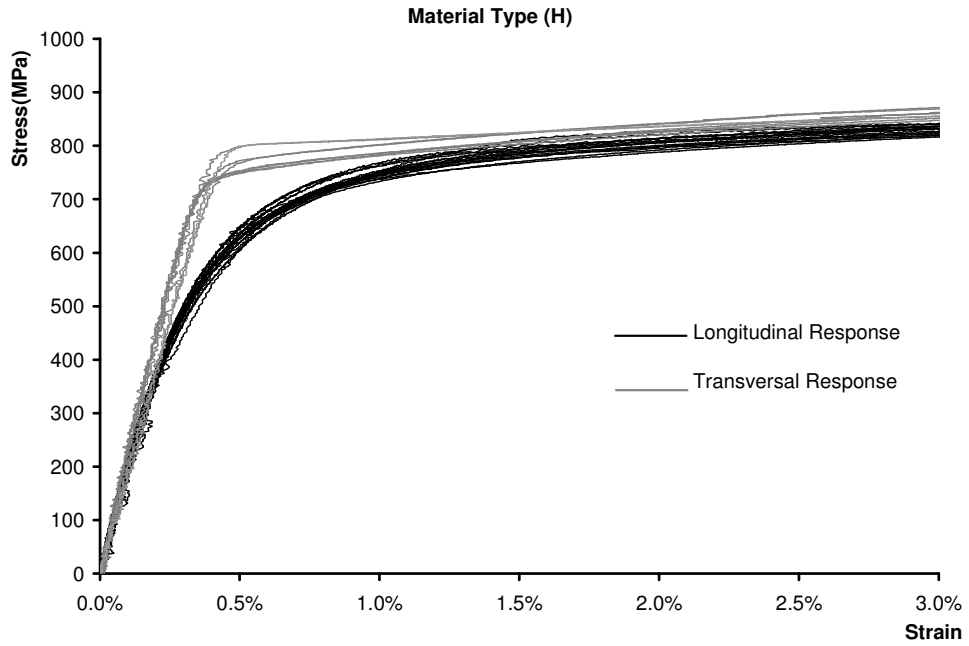


Figure 2-17 Longitudinal and transverse tensile stress-strain curves for the material type H – 0.0% to 3.0% total strain

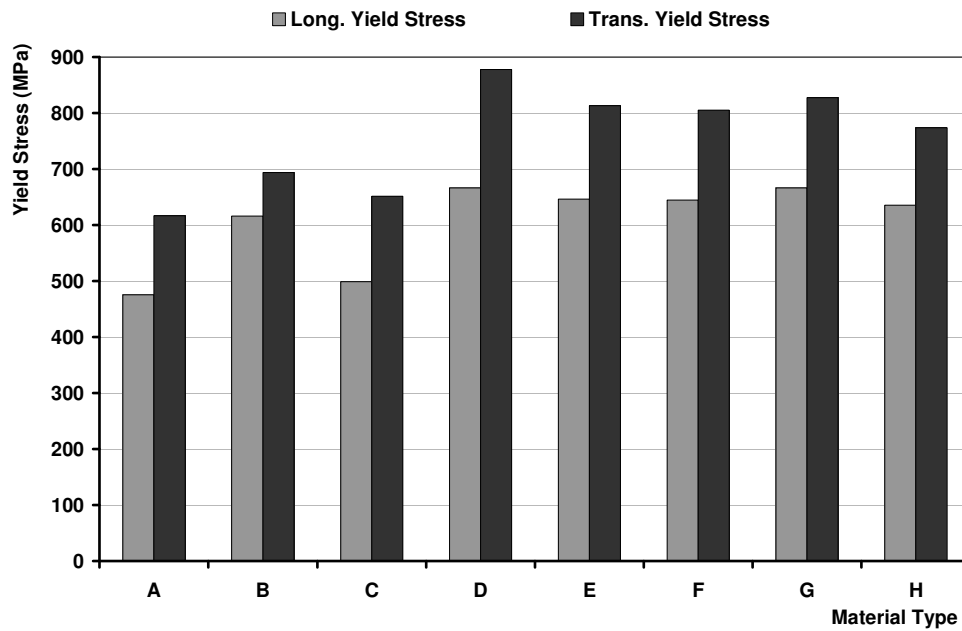


Figure 2-18 Longitudinal and transverse tensile yield strength for material A to H

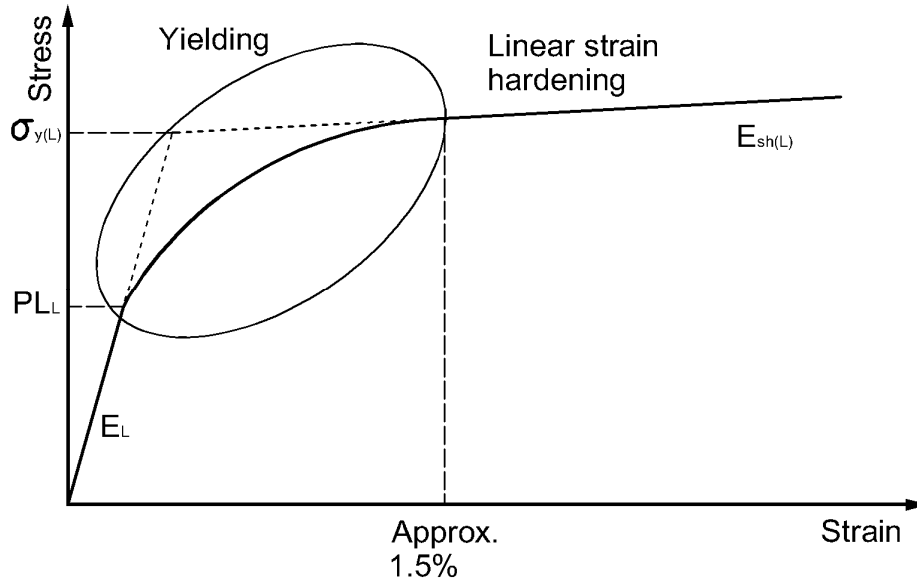


Figure 2-19 Schematic shape of the longitudinal tensile stress-strain curve of HSS pipes' materials – 0.0% to 3.0% total strain

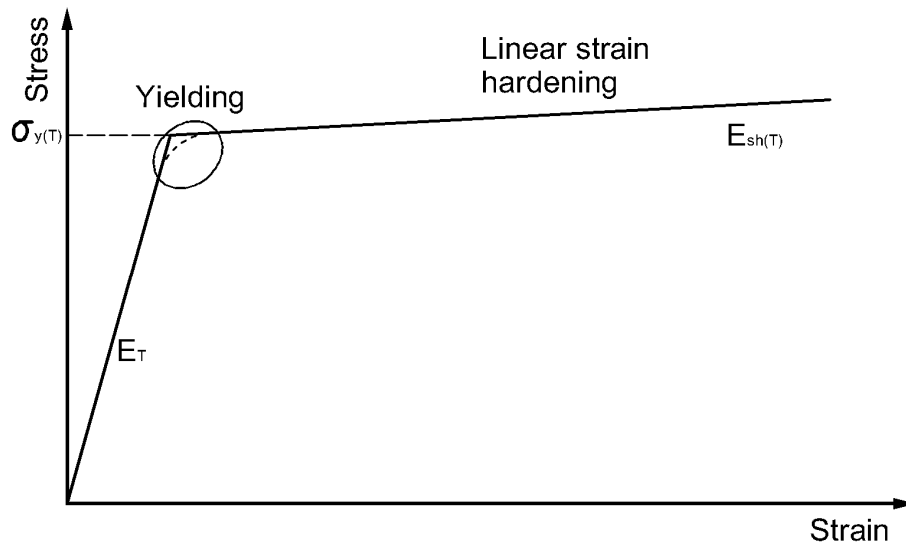


Figure 2-20 Schematic shape of the transversal tensile stress-strain curve of HSS pipes' materials – 0.0% to 3.0% total strain

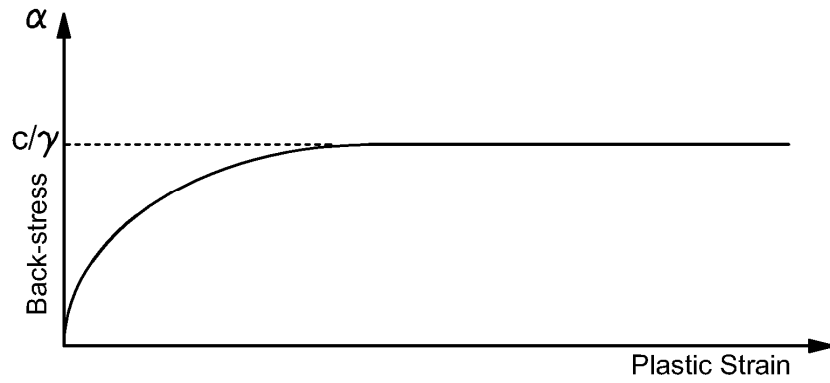


Figure 2-21 Evolution of back-stress according to Armstrong-Fredrick kinematic hardening law

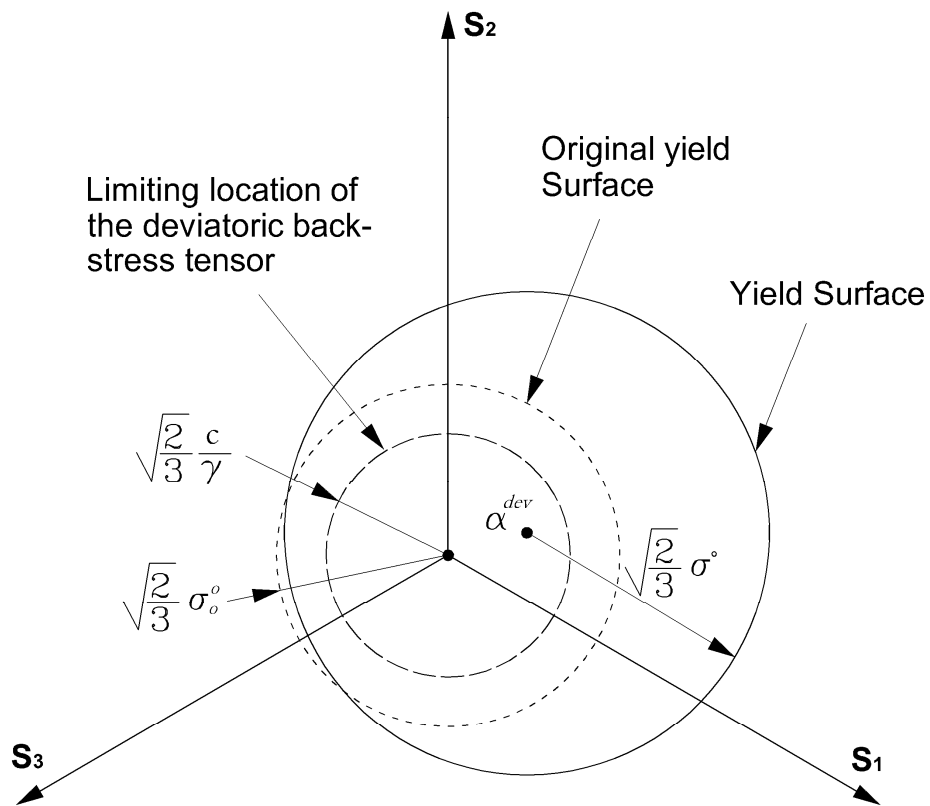


Figure 2-22 Evolution of the yield surface in the stress space when combined hardening is used

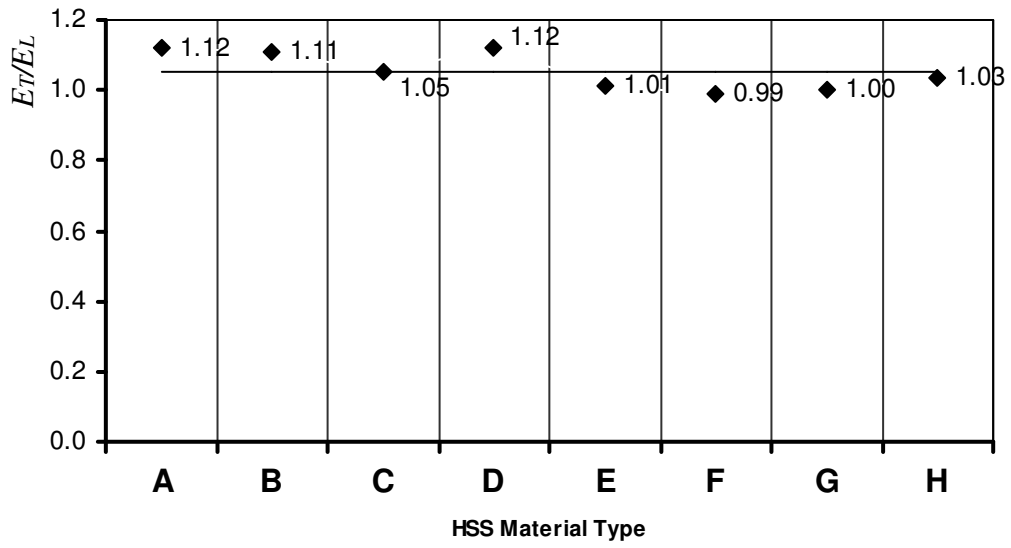


Figure 2-23 Distribution and average of  $E_T/E_L$  ratio in the material database

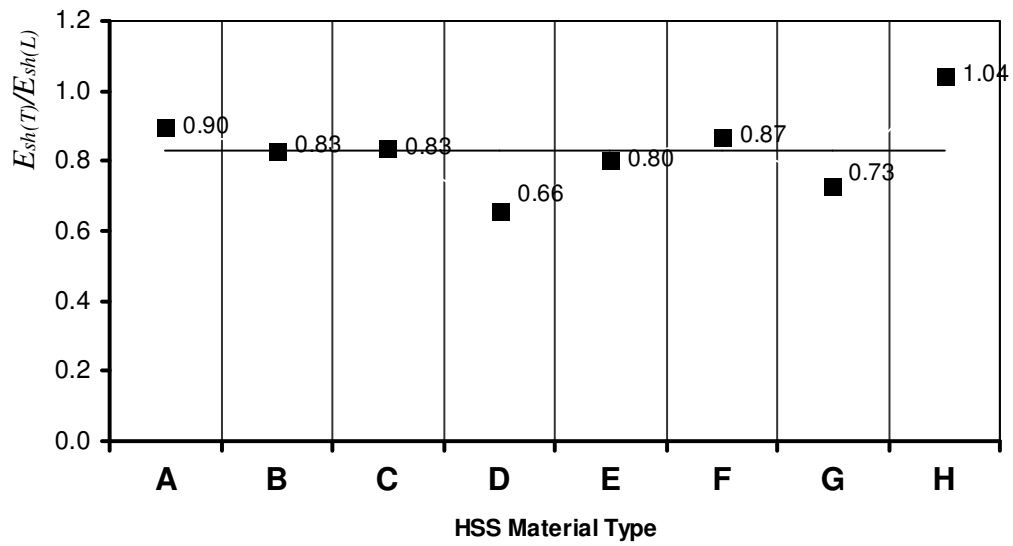


Figure 2-24 Distribution and average of  $E_{sh(T)}/E_{sh(L)}$  ratio in the material database

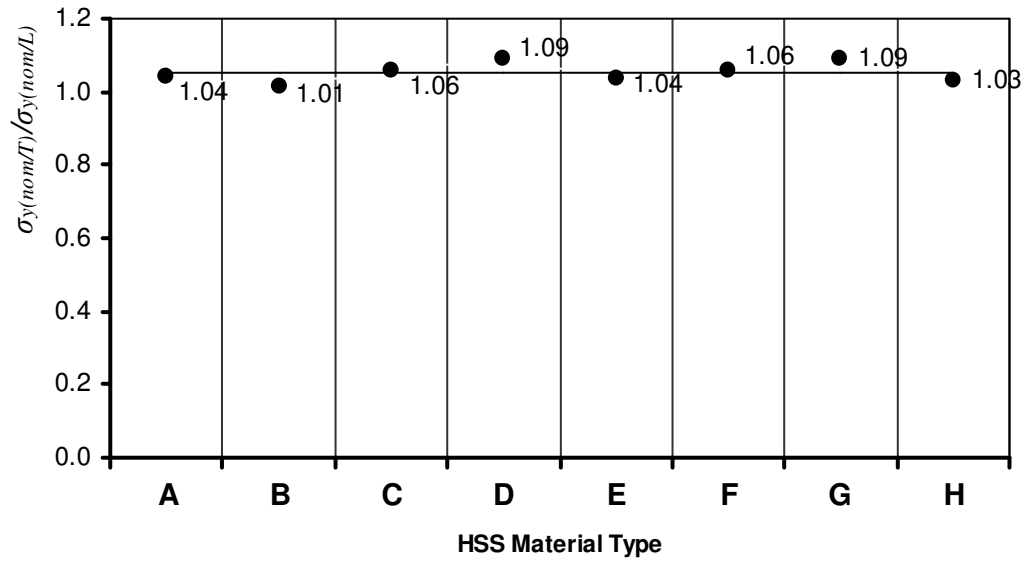


Figure 2-25 Distribution and average of  $\sigma_{y(nom/T)}/\sigma_{y(nom/L)}$  ratio in the material database

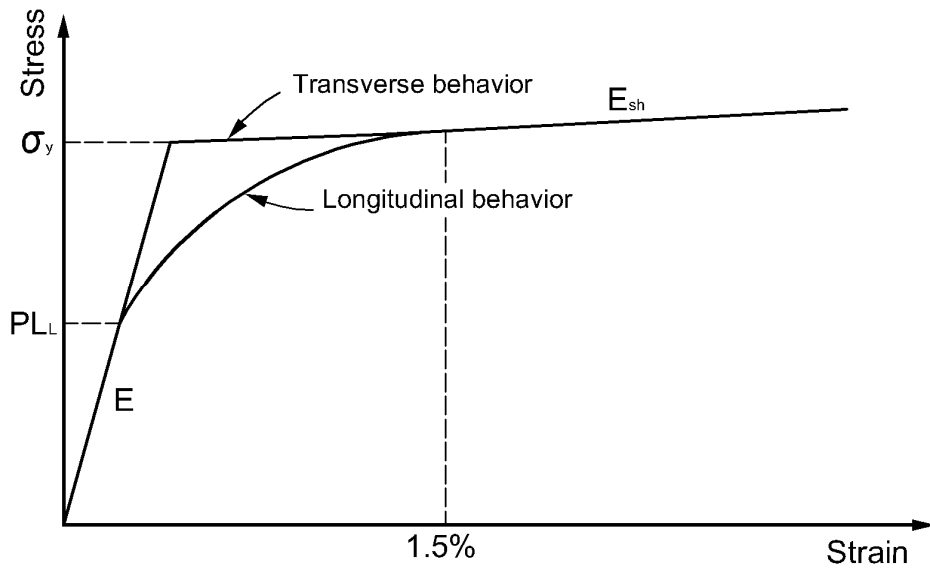


Figure 2-26 Idealized stress-strain curves in the longitudinal and transverse directions of HSS pipes

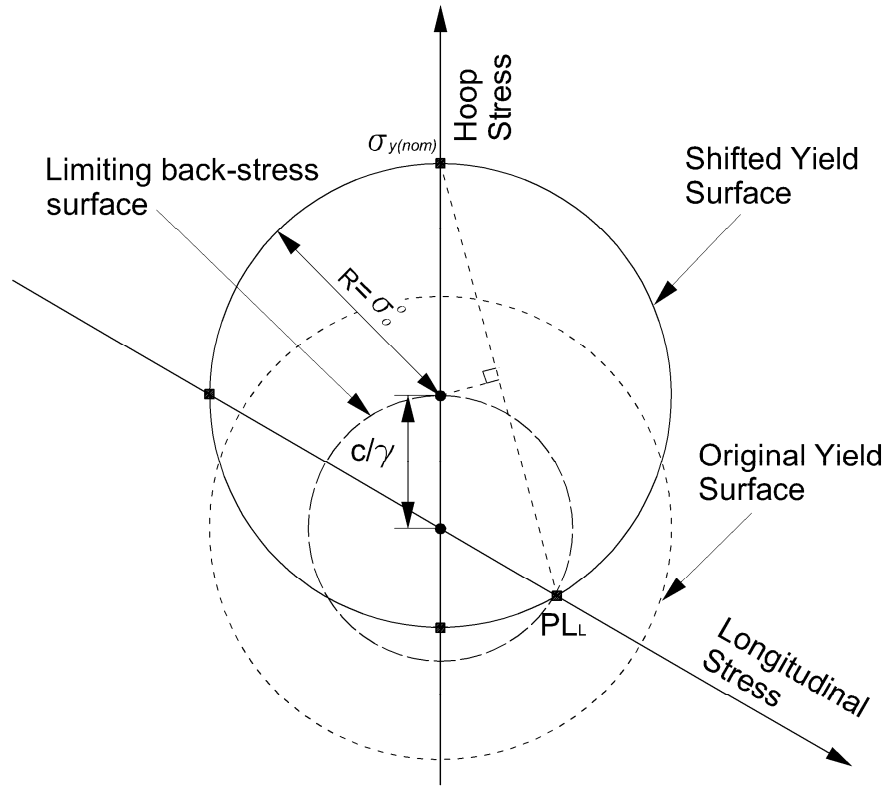


Figure 2-27 Shifted yield surface in stress space (for plane stress)

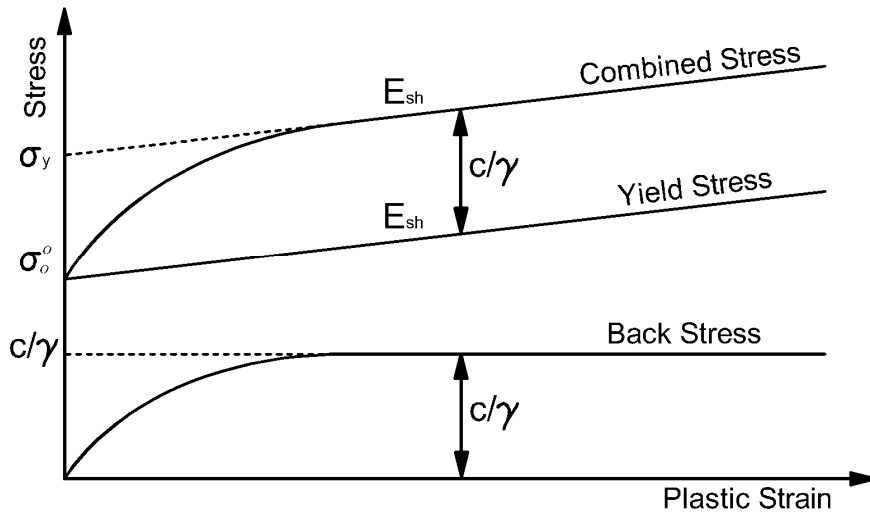


Figure 2-28 Evolution of back-stress, yield stress, and total stress of the proposed material model (linear isotropic and Armstrong-Fredrick kinematic hardening)

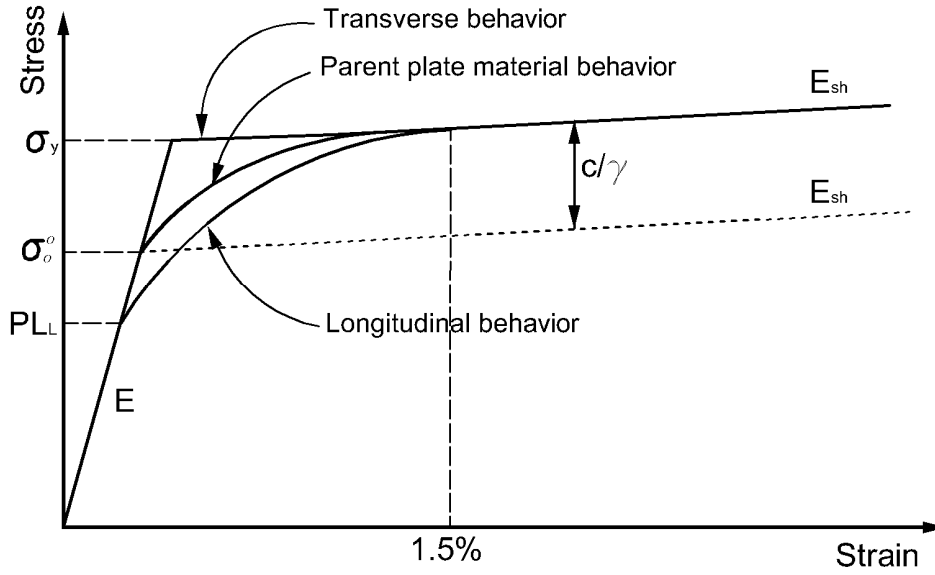


Figure 2-29 A material with combined hardening changes behaviour in two perpendicular directions after applying initial back-stress

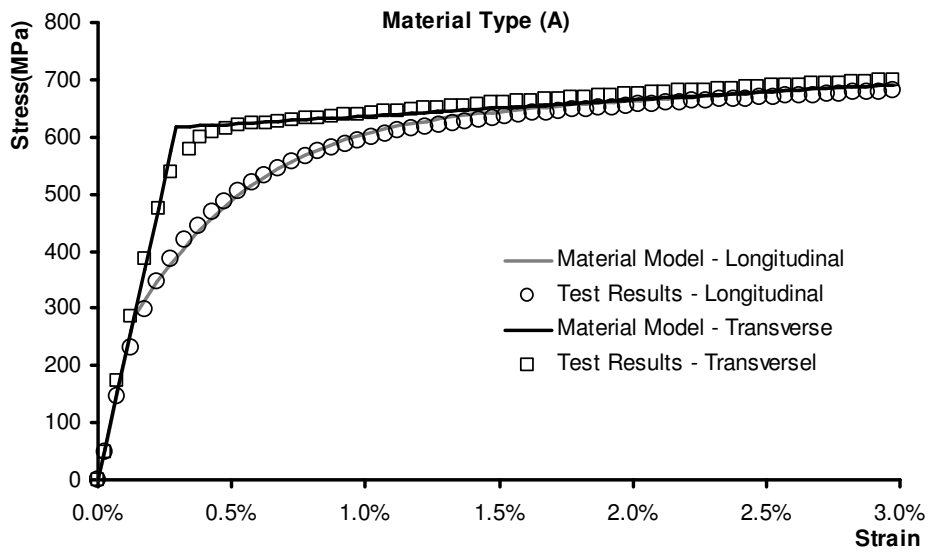


Figure 2-30 Tensile stress-strain data from the material model and average experimental results for material types A

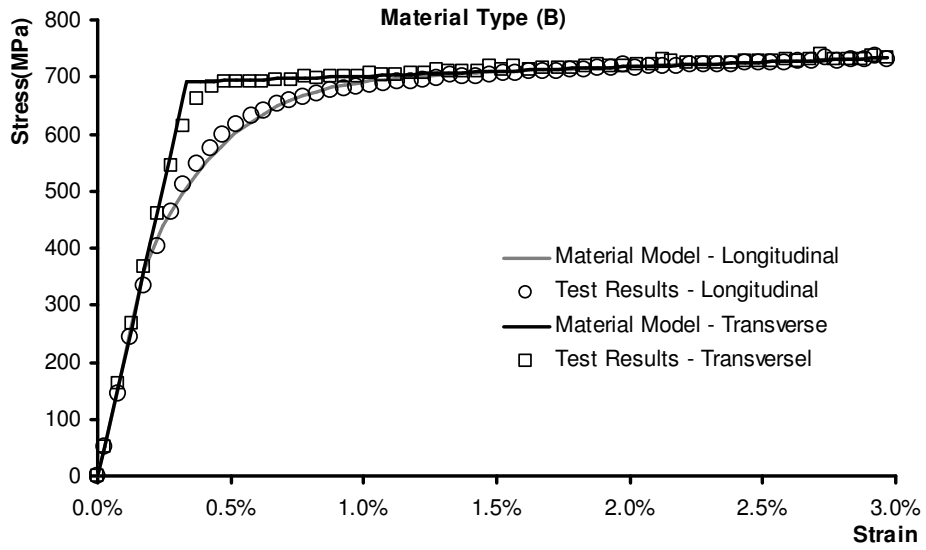


Figure 2-31 Tensile stress-strain data from the material model and average experimental results for material types B

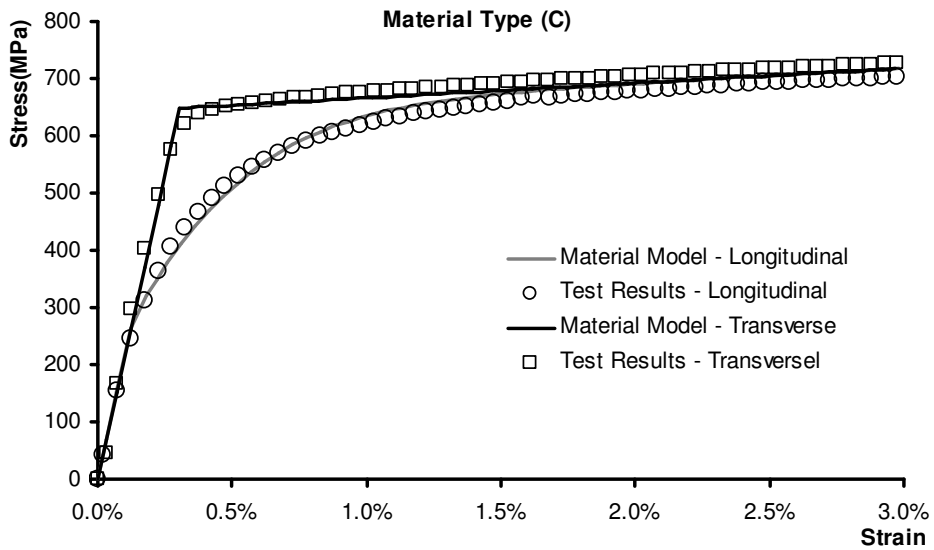


Figure 2-32 Tensile stress-strain data from the material model and average experimental results for material types C

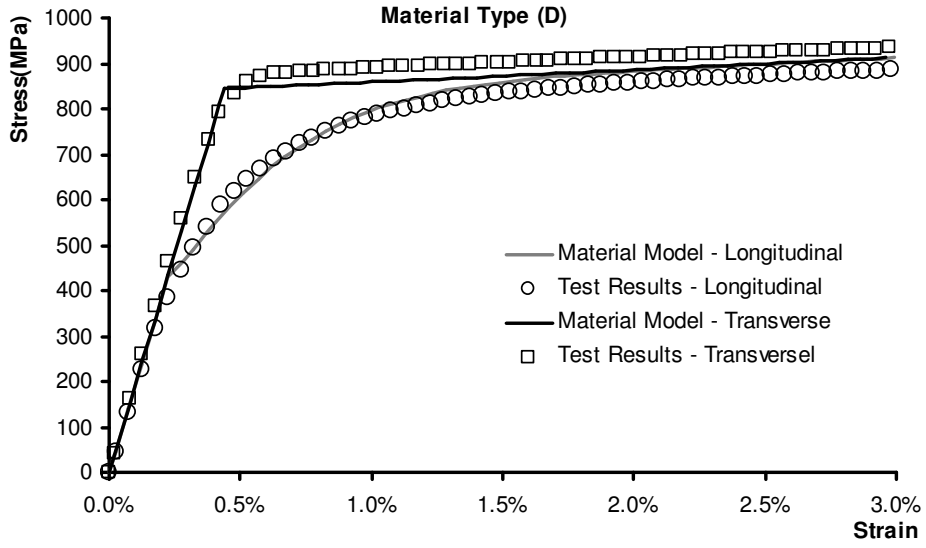


Figure 2-33 Tensile stress-strain data from the material model and average experimental results for material types D

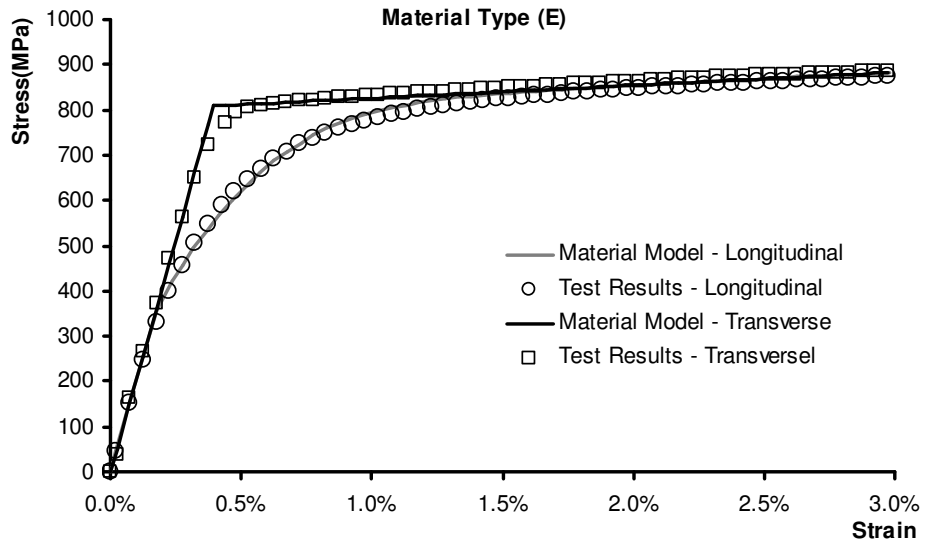


Figure 2-34 Tensile stress-strain data from the material model and average experimental results for material types E

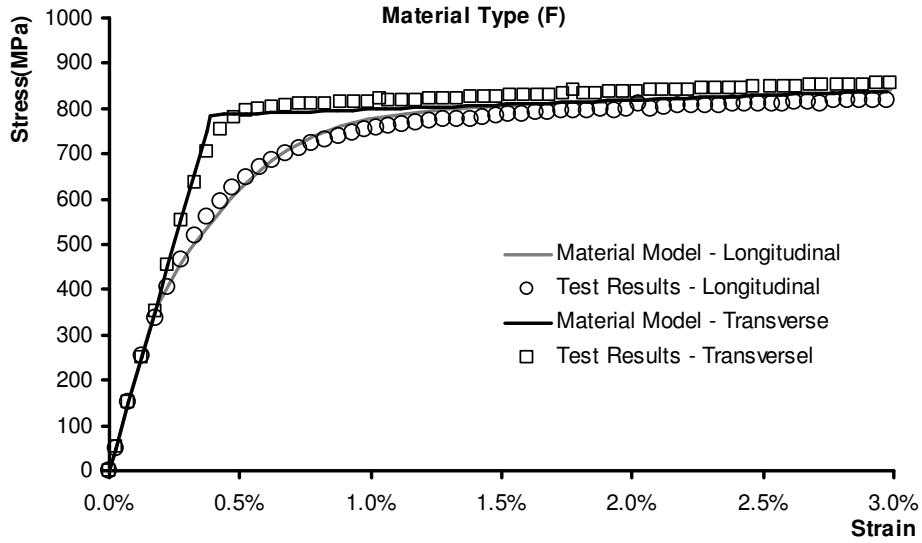


Figure 2-35 Tensile stress-strain data from the material model and average experimental results for material types F

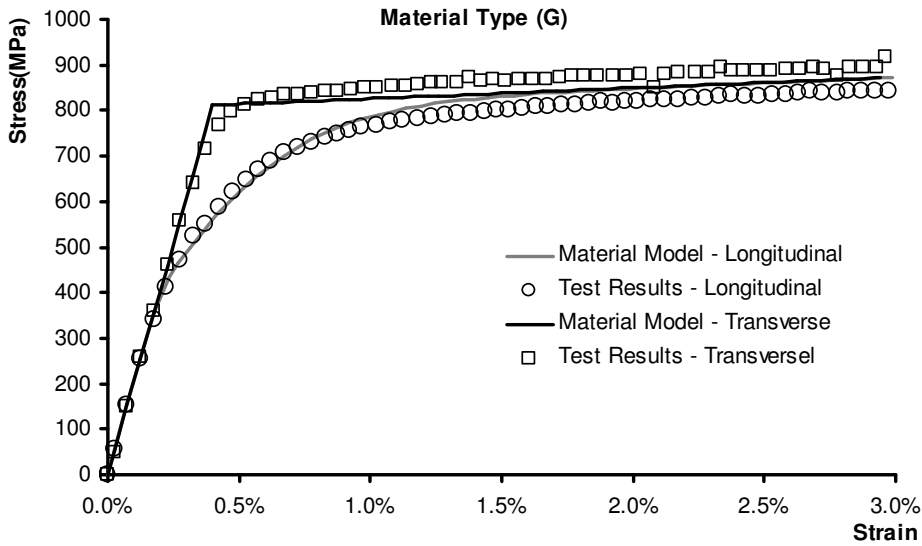


Figure 2-36 Tensile stress-strain data from the material model and average experimental results for material types G

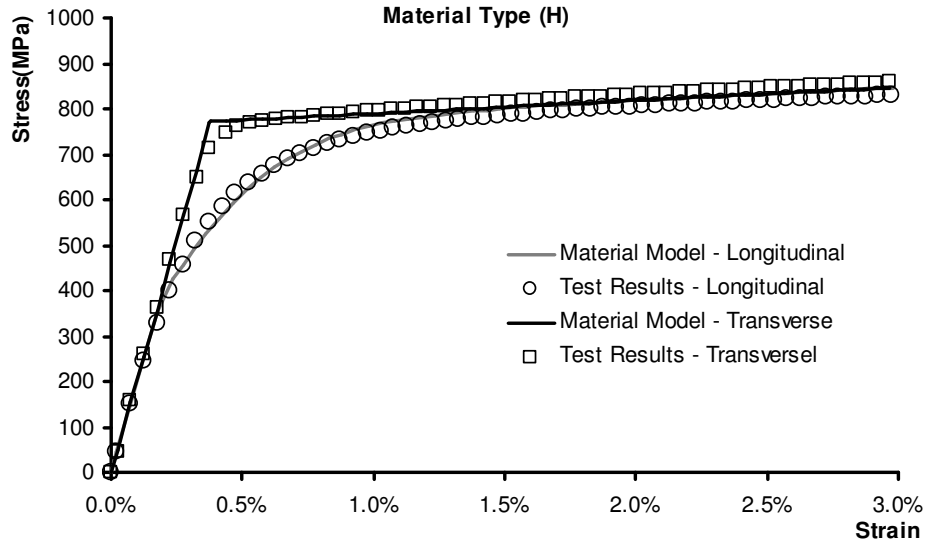


Figure 2-37 Tensile stress-strain data from the material model and average experimental results for material types H

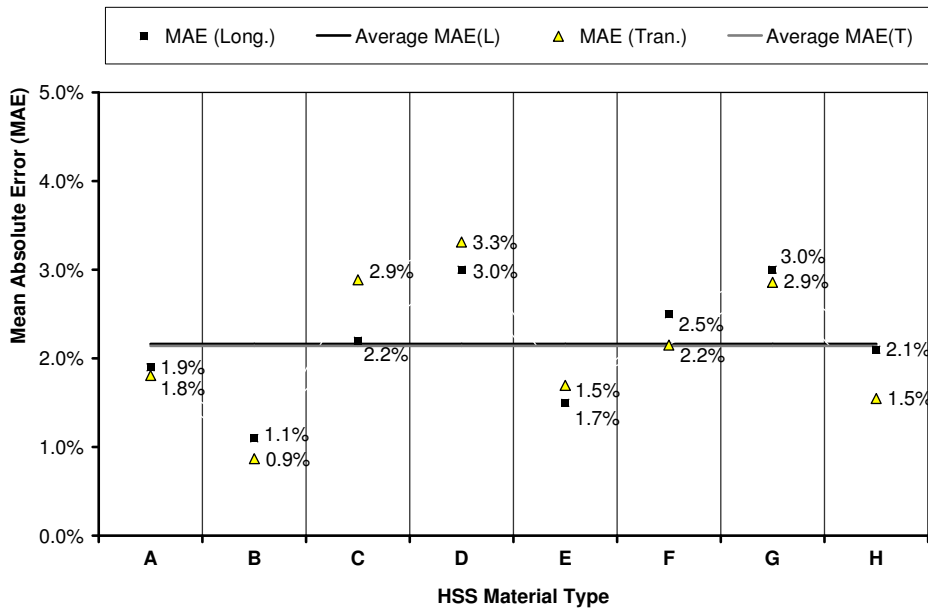


Figure 2-38 MAE in predicting tensile stress-strain relationship by the material model in the longitudinal and transverse directions

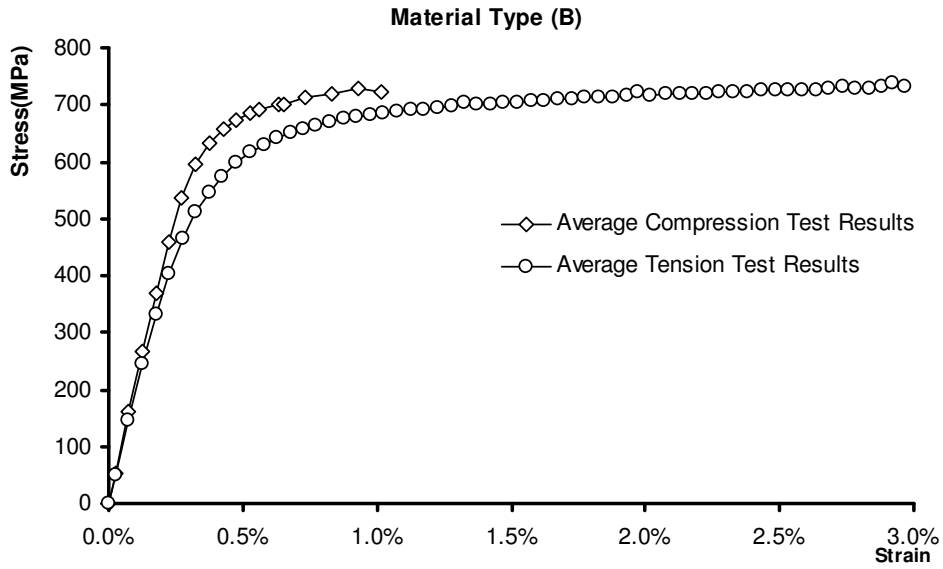


Figure 2-39 Longitudinal tensile and compressive experimental stress-strain curves for the material type B

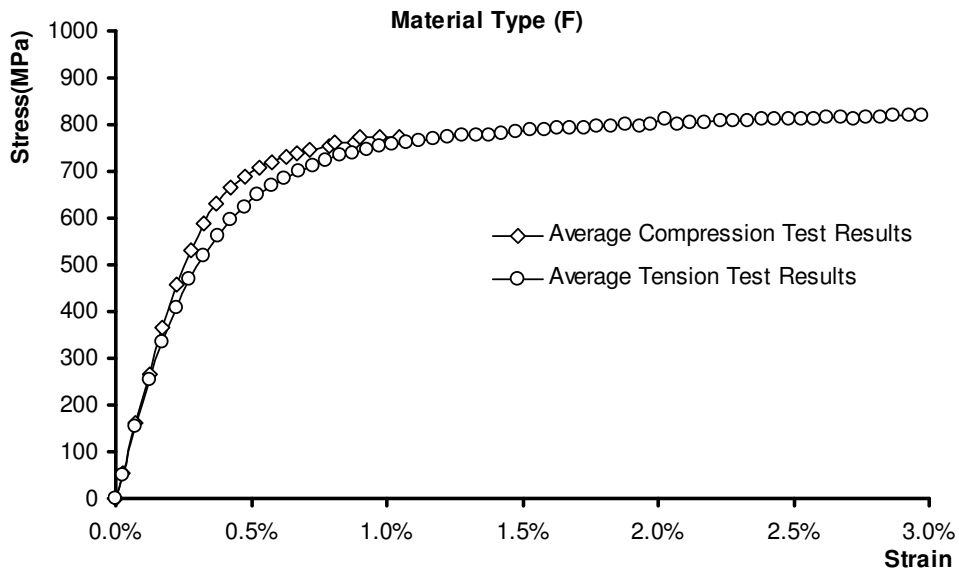


Figure 2-40 Longitudinal tensile and compressive experimental stress-strain curves for the material type F

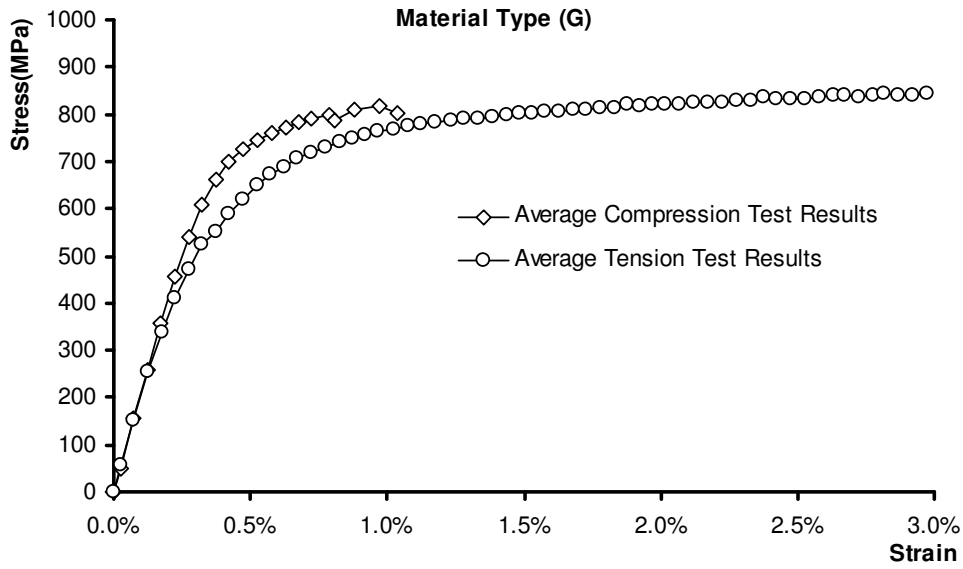


Figure 2-41 Longitudinal tensile and compressive experimental stress-strain curves for the material type G

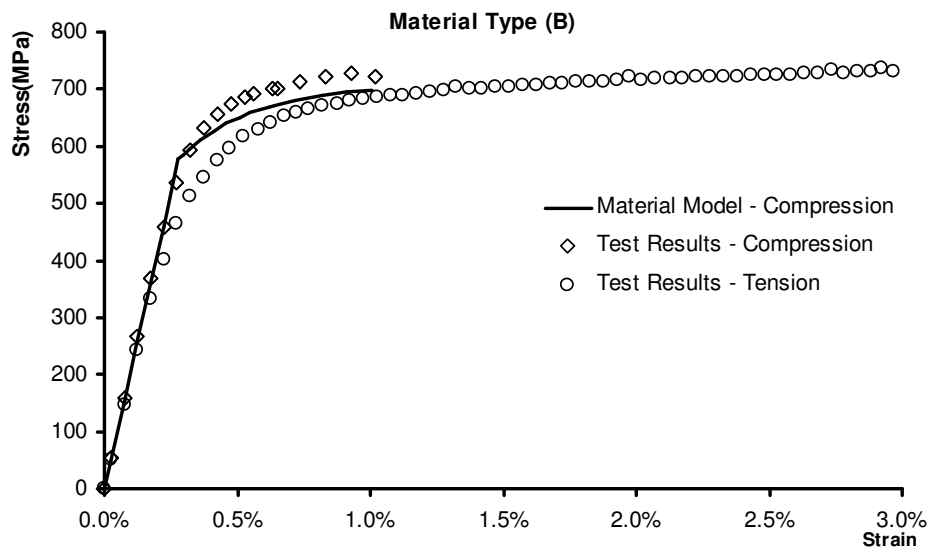


Figure 2-42 Modeled material behaviour under longitudinal compression and average longitudinal stress-strain data from tests for material type B

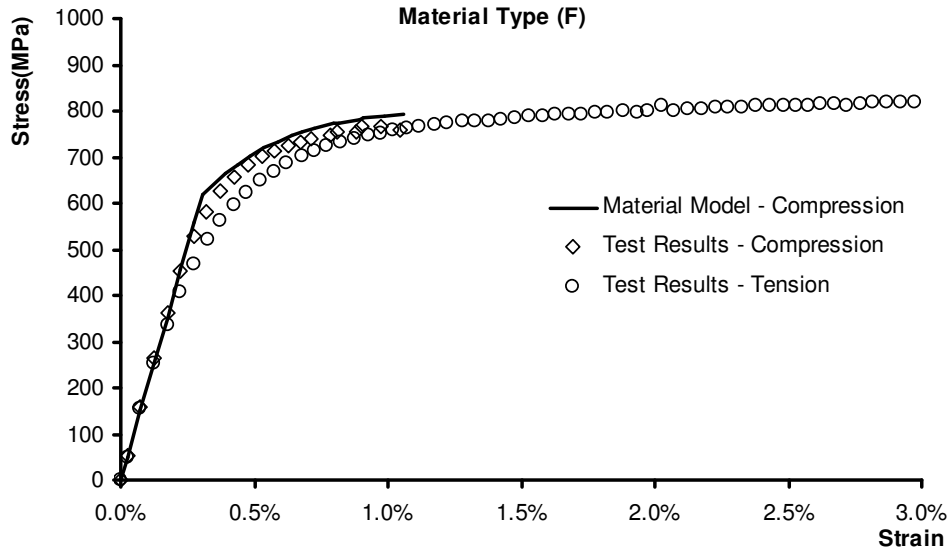


Figure 2-43 Modeled material behaviour under longitudinal compression and average longitudinal stress-strain data from tests for material type F

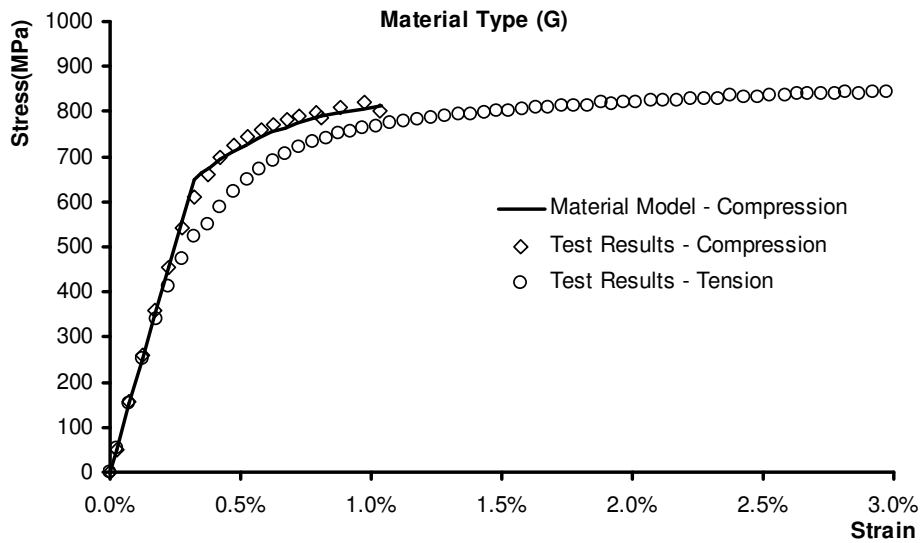


Figure 2-44 Modeled material behaviour under longitudinal compression and average longitudinal stress-strain data from tests for material type G

### **3 BUCKLING ANALYSIS OF HSS PIPES WITH ANISOTROPIC MATERIAL MODELING**

Experimental testing is widely accepted as the most effective and reliable method for determining and understanding the behaviour of structures including high strength steel (HSS) pipelines. However, it is not practical to test all possible combinations of loading, material properties, and pipe sizes. Therefore, the development of a reliable numerical model is a much more practical approach to building up a comprehensive database of HSS pipelines. Once the numerical model is developed, its competence should be validated by comparison against experimental measurements.

In this chapter, a non-linear numerical modeling technique using finite element analysis was employed to simulate the behaviour of HSS pipes previously tested for buckling. This experimental database consists of unpressurized and pressurized HSS pipes made of the same HSS materials described in Chapter 2. The combined hardening material model was used in the finite element analyses of HSS pipes. This was done to examine the material model's adequacy and also to show how material anisotropy affects the buckling response of HSS pipes.

The validation of the numerical models usually consists of two main components: the load-carrying response and the deformation response. Since strength is usually the main concern in structural design, the load-carrying response has been the conventional measure to determine the finite element models' accuracy. In this study, however, the primary focus was on the deformation response. As discussed in Chapter 1, in strain-based design, exceeding a specified deformation is defined as a limit state. The critical buckling strain (CBS), which was the main focus of this study, is one such deformation limit state. Hence, while substantial attention is given to the numerical model's ability to predict the buckling load, its chief

objective was to accurately predict the deformation of the tested specimens up to the onset of buckling.

Once the finite element model is developed and validated, additional numerically generated cases can be used to expand the database of the HSS pipes' buckling. This chapter describes the details used to develop finite element models that simulate HSS pipes with material anisotropy.

### **3.1 The Database of HSS Pipes Buckling Tests**

The experimental database used to verify the results of this chapter was extracted from a comprehensive full-scale buckling test project on HSS pipes made of grades X80 and X100 steel. This test project was conducted by TransCanada Pipeline Ltd. in collaboration with the JFE Steel Corporation and was carried out by C-FER Technologies. The project objective was to experimentally assess the compressive buckling performance of HSS large-diameter pipe specimens subjected to different combinations of internal pressure and bending moment (Timms et al., 2005).

#### **3.1.1 HSS Pipe Specimens**

The database used in this chapter contains the results of buckling tests on 15 unpressurized and pressurized HSS pipes with various geometry and material properties. Table 3-1 shows the specimens' grade, dimensions and the internal pressure applied during the test. These pipes were made of the same steel material types described in Chapter 2 (with SMYS equal to 550MPa and 690MPa). The material types of pipe specimens are also depicted in Table 3-1. All pipe specimens were provided by the JFE Steel Corporation from their HSS pipe products made specifically to cross permafrost areas and seismic zones. All

specimen fabrication had been undertaken by TransCanada, including welding 10mm thick plates to the pipe ends. C-FER Technologies designed the end plates for pressure containment and transfer of applied bending forces.

### **3.1.2 Buckling Tests**

#### **3.1.2.1 Test Setup**

Buckling tests of the specimens were performed in C-FER's Universal Testing System (UTS), a servo-hydraulic loading frame capable of 15 MN of tensile or compressive load. Figure 3-1 shows the experimental set-up used for testing the HSS pipes. Bending forces were applied to each specimen using stiff moment arms specifically designed for the test. These steel moment arms were attached to the specimens' end plates with high-strength bolts and then pin-connected to the UTS machine. A pair of hydraulic rams were fastened to the cantilevered ends of the moment arms and used to push them apart, thereby applying the bending moment to both ends of the specimens. The UTS machine was used to adjust the axial load in the specimens. Applying an equal and opposite axial force to a specimen, to react against the force applied by the hydraulic rams, resulted in a pure bending moment on the (unpressurized) pipes. During the pressurized tests, an adjusting axial force was applied by the UTS to offset the axial load generated in the pipes due to the internal pressure on the specimen end caps.

During the tests, 75mm long confining collars made of the same pipe material were attached to each end of the pipes next to the end plates, to prevent the pipes from buckling locally due to the end constraints. This set-up allows independent control of the applied bending and axial forces, and essentially makes it possible to test pipe specimens under any combination of internal pressure, axial force, and bending moment. Except for one HSS pipe that was tested under axial tensile

force and bending moment, all specimens were tested under pure bending conditions.

### **3.1.2.2 Data Acquisitions**

The following items were included in the instrumentation on the specimens:

- a) Eight equally spaced strain gauges installed on the extreme tension and compression fibers to measure local tensile and compressive strains.
- b) Four clinometers installed on the original neutral axis of each specimen to allow the calculation of specimens' curvatures over a number of different gauge lengths.
- c) Hydraulic ram extend and retract pressure transducers used to calculate the bending strut force.
- d) A specimen internal pressure transducer.
- e) The UTS machine load and stroke measurement devices.

Instruments were monitored using a computer-based digital data acquisition system. Data was acquired continuously from all instruments throughout each test. The data gathered from the instrumentation were used for load-displacement relationship calculations in this chapter

### **3.1.2.3 Loading Procedure**

Specimens were aligned in the test frame with the longitudinal seam weld located on the neutral axis of in-plane bending. The test loading on each specimen was applied with the following sequence:

- a. Specimens with internal pressure were first pressurized with water, while the UTS applied an equal and opposite compressive axial load to the specimen. For the pressurized pipes, internal pressure was adjusted to

cause hoop stress around 75% of specified minimum yield strength (SMYS).

- b. Bending moment and axial force were then applied using the moment arms and UTS system.
- c. Loading was stopped at regular intervals to allow static readings.
- d. Loading continued in this pattern, up to and past the peak moment, until the stroke or load limit of the test frame was reached or until further loading was deemed to be inadvisable, due to concerns for personnel safety and equipment damage.

Six pipes were tested under pure bending with zero internal pressure; eight pipes under both bending and internal pressure; and one pipe, HSSP#15, under internal pressure, bending moment, and constant axial tensile load causing longitudinal normal stress equal to 24% of SMYS. The testing conditions for each pipe are demonstrated in Table 3-1.

### **3.1.3 Initial Imperfection Measurements**

Prior to each test, specimen length, wall thickness, and diameter were measured. For each pipe, the measurements of the pipe's average diameter and ovality were carried out in three stations: X, Y, and Z, equally spaced along the pipe, where station Y was located in the middle and stations X and Z were the distance of one pipe's diameter from station Y. The wall thickness was calculated as the average of 16 measurements equally distributed in eight locations of pipe circumference at stations X and Z. The pipe lengths were measured at four longitudinal lines parallel to pipes axes and equally placed around the circumference.

Table 3-2 shows the variation range of wall thickness, outside diameter, and ovality among all measurements carried out for each pipe (the measured imperfections are expressed as a percentage of each pipe's average wall thickness).

## **3.2 Finite Element Modeling of HSS Pipes Bending Tests**

The material modeling method proposed in Chapter 2 was used in the buckling analyses of the tested HSS pipes using the finite element method. The primary objective of this modeling and analysis process was to verify if considering material anisotropy in pipe buckling analysis improves the simulation results.

### **3.2.1 Finite Element Method**

#### **3.2.1.1 Finite Element Concept**

The finite element method was originally developed to solve the complex elasticity and structural analysis problems in civil engineering. Nowadays, a variety of specializations in the civil and mechanical engineering disciplines (such as the structural, aeronautical, biomechanical, and automotive industries) commonly use the integrated finite element method to design and develop their products.

The finite element method is a numerical technique for finding approximate solutions for partial differential equations as well as integral equations. As considered in structural applications, finite element analysis is based on applying the principle of virtual work through the structural stiffness method. The structural stiffness method requires subdividing a structure into a series of discrete finite elements with their corners being identified as set of points in space known

as nodes. Once the force displacement properties are determined; they are related to each other through matrix mathematics using the force equilibrium equations written at the nodes. These relationships are then grouped together into the global structural stiffness matrix for the whole structure. After the global structural stiffness matrix has been compiled, the unknown displacements of the nodes can be determined for any given loading on the structure. Once the nodal displacements are known, the external and internal forces in the structure can be calculated using the force-displacements relationships for each element. For non-linear analyses, these external and internal forces are usually determined in an incremental loading basis. A complete description of the finite element method process is beyond the scope of this report, but can be readily reviewed in numerous references.

### **3.2.1.2 Finite Element Analysis Package**

Several modern finite element method packages, including specific components such as thermal, electromagnetic, fluid, and structural working environments, are commercially available. Finite element method software provides a wide range of simulation options for controlling the complexity of both modeling and analyzing a system. Similarly, the desired level of accuracy required and associated computational time requirements can be managed simultaneously to address most engineering applications. These packages allow a detailed visualization of where structures bend or twist, and illustrate the distribution of stresses and displacements.

In the present project, the finite element models were developed using the commercial finite element software, ABAQUS/Standard version 6.7-1 (Hibbit, Karlsson & Sorenson, Inc., 2003), hereafter referred to as “ABAQUS”. This software package is appropriate for the pipe buckling analysis for several reasons. The chief feature that makes ABAQUS suitable for this particular problem is its

capacity to deal with large non-linear deformations. Large non-linear deformations might be difficult to model and usually require special formulation techniques (Horrigmoe and Bergan, 1976). All tested specimens introduced in the previous section underwent large plastic deformations, which the selected finite element package would have to be able to accommodate. The solution technique used in ABAQUS is based on the Newton-Raphson method using an updated Lagrangian incremental formulation, in which the stress and strain measured at time  $t+\Delta t$  are referred back to time  $t$  at the end of the previous step. That is, “each step has its own step time which begins at zero in each step” (Hibbit, Karlsson & Sorenson, Inc., 2003). The updated Lagrangian formulation is particularly suited to this project because it is capable of all kinematic non-linear effects due to large displacements, large rotations, and large strains. The Lagrangian formulation also has a greater level of numerical efficiency compared to other similar techniques (Bathe, 1996).

The automated increment size control feature is another advantageous capability of ABAQUS. This program automatically updates the increment's size to optimize the solution time. If convergence is achieved quickly, then ABAQUS will automatically increase the increment size for the next step. If convergence is not achieved, then ABAQUS will automatically reduce the increment size and make another attempt to achieve convergence. This assists in achieving convergence of the finite element solution when a local maximum is encountered in the behaviour.

Figure 3-2 shows a typical load displacement of tubular shell structures under compressive loads or bending moments (Bushnell, 1980). Generally, a buckling point may be identified as either a bifurcation point in this figure or a limit point. Due to the inevitable initial imperfections existing in real pipes, the recorded buckling response of tested pipes is usually similar to the curve shown in the dash line in Figure 3-2.

All deformations beyond the buckling point are in the post buckling region, in which the pipe shows a softening response. If the external load continues to act without reduction regardless of the structure's displacement, the buckling point becomes the point of catastrophic collapse. This is because the energy delivered by the load during any incremental displacement in the post-buckling region is greater than the energy that the structure can absorb. Consequently, the structure accelerates and does not experience the post buckling response shown in Figure 3-2.

In a typical case in which a real pipe buckles (under induced geotechnical deformations in the field or displacement-control buckling tests), the structure will not collapse but will start to show negative stiffness and release strain energy to remain in equilibrium. In displacement-control buckling, the rate at which the structure deforms is governed by the applied displacement. Due to the unstable nature of the load-displacement in the post-buckling region, finite element simulations of the pipe-buckling process need special care to guarantee that the solution will converge.

As demonstrated by the load-displacement response of the imperfect shell structure shown in Figure 3-2, at smaller displacements the load increments can be large because convergence is achieved very quickly due to the linearity of the response curve. However, as the load increases, the structural response becomes increasingly nonlinear until buckling occurs at the peak load. As the solver passes the peak, special solution strategies are required in order to achieve convergence (Ramm, 1980). In order to capture the true response across the peak, smaller load increments are required. To achieve a response similar to the one shown in Figure 3-2, a load-displacement constraint method can be used (Riks, 1979). ABAQUS contains a Riks solution strategy feature, which was employed in the solution of the finite element models in this project. Although the pipe response up to the incipient buckling was the main focus of this research project, the post-buckling

response was also important to ensure that the model adequately simulated the true behaviour of the tested pipes.

Another feature of ABAQUS is that it allows for both load and displacement control. This feature is exceptionally important because based on the general loading scheme, the internal pressure should be applied as a load-control, and the bending moment should be applied as a displacement-control scheme.

In addition, ABAQUS was deemed to be advantageous to this project since it has an elastic-plastic material model that allows the constitutive law to be entered as a multi-linear curve with isotropic hardening. It also supports linear and nonlinear (Armstrong-Fredrick) kinematic hardening that facilitates the material modeling method introduced in Chapter 2. Furthermore, ABAQUS also has the ability to model the internal pipeline pressure as a follower force. As pressurized pipes deform, the orientation of the vector normal to the surface of the individual elements will change. The follower force feature allows the pressure to remain normal to the surface of the shell elements, as would be the case in an experimental test or under actual field operating conditions.

Finally, ABAQUS is the most powerful software available at the University of Alberta. All the above features combined to make ABAQUS an ideal choice for the finite element analyses of the tested HSS pipes.

### **3.2.2 Features of the HSS Pipe Models**

Figure 3-3 shows the general attribute of the HSS pipe models developed in ABAQUS to simulate the buckling test performed on the pipe specimens. All different features of the model are described in the following subsections.

### 3.2.2.1 Shell Elements

Each test specimen described in Section 3.1.2, including pipe, end plates, and collars, was divided into a series of discrete planar elements for the finite element modeling. A four-node double-curved shell element, S4R, was used to model the pipe's body. S4R is a quadrilateral reduced integration element with hourglass control, intended for both thick and thin shell applications (Hibbit, Karlsson & Sorenson, Inc., (2003)). This element accounts for finite membrane strains and allows for transverse shear stress. It allows for large deformations and for nonlinear material properties. It has been shown that S4R is particularly effective in modeling segments of pipe under the load conditions used in the above-mentioned test program (Del Col et al, 1998).

The S4R element accounts for finite membrane strains that exist in thin shells, but are not caused by bending. The membrane strains on the surface are determined from the derivatives of the position vector of a point on the deformed reference surface, with respect to the same point on the undeformed reference surface. Since these position vectors can be determined in the element at any level of deformation, the membrane strains can be evaluated in the element at any load level. As a result, this element is able to account for large deformations. This allows for a variation in the thickness of the shell element at different load increments, as occurs in a real pipe test.

The S4R element has an iso-parametric formulation, meaning that the same interpolation functions are used for the displacement field as for the nodal position vectors. Bathe (1996) states that “the basic requirements for monotonic convergence, namely compatibility and completeness, are satisfied by the iso-parametric elements when these elements are of general geometric shape.” This is because the iso-parametric elements have the ability to represent rigid body motions and constant strain states; thus they guarantee the convergence.

The S4R element uses reduced integration, meaning that approximations have been made that result in the integration formula having an order less than that required for exact integration (Pugh et al., 1978). This significantly reduces the computational effort required to achieve convergence. The numerical integration through the thickness was performed using Simpson's Rule. Up to seven integration points can be used through the thickness of the element, to allow accurate through thickness nonlinear material response to be captured.

There are six independent degrees of freedom, three rotational and three translational, at each node of the S4R element. The two out-of-plane rotational degrees of freedom, with respect to the vector normal to the reference surface, are directly associated with the stiffness of the element. The third rotational degree of freedom, which is the rotational degree of freedom about the vector normal to the element's surface, is rarely activated in thin shell applications. Therefore, hourglass control is required in the element formulation in order to prevent spurious energy modes. The hourglass control is achieved by assigning a small artificial stiffness to the third rotational degree of freedom, either as a user input or using the default value in ABAQUS, to prevent a singular global stiffness matrix. In this study the default artificial stiffness was used.

The S4R element has been constructed to be shear flexible, thereby allowing shear deformations. Transverse shear strains are measured using the change in the direction of the vector originally normal to the reference surface. A constraint is imposed on this element that forces the material line originally normal to the shell reference surface to remain approximately normal to the surface throughout the deformation. This results in a behaviour that is consistent with the Kirchhoff assumption in classical thin shell and plate theory. The capability of the S4R shell element to accommodate shear deformations makes it practical for both thick and thin shell analyses (Hibbit, Karlsson & Sorenson, Inc., 2003). If the shell is thin,

as is the case with the specimens modeled in this study, the shear deformation in the through-thickness direction will be negligible.

As mentioned before, restraining collars were placed around the outside faces of the test specimens adjacent to the end plates' welds. The function of these collars was to help make a smooth transition in the region that was disturbed by the rigid plates at the ends of the specimens. The collars used in the actual test specimens were fabricated from the same section as the test specimens. In the finite element models, the collars were modeled by increasing the wall thickness at the top and bottom collars' locations. In previous research, this technique has been shown to be successful in reducing the incidence of end buckles (Del Col et al., 1998). While this method of modeling does not truly describe the actual physical arrangements that exist between the collars and test specimens, it is nevertheless considered an acceptable approximation.

The end plates have small deformations during the tests, as they had been designed to remain in their elastic range throughout the entire buckling test. These plates were modeled by three-node elements STRI3. This element type is appropriate for arbitrarily large rotations and small strains. STRI3 has six degrees of freedom at the nodes and is a flat-faceted element. The change in thickness that happens along with deformation is ignored in this element. This feature is not expected to have any significant effects on the analyses results, since the deformation in the end plates is negligible during the tests (and analyses) due to their robustness.

### **3.2.2.2 Symmetry**

In order to save the analysis time through significant reduction in the degrees of freedom, symmetry has often been used to model test specimens in previous finite element analyses of pipe specimens (Zhou and Murray, 1993 and Vitali et al., 1999). Based on the specimens and testing conditions, one plane of symmetry can

pass the pipe axis while being perpendicular to the axis of bending moment and/or one plane of symmetry can pass through the specimen's middle cross-section while being perpendicular to the pipe axis. Therefore, modeling one-quarter of a pipe specimen can provide response behaviour that is representative of the entire test specimen.

During the development of the finite element models for this project, one plane of symmetry was used passing along the length of the pipe specimens through the radial axis within the plane of bending. Thus, half the pipes, end plates, and collars were modeled to save analysis time. The nodes placed on the plane of symmetry were restrained to remain on the plane but were free to move within it.

The initial imperfection pattern used in the finite element models was symmetrically distributed in the pipe circumference but not in the length; therefore it was not possible to use the second plane of symmetry that cut the pipe in its half-length.

### **3.2.2.3 Boundary Conditions**

Due to the robust nature of the loading arms and their associated components, it was assumed that they were essentially rigid for modeling purposes. Based on this assumption, the multi-point constraints (MPC) feature in ABAQUS was used to impose constraints between the degrees of freedom of the end plates' centres and the pivot points. A BEAM-type MPC was used to make a constraint between the end plates' centres and their associated pivot points. Using this type of MPC, the program assumes that one rigid beam connects the centre of the top end plate to the top pivot point and another rigid beam connects the centre of the bottom end plate to the bottom pivot point (shown by dashed line in Figure 3-3).

In addition to the components that make the physical features at the end of the test specimens, the global boundary constraints also had to be included in the finite

element models. The pivot points were selected as the effective points of load application and the boundary conditions. As can be seen in Figure 3-3, the top and bottom ends of the test specimens had different physical restraints. At the bottom end, the bearing on the floor of the lab prohibited the end-loading arm assemblies from any type of translational motion.

As mentioned before, the nodes placed on the plane of symmetry were restrained to remain on the plane but were free to move within it. This restraint guarantees bending within the plane of symmetry and does not allow the specimen to rotate out of the plane of symmetry or around its longitudinal axis. Nevertheless, there are no applied loads that generate moments out of the symmetry plane or rotation around the longitudinal axis of the specimens. Out-of-plane rotation might have occurred during the tests due to the un-symmetric buckling of the test specimens; however, the resulting out-of-plane bending was considered small enough to be neglected.

At the top end of the test setup, a different set of restraints exists. The top end of the test setup was connected to the loading head of the UTS machine. Since axial load was one of the applied loads during testing, the test specimens had to be allowed to deform in the axial direction, allowing for the effects of this load to be accounted for. The translational degree of freedom within the plane of symmetry and perpendicular to the pipe axis was constrained to prevent instability of the model. The third translational degree of freedom (perpendicular to the plane of symmetry) was set free. Nevertheless, as the pipe nodes on the plane of symmetry were restrained to stay on that plane and, on the other hand, no loading was applied in the direction perpendicular to the symmetry plane, it did not make any difference if the third translational degree of freedom was constrained or not. Similar to the bottom pivot point, all of the top pivot point's rotational degrees of freedom were set free.

### 3.2.3 Material Modeling

Two different steel material types were used in each specimen model: the steel material of the end plates and the steel material of the pipe and collars. Since the end plates were designed thick enough to remain elastic during the test, they were modeled as an elastic material. The modulus of elasticity and the Poisson's ratio are sufficient to define the elastic material properties. There were no material test results available for the end plates; therefore, they were modeled with modulus of elasticity similar to the pipe material, and assumed Poisson's ratio equal to 0.3, which is a widely accepted value for steel materials. Although the modulus of elasticity of end plates and the pipes might have been slightly different, it is very unlikely that this difference changes the behaviour of the pipe, since the modulus of elasticity has small variation in steel.

For the elements forming the pipes and collars, buckling analyses were performed with two material modeling methods. The first method was the isotropic material model using the longitudinal stress-strain data from the tension coupon test. The second method was the anisotropic model introduced in Chapter 2 of this thesis.

#### 3.2.3.1 Isotropic Model

The material properties of the isotropic models were defined similar to the most conventional method of material modeling for energy pipes, i.e., using the longitudinal tension material test data with choosing the isotropic hardening material plasticity.

In order to define the elastic constitutive relationship, the average longitudinal modulus of elasticity,  $E_L$  from all material tests on the same pipe, was used in the input file along with the Poisson's ratio,  $\nu$  equal to 0.3.

In order to define the plastic range, however, a yield criterion and a hardening rule should be specified. Here, the von Mises yield surface was used as the yield criterion.

$$f = J_2(s) - \sigma_y \leq 0 \quad (3-1)$$

where

$J_2$ : second invariant of the deviatoric stress tensors

$s$ : deviatoric stress tensor.

This criterion is based on the determination of the distortion energy in a given material. Assuming an isotropic material response along with the von Mises yield criterion, yield stresses associated with the three orthogonal principal stresses are equal. Hence, in the three-dimensional stress space, the von Mises yield surface has a cylindrical shape, centred on the hydrostatic stress line. As a result, the material property is independent of the stress path (i.e., the material response is independent of either direction of the material or tension and compression types of loading).

In the isotropic material modeling, the hardening rule for plastic behaviour is also isotropic. Isotropic hardening means that the von Mises yield surface has a uniform post yielding expansion about the hydrostatic stress line. The expansion rate of the yield surface can be defined based on the stress-plastic strain data at different magnitudes of plastic strain. For each pipe model, the average value of longitudinal stress-strain curves was used for the stress-plastic strain data in order to define the hardening rule for each material type. By inserting the stress-plastic strain data in the input file, ABAQUS is able to define the isotropic hardening rate at any plastic deformation in the given range.

### 3.2.3.2 Anisotropic Model

One of the beneficial features of ABAQUS version 6.7-1 is that it supports the combined hardening (isotropic/kinematic) material modeling with a variety of hardening patterns. The material modeling method and the material model calibration used for the anisotropic finite element models were similar to what was described in Chapter 2.

As the main focus of this study is the response of HSS pipes up to the onset of buckling, the most important parts of the material response were elastic and early plastic ranges. Therefore, the range of 0.0% to 3.0% total strain was considered for the material simulation and model calibration as the CBS in HSS pipes hardly exceeds 3.0% (Hart et al., 1996). The material properties used to build the anisotropic models for each material type were extracted from the longitudinal and transverse stress-strain data by the calibration process described in Chapter 2 of this thesis.

In the anisotropic model, the anisotropy only exists in the plastic range, and the elastic response was considered isotropic. Defining the modulus of elasticity along with the Poisson's ratio is adequate to define the elastic response of the material. The average of longitudinal and transversal moduli of elasticity was used for the elastic modulus of elasticity. The Poisson's ratio was set at 0.3.

For the plastic region of the anisotropic model, the von Mises yield surface was used as the yield criterion with respect to the deviatoric parts of the stress and back-stress tensor as

$$f = J_2(\sigma - \alpha) - \sigma_y \leq 0 \quad (3-2)$$

In the three-dimensional stress space, the Von Mises yield surface has a cylindrical shape, centred on the line passing the back-stress point and parallel to

the hydrostatic stress line. As a result, the material property is dependent on the stress path.

Using the combined hardening law in ABAQUS, the evolution of the total stress is a combination of yield stress and back-stress evolutions (i.e., translation and expansion of the yield surface) which represent isotropic and kinematic hardening, respectively.

$$\sigma = \sigma^o + \alpha \quad (3-3)$$

where

$\sigma^o$  : size of yield surface

$\alpha$  : magnitude of back-stress.

The evolution of yield stress and back-stress should be defined by isotropic and kinematic hardening laws, respectively.

In the proposed anisotropic material model, the original size of the yield surface at zero plastic strain is  $\sigma_o^o$  and the size of the yield surface evolves linearly during plastic deformations. In uniaxial form we have

$$\dot{\sigma}^o = E_{sh} \times \dot{\epsilon}^p \quad (3-4)$$

where

$\dot{\sigma}^o$  : yield stress rate

$\dot{\epsilon}^p$  : plastic strain rate

$E_{sh}$ : strain hardening modulus.

As ABAQUS can calculate the isotropic hardening rate provided the stress-plastic strain data, giving two pairs of stress-plastic strain data at zero plastic strain and the end of the deemed plastic range was enough to adequately define the linear evolution of the yield surface of the model.

The translation of the yield surface was defined by the back-stress evolution through the Non-linear Armstrong-Fredrick kinematic hardening law.

$$\dot{\alpha} = c \frac{1}{\sigma^0} (\sigma - \alpha) \dot{\epsilon}^p - \gamma \alpha \dot{\epsilon}^p \quad (3-5)$$

where

$\dot{\alpha}$ : back-stress rate

$\dot{\epsilon}^p$ : plastic strain rate

$c$ : kinematic hardening constant

$\gamma$ : kinematic hardening constant.

After defining the yield criteria and hardening rules for the anisotropic model, the yield surface was shifted in the stress space to complete the modeling and achieve different responses in longitudinal and transverse direction and under tension and compression.

In ABAQUS, the initial condition of the material with combined hardening material properties can be defined in terms of the initial back-stress matrix. For each material model, an initial value of normal back-stress (equal to  $c/\gamma$ ) was inserted to the material back-stress tensor in a transverse direction. The rest of the back-stress tensor components (i.e., normal back-stress in the longitudinal direction and shear back-stress) were set to zero. The initial back-stress shifted the yield surface; subsequently, the elements of the pipes' model showed different responses in longitudinal and transverse directions close to the material test results.

### 3.2.4 Mesh Study

In any finite element modeling, the selection of an appropriate sized mesh is an important part of the efficiency of the analysis. A coarse mesh may have difficulty

in predicting the actual behaviour of the tested specimen, a fine mesh significantly increases the processing time. Previous finite element analyses on pipelines at the University of Alberta (Del Col, et al., 1998 and Dorey et al., 2001) showed that if 40 quadrilateral, reduced integration elements with aspect ratios smaller than 2.0 are used around half of the pipe's model circumference, the model shows an optimum performance in terms of processing time and accuracy. The same configuration was adopted for this study; yet, a finer mesh study was performed in this project to ensure that the mesh size does not influence the finite element analyses results.

#### **3.2.4.1 Selection of Mesh Sizes**

As Figure 3-3 shows, the basic meshing scheme selected for the pipe models consisted of 40 elements around 180° of model's circumference and 104 elements along the full length (40×104). Five rows of elements formed the collars in both ends and 94 rows of elements formed the pipe body. For all different categories of length-to-diameter ( $L/D$ ) ratios of HSS pipes in the experimental database (i.e. between 3.4 and 4.4), the aspect ratios of the pipe elements became between 1.06 and 1.20.

In order to verify that the basic meshing scheme is adequate in processing time and accuracy, one coarser and one finer meshing schemes were also tried. In the coarser meshing, the pipe elements' sizes were double that of the basic model (20×52), and in the finer, the elements' sizes were half that of the basic model's size (i.e. 80×208). The element aspect ratios for the finer and coarser mesh schemes were similar to that of the basic model.

As Figure 3-3 shows, STRI3 elements forming the end plates were arranged in such a way that one of their three nodes was placed on the pipe's longitudinal axis and two other nodes were placed on the pipe's perimeter. Hence, the number of three-node elements forming each end plate was 20, 40, and 80 in the coarser,

basic, and finer models, respectively. According to the ABAQUS manual, in order to accurately model bending of a curved shell, dense mesh should be used for this element type (Hibbit, Karlsson & Sorenson, Inc., 2003). Nevertheless, the above arrangement was considered satisfactory as the robust end plates had very small deformations during the buckling analyses.

### **3.2.5 Initial Imperfection Modeling**

The next step in the finite element modeling of HSS pipes was to include initial imperfections to trigger the buckling process. As Figure 3-2 shows, initial imperfections reduce the pipe's buckling strength and deformability compared to a perfect circular shell structure. Initial imperfections of a pipe segment appear in forms of out-of-straightness, radii variation along the length, cross section out-of-roundness, and thickness variations.

The type, pattern, amplitude, and location of the initial imperfections affect the buckling of the pipelines (Sato et al., 2009). Finite element models of pipes should include appropriate initial imperfections in order to achieve reasonable buckling results. The most accurate way to implement initial imperfections in finite element models is to model the pipes with their actual initial imperfections. This approach requires careful measurement of the initial imperfections of each pipe before conducting the buckling test.

The actual initial imperfections had not been measured systematically prior to the buckling tests of the HSS pipes in the available database. The variation in the cross sectional measurements shown in Table 3-2 could not be used for imperfection modeling because they provided imperfection data for only a few locations. Although Sen and Cheng (2010) detected that the initial imperfection patterns are repetitive along the pipe's length, the limited available imperfection data cannot be expanded to map any pattern for each type of imperfections. But

rather, they can provide an intuition of expected magnitude of different imperfections on the pipe body in terms of out-of-roundness, radii variation, and variation in wall thickness.

In the absence of actual initial imperfection data, researchers use idealized imperfection patterns to trigger the buckling in finite element analyses. One of these imperfection patterns has been introduced by Dorey et al. (2006) for applying ovality to pipe models under bending load whenever the actual imperfection data are not included in the model. If the imperfection is applied in an appropriate zone along the pipe model's length, the buckling location and the pipes buckled shape will be similar to the test results. The pattern introduced by Dorey et al. (2006) was used for the finite element models developed in this chapter.

Figure 3-4 exaggeratedly shows the type of imperfection pattern used in the finite element models of pressurized HSS pipes. In this so-called half-ring imperfection, the pipe radius smoothly increases within a specific gauge length,  $L_{II}$  (usually equal to the pipe diameter) in a way that it comes to its maximum value in the middle of the gauge length on the compression side of the pipe (under bending moment). The other half of the model (tension side) remains perfectly circular in cross-section along the model's entire length. In each cross section of the imperfect zone, the radius deviation from the original radius increases from zero in the original neutral axis to its maximum value in the extreme compression fiber. This pattern of the imperfection forms a subtle bulge-type shape in the pipe's compression side.

For this imperfection pattern, the distance from the pipe axis to any grid point located on the compression side of any cross-section within the imperfect zone, is given by

$$R = \left( R^{\circ} + 0.25I_{max} \times \left[ \sin \left( \frac{2x\pi}{L_H} - \frac{\pi}{2} \right) + 1 \right] \times [\cos(2\beta) + 1] \right) \quad (3-6)$$

where

$R$ : distance of the imperfect grid point to the pipe axis

$R^{\circ}$ : original radius of the pipe

$I_{max}$ : maximum magnitude of imperfection

$L_H$ : gauge length of the imperfect section (usually equal to the pipe's diameter)

$x$ : longitudinal distance of the grid point from the cross-section where imperfection begins

$\beta$ : angular distance between the grid point and the point of extreme compression fiber.

Using this idealized imperfection pattern only provides out-of-roundness in a certain gauge length of the pipe, while it ignores the wall thickness variations and radii variations.

Using different values for  $I_{max}$  changes the onset of buckling and essentially the CBS of the pipe model. Therefore, appropriate magnitude should be used to make imperfection effects on the buckling response of the pipe models similar to the tested pipes. As Table 3-2 shows, the out-of-roundness (ovality) range is between 3.7% and 24.2% of pipe's wall thickness. These values may not be the actual maximum and minimum of ovality in the tested specimens because the measurement had been done on limited locations of each specimen. Furthermore, the real pattern of imperfection is not necessarily similar to what is assumed in the above half-ring imperfection pattern. Therefore, to avoid using a subjective value for  $I_{max}$ , each pipe model was analyzed with a range of initial imperfections. Four different  $I_{max}$  were used for each pipe model, providing ovalities equal to 2.5%, 5.0%, 10.0%, and 25.0% of the pipe's wall thickness. These values were selected to cover the observed range of ovality magnitudes.

Preliminary analyses on unpressurized and pressurized models show that the pressurized models better respond to the bulge shape imperfection pattern shown in Figure 3-4. On the other hand, the larger amplitude of  $II_{max}$  was required to trigger buckling in the unpressurized pipes. In some cases, the required ovality magnitude becomes larger than the normal imperfection that usually exists in pipelines. This is expected because the bulge shape better agrees with the buckled shape of pressurized pipes in which the pipe wall moves outward. In unpressurized pipes however, the buckled area has a diamond shape in which the pipe wall moves inward. Therefore, the bulge shape imperfection pattern better facilitates the buckling process in pressurized pipes compared to unpressurized pipes.

Taking into consideration the conditions explained in the previous paragraph, an imperfection pattern that generates a smooth dent shape in the compression side of the buckling zone was used in the unpressurized pipe models. Pilot analyses showed that using a dent-type imperfection in unpressurized models leads to better agreement with the experimental results. Therefore, a dent-type imperfection was used for unpressurized pipes. The following equation was used to generate this type of imperfection for the unpressurized pipes

$$R = \left( R^{\circ} - 0.25II_{max} \times \left[ \sin \left( \frac{2x\pi}{L_{II}} - \frac{\pi}{2} \right) + 1 \right] \times [\cos(2\beta) + 1] \right) \quad (3-7)$$

where the parameters are the same as Equation (3-6).

The distribution of imperfection along the gauge length and around the pipe circumference is similar to the bulge-type imperfection, but the local radius of the pipe is decreased in the imperfection zone. Figure 3-5 exaggeratedly shows this imperfection pattern.

### 3.2.6 Loading Scheme

In ABAQUS, the loading scheme of any specimen can be divided into a series of load steps. In the pipe models developed in this research, two major steps were used to simulate the loading scheme in the actual pipe-buckling test. The first step was to pressurize the test specimens and apply the axial load. For the unpressurized models, the magnitude of the internal pressure was defined as 0.0, and for the pressurized pipes, the magnitude of the internal pressure for each pipe was applied according to its testing pressure. The internal pressure was applied as a distributed load on the internal surface of shell elements forming the pipe, collars, and end plates. This internal pressure was applied normal to the reference surface of the shell elements as a follower-force throughout the analysis.

Internal pressure on the end plates generated an axial tensile load on the pipe body. In the same loading step, a concentrated force was also applied on the top pivot point of the pressurized pipes to generate an axial load that balanced the axial load generated due to the internal pressure. As described before, all pipe specimens were tested in a pure bending condition except one specimen (HSSP#15). Hence, the magnitude of the concentrated force was applied such that it provided the desired longitudinal uniform normal stress in HSSP#15; and cancelled out the axial tensile load that was built due to the internal pressure in the eight other pressurized pipes. The first load step including the internal pressure and the axial load was applied with a single increment of loading.

The second and final step was to monotonically apply an equal and opposite moment at the pivot points. The arc-length control technique (referred to as the Riks method) was used to carry out the buckling analysis. The Riks method is one of the solution strategies available in ABAQUS (Hibbit, Karlsson & Sorenson, Inc., (2003)). If the default solution strategy of ABAQUS, the Newton-Raphson approach, is used, the solution is not able to converge as it passes over the peak on the curve (Dorey et al., 2001). If the Riks method is used, ABAQUS is able to

converge over the limit points and continue the analysis through the post-buckling region.

### 3.3 Results and Discussion

Examining the behaviour in the buckling area is the most common method used to verify a pipe segment's overall strength and stability. During the buckling tests, the pipe segments were under a uniformly distributed bending moment; therefore, the global end moments are equal to the internal bending moment carried by the buckling area. For the finite element models, the applied concentrated moments at both ends represent the global moment in pipe models. In the pipe tests, however, the end moments applied during the tests should be calculated based on the loads applied by the hydraulic jack and the length of the lever arms. The associated lever arms need to be updated taking into consideration the deformations of the test set-up during the test. Dorey et al. (2001) provide detailed information on how to calculate the global and local moment in these test set-ups.

In addition to the load parameter (which, in this instance, is the applied bending moment), we need a deformation parameter in the buckling zone to define the pipe behaviour in order to assess the models. The CBS is defined as the average compressive strain in the buckling zone (usually with  $2D$  gauge length) associated with the maximum internal moment (or compressive axial load). Therefore, the average compressive strain in the buckling area should be the second variable used as the deformation parameter when assessing the models' behaviour. The evolution of the average compressive strain at each load increment during the pipe tests and finite element analyses was calculated by Equation (3-8).

$$\varepsilon_c = \varepsilon_t - \kappa D \quad (3-8)$$

where

$\varepsilon_c$ : average compressive strain in the specified gauge length (here is  $2D$ ) in the buckled zone

$\varepsilon_t$ : tensile strain of the extreme tension fiber located at the buckled section

$\kappa$ : pipe's curvature for the given gauge length

$D$ : outside diameter of the pipe.

Assuming that plain sections remain plain, Equation (3-8) is valid in both the elastic and plastic ranges. This equation can be used for pipes with any values of internal pressure. This is more important for pressurized specimens in which the neutral axis moves to the compression side due to an earlier yield of the biaxial tension-compression stress state caused by internal pressure and longitudinal compressive stress.

Therefore, the major output from the finite element analyses of pipe models used to assess the pipe response under the buckling load was a variation of the internal moment with respect to the average compressive strain in the buckling zone. For each pipe model, the finite element analysis results are represented here as the bending moment (vertical axis) versus the average compressive strain (horizontal axis). In order to validate the results of finite element analyses, these curves were compared to similar curves from experimental data from pipe buckling tests. This comparison is considered the best way to verify the analysis results with the experimental measurements (Dorey et al., 2001).

### **3.3.1 Preliminary Results**

Two categories of preliminary studies were performed to answer the following questions:

1. Which mesh configuration gives the optimum results?
2. How do the initial imperfections affect the performance of the models in the buckling analysis?

Since it was rather unnecessary to perform the mesh study on all pipe models, it was decided to perform this study on one pressurized and one unpressurized pipe. These two pipes were selected in a way that their anisotropic material model can represent all available anisotropic material models. It was shown in Chapter 2 that the anisotropic material model developed for the material type F had the simulation errors close to the average value of the modeling error in the whole database. The mean absolute errors (MAE) in simulations of longitudinal and transverse responses were around 2.5% and 2.2% (in the range of 0.0% - 3.0% total strain) for material type F. These MAE values were close to the values of the entire material database (i.e. 2.2% and 2.1% in longitudinal and transverse directions, respectively). One unpressurized pipe (i.e. HSSP#11) and two pressurized pipes (i.e. HSSP#12 and HSSP#14) were made of material type F. Therefore, the finite element models of HSSP#11 and HSSP#14 were selected for the mesh study.

### **3.3.1.1 Results of Mesh Study**

Since the buckling analyses were performed on both isotropic and anisotropic models of each pipe specimen, the mesh study was performed on both isotropic and anisotropic models of HSSP#11 and HSSP#14.

Initial imperfections have to be included in the pipe models to trigger the buckling. Similar initial imperfection patterns selected for unpressurized (half-ring dent) and pressurized (half-ring bulge) pipes were used in the finite element models of HSSP#11 and HSSP#14, respectively. Dorey et al. (2001) showed that the optimum mesh size is not affected by the magnitude of the imperfection. For this mesh sensitivity analysis, the magnitude of the imperfection pattern was selected to provide maximum ovality in the middle section of the pipes equal to 10% of wall thicknesses.

The mesh study results of HSSP#11 are shown in Figure 3-6 and Figure 3-7 for isotropic and anisotropic models, respectively. The results are shown in these graphs in the form of a global bending moment versus the average compressive strain in  $2D$  gauge length. As these figures show, all three mesh sizes resulted in similarly smooth responses prior to buckling. However, the post-buckling behaviours are slightly different depending on the mesh sizes. The response curves of the  $40 \times 104$  and  $80 \times 208$  meshes are closer compared to the  $20 \times 52$ . Therefore, it can be concluded that there is a greater improvement in the modeling results when moving from the  $20 \times 52$  mesh size to the  $40 \times 104$  compared to moving from the  $40 \times 104$  to the  $80 \times 208$  mesh sizes.

Figure 3-8 and Figure 3-9 show the mesh study results of HSSP#14 for isotropic and anisotropic material models, respectively. Similar to HSSP#11, all three mesh sizes resulted in similar responses prior to buckling. The post-buckling behaviours are different depending on the mesh sizes, while the response curves for the  $40 \times 104$  and  $80 \times 208$  meshes are closer compared to the  $20 \times 52$ . It was concluded that the internal pressure has no effects on the mesh refinement study for either the isotropic or anisotropic models. In all cases of different internal pressure and material modeling methods, the  $20 \times 52$  and  $80 \times 208$  meshes give the upper and lower bound responses, respectively.

Since the  $40 \times 104$  mesh provides acceptable results while requiring reasonable processing time, it was selected for developing all isotropic and anisotropic models of both pressurized and unpressurized pipes. Although the  $80 \times 208$  mesh provided a lower bound solution, the additional refinement from  $40 \times 104$  to  $80 \times 208$  did not seem to be favourable, because it would significantly increase the processing time while being insignificantly beneficial.

One of the important concerns about mesh size is the ability of the model to adequately simulate the physical geometry of the failed specimens. Figure 3-10

and Figure 3-11 show the deformed shapes of HSSP#11 and HSSP#14, respectively (with  $40 \times 104$  mesh size). The overall buckled shapes of both unpressurized and pressurized pipes, as well as the smooth transition of the elements across the buckled region of failed specimens, completely agree with the experimental observations.

### **3.3.1.2 Initial Imperfection Effects**

Since the actual initial imperfections of tested pipes were not available, in order to assess the performance of the anisotropic material model, the buckling analyses on each pipe were performed with a range of different magnitude of initial imperfections. This approach was adopted to prevent subjective conclusions when the results of anisotropic models were compared with the isotropic models.

For the selected imperfection patterns, the ovality magnitude had considerable effects on the results. Each pipe model was analyzed with four different imperfection magnitudes with a gauge length equal to  $D$ . Similar to the mesh study, HSSP#11 and HSSP#14 were selected among all finite element models to show the effects of different initial imperfections on the buckling responses. The analyses results of HSSP#11 with different values of ovality are shown in Figure 3-12 and Figure 3-13 for isotropic and anisotropic models, respectively. The results of buckling analyses on HSSP#14 are shown in Figure 3-14 and Figure 3-15 for isotropic and anisotropic models, respectively. The figures also show the global moment versus average compressive strain (measured in  $2D$  gauge length of buckling area).

The pipe maximum ovality in these figures is the maximum out-of-roundness expressed as percentile of pipe wall thickness ( $WT$ ).

$$Ovality = \left( \frac{H_{\max}}{WT} \right) \times 100 \quad (3-9)$$

As these figures show, a higher ovality ratio results in a lower buckling moment and lower CBS. For each pipe, the response curves of different magnitudes of initial imperfection diverge around the onset of buckling. This means that different initial imperfections mostly change the onset of buckling, rather than the bending response before and after the buckling. In a study of imperfection effects on the buckling responses of HSS pipes, Suzuki et al. (2007) showed that modeling different types of imperfections only changes the onset of buckling and does not change the ascending part of the bending response (up to the buckling point), which is essentially dominated by the material response.

Comparing the results of the isotropic models and the anisotropic models of HSSP#11 and HSSP#14, it is evident that the anisotropic models better simulate the bending response of the unpressurized and the pressurized pipes. Regardless of the magnitude of imperfection, the isotropic model fails to follow the nonlinear response of material in the pipe behaviour. The response curves of isotropic models start to deviate from the experimental response curve in earlier stages of the behaviour, showing lower bending stiffness compared to a real response. On the other hand, the anisotropic model better simulates the nonlinearity in the bending, and if appropriate imperfection is used, the anisotropic model results in an adequately accurate simulation of the pipe response up to the onset of buckling. Similar results were observed in the rest of the pipe models.

In conclusion, using the idealized initial imperfection pattern in the finite element models of pipes will not result in subjective comparisons between the isotropic and anisotropic modeling methods.

### 3.3.2 Results of All 15 HSS Pipes

The results of the buckling analyses are compared to the experimental measurements of all HSS pipes in Figure 3-16 to Figure 3-30. The results are shown in the form of global moment versus average compressive strain measured in a  $2D$  gauge length of the buckling area. Each graph shows the results of the isotropic and anisotropic models along with the experimental results. Although each isotropic and anisotropic model was analyzed with four different magnitudes of initial imperfection, the finite element results shown in Figure 3-16 to Figure 3-30 belong to the models with initial imperfection magnitudes that result in the onset of buckling close to the experimental measurements.

Table 3-3 shows the CBS from the buckling tests and finite element analyses with isotropic and anisotropic material models, as well as the magnitude of imperfection used in the buckling analysis. As this table shows, the anisotropic models resulted in better predictions of the CBS, and except for the HSSP#6, the average error was less than 6.0%. The average error in isotropic modeling results was as high as 33%. In all specimens of HSS pipes, the CBSs from the isotropic model were larger than those from the experimental measurements and the anisotropic model (with a similar imperfection magnitude).

The curves of all HSS pipe specimens shown in Figure 3-16 to Figure 3-30 explain the grounds behind the weakness of isotropic models and better performance of anisotropic models. In all HSS pipes, the isotropic model shows lower bending stiffness compared to the anisotropic model and the tested specimen. This lower stiffness affects the ascending parts of the moment-compressive strain response. In some cases, the curves of isotropic models started to deviate from the actual experimental curves at very early stages. This deviation resulted in a larger compressive deformation before the pipe reached its ultimate internal load/moment (onset of buckling).

On the other hand, anisotropic models better followed the real behaviour of the tested HSS pipes and predicted the bending stiffness more accurately. The reason behind this accurate prediction is that the anisotropic models were capable of simulating the material responses under all basic possible stress paths that develop in the pipe body (i.e., longitudinal tension, longitudinal compression, and transverse tension). If an isotropic material modeling is used, the pipe elements respond in a similar manner in all directions, under tension and compression.

The difference between the isotropic and anisotropic modeling can be better understood by looking at the stress paths in the stress space of tension and compression elements on both sides of the pipe's neutral axis. Figure 3-31 shows the stress paths of pipe elements located under and above the neutral axis of an unpressurized pipe under pure bending. If an isotropic model is used, both tension and compression elements have the same elastic ranges and start the plastic deformation when the stress reaches the longitudinal proportional limit measured in the tension coupon test. In the plastic range of an isotropic model, the strength and hardening pattern of the tension and compression elements will be exactly the same.

Using an anisotropic model, the elastic and plastic responses of the tension elements will be similar to the material response in the tension coupon test (same as the isotropic model), but the compression elements will show a higher proportional limit. (As Figure 3-31 shows, the part of the stress path in the elastic range is larger for a compression element). The compression plastic response of the anisotropic model will show higher strength compared to the tension response in the longitudinal direction.

The isotropic and anisotropic bending behaviour of pipes is the result of elements' responses under tension and compression. In the isotropic model the smaller elastic range of compression elements results in deviation from the real bending

behaviour of unpressurized pipes (as evident in Figure 3-16 to Figure 3-20 and Figure 3-26). In an anisotropic model, however, the elements have a larger elastic domain and higher plastic strength in longitudinal compression, which increase the bending stiffness and result in responses closer to the real behaviour.

Since the pipe elements are nearly under uniaxial normal stress conditions in unpressurized pipes, the difference between the bending responses of anisotropic and isotropic models can also be explained by looking at coupon test results. As discussed in Chapter 2, HSS pipes show more longitudinal strength under compression compared to tension. The anisotropic model has the ability to capture the difference between the longitudinal tension and compression and simulates the tension and compression responses with acceptable errors. This feature of the anisotropic model resulted in better simulation of pipe bending with more accurate bending stiffness. On the other hand, the longitudinal compression response of the isotropic model is essentially similar to tension behaviour which has less stiffness and strength. Therefore, the isotropic modeling of unpressurized pipes resulted in bending stiffness lower than the actual stiffness, and made the isotropic curve deviate from the experimental results.

The deviation of the isotropic model from the anisotropic model (and the experimental response) was more dramatic in pressurized pipes. As the pipe elements of a pressurized pipe under bending are under a biaxial normal stress state, the stress paths better explain this phenomenon (compared to stress-strain curves). Figure 3-32 shows the stress paths of elements of a pressurized pipe under longitudinal tension and compression. Under internal pressure applied before the bending moment, all elements will have tensile hoop (transverse) stress,  $\sigma_h$ . If the hoop stress is larger than the longitudinal proportional limit (which is not rare, since among all pressurized tested pipes in the present database, the hoop stress was 30% higher than the longitudinal proportional

limit), applying the internal pressure in an isotropic model causes a plastic deformation that expands the original yield surface radius from  $PL_L$  to  $\sigma_h$ .

When the bending moment is applied to an isotropic pressurized pipe, although the tension elements are already on the yield surface, they respond elastically in the longitudinal direction due to the biaxial tension-tension stress state. The new elastic limit for tension elements is the expanded yield surface due to the internal pressure. The compression stress path of the isotropic model is located outside of the yield circle; therefore, the compression elements' deformation in the longitudinal direction is plastic in the entire range of the bending moment application. This is because of the biaxial tension-compression stress state and previous yielding, due to the internal pressure. The plastic response of the compression elements results in a larger deformation in the compression side of the pipe and eventually leads to a lower bending stiffness compared to the real behaviour of HSS pipes.

This behaviour of the isotropic pressurized models contradicts the real behaviour of pressurized HSS pipes. In a real HSS pipe, applying operational pressure (up to 80% SMYS) does not cause any plastic deformation in the transverse direction. This is because the expansion of HSS pipes during pipe-making process, the proportional limit and yield stress in the transverse direction increase to well above the expected hoop stress due to the operational pressure. The other contradiction of isotropic modeling of pressurized HSS pipes is the absolute plastic deformation of compression elements. This essentially results in lower bending stiffness in the isotropic models of pressurized pipes, and substantial deviation from the real response while, as shown in Figure 3-21 to Figure 3-25 and Figure 3-27 to Figure 3-30, the bending stiffness of the pressurized pipes was close to the elastic stiffness, up to around 60% of the maximum moment. This early deviation from the elastic response is more significant compared to the isotropic model of an unpressurized pipe. (Comparing the results of unpressurized

and pressurized pipes shows that the gap between the isotropic curve and real curves is larger in pressurized pipes).

On the other hand, the anisotropic model's responses to the pressurized bending load cases are more realistic and in better agreement with the real behaviour. Because of the high proportional limit and yielding stress in the transverse direction, applying operational pressure to the anisotropic model does not bring the HSS pipes' material out of the elastic limit (see Figure 3-32). By applying the bending moment on a pressurized HSS pipe, both tension and compression elements start to respond elastically, and the bending stiffness is close to the elastic stiffness up to a considerable portion of the maximum moment. They start to deform plastically at a higher bending moment. Due to the biaxial tension-compression stress state, the compression elements have a smaller elastic range compared to the tension elements which have a biaxial tension-tension stress state.

Although the focus of this study was on the pipe's behaviour up to incipient buckling, the anisotropic curves better agree with the experimental results, even for post-buckling behaviour. This feature of the anisotropic curves is depicted in Figure 3-16 to Figure 3-30. Chapter 5 of this dissertation presents a detailed study on how the buckling response of anisotropic HSS pipes is affected by different responses observed in the material tests.

### **3.4 Summary**

Local buckling of energy pipelines is an inelastic stability phenomenon highly affected by material plasticization. A precise study of the way HSS pipes response, and an accurate prediction of the CBS require appropriate simulations of material behaviour, especially in the elastic and early plastic ranges. HSS pipes show different responses in longitudinal and transverse directions, and under

tension and compression loads. This significant material anisotropy highly affects the bending response of HSS pipes. Therefore, using the conventional isotropic material model does not generate good agreement with test results. On the other hand, anisotropic modeling of HSS pipes material shows a good agreement with real bending behaviour of HSS pipes. This is because anisotropic modeling adequately mimics the material response in longitudinal and transverse directions under tensile and compressive loads.

The CBS is also affected by the pipe's initial imperfections. Idealized initial imperfection patterns were used in this chapter due to the absence of experimentally measured imperfections. The buckling results show that regardless of the magnitude of the imperfection, the anisotropic model accurately followed the experimental curve up to the onset of buckling. Hence, the adequacy of the proposed anisotropic model is not affected by the initial imperfections of the pipes.

Capability of the anisotropic material modeling in HSS pipe modeling makes it a good candidate to study the HSS pipes behaviour including determination of CBS. Using this material modeling method along with an appropriate model of pipe imperfections (either actual modeling or idealized models of imperfections) can result in an accurate simulation of pipe buckling behaviour and an estimation of the CBS.

## References

Bathe K-J., (1996), "Finite Element Procedures", Prentice-Hall Inc., Englewood Cliffs, New Jersey.

Bushnell D., (1980), "Buckling of Shells – Pitfall for Designers", AIAA/ASME/ASCE/AHS 21<sup>st</sup> Structures, Structural Dynamics & Materials Conference, Seattle, Washington.

Del Col P.R., Grondin G.Y., Cheng J.J.R. and Murray D.W., (1998), "Behaviour of Large Diameter Line Pipes Under Combined Loads", Structural Engineering Report No. 224, Department of Civil and Environmental Engineering, University of Alberta, Edmonton, Alberta, 174 pages.

Dorey A.B., Murray D.W. and Cheng J.J.R., (2006), "Initial Imperfection Models for Segments of Line Pipe" Journal of Offshore Mechanics and Arctic Engineering, 128(4) pp. 322-329.

Dorrey A.B., Cheng J.J.R. and Murray D.W., (2001), "Critical Buckling Strain in Energy Pipelines", Structural Engineering Report No. 237, Department of Civil and Environmental Engineering, University of Alberta, Edmonton, Alberta, 346 pages.

Hart J.D., Powell G.H. and Zulfigar N., (1996), "A Material Model for Pipeline Steels", International Pipeline Conference, IPC, ASME, 1996, v 2, pp 613-627.

Hibbit, Karlsson & Sorenson, Inc., (2003), "ABAQUS/STANDARD Theory Manual, Version 6.7".

Horrigmoie G. and Bergan, P.G., (1976), "Incremental Variation Principals and Finite Element Methods for Non-linear Problems", Computer Method in Applied Mechanics and Engineering (7), North Holland Publishing Company.

Pugh E.D.L., Hinton E. and Zienkiewicz O.C., (1978), "A Study of Quadrilateral Plate Bending Element with Reduced Integration", International Journal for Numerical Methods in Engineering, vol. 12.

Ramm E., (1980), "Strategies for Tracing Nonlinear Response Near Limit Points", Europe-U.S. Workshop on Nonlinear Finite Element Analysis in Structural Mechanics, Bochum, Germany, July 28-31.

Riks E., (1979), "An incremental Approach to the Solution of Snapping and Buckling Problems", International Journal of Solids and Structures, vol. 15, pp. 529-551.

Sato T., Mikami Y., Mochizuki M., Suzuki N. and Toyoda, M., (2009), "Parametric study on the effect of geometric imperfections on the bending capacity of high-strength linepipes" 2008 ASME International Pipeline Conference, IPC 2008, September 29, 2008 - October 3, American Society of Mechanical Engineers, Calgary, AB, Canada, v3, pp 745-753.

Sen M., and Cheng J.J.R., (2010), "Finite Element Analysis of Cold Bend Pipes Under Bending Loads" Proceeding of the International Pipeline Conference, American Society of Mechanical Engineers, Calgary, Alberta, v4, pp 257-267.

Suzuki N., Kondo J., Endo S., (2007), "Effects of geometric imperfection on bending capacity of X80 linepipe" 6th International Pipeline Conference, IPC 2006, September 25, 2006 - September 29, American Society of Mechanical Engineers, Calgary, AB, Canada, v1, pp. 111-120.

Timms C. and Zimmerman T., (2005), "Local Buckling and Post Buckling Behaviour of High-Strength Linepipe" C-FER Technologies, 19 pages.

Vitali L., Bruschi R., Mork K.J., Levold E. and Verley R., (1999), "Hotpipe Project – Capacity of Pipes Subjected to Internal Pressure, Axial Force and

Bending Moment”, 9<sup>th</sup> International Offshore and Polar Engineering Conference, ASME. Brest, France, v2, pp 22-33.

Zhou Z. and Murray, D.W., (1993), “Numerical Structural Analysis of Buried Pipelines”, Structural Engineering Report No.181, Department of Civil and Environmental Engineering, University of Alberta, Alberta, 355 pages.

## Tables

Table 3-1 HSS pipe specimens' grade, dimensions and testing conditions

Specimen ID	Steel Grade	Material	Diameter (D)	Wall Thickness (t)	D/t	Length (L)	L/D	internal pressure
		Type	(mm)	(mm)		(mm)		(Mpa)
HSSP#1	X80	A	761.98	13.01	59	2668	3.5	0
HSSP#2	X80	A	762.07	13.19	58	2666	3.5	0
HSSP#3	X100	E	762.77	13.24	58	2656	3.5	0
HSSP#4	X100	H	610.39	15.62	39	2666	4.4	0
HSSP#5	X80	A	762.27	13.26	57	2656	3.5	0
HSSP#6	X80	C	610.72	15.56	39	2667	4.4	21.8
HSSP#7	X80	A	762.21	13.30	57	2664	3.5	14.7
HSSP#8	X100	H	610.20	15.67	39	2652	4.3	27.3
HSSP#9	X100	D	914.85	13.19	69	3207	3.5	15.3
HSSP#10	X100	E	761.76	13.20	58	2666	3.5	18.4
HSSP#11	X100	F	762.01	13.90	55	2667	3.5	0
HSSP#12	X100	F	762.38	13.78	55	2667	3.5	18.4
HSSP#13	X80	B	761.97	13.85	55	2654	3.5	14.7
HSSP#14	X100	F	761.90	13.74	55	2661	3.5	18.4
HSSP#15	X100	G	761.84	13.83	55	2613	3.4	18.4

Table 3-2 Specimens' initial imperfections

Specimen ID	Measured Imperfection Range (%WT)		
	Wall Thickness Variation	Radius Variation Along the Length	Ovality $\left( \frac{D_{\max} - D_{\min}}{t_{\text{average}}} \right)$
HSSP#01	1.4%	3.5%	5.3%
HSSP#02	1.2%	7.4%	10.5%
HSSP#03	1.0%	5.6%	4.8%
HSSP#04	2.3%	3.6%	19.9%
HSSP#05	1.1%	3.9%	3.7%
HSSP#06	0.7%	4.2%	5.3%
HSSP#07	1.3%	1.6%	5.3%
HSSP#08	2.3%	2.2%	18.2%
HSSP#09	2.9%	7.9%	14.9%
HSSP#10	1.3%	4.6%	8.2%
HSSP#11	1.6%	5.2%	13.8%
HSSP#12	1.1%	2.6%	8.4%
HSSP#13	2.0%	5.9%	10.9%
HSSP#14	1.5%	6.0%	24.2%
HSSP#15	0.9%	2.3%	16.5%

Table 3-3 Comparison of experimental CBS with predicted values by isotropic and anisotropic models

Specimen ID	Buckle Location	Imperfection Type	Ovality Magnitude (% WT)	Location of Maximum Imperfection	Critical Buckling Strain		
					Buckling Test	Isotropic Model	Anisotropic Model
HSSP#01	Middle	Half Ring Dent	25.0%	0.50L	-0.84	-1.18	-0.97
HSSP#02	Middle	Half Ring Dent	25.0%	0.50L	-0.73	-1.19	-0.89
HSSP#03	Middle	Half Ring Dent	12.5%	0.50L	-0.69	-0.98	-0.79
HSSP#04	Middle	Half Ring Dent	25.0%	0.50L	-1.53	-1.77	-1.59
HSSP#05	Middle	Half Ring Dent	25.0%	0.50L	-0.91	-1.16	-0.91
HSSP#06	Middle	Half Ring Bulge	10.0%	0.50L	-2.87	-2.22	-2.11
HSSP#07	Bottom	Half Ring Bulge	10.0%	0.12L	-1.59	-1.69	-1.52
HSSP#08	Middle	Half Ring Bulge	10.0%	0.50L	-1.75	-2.04	-1.83
HSSP#09	Bottom	Half Ring Bulge	12.5%	0.12L	-0.83	-1.20	-0.83
HSSP#10	Middle	Half Ring Bulge	25.0%	0.50L	-0.91	-1.25	-1.12
HSSP#11	Middle	Half Ring Dent	10.0%	0.50L	-1.08	-1.52	-1.10
HSSP#12	Middle	Half Ring Bulge	10.0%	0.50L	-1.23	-1.52	-1.20
HSSP#13	Middle	Half Ring Bulge	5.0%	0.50L	-1.09	-1.57	-1.09
HSSP#14	Middle	Half Ring Bulge	10.0%	0.50L	-1.22	-1.52	-1.20
HSSP#15	Middle	Half Ring Bulge	10.0%	0.50L	-1.15	-1.88	-1.37

Figures

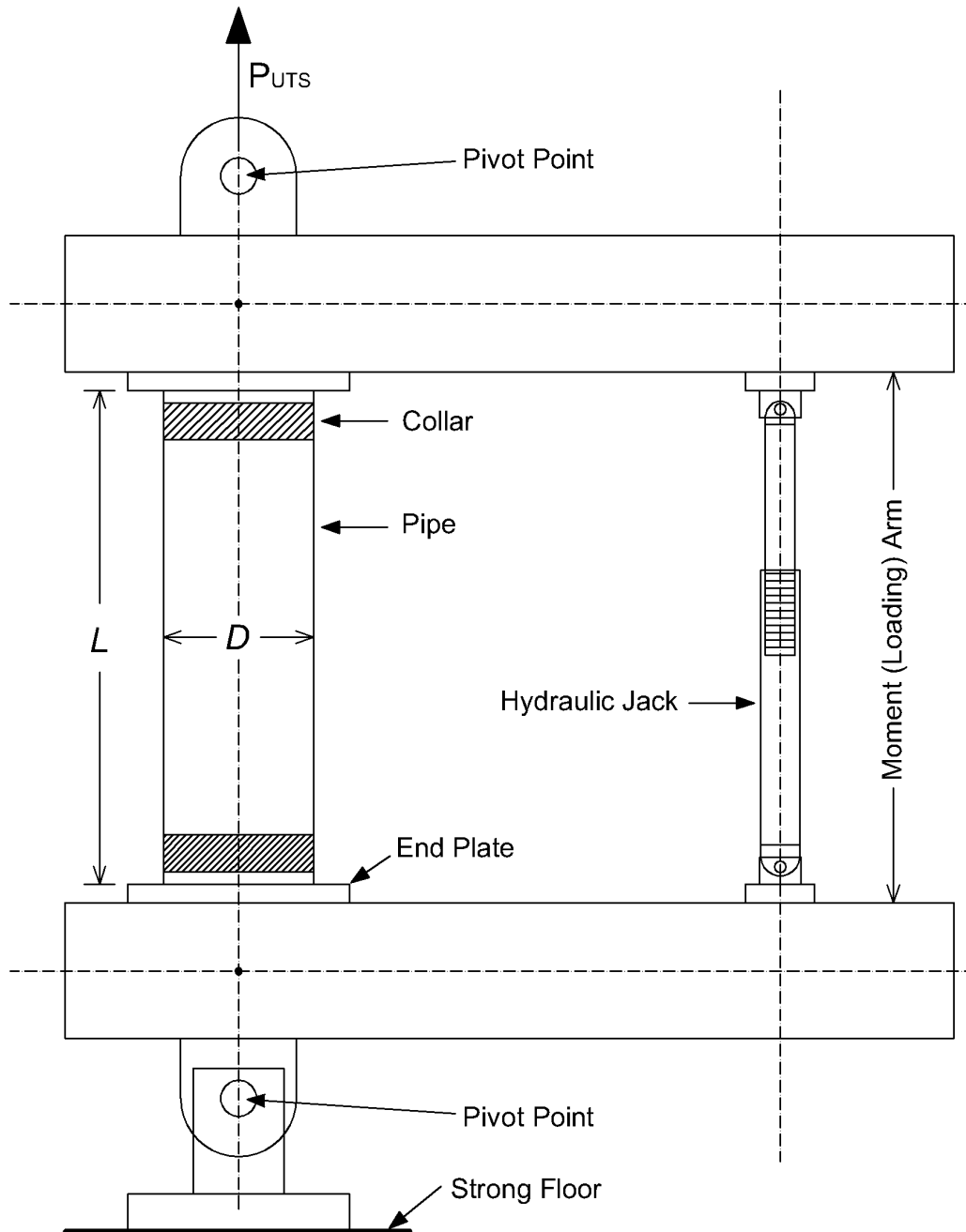


Figure 3-1 The set-up used for the buckling test on HSS pipes

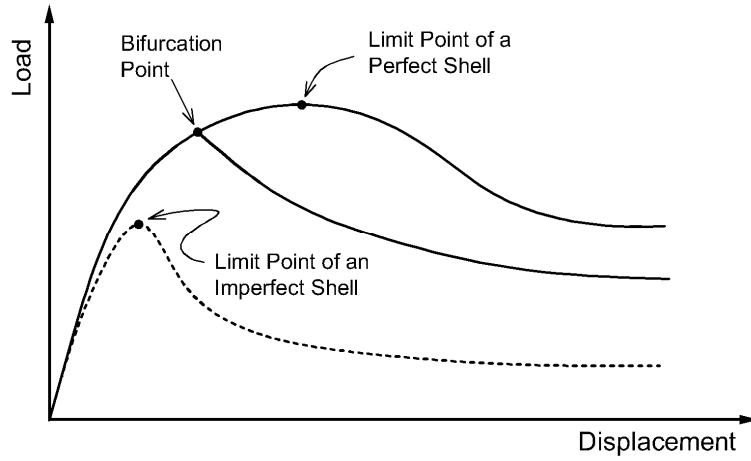


Figure 3-2 Typical load-displacement response of shell structures

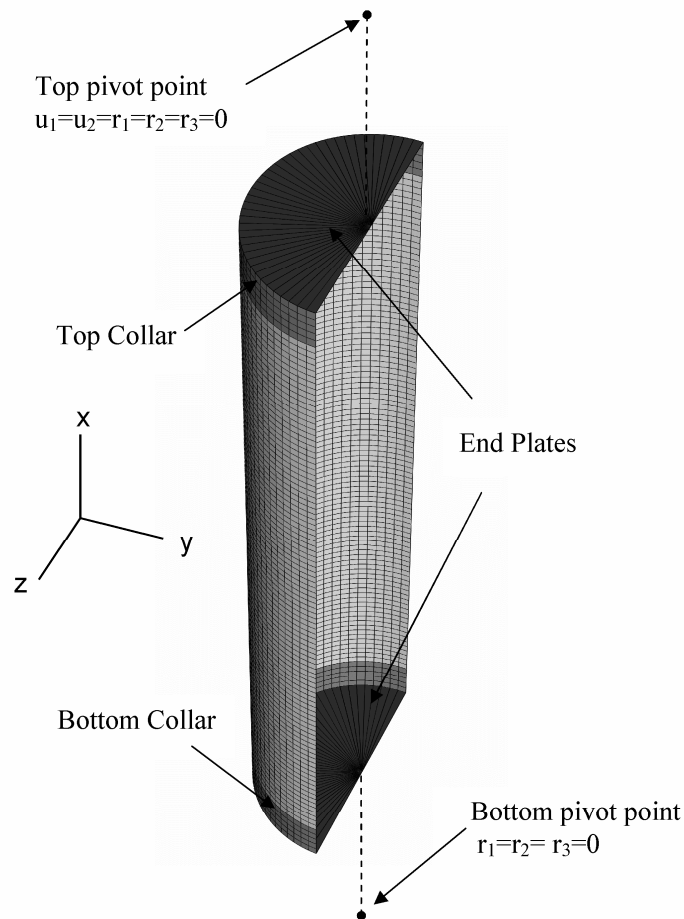


Figure 3-3 General attribute of the finite element model of HSS pipe specimens developed in ABAQUS

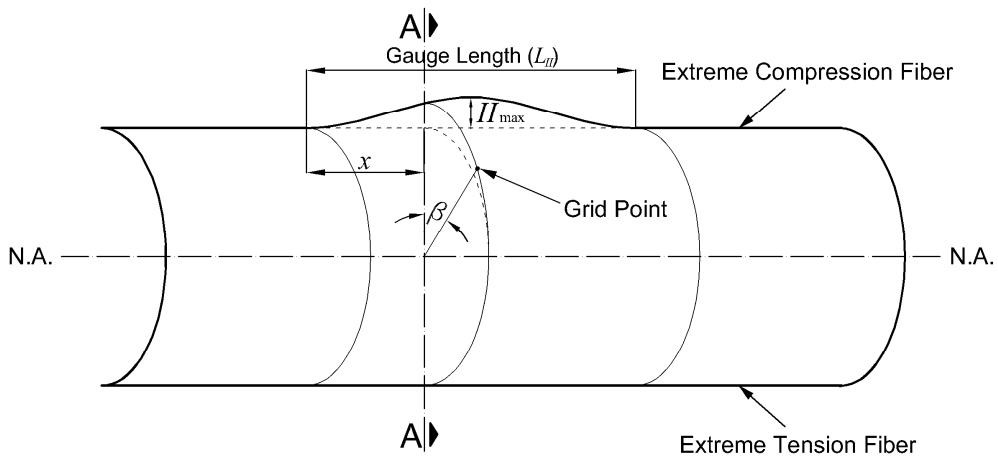


Figure 3-4 Bulge-type imperfection used for pressurized pipes

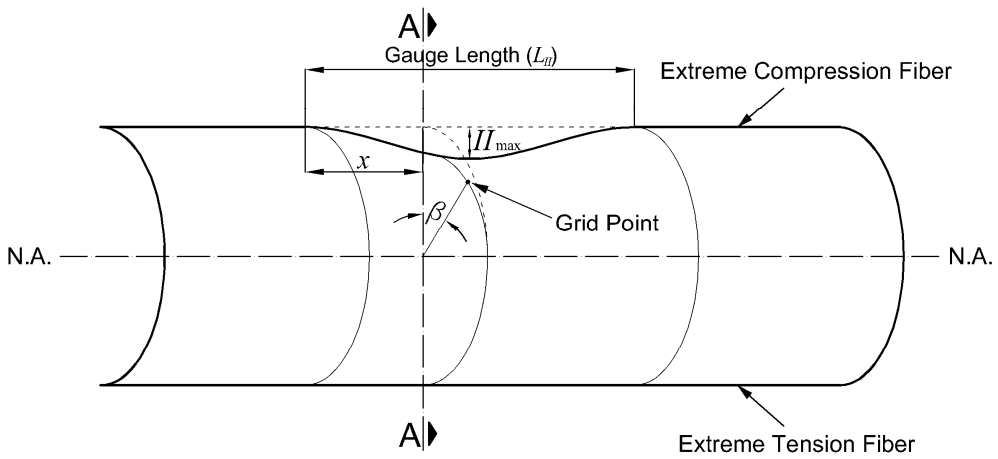


Figure 3-5 Dent-type imperfection used for pressurized pipes

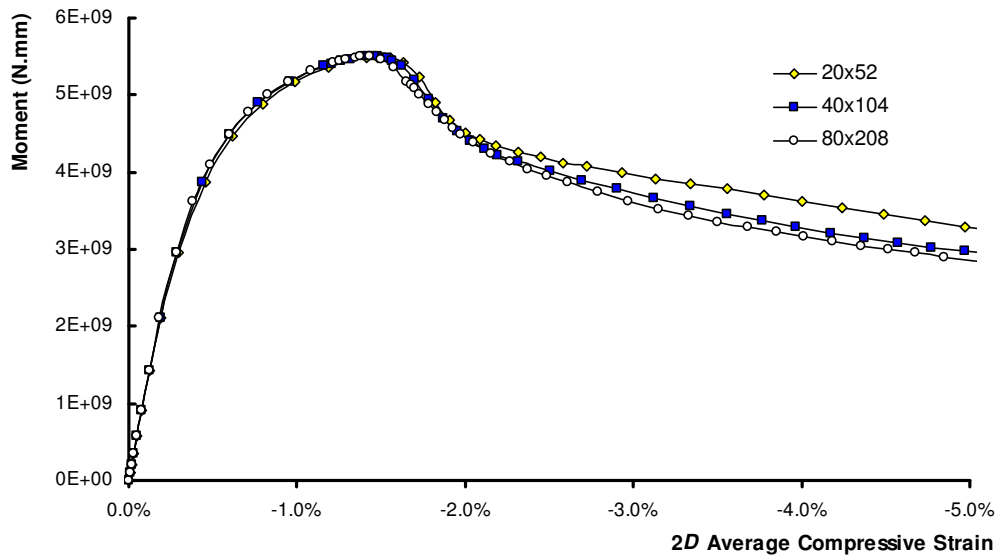


Figure 3-6 Results of mesh study on the isotropic model of HSSP#11

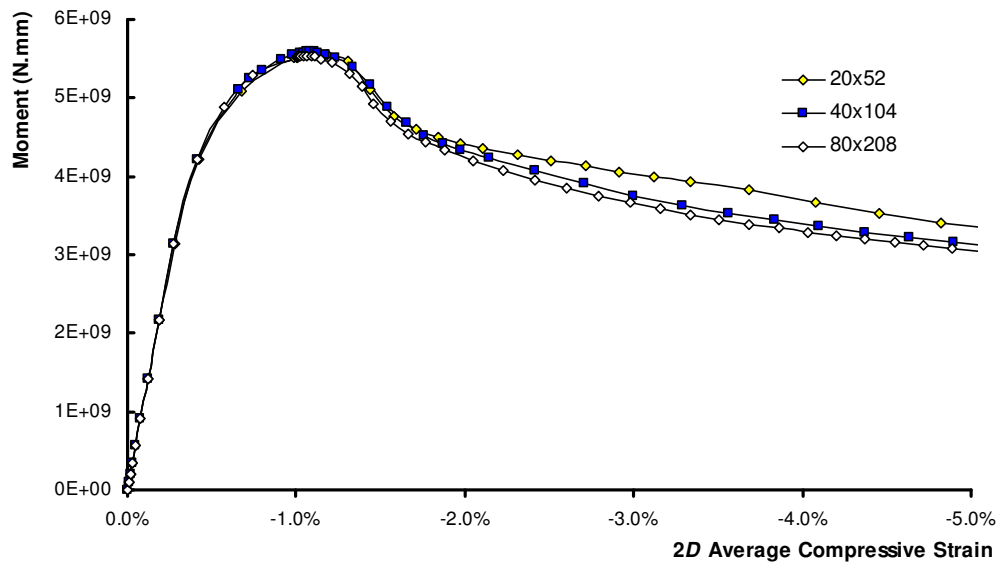


Figure 3-7 Results of mesh study on the anisotropic model of HSSP#11

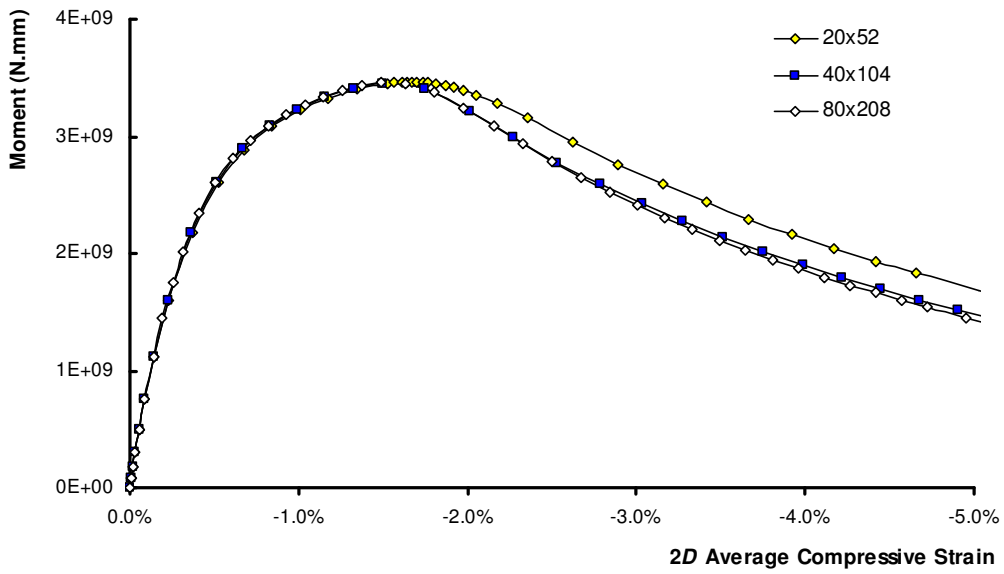


Figure 3-8 Results of mesh study on the isotropic model of HSSP#14

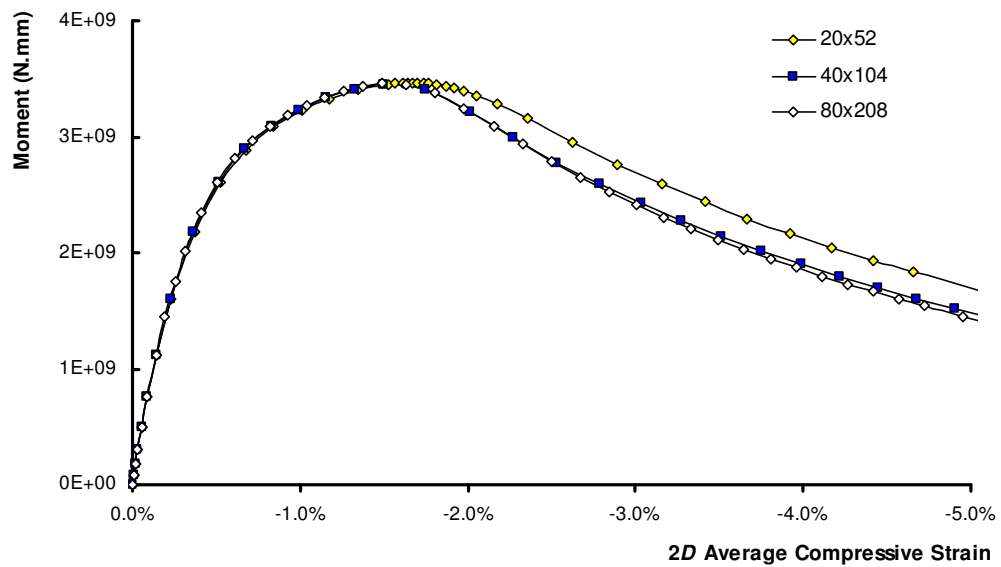


Figure 3-9 Results of mesh study on the anisotropic model of HSSP#14

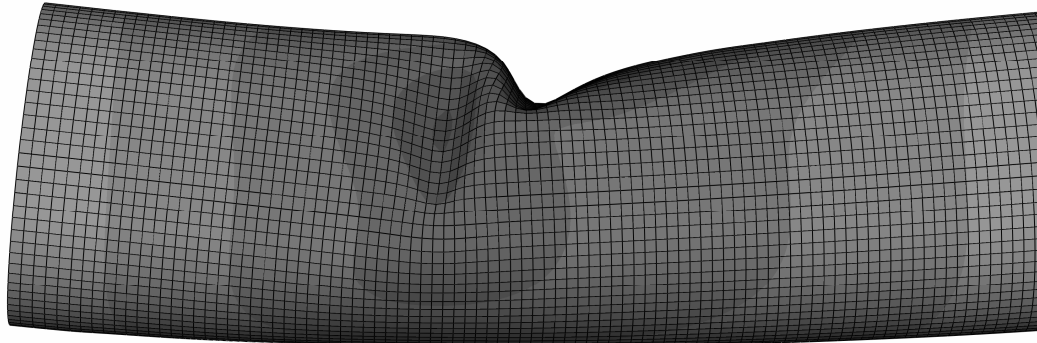


Figure 3-10 Deformed shape of the pipe HSSP #11 (unpressurized)

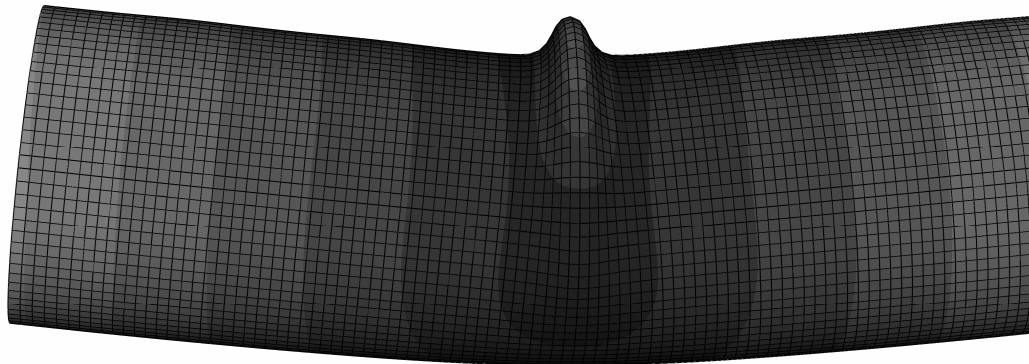


Figure 3-11 Deformed shape of the pipe HSSP #14 (pressurized)

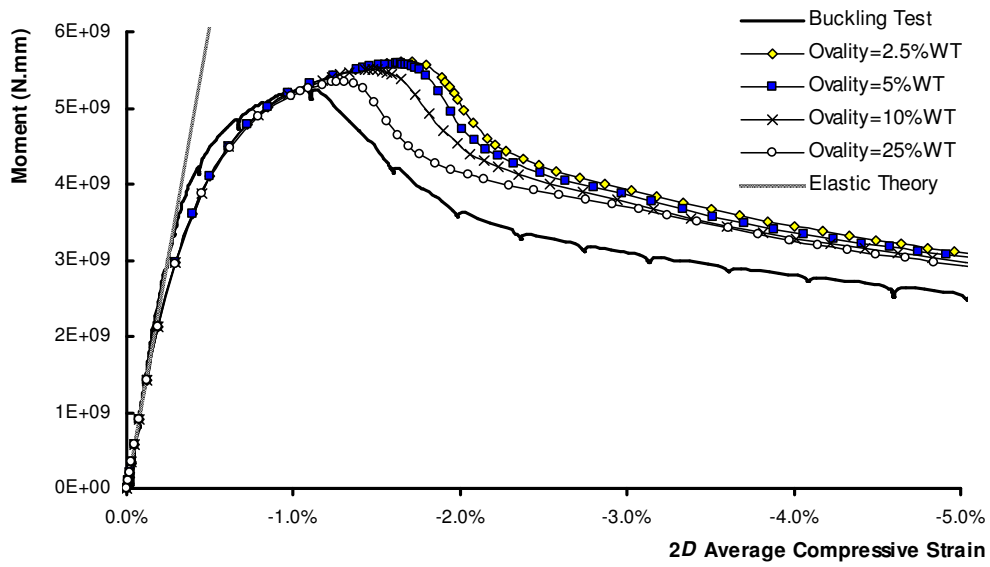


Figure 3-12 Effects of imperfection magnitudes on the buckling response of HSSP#11 - isotropic model

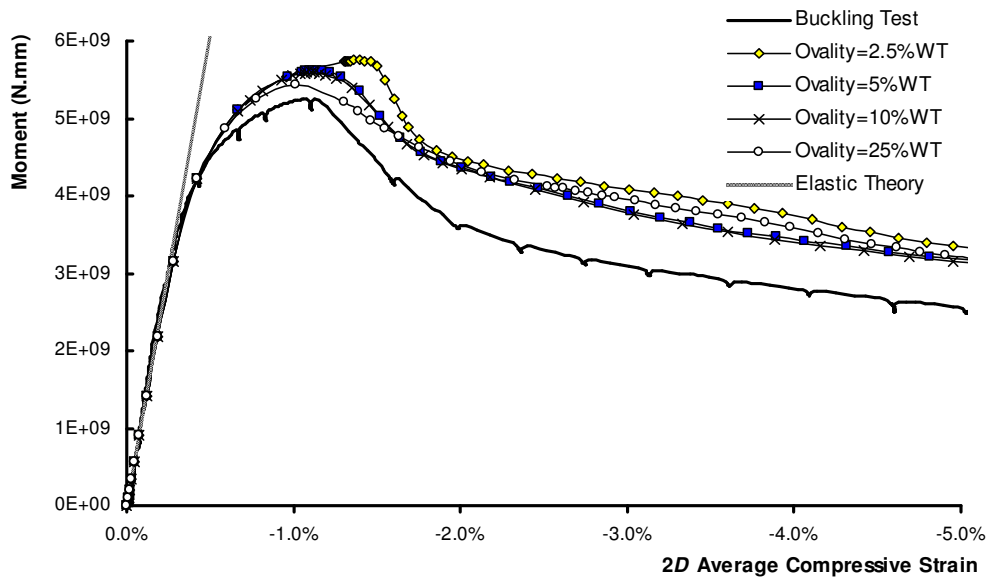


Figure 3-13 Effects of imperfection magnitudes on the buckling response of HSSP#11 - anisotropic model

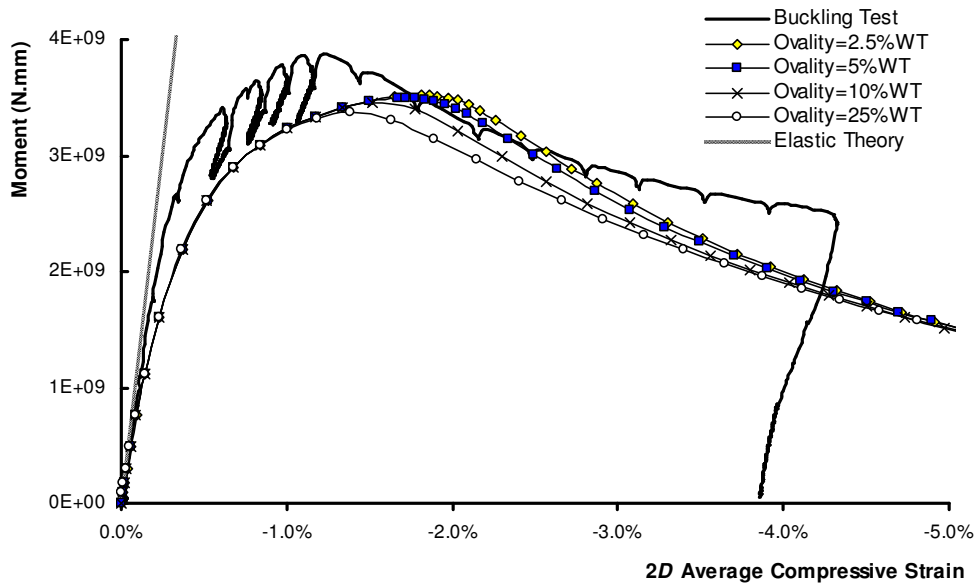


Figure 3-14 Effects of imperfection magnitudes on the buckling response of HSSP#14 - isotropic model

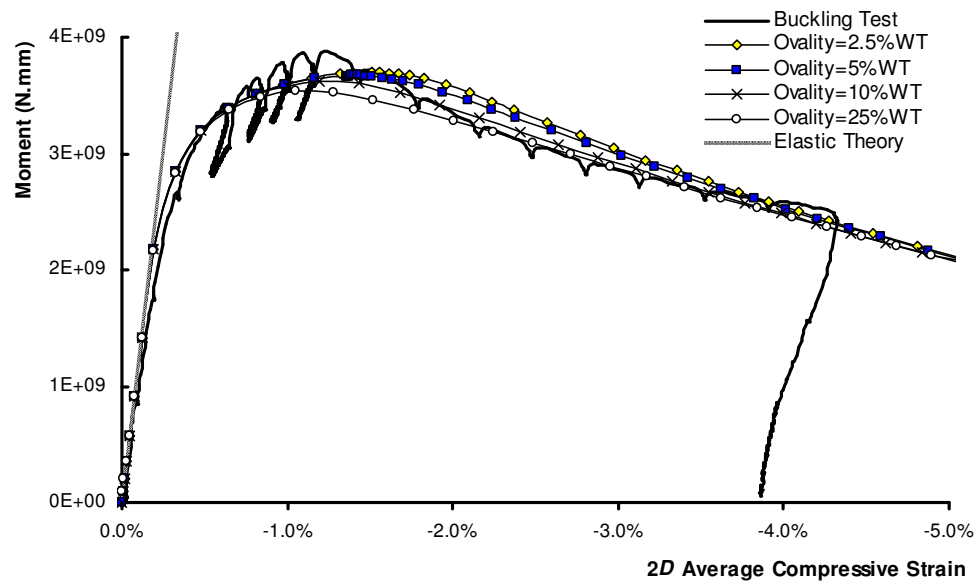


Figure 3-15 Effects of imperfection magnitudes on the buckling response of HSSP#14 - anisotropic model

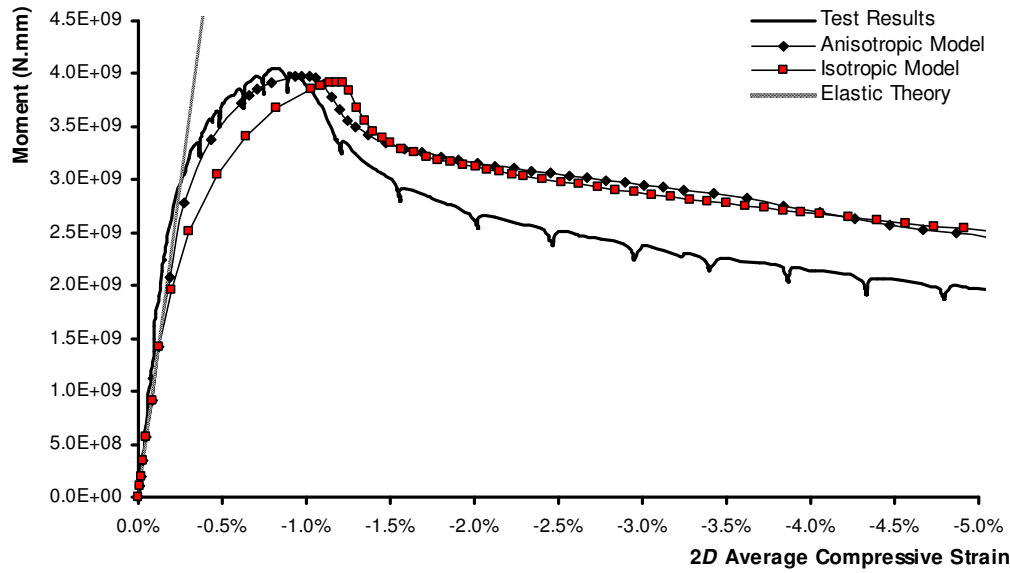


Figure 3-16 Global moment versus *2D* average compressive strain of the buckling zone – from experimental measurements and isotropic and anisotropic models of HSSP#01

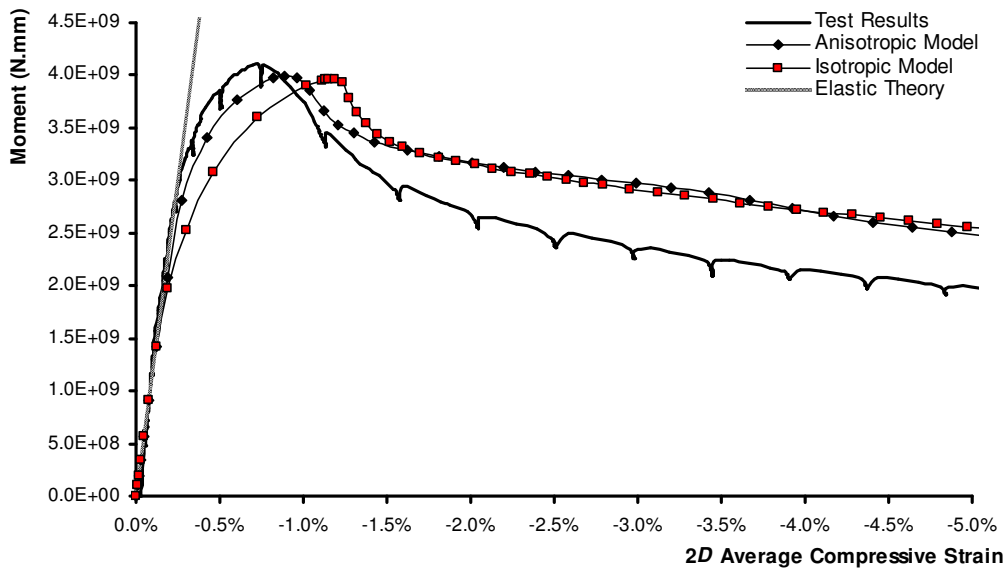


Figure 3-17 Global moment versus *2D* average compressive strain of the buckling zone – from experimental measurements and isotropic and anisotropic models of HSSP#02

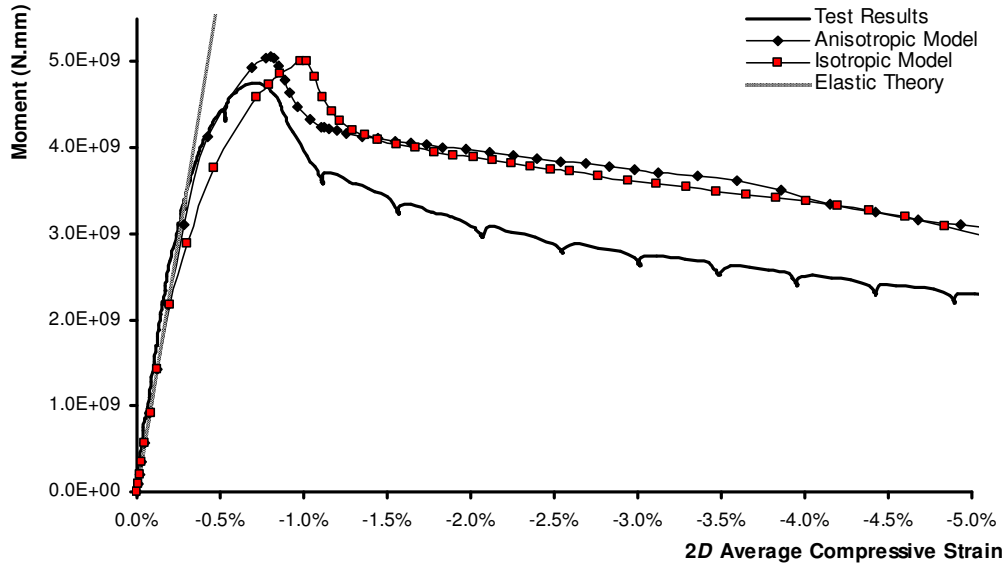


Figure 3-18 Global moment versus 2D average compressive strain of the buckling zone – from experimental measurements and isotropic and anisotropic models of HSSP#03

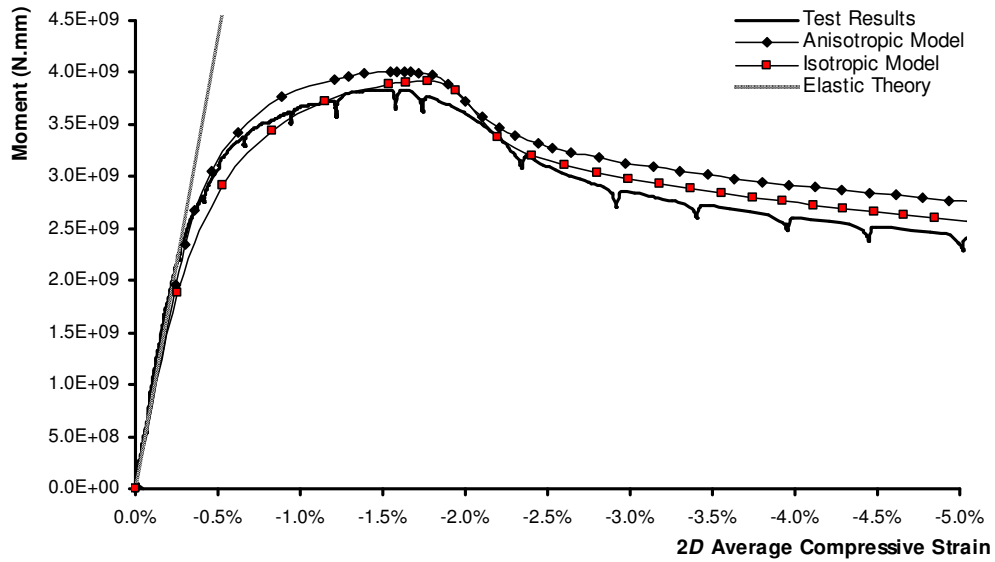


Figure 3-19 Global moment versus 2D average compressive strain of the buckling zone – from experimental measurements and isotropic and anisotropic models of HSSP#04

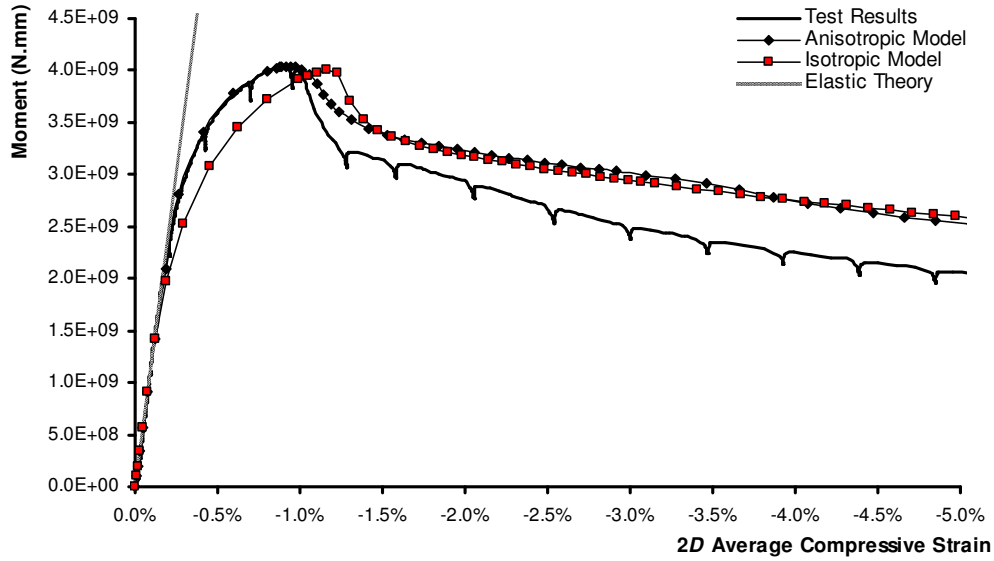


Figure 3-20 Global moment versus 2D average compressive strain of the buckling zone – from experimental measurements and isotropic and anisotropic models of HSSP#05

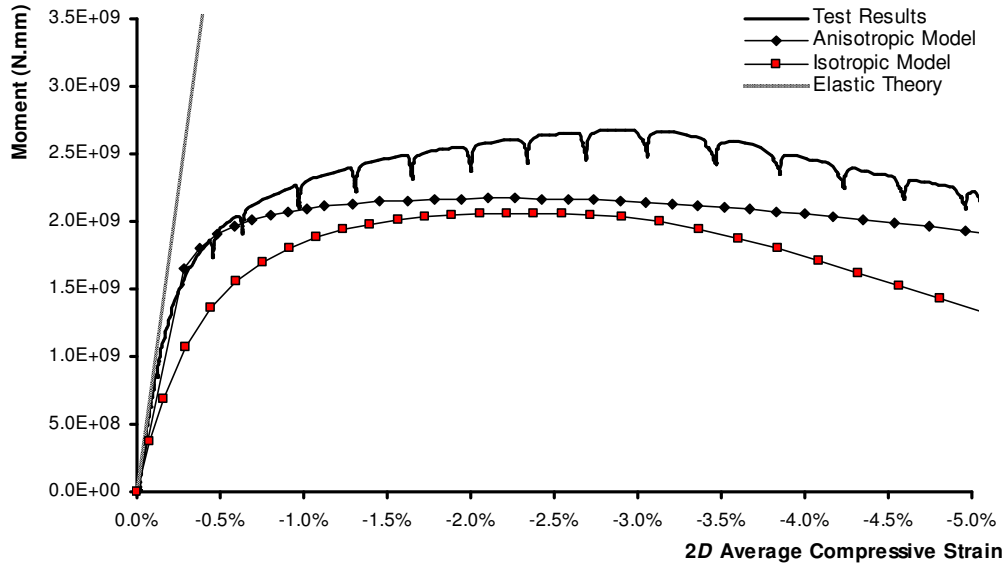


Figure 3-21 Global moment versus 2D average compressive strain of the buckling zone – from experimental measurements and isotropic and anisotropic models of HSSP#06

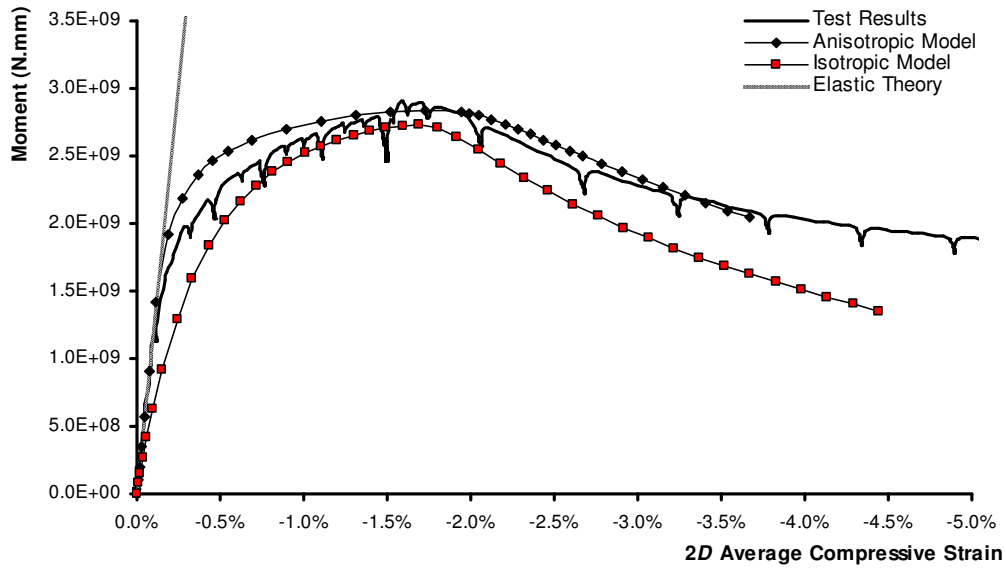


Figure 3-22 Global moment versus *2D* average compressive strain of the buckling zone – from experimental measurements and isotropic and anisotropic models of HSSP#07

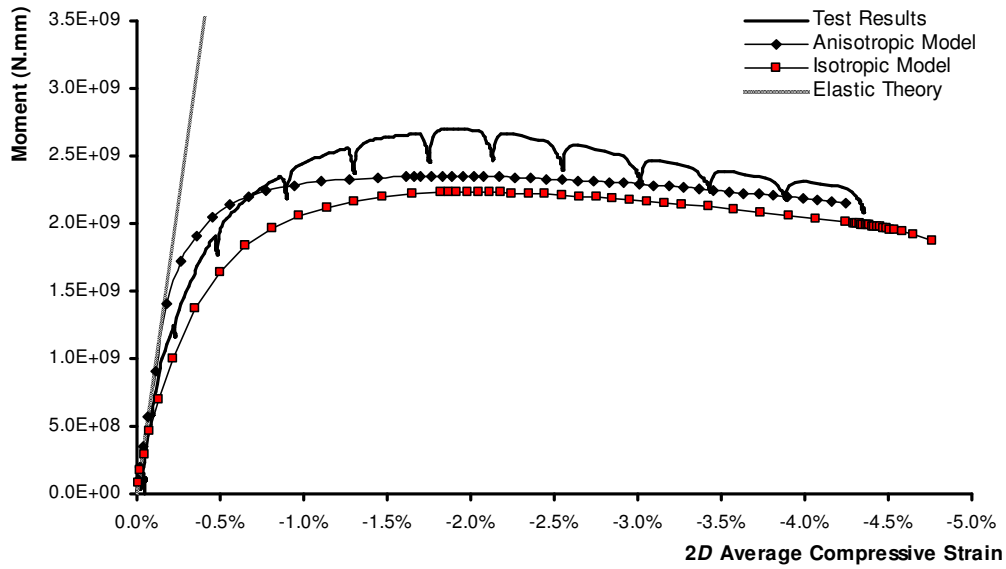


Figure 3-23 Global moment versus *2D* average compressive strain of the buckling zone – from experimental measurements and isotropic and anisotropic models of HSSP#08

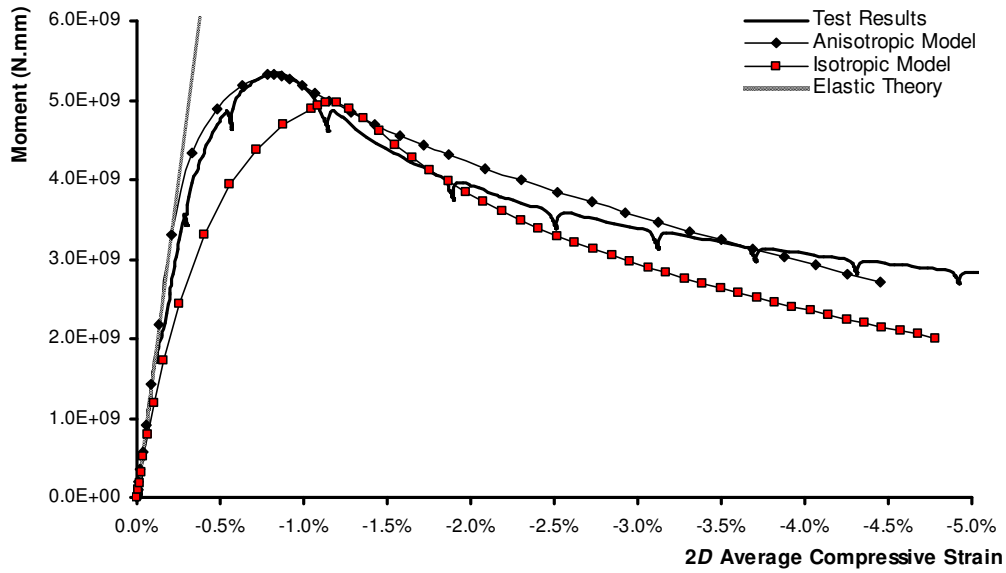


Figure 3-24 Global moment versus 2D average compressive strain of the buckling zone – from experimental measurements and isotropic and anisotropic models of HSSP#09

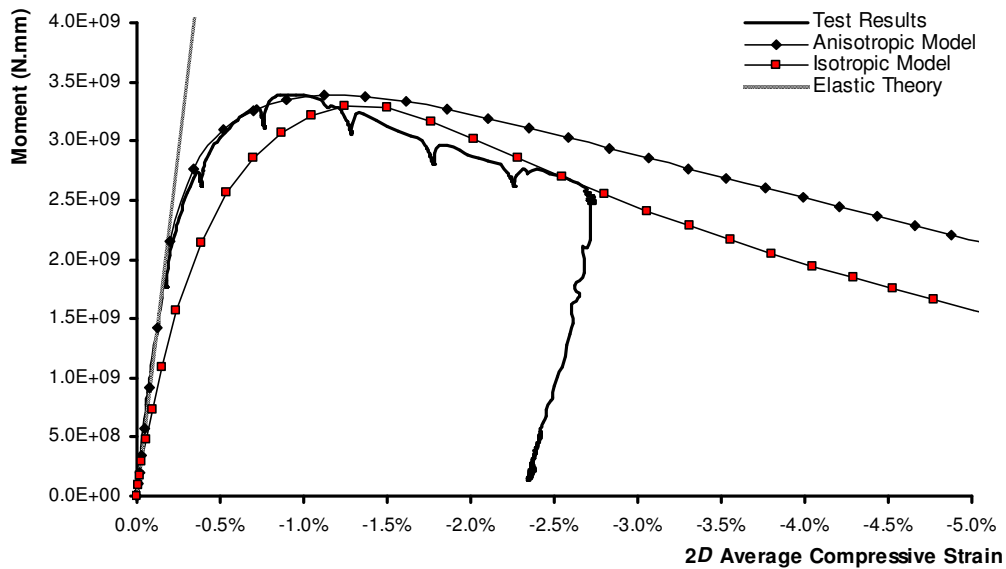


Figure 3-25 Global moment versus 2D average compressive strain of the buckling zone – from experimental measurements and isotropic and anisotropic models of HSSP#10

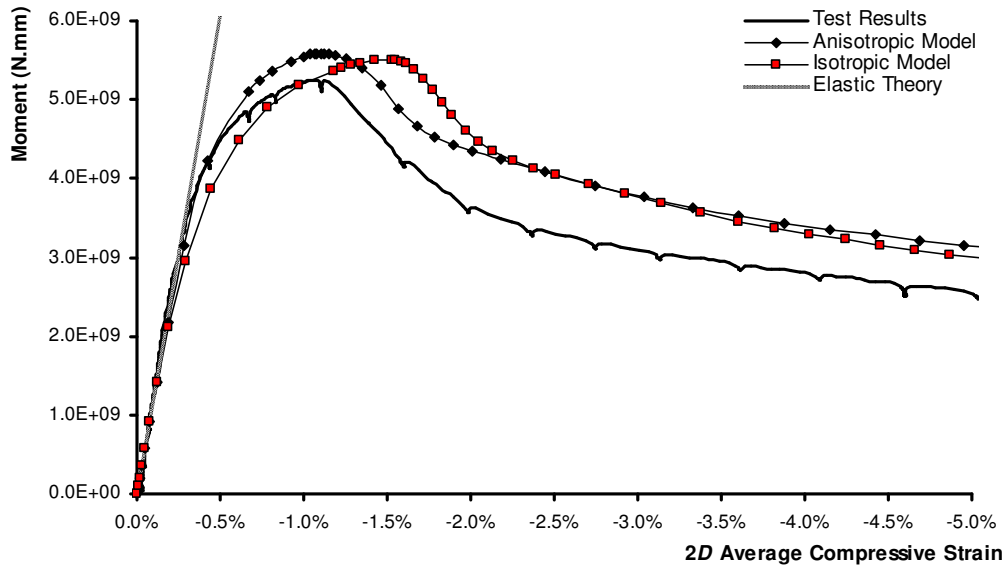


Figure 3-26 Global moment versus *2D* average compressive strain of the buckling zone – from experimental measurements and isotropic and anisotropic models of HSSP#11

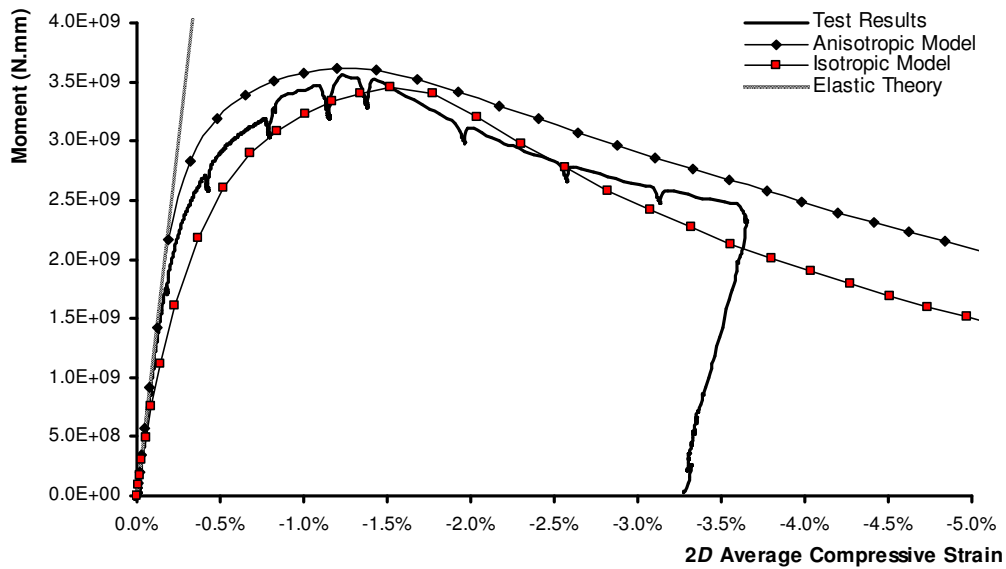


Figure 3-27 Global moment versus *2D* average compressive strain of the buckling zone – from experimental measurements and isotropic and anisotropic models of HSSP#12

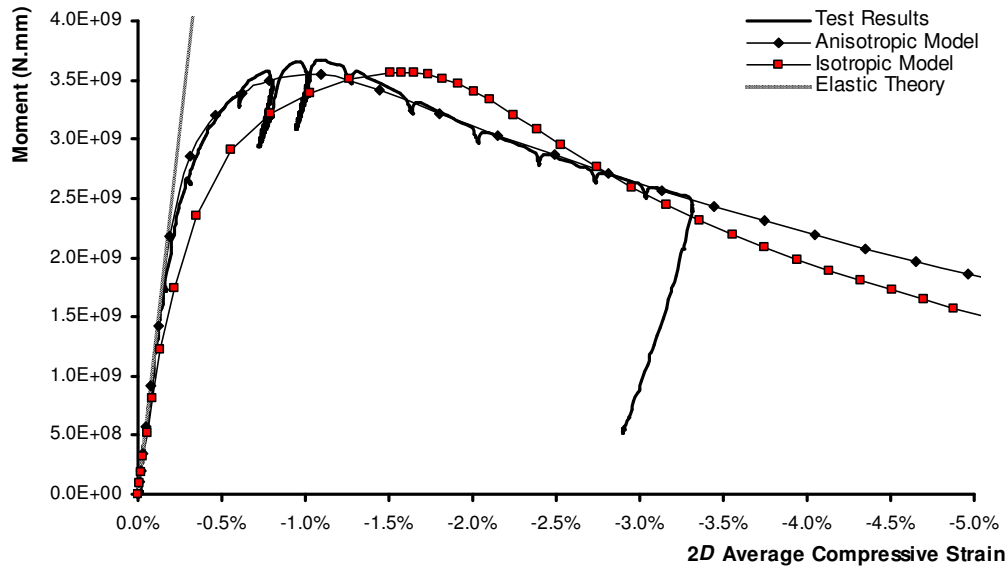


Figure 3-28 Global moment versus 2D average compressive strain of the buckling zone – from experimental measurements and isotropic and anisotropic models of HSSP#13

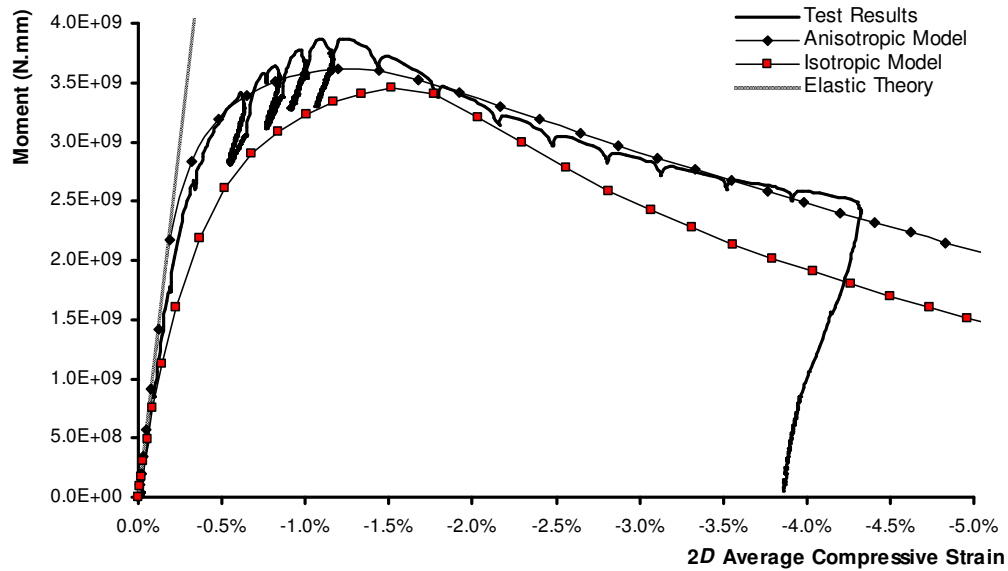


Figure 3-29 Global moment versus 2D average compressive strain of the buckling zone – from experimental measurements and isotropic and anisotropic models of HSSP#14

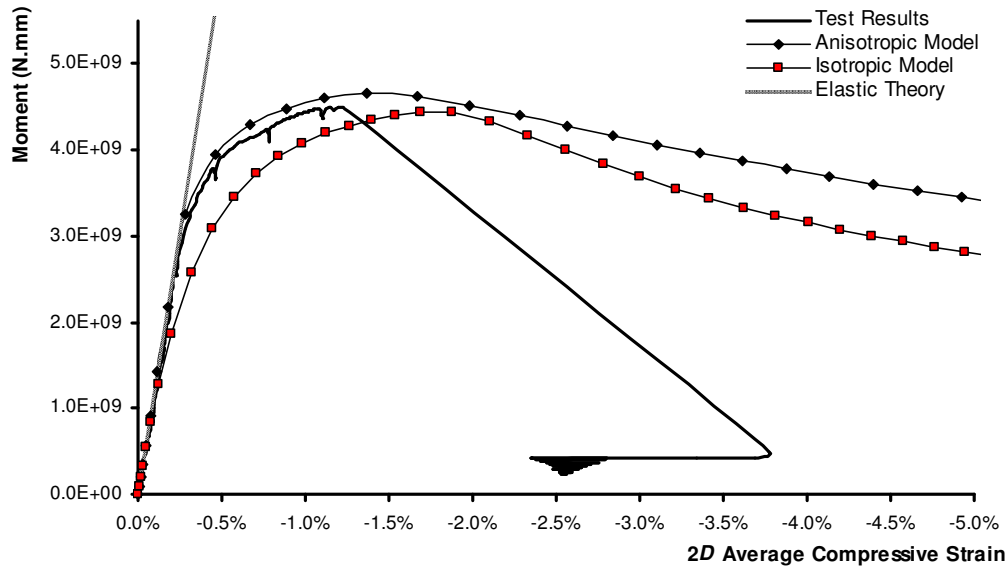


Figure 3-30 Global moment versus 2D average compressive strain of the buckling zone – from experimental measurements and isotropic and anisotropic models of HSSP#15

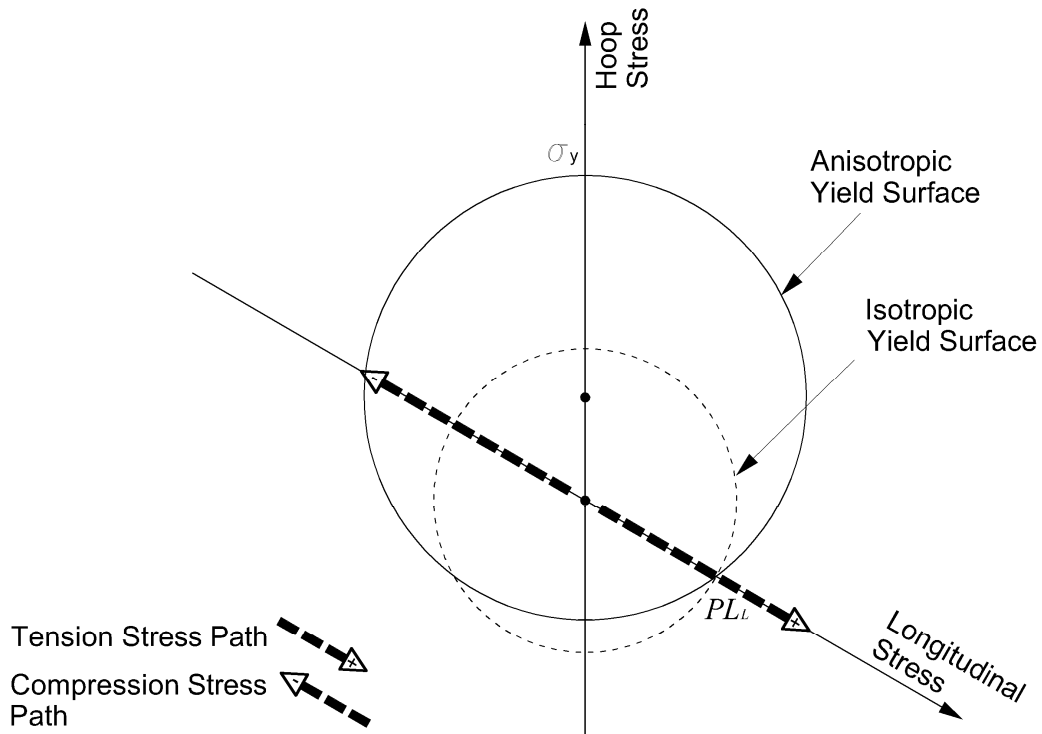


Figure 3-31 Stress paths for tension and compression elements of an unpressurized pipe under bending moment

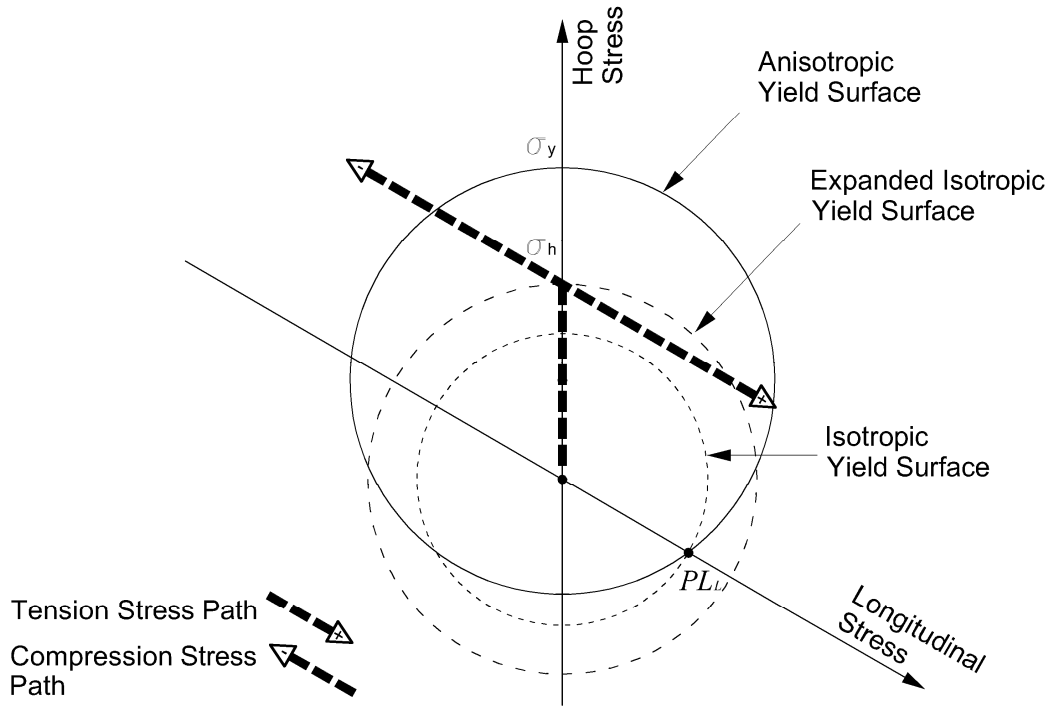


Figure 3-32 Stress paths for tension and compression elements of a pressurized pipe under bending moment

## 4 PARAMETRIC STUDY

The primary goal of this research was to develop a practical finite element modeling technique for high strength steel (HSS) pipes that captures material anisotropy caused by the pipe-making process. After this material model has been developed, it can be used to study the effects of anisotropy on the buckling behaviour of HSS pipes. In order to perform such a study in a comprehensive way, it is necessary to consider a sufficient number of cases with various combinations and different ranges of all affecting parameters, including anisotropy. Having the buckling analysis results of all these cases helps to investigate the effects of anisotropy on the critical buckling strain (CBS) of HSS pipes under different conditions. In addition, it shows how other affecting parameters are involved in the buckling process when anisotropy is present.

Finally, the above-mentioned study can be used to develop a new design tool to predict the CBS of HSS pipes. The review of current CBS criteria presented in Chapter 1 shows that all available equations have been developed for normal-strength steel pipes; consequently, they cannot be used to predict the CBS of HSS pipes with anisotropic material properties. Hence, there is a need to establish a new understanding about the buckling response of HSS pipes under different conditions.

The anisotropic material and finite element modeling method described in Chapter 2 and Chapter 3 were used to build a large numerical database of HSS pipe buckling responses. This database consists of HSS pipes with different geometrical, material, and loading conditions. This chapter presents the characteristic values used to describe different cases and the details of the parametric study.

## 4.1 Response Surface Methodology

In order to describe the CBS of HSS pipes as a function of all affecting parameters, it is useful to employ the Response Surface Methodology technique. In this technique, a set of experiments that yield adequate and reliable measurements of the response of interest are designed; subsequently, a mathematical model that best fits the data collected from the experiments is determined using regression analysis. The response is a dependent variable that is influenced by independent variables known as factors (DiBattista et al., 2000). The mathematical relationship between the response and the factors is known as the response function. The true value of the response,  $\eta$ , depends on  $k$  factors,  $X_1, X_2, \dots, X_k$ ,

$$\eta = \phi(X_1, X_2, \dots, X_k) \quad (4-1)$$

where

$\eta$ : true response function.

The form of the true response function is usually unknown and if it is continuous and smooth in the range of interest, it can be represented locally as a polynomial by means of a Taylor series expansion with any required level of accuracy. Only a finite number of terms is used in the Taylor series to define the response. Depending on the desired level of accuracy, higher order terms can be employed. In the simplest type of approximation, only up to the first order terms are used and the resulting function will be first order (i.e., linear). If up to the second order terms of the Taylor series are used, the model is considered to be second order and so on.

After an appropriate number of terms has been selected from the Taylor series expansion, the best fit to the selected pattern of the response can be obtained using the well-known least squares or similar error minimization techniques (see,

for example, Box et al., 1978). The predicted response function is not exactly the same as the real response function because of approximations in eliminating higher order terms of the Taylor series and other sources of experimental errors.

The first step in developing the predicted response surface is to identify the factors and a reasonable range of variation for each factor that affects the response. This step defines the solution space and the domain that is relevant to the problem being investigated. The next step is to build up a database of different combinations of factors. Each data set in this database gives a point on the response surface in the solution space. An accurate predicted surface requires a good definition of the response space and its domain related to the problem, as well as a good coverage of the solution space by the experiments (here is a finite element database). The following sections present detailed descriptions about the selection of each factor and its corresponding variation range.

## **4.2 Parameters to Investigate**

Based on all the previous research about the buckling response of steel pipelines, the CBS of a plain pipe is believed to be a function of four major groups of factors: the pipe's cross sectional dimensions (diameter and thickness), internal pressure, initial imperfections, and material properties. In this chapter these four groups of factors are considered to carry out the parametric study.

To date, the CBS in available criteria and research is considered to be independent of load functions (except for internal pressure) including different combinations of axial load and bending moment. That is, the CBS is a function of the level of longitudinal strain in the wall of the pipe, and is independent of how the longitudinal strain distributes in the pipe's cross-section.

This independency is expanded further to the load history of the specimen. Dorey et al. (2001) have shown that the load history to which a segment of a pipeline has been subjected often has an effect on the specimen's strain behaviour. However, since the CBS strain is assumed to be a specific level of strain, it is considered independent of the path by which the critical level of strain is reached. That is, a test specimen will not buckle until the critical strain is reached, regardless of the load history.

Since the finite element models developed in Chapter 2 and Chapter 3 have combined hardening plasticity, the pipe response to the load combination and load history will be different from normal-strength steel pipes with isotropic plasticity. These differences come from the kinematic component in two aspects:

- Different material responses in the longitudinal direction of the pipe under tension and compression, which eventually results in responses different from isotropic pipes under similar load combinations.
- The Bauschinger effects under any loading beyond the elastic limit, which changes the material response under any loading-unloading-reloading process.

Therefore, elimination of the load combinations and load history effects in the HSS pipes needs more investigation. Furthermore, the existing analytical and experimental evidence behind eliminating the load combination and load history is not persuasive, even for normal-strength steel pipes (Dorey et al., 2011).

However, the finite element models developed in this study were validated by experimental results from HSS pipe specimens which were tested under quasi-static testing conditions and pure bending loading (except HSSP#15). Covering the area of load combination and loading history effects in the parametric study requires supports of sufficient experimental and numerical data, which were not accessible at the time of this project. Besides, adding these factors to the affecting

parameters would increase the size of the database required for the parametric study by (at least) nine times. Therefore, the scope of the parametric study was limited to (and its results are only recommended for) HSS pipes under loadings dominated by a quasi-static bending moment with no plastic loading history in the longitudinal direction.

In Chapter 5 of this thesis, the effects of bending and axial compression combinations on the CBS are numerically investigated for limited cases of HSS pipes. Nevertheless, more study is needed about the load combination and load history effects on the buckling behaviour of HSS pipes.

Another factor that pipeline researchers report as affecting the CBS of steel pipelines is girth weld. Girth weld imposes two types of disturbance along the pipe length. The first disturbance is the localized imperfections induced by the girth weld, since the ends of two pipe pieces do not exactly match. This imperfection appears in a form of offset between the pipes' wall coming to the joint, and reduces the CBS. The second change caused by the girth weld is the change of material property due to the presence of the weld material and heat affected zone. The primary criterion for an acceptable weld for a pipeline is that the weld strength overmatches the pipe's strength in the welding area. This ensures that the longitudinal strain does not accumulate in the cross section of girth weld.

Dorey et al. (2001) addressed girth weld effects on the CBS by incorporating an offset imperfection pattern in the pipe models. This practice resulted in buckling at the girth weld location. Shitamoto et al. (2010) showed that modeling a pipe with girth weld should include both of the above-mentioned changes in the finite element model. They showed that exact modeling of the weld material and heat-affected zone might move the buckling location to the area adjacent to the girth weld. This relocation of the buckling zone increases the buckling load and the

corresponding compressive strain. The finite element models developed in Chapter 3 simulated plain pipes and the validated finite element models could not be used for HSS pipes with girth welds. Extending the study to girth welded pipes required a sufficient number of full-scale buckling tests of girth-welded HSS pipes with adequate information on the material properties of the weld material and heat affected zone. This information was not available at the time of this study; therefore, the parametric study in this chapter was restricted to plain pipes only.

## **4.2.1 Material Parameters**

The material modeling technique proposed in Chapter 2 is highly capable of reproducing the responses in longitudinal tension and compression and transverse tension when it is calibrated by longitudinal and transverse tension stress-strain data. Figure 4-1 shows the general format of the longitudinal and transverse responses of the proposed material model under tensile stress. Having longitudinal and transverse tension coupon test results, both the elastic and plastic ranges of the anisotropic model can be regenerated if five material parameters are defined. These five parameters are the modulus of elasticity,  $E$ ; nominal yield stress,  $\sigma_{y(nom)}$ ; longitudinal proportional limit,  $PL_L$ ; linear strain hardening modulus,  $E_{sh}$ ; and the kinematic parameter  $\gamma$ , the latter of which defines the longitudinal yielding curve. The material elastic and plastic responses are built upon these material parameters. Changing each parameter might change the pipe response and its CBS. These parameters are discussed in detail in the following sections.

### **4.2.1.1 Modulus of Elasticity**

Previous studies by DiBattista et al. (2000) showed that the pipe's elastic stiffness should be included in non-dimensional analyses, and that omitting  $E$  as a variable

in such analyses “will lead to incorrect predictions of the behaviour.” This seems rational because the modulus of elasticity defines material stiffness and, eventually, elastic deformations. As the local buckling of pipelines is an elastic-plastic phenomenon, the elastic deformation before buckling affects the total deformation of the buckled zone. Therefore, the magnitude of the CBS depends on the modulus of elasticity. Nevertheless, the variation of the modulus of elasticity in pipeline steels is not generally significant and can be assumed to be a constant value.

#### 4.2.1.2 Nominal Yield Stress

As shown in Figure 4-1 and also discussed in Chapter 2, in the idealized longitudinal and transverse stress-strain curves of HSS pipes, the nominal yield stress,  $\sigma_{y(nom)}$ , is defined as the stress value of the intersection point between linear-elastic and linear strain hardening regions. This parameter comes from the idealized material stress-strain curve developed for the combined hardening model and it has a theoretical nature. Hence, it cannot be easily found in common material properties of steel pipelines. Therefore, it was decided to replace  $\sigma_{y(nom)}$  with a parameter that is more common for pipeline materials. A good option for replacing  $\sigma_{y(nom)}$  can be the pipe’s transverse yield stress,  $\sigma_{y(T)}$ , which is one of the important material properties in the design process for selecting a steel grade. The longitudinal and transverse yield stresses defined as the strength at 0.2% plastic strain are also shown in Figure 4-1. In the idealized model, the nominal yield stress can be related to the transverse yield stress (transverse stress at 0.2% plastic strain), knowing the linear strain hardening modulus as:

$$\sigma_{y(nom)} = \sigma_{y(T)} - 0.002E_{sh} \quad (4-2)$$

Therefore, from this point on, in the parametric study,  $\sigma_{y(T)}$  will be used as a primary variable to define  $\sigma_{y(nom)}$  and, eventually, the properties of the material model.

#### **4.2.1.3 Longitudinal Proportional Limit**

The longitudinal proportional limit,  $PL_L$ , is the stress associated with the point at which the longitudinal stress-strain curve starts to deviate from the linear-elastic response. In the idealized stress-strain curves in Figure 4-1,  $PL_L$  and  $\gamma$  determine the yielding region of the longitudinal stress-strain curve. The lower values of  $PL_L$  (compared to the nominal yield stress), indicate a higher degree of anisotropy for each steel material grade. The appropriate range and values for  $PL_L$  for the parametric study are considered based on the ratio of  $PL_L/\sigma_{y(T)}$  in the HSS pipe material database presented in Chapter 2.

#### **4.2.1.4 $\gamma$ Value for Kinematic Hardening Response**

According to the Armstrong-Fredrik kinematic evolution law,  $\gamma$  defines the saturation rate of the kinematic component during plastic deformations. If the material model has a higher value of  $\gamma$ , its kinematic hardening component saturates faster; this means that the longitudinal stress-strain curve in Figure 4-1 converges to the transverse curve in a lower plastic strain. This essentially indicates that higher  $\gamma$  values result in lower material anisotropy and vice versa. In Figure 4-1, the hatched area between the longitudinal and transverse stress-strain curves shows the material model's level of anisotropy. This area is defined by both  $\gamma$  and  $PL_L$ ; i.e., for each material grade, higher  $\gamma$  and higher  $PL_L$  values result in lower anisotropy of the modelled material.

#### 4.2.1.5 Strain Hardening Modulus

The last factor that defines the material model for HSS pipes is the slope of the linear strain hardening region in both longitudinal and transverse directions (i.e.,  $E_{sh}$ ). In the proposed combined hardening model, the entire plastic response in the transverse direction is linear, which can be defined by  $E_{sh}$ . In the longitudinal direction, however, yielding starts with a combination of kinematic and linear isotropic responses. After the kinematic component is saturated, only the isotropic hardening component defines the material stress-strain relationship.

As this parameter describes the isotropic hardening component, it indicates the material plastic deformability after yielding process is complete. The yield-to-tensile stress ratio is a more popular indicator of material plastic deformability, especially when large plastic deformations are involved. As discussed in Chapter 2 and Chapter 3, the CBS of HSS pipes is highly affected by elastic, yielding, and early plastic material responses usually up to 3.0% total strain. This fact makes it difficult to use a yield-to-tensile stress ratio to define the plastic deformability in early plastic deformations, because the hardening rate in the early plastic range changes depending on the ultimate strength and tensile strain. On the other hand, there can be a large variation in the ultimate strength achieved by any grade of pipeline. Besides, there is no standardized value of the strain at ultimate strength for different grades of pipelines. Hence,  $E_{sh}$  was used as a factor of the material properties in the material model to define the material plastic hardening.

#### 4.2.2 Pipe's Diameter and Thickness

A short parametric study conducted by Dorey et al. (2001) showed that it is not the size of the pipe diameter or thickness that affect the CBS but, rather, the diameter-to-thickness ratio changes the pipes' buckling responses. Their parametric study was designed to determine if there was a size effect on the CBS

due to the variation in the diameter while holding all non-dimensional parameters constant. The results showed that the moment capacity of a pipe segment increased when the pipe's diameter increased (due to the increased area and stiffness of a larger diameter cross section). However, the CBS appeared to remain essentially constant when only the diameter size changed, while other affecting parameters remained unchanged. Other approaches by different researchers also showed that it is the ratio of diameter to thickness that influences the CBS, not the absolute magnitude (Dorey et al., 2001).

### **4.2.3 Internal Pressures**

Internal pressure was the only load parameter that was included in this parametric study for evaluating the CBS. The discussion in Chapter 3 showed that using the von Mises yield criterion, the internal pressure changes the stress path and the buckling response. Tension stress in the hoop direction leads the pipe's compression fibres to yield earlier under longitudinal compressive stresses. Decreasing the yielding stress under longitudinal compression decreases the longitudinal stress-carrying capacity. Therefore, higher internal pressure results in lower longitudinal compressive resistance and bending capacity.

However, internal pressure has an additional effect that changes a pipeline's longitudinal strain capacity. Numerous pipe-testing projects performed by different researchers has established that the buckling mode depends on the level of internal pressure. While unpressurized pipes buckle with a diamond inward buckled shape, pressurized pipe specimens form a bulge in the buckling area. This is interpreted as changing to a higher energy mode of buckling, which accommodates a larger longitudinal strain before buckling. This change in the buckling mode is due to the stabilizing effects of internal pressure.

Because of this effect, the level of internal pressure should be included in parametric studies of pipelines, because it plays an important role in the pipe's stability. For HSS pipes with anisotropic material, however, this stabilizing effect might have a pattern and magnitude that differs from those of isotropic pipes. As discussed in Chapter 3, considering a higher yield stress in the transverse direction (by using a combined hardening material model) results in a more realistic bending stiffness. This automatically changes the longitudinal strain capacity of HSS pipes compared to that of pipes with isotropic material. Therefore, the internal pressure was included in the parametric study to help to understand how it changes the HSS pipes' longitudinal compressive strain capacity, and how these effects differ from those on normal-strength steel pipes.

#### **4.2.4 Initial Imperfections**

Actual pipeline segments do not come in perfect cylindrical shapes; therefore they always buckle with buckling loads and deformations smaller than what is theoretically calculated for an ideal cylinder. This reduction in the load and deformation capacity before buckling is a result of a pipe's imperfections in terms of radius and thickness variations, and out-of-roundness and out-of-straightness. These effects necessitate including the pipe's imperfections in the finite element models for studying the CBS. The most accurate way to incorporate the imperfection effects in a finite element model is to model all of the pipe's actual imperfections. This is manageable for finite element models that simulate buckling tests on real pipe specimens by careful measurements of pipe imperfections. However, in a parametric study dealing with hypothetical pipe specimens, the best approach is to incorporate imperfection patterns that are closest to the real imperfection patterns of pipes.

Steel pipes' imperfection patterns have a random nature. A comprehensive definition which describes imperfections in HSS pipes both qualitatively and

quantitatively is still lacking. Some researchers at the University of Alberta are now thoroughly investigating the initial imperfection of HSS pipes.

Dorey et al. (2001) had introduced a number of idealized imperfection patterns to incorporate in finite element models when actual imperfection measurements were not available. They showed that each imperfection pattern had particular effects on the response of the models under different load cases. Therefore, they recommended each one of their imperfection patterns to be used for a specific load case in buckling analysis.

In the absence of validated and inclusive imperfection patterns for HSS pipes, among all idealized patterns introduced by Dorey et al. (2010), it was decided to use one pattern that makes the pipe susceptible to buckling under the load case employed in the parametric study (i.e., pure bending). In this parametric study, the initial imperfection was defined as the maximum out-of-roundness of the pipe wall in a half-ring imperfection pattern. This is consistent with the developed finite element models in Chapter 3 and with the fact that the models for the parametric study were analyzed under pure bending conditions. Chapter 3 includes the detailed description of the imperfection pattern. The next section includes a discussion of the magnitudes of maximum out-of-roundness,  $I_{max}$ , considered for the parametric study.

### 4.3 Dimensional analysis

From the previous sections and the scope of this parametric study, the CBS for plain HSS pipes under a pure quasi-static bending moment is a function of nine variables. Mathematically, it can be expressed as

$$\varepsilon_{cr} = \varepsilon(E, \sigma_{y(T)}, PL_L, \gamma, E_{sh}, D, t, p, I_{max}) \quad (4-3)$$

where

$\sigma_{y(T)}$  : transverse yield stress that replaces  $\sigma_{y(nom)}$  as discussed in section 4.2.1.2

$t$  : pipe's wall thickness

$p$ : internal pressure

$H_{max}$ : initial imperfection's magnitude

A large number of analyses would be needed to investigate the effects of each parameter in the parametric study. Therefore, it was decided to use dimensional analysis to reduce the size of the parametric study for each of these different variables.

Dimensional analysis relates the effect of two or more variables to produce a new non-dimensional parameter, which represents the effects of variables combined together. Further details of dimensional analysis will not be presented in this thesis, but can be readily reviewed in a variety of sources, including Taylor (1974). Using the non-dimensional parameters that consist of a combination of two or more variables, the number of independent variables can be reduced to a more manageable number of parameters to carry out the parametric study. The design criteria generated by a parametric study using dimensional analysis will be more simplified but can accommodate the same spectrum of variables.

There are different methods that can be used to reduce the number of variables in dimensional analysis (Langhaar, 1951). One of the widely used and more popular methods for engineering applications is the Buckingham-Pi Theorem which was used in this project. This theorem states that "if an equation is dimensionally homogeneous, it can be reduced to a relationship among a complete set of dimensionless products." If the total number of variables used to construct a dimensional matrix of the variable is "v" and the highest rank of dimensional matrix is "r," the number of dimensionless variables that are required to form a complete set of dimensionless products will be "v-r."

Among all nine variables that are introduced in this section to affect the CBS of HSS pipes,  $\gamma$  is the only non-dimensional parameter. Based on the Armstrong-Fredrick kinematic hardening law,  $\gamma$  is a scalar that adjusts the back-stress rate according to back-stress magnitude (relaxation term). Therefore, omitting or including  $\gamma$  does not affect the total number of non-dimensional parameters determined using the Buckingham-Pi Theorem.  $\gamma$  was included in the dimensional analysis for completeness.

The dimensional matrix, expressed in the fundamental units of mass (M), length (L), and time (T), used to describe each of the nine variables in Equation (4-3) takes the following form:

	$E$	$\sigma_{y(T)}$	$PL_L$	$\gamma$	$E_{sh}$	$D$	$t$	$p$	$H_{max}$
M	1	1	1	0	1	1	1	1	0
L	-1	-1	-1	0	-1	0	0	-1	0
T	-2	-2	-2	0	-2	0	0	-2	0

According to the Buckingham-Pi Theorem, the variables in Equation (4-3) were reduced to seven independent non-dimensional  $\pi$ -terms, because the total number of variables is nine and the rank of the dimensional matrix is two. The first five variables presented in the dimensional matrix are the material properties. Except for  $\gamma$ , which is already a non-dimensional variable,  $E$ ,  $\sigma_{y(T)}$ ,  $PL_L$ , and  $E_{sh}$  have similar dimensions. Dividing one of these variables by the other generates a non-dimensional variable that can be used in the parametric study.

The first variable was  $PL_L/\sigma_{y(T)}$ , which is an indicator of material anisotropy (the other material anisotropy indicator is  $\gamma$ ). Other non-dimensional parameters were  $\sigma_{y(T)}/E$ , and  $E_{sh}/E$ . Considering that the modulus of elasticity does not have significant variations (and it was considered constant in this parametric study), using  $\sigma_{y(T)}/E$  and  $E_{sh}/E$  as non-dimensional variables incorporated the effects of the material's grade and plastic hardening in the study.

Hence, out of seven non-dimensional variables, four variables were for material properties. As discussed before, the fifth non-dimensional variable could be defined as the  $D/t$  ratio, as an indicator of pipe geometry. For the effects of internal pressure, the sixth non-dimensional variable could be defined as the ratio of the pipe's hoop stress due to the internal pressure,  $\sigma_h$ , to the transverse yield stress,  $\sigma_{y(T)}$ . This variable is a well-known parameter in pipeline design and is called the design factor. The seventh non-dimensional variable was defined as  $H_{\max}/D$ , which is the maximum amplitude of out-of-roundness in units of mm, divided by the pipe's diameter, also in units of mm.

Therefore, the CBS as a function of seven non-dimensional parameters derived from the Buckingham-Pi Theorem was expressed as

$$\varepsilon_{cr} = \varepsilon(\pi_1, \pi_2, \pi_3, \pi_4, \pi_5, \pi_6, \pi_7) \quad (4-4)$$

where

$$\begin{aligned} \pi_1 &= \frac{\sigma_{y(T)}}{E} && \text{that incorporated the effects of material grade} \\ \pi_2 &= \frac{PL_L}{\sigma_{y(T)}} && \text{that incorporated the effects of material anisotropy} \\ \pi_3 &= \gamma && \text{that also incorporated the effects of material anisotropy} \\ \pi_4 &= \frac{E_{sh}}{E} && \text{that incorporated the effects of material plastic isotropic} \\ &&& \text{hardening} \\ \pi_5 &= \frac{D}{t} && \text{that incorporated the effects of pipes geometry} \\ \pi_6 &= \frac{\sigma_h}{\sigma_{y(T)}} && \text{that incorporated the effects of internal pressure} \\ \pi_7 &= \frac{H_{\max}}{D} && \text{that incorporated the effects of initial imperfections.} \end{aligned}$$

### 4.3.1 Ranges of $\pi$ -Parameters to Investigate

After defining the non-dimensional variables, the next step was to define their maximum and minimum limits to describe the so-called *region of interest* in the k-dimensional space of all possible combinations of these variables. If the response surface is approximately planar within the region of interest, the maximum and minimum values of each variable will provide adequate cases for building the combination of variables in the database of experiments. This essentially leads to a first-order regression analysis. If a significant curvature is present in the response surface, the first order regression (in which each factor is sampled only in two levels) will not be able to capture the response surface adequately.

Using more design points within the region of interest results in a more accurate approximated shape of the response function. On the other hand, the number of design experiments grows rapidly with an increase in the number of factors levels. At least three levels of the variables must be sampled to capture the curvature in the response function. In the case of this parametric study with seven non-dimensional variables, using three levels for each parameters led to  $3^7$  combinations of factors (i.e. 2187 experiment), which was quite a large number to investigate.

To maintain a reasonable level of accuracy as well as a practical number of experiments, it was decided to start the parametric study with three levels for each parameter. Therefore, in addition to the maximum and minimum values for each variable defining the range of each parameter variation, an intermediary value was selected as the third point for each parameter level. This combination results in a second-order approximation of the response surface, which addresses the non-linearity of the response surface with the minimum number of experiments.

#### 4.3.1.1 Transverse Yield Stresses-to-Modulus of Elasticity Ratio, ( $\sigma_{y(T)}/E$ )

The modulus of elasticity does not have significant variations in pipeline steels. A constant value of 207000MPa is assigned for it in CAN/CSA Z662-07. Looking back to Chapter 2, the average value of  $E$  among all HSS pipe material types in the database was 206000MPa and the coefficient of variation was 3.16%. Therefore, it was decided to assign a constant value of  $E$  for the parametric study. A constant value of 207000MPa was considered for the modulus of elasticity in the parametric study, similar to the value recommended by CAN/CSA Z662-07. The transverse yield stress defined the variation of the first  $\pi$ -parameter,  $\sigma_{y(T)}/E$  since a constant value was considered for the denominator.

This study was focused on the behaviour of the pipelines made of HSS classes that share similar aspects of anisotropy. Three steel pipe material classes, i.e. X80, X100 and X120, which are described as HSS pipes in the literature, fall under this category. The HSS pipes in the database discussed in Chapter 2 and Chapter 3 were from X80 and X100 classes. Pipe producers are making grade X120 pipes via similar steel production and pipe-making processes. Their final product shows the main aspects of material behaviour and anisotropy similar to what was described in Chapter 2. Therefore, grade X120 was also considered to build up the parametric material response in the parametric study.

The industry defines the specified minimum yield stress (SMYS) for each steel grade based on the yield stress in the transverse direction, because the primary design check in an energy pipeline is the resistance against internal pressure. The SMYS for grades X80, X100, and X120 are 550MPa, 690MPa, and 825MPa, respectively.

For the purposes of this parametric study, the value of  $\sigma_{y(T)}$  was equated to SMYS for grades X80, X100, and X120. It is acknowledged that this is not the case for actual steel pipeline materials; however, there is no industry standard that relates

the value of SMYS to  $\sigma_{y(T)}$ . Furthermore, it is common practice in industry to use SMYS as  $\sigma_{y(T)}$  when performing numerical calculations. Using SMYS provided a lower bound on  $\sigma_{y(T)}$ .

Based on the above discussion, the minimum, intermediary, and maximum values considered for the first  $\pi$ -parameter,  $\sigma_{y(T)}/E$ , were respectively considered as

$$\frac{550}{207000} = 0.00266, \quad \frac{690}{207000} = 0.00333 \quad \text{and} \quad \frac{825}{207000} = 0.00399$$

It is worth mentioning that in addition to the modulus of elasticity, Poisson's ratio should be defined to complete the definition of the material elastic behavior. The accepted industry value for  $\nu$  equal to 0.3 was used throughout the parametric study.

#### **4.3.1.2 Longitudinal Proportional Limit-to-Transverse Yield Stresses Ratio, ( $PL_L/\sigma_{y(T)}$ )**

As discussed in Chapter 2, the yielding region in the longitudinal direction of HSS pipes is fairly large compared to the transverse direction. The yielding region starts from the longitudinal proportional limit which is quite low compared to the nominal yield stress in HSS pipes. Although the proportional limit is not a primary material property used in the design of pipelines, it was used as a parameter to define the material properties. The second non-dimensional variable in the parametric study, ratio of  $PL_L/\sigma_{y(T)}$ , was used as one of two indicators of material anisotropy.

Among all material models developed in Chapter 2 for HSS pipe material types, the average value for the  $PL_L/\sigma_{y(T)}$  ratio was 0.481, with a minimum and maximum of 0.440 and 0.576, respectively. As there is no way to acquire a range for this variable that embraces all levels of this parameter among HSS pipe materials available in the market, it was decided to use a range that covers

different values of this parameter in the available database. Therefore, the minimum, intermediate, and maximum levels considered for the second  $\pi$ -parameter,  $PL_L/\sigma_{y(T)}$ , were 0.4, 0.5 and 0.6, respectively.

#### **4.3.1.3 Kinematic Hardening Parameter, $\gamma$**

In the proposed material model, the start point of the longitudinal yielding region was defined by the proportional limit, and the length of this region was defined by the kinematic parameter,  $\gamma$ . Higher values of  $\gamma$  result in faster saturation of the kinematic component (i.e., smaller yielding region in longitudinal direction) and vice versa. This variable is the second non-dimensional parameters that were used to define the level of anisotropy in the material.

Similar to  $PL_L/\sigma_{y(T)}$ , the only way to define an appropriate range for the  $\gamma$  value was to look at its variation in the available database. Among all material models developed in Chapter 2 for HSS pipe material types, the average value for  $\gamma$  was 519, with a minimum and maximum of 394 and 709, respectively. Therefore, the minimum, intermediate, and maximum values for the third  $\pi$ -parameter,  $\gamma$ , were considered as 350, 550, and 750, respectively. These values adequately cover different values of  $\gamma$  in the available database.

#### **4.3.1.4 Strain Hardening Modulus-to-Modulus of Elasticity Ratio, ( $E_{sh}/E$ )**

The fourth non-dimensional variable is a common parameter in elastic-plastic analysis and the design of steel structures. This variable defines the ratio of the plastic to elastic stiffness in an ideal bilinear stress-strain curve that represents the material response of steel structures. The material's higher plastic stiffness delays the plastic deformation's localization and results in larger range of stable plastic deformation of the structure.  $E_{sh}/E$  is a suitable non-dimensional indicator of material plastic ductility considering that the modulus of elasticity does not have a large variation range in steel material.

Among all material models developed in Chapter 2 for HSS pipe material types, the average value for the  $E_{sh}/E$  ratio was 0.0123, with a minimum and maximum of 0.0078 and 0.0142, respectively. It was decided to use a range that covers this parameter's variations in the available database. As a result, the minimum, intermediate, and maximum values considered for  $\pi_4$  ( $E_{sh}/E$ ) were 0.0067, 0.0133, and 0.020, respectively. Since the value for the modulus of elasticity was considered constant in the parametric study, the variation of  $\pi_4$  was only a function of the strain hardening modulus (similar to the first  $\pi$ -parameter). Comparing the absolute value of  $E_{sh}$  with the range of this value in the HSS pipe material database in Chapter 2 shows that the considered range of variation for  $E_{sh}$  adequately covers the range of variation of  $E_{sh}$  in the database.

The fourth  $\pi$ -parameter is the last of four non-dimensional variables that define the material properties of the experiments. Table 4-1 illustrates the distributions of these four parameters in the material database used in Chapter 2.

#### **4.3.1.5 Diameter-to-Thickness Ratios, ( $D/t$ )**

Pipelines currently in service in Canada have a  $D/t$  ratios that range from as low as  $D/t=10$  to as high as  $D/t=120$ . While it would be favourable to cover the entire spectrum of these  $D/t$  ratios, it would not be practical. The average value of the  $D/t$  ratio in the pipe specimens used to validate finite element analyses results was around 55; however, it was decided to use  $D/t$  ratios of 50, 70, and 90 for the  $\pi_5$  parameter ( $D/t$  ratio). The reason that the  $D/t$  ratio skewed toward higher values was that most of the HSS pipes produced by steel pipe producers, as well as those studied in the literature, had  $D/t$  ratios higher than 50. This is the result of the well-known advantage of using HSS pipes in pipeline projects: that is, “for any pipeline with a specific designed diameter and internal pressure, using HSS pipes results in smaller wall thickness (higher  $D/t$  ratio) and considerable saving of steel material compared to normal-strength steel pipes”.

As discussed earlier, pipe diameter has no effect on the CBS. Therefore, it was decided to use a specimen with a diameter of 762mm, equivalent to 30 inches of pipe segment. Accordingly, three different thicknesses associated with the selected  $D/t$  ratios were 15.2mm, 10.9mm, and 8.5mm. These values of thickness are not necessarily similar to what exists among the HSS pipes available in the market.

#### **4.3.1.6 Hoop Stress-to-Transverse Yield Stress Ratio, ( $\sigma_h/\sigma_{y(T)}$ )**

As defined in the current CAN/CSA Z662-07 standard, under field operation conditions, the level of internal pressure can range from zero to full operating pressure. The current CAN/CSA Z662-07 limits the maximum operating pressure in any segment of pipelines to the level that corresponds to tensile stress of 80% SMYS in the pipe's hoop direction. It was reasonable to use this range for the parametric study. Hence, the two extremes of zero internal pressure (hereafter referred as 0.0% pressure) and full operating internal pressure (hereafter referred as 80.0% pressure) were to be used as the lower and upper limits of internal pressure for the parametric study.

It should be noted that for the purposes of this parametric study, the value of yield stress in the transverse direction was equated to SMYS. It can be rather unlikely for a real pipe segment in the field under buckling conditions to have a hoop stress caused by the internal pressure reaching as high as 80.0% of its actual yield stress in the transverse direction. The possibility is so low because the following four conditions must occur simultaneously:

- The pipe segment must belong to a highly pressurized pipeline. Due to various circumstances, not all energy pipelines use the full operating pressure needed to raise the pressure so high as to cause hoop stress up to 80.0% SMYS.)

- The operating pressure drops from one compressor station to the next, therefore, the maximum internal pressure in pipeline segment between two compressor stations exists in the segments close to the upstream compressor station. A pipeline operator can apply the pressure with a limit so that the internal pressure in the pipe segments right after the compressor station does not exceed the maximum allowable level. Therefore, the second condition is that the pipe segment must be close to the upstream compressor station.
- SMYS defines a lower bound of yield stress in steel material and major percentage of pipe segments have actual yield stress above SMYS. Hence, the third condition is that the pipe segment must have yield stress close to the SMYS.
- The fourth and last condition is that the pipe segment having all above conditions happen to be under externally induced longitudinal deformation that brings it to the critical condition and buckling.

Based on the above discussion, it might be quite rare for a buckling pipe that has internal pressure corresponding to hoop stress up to 80.0% of the actual transverse yield stress. But there is no other way to define a lower maximum limit that reflects real conditions. Besides, using internal pressure corresponding to 80.0% SMYS hoop stress provides an upper bound for the effects of internal pressure.

Nevertheless, one should use extreme caution before assuming the  $\sigma_h/\sigma_{y(T)}$  ratio as high as 80% in a pipe segment for buckling assessments, because this factor improves the buckling response and might overestimate the longitudinal compressive strain capacity.

A third value for internal pressure was considered in order to capture the non-linear behaviour between these two limits. This intermediary pressure corresponds to a hoop stress of 40% SMYS (hereafter referred to as 40.0% pressure).

#### 4.3.1.7 Initial Imperfections-to-Diameter Ratio, ( $I_{max}/D$ )

The seventh  $\pi$ -parameter,  $I_{max}/D$ , accounts for the initial imperfection in the pipes. As discussed earlier, no comprehensive study has been done in HSS pipes that introduces a pattern for each type of initial imperfections (i.e., radius variations, out-of-roundness, and thickness variations) built upon qualitative and qualitative studies. For this parametric study, the half-ring imperfection pattern introduced by Dorey et al. (2001) was used to incorporate out-of-roundness in the critical section of the pipe segment and trigger the pipe buckling. Dorey et al. (2001) recommends this pattern for pipe models under bending loadings, and incorporates out-of-roundness of the pipe wall in 180° of the pipe's circumference in a specific gauge length of pipe segments. By using this pattern, out-of-roundness (ovality) was incorporated in the finite element models of the parametric study, while other forms of imperfection (i.e., the pipe's thickness and radius variations) were neglected.

Similar to the procedure used in Chapter 3, the half-ring imperfection pattern was applied to the pipe models in a way that the grid point with maximum distance from the pipe's axis was placed on the extreme compression fibre, one element away from the pipe's mid-length. This longitudinal asymmetry prevented unrealistic buckling modes from occurring in perfectly symmetric pipe models (Dorey et al., 2001).

The gauge length used for the imperfect zone was  $0.75D$ . This gauge length was selected after a trial-and-error process in the preliminary parametric study, as it always caused buckling in the mid-length of all pipe models. This uniform buckling location among all models is favourable for the parametric study because it unifies the buckling process and makes the average compressive strain from all models comparable. Chapter 3 presents details of the imperfection application.

The above-mentioned pattern of initial imperfection was used in all finite element models in the parametric study. The only variation of initial imperfection was the scale of the imperfection in the imperfect area, based on the maximum imperfection,  $I_{max}$ . This variable is the difference between the pipe's radius and the distance between the point of maximum ovality (which is placed on the pipe's extreme compression fibre in the middle of imperfection gauge length) and the pipe's longitudinal axis. The seventh  $\pi$ -parameter,  $I_{max}/D$ , is the ratio of this difference to the pipe's diameter.

The initial imperfection's variation range can be defined by assigning a variation range to  $I_{max}/D$ . Neither the CSA nor API directly indicate a limit for initial imperfections of the pattern used here. They recommend wall thickness and out-of-roundness limits, but neither of these could be translated directly to the half-ring ovality type of imperfection. Therefore, the lower and upper limits selected for the parametric study were based on the imperfection measurements performed on the HSS pipes in Chapter 3. In the HSS pipe database used in Chapter 3, the pipe radii had been measured on four points around the pipes' circumference as the local equivalent radius for the 180° arc centred at the point of interest. The difference between the maximum and minimum local radii divided by the average radius of each cross section was reported as the ovality.

$$\frac{D_{max} - D_{min}}{D_{average}} \quad (4-1)$$

The maximum ovality measured in that database ranges from 0.05% to 0.50% of average pipe diameter.

Although this definition of maximum ovality is slightly different from the above definition of  $I_{max}/D$ , it was decided to use the same range for the imperfection range of finite element models in the parametric study. However, it is rather

unlikely that the critical section of the pipe under buckling load has the maximum initial imperfection located on the extreme compression fibre of the critical cross section. Using the half-ring imperfection pattern and putting the point of maximum ovality on the extreme compression fibre incorporates the full effect of the imperfection amplitude; therefore, it was considered unnecessary to extend the maximum ovality beyond the range measured on the HSS pipe specimens.

For pressurized pipe models, if the applied imperfection magnitude is less than a certain value, the effects of the initial imperfection become too small to trigger the buckling at the point of the maximum imperfection. Instead, the buckling initiates close to the pipe ends (next to the collar). To avoid these situations and guarantee a uniform buckling location among all finite element models in the parametric study, a preliminary analysis was performed. In this analysis, the minimum range of  $I_{\max}/D$  (0.05%) was tested with different types of pipe geometry and material properties. After ensuring that it always resulted in the favourable buckling mode, this value was selected as the minimum  $I_{\max}/D$  limit for the parametric study.

The intermediary value for the imperfection magnitude was considered equal to 0.025%, almost in the middle of the assigned range. Hence, the minimum, intermediate, and maximum values considered for  $I_{\max}/D$  were 0.05%, 0.025%, and 0.50%, respectively.

### **4.3.2 Geometry and Loading Scheme of the Pipe Models**

Finite element models used for the parametric study were basically similar to the models developed in Chapter 3. These models were used in the parametric study to simulate hypothetical pipes whose properties were defined through the seven assigned non-dimensional variables and predefined fixed parameters such as the modulus of elasticity and the pipe radius. Other parameters that define the pipe

model and were not directly linked to the non-dimensional parameters were assigned properly so that they had a minimum effect on the analysis results.

The first parameter defined was the model length. The length of a pipe segment for an experimental testing program is restricted by the testing facilities. In finite element analyses however, there is no restriction on the model's length, but enlarging the pipe's length increases the number of elements and analysis time. The lengths of the tested pipes in Chapter 3 were between 3.5 and 4.4 times their outside diameter. Dorey et al. (2001) recommended using a model length,  $L$  five times the diameter, to avoid the end effects. This ratio of  $L/D$  was used to scale the lengths of the models at five times their diameters.

Similar to the models in Chapter 3, 40 elements were used in the 180° circumference of the model. Considering that the model length was five times larger than its diameter, 130 rows of elements were used in the entire length of the pipe models. This meshing configuration resulted in an identical mesh in all types of the model's geometry in the parametric study, with a uniform aspect ratio of pipe elements equal to 1.02.

The relative end stiffness of the pipe models was aimed to be uniform among all models in the parametric study. The first and last six rows of elements were assigned to collars with the same material properties as the pipe elements. These collars were modeled with a wall thickness two times the pipe body's wall thickness. The end plates were modeled with fully elastic behaviour with the same modulus of elasticity as the pipe material. The end plates' thickness was modeled as six times the pipe thickness (relatively close to the average of the same ratio in Chapter 3's experimental data).

As the pipe models were under a pure bending condition, the distances to the pivot points could not change the longitudinal strain distribution. Therefore, the distance to the pivot point used in Chapter 3 was also employed for the parametric

study. The boundary conditions of the pivot points and nodes on the longitudinal symmetry plain of the pipe models were also similar to those of the models used in Chapter 3.

### 4.3.3 Screening Study

From the discussion in Section 4.3.1, realistic limits were selected for the ranges of non-dimensional parameters. Since some of the factors might have non-linear effects on the response function, three discrete values of interest were selected for each parameter. These values set the framework for the parametric study's experimental design. Specifically, the selected factor levels are

$$\pi_1 = \frac{\sigma_{y(T)}}{E} : \quad 0.00266, 0.00333 \text{ and } 0.00399$$

$$\pi_2 = \frac{PL_L}{\sigma_{y(T)}} : \quad 0.4, 0.5 \text{ and } 0.6$$

$$\pi_3 = \gamma : \quad 350, 550 \text{ and } 750$$

$$\pi_4 = \frac{E_{sh}}{E} : \quad 0.0067, 0.0133 \text{ and } 0.020$$

$$\pi_5 = \frac{D}{t} : \quad 50, 70 \text{ and } 90$$

$$\pi_6 = \frac{\sigma_h}{\sigma_{y(T)}} : \quad 0.0\%, 40.0\% \text{ and } 80.0\%$$

$$\pi_7 = \frac{H_{\max}}{D} : \quad 0.05\%, 0.25\% \text{ and } 0.50\%.$$

Before doing a thorough parametric study, it is advisable to perform an experiment at a small number of design points in order to gain a basic understanding of the system. Having seven parameters with three different levels,  $3^7$  (i.e., 2187) combinations were possible. Since it was not practical to do all 2187 analyses for this parametric study, a preliminary study, a *screening study*,

was carried out on the parameters involved in the response function. The goal of the screening study was to obtain insight into the shape of the response surface. The screening study could reduce the number of parameters and their assigned levels, which would eventually reduce the study's complexity and expense.

Fifteen finite element models were used with the factor levels based on the classical *one-factor-at-a-time* method of experimental design. In this method, each factor varies through all of its levels while all other factors remain constant (see, Box et al., 1978). The relevance of this approach is limited to those instances in which the variables act additively, but it provides a useful first estimate of the behaviour. Table 4-2 shows the parameters used in the finite element analyses of the screening study employing the *one-factor-at-a-time* method. These models are named based on the value of their eight variables. The eighth model in this table is 0.00333-0.5-550-0.0133-70-0.4-0.0025, which is the base model in the screening study. This model has intermediate values of all non-dimensional variables:  $\sigma_{y(T)}/E=0.00333$ ,  $PL_L/\sigma_{y(T)}=0.5$ ,  $\gamma=550$ ,  $E_{sl}/E=0.013$ ,  $D/t=70$ ,  $\sigma_H/\sigma_{y(T)}=40\%$ , and  $H_{max}/D=0.25\%$ .

In statistical terminology, such an experiment is known as the *design centre point*, because all factors are set at the intermediary values. Varying only one  $\pi$ -parameter at a time in the base model forms the other models. If these models are sorted based on their names, the design centre point will be placed in the middle of models' list. As shown in Table 4-2, the first model has variables similar to those in the design centre point, except the first non-dimensional variable, which is the minimum value for the first parameter. In the second model, the second  $\pi$ -parameter is set at the minimum assigned value. This pattern continues to the centre model. After the centre model, the change of the variables to the maximum assigned value moves back from the last  $\pi$ -parameter in the ninth model to the first  $\pi$ -parameter in the 15<sup>th</sup> model.

Models 5 to 7 and 9 to 11 reflect the changes in geometry, internal pressure, and imperfections, while having similar material properties as the design centre point. Models 1 to 4 and models 12 to 15 in Table 4-2 reflect the changes in the material properties. Figure 4-2 to Figure 4-5 show all material stress-strain curves for finite element models used in the screening study. There are three curves in each of these figures; the middle curve has the intermediary values of all four material variables. This curve belongs to models 5 to 11. The other two curves in each figure have a maximum and minimum value of each non-dimensional material variable, one at a time. Material models with maximum and minimum value of  $\sigma_{y(T)}/E$ ,  $PL_L/\sigma_{y(T)}$ ,  $\gamma$  and  $E_{sh}/E$  are illustrated in Figure 4-2 to Figure 4-5, respectively.

#### **4.3.3.1 Results and Discussion of Screening Study**

Results of the 15 finite element analyses of the screening study are depicted as plots of the global bending moment versus the *2D* average compressive stress in Figure 4-6 to Figure 4-12. These figures show the mechanism by which each parameter affects the CBS. In each figure, there are three graphs showing the variation of the bending response of pipe specimens by changing one of the non-dimensional variables. For example, Figure 4-6 shows the variation of the bending response with respect to the first non-dimensional variable,  $\sigma_{y(T)}/E$ . The results depicted in this figure belong to the models with minimum, intermediate, and the maximum values of  $\sigma_{y(T)}/E$ , while all other non-dimensional variables are set to their intermediate levels. As the design centre point has the intermediate value for all the non-dimensional parameters, its results appear in all seven figures, whereas its corresponding curve is located between the other two. For ease of comparison, Figure 4-6 through Figure 4-12 are all plotted to the same scale (except Figure 4-10, in which the moment capacity significantly increases by increasing the wall thickness of the pipe specimen).

Table 4-3 shows the compressive 2D strains corresponding to the maximum global moments (i.e., CBS) for each case in the screening study. Figure 4-13 through Figure 4-19 show the variation of the CBS with respect to each non-dimensional variable. Each graph shows the CBS of the *design centre point* along with the CBS corresponding to the extreme values of the particular variable under consideration. By observing the results of each analysis with respect to the design centre point, the significance and influence pattern of each factor can be assessed.

In order to assess the level of non-linearity of the response function to each variable, linear regression lines, as well as the corresponding  $R^2$  factors, are shown in each graph. In general,  $R^2$  factor ranges between 0.0 (indicating no correlation between the two variables under consideration) and 1.0 (indicating a complete linear relationship between the two variables under consideration). As shown in Figure 4-13 through Figure 4-19, the minimum value of  $R^2$  among all variables is 0.78, and six variables have an  $R^2$  greater than 0.9. High values of  $R^2$  among the considered variables verify the affecting parameters' selection process.

$R^2$  values close to 1.0 indicate an almost linear relationship between the response function and the variable under consideration. In other words, in these cases, the rate of variation of the response function is uniform throughout the variation range.

For other variables that have non-linear effects on the buckling response, the CBS rate is not uniform throughout their variation range. For example, for  $\pi_6$  with  $R^2$  factor equal to 0.78, the increase in the CBS due to the internal pressure does not show a uniform rate; as shown in Figure 4-18, the intermediate values of the hoop stress to the transverse yield stress ratio do not considerably improve the pipes' buckling resistance, but higher internal pressures increase the CBS significantly. This phenomenon can be visually verified in Figure 4-11, showing that the specimen with highest  $\sigma_h/\sigma_{y(T)}$  starts to yield under a relatively lower moment, but

it can continue a stable response to a considerably long plateau. This shows that the stabilizing effect due to the internal pressure is more significant when the internal pressure is higher.

Three variables had  $R^2$  factors greater than 0.95 (i.e.  $\pi_2$ ,  $\pi_3$ , and  $\pi_4$ ) which indicates a linear relationship between the CBS and the variables under the screening study conditions. Generally, when there is a linear relationship between the response and input variables, it is possible to reduce parameters' variation levels from three to two. Reducing the variation level could be quite advantageous since it significantly reduces the number of required analyses in the parametric study. But this reduction required careful consideration of the phenomenon being studied, because the linear responses of the CBS to  $\pi_2$ ,  $\pi_3$ , and  $\pi_4$  in the screening study were under the same condition that all the other non-dimensional parameters were at their intermediary values.

As discussed in Chapter 3, the level of internal pressure affects the stress level at which the material starts to yield under longitudinal compression. This stress level is lower in pressurized pipes compared to unpressurized pipes. This early yield in the pipe compression side changes the stiffness and eventually affects the CBS (this is not the only effect of the internal pressure; it also changes the buckling response to a higher mode).

The internal pressure in the models with different values of  $\pi_2$  and  $\pi_3$  is set to the intermediary level (i.e., 40.0% pressure). The CBS's response pattern to these variables might be different when the internal pressure changes. Therefore, it is irrational to extend the linear relationship between the CBS and the variables related to the pipe material's longitudinal yield region (i.e.,  $\pi_2$ ,  $\pi_3$ ) to the whole region of interest. Based on this discussion, three levels of variation are reserved for  $\pi_2$ ,  $\pi_3$ .

For  $\pi_2$ , however, the intermediary value was eliminated from the parametric study and only the lower and upper limits were considered. This elimination reduced the number of required analyses from  $3^7$  to  $3^6 \times 2$ .

#### **4.3.3.2 Combining $PL_L/\sigma_{y(T)}$ and $\gamma$ into the Longitudinal to Transverse Yield Stress Ratio, $\sigma_{y(L)}/\sigma_{y(T)}$**

Four out of seven non-dimensional variables in the screening study are material variables. As discussed before, in the combined hardening model, the elastic response and strain hardening response are similar in both longitudinal and transverse directions. The difference between material behaviour appears in the yielding region. This region is relatively small in the transverse direction compared to the longitudinal direction, where it is rather large and curvilinear. The second and third material variables,  $\pi_2$  and  $\pi_3$ , define the yield region in the longitudinal direction as well as the level of anisotropy.

In generating the non-dimensional parameters, it is better to define variables that are more common in the pipeline industry. The first and fourth material variables consist of common parameters in the pipeline industry (i.e., the modulus of elasticity, transverse yield stress, and strain hardening modulus). On the other hand, the longitudinal proportional limit and  $\gamma$  that appear in  $\pi_2$  and  $\pi_3$  are not common industrial values.

As the longitudinal yield region is dependent on both  $PL_L/\sigma_{y(T)}$  and  $\gamma$ , the longitudinal yield stress is also a function of these two parameters. It would be beneficial to combine  $PL_L/\sigma_{y(T)}$  and  $\gamma$  into a single non-dimensional variable that includes the longitudinal yield stress. This combination would not only replace less (industrially) familiar parameters (i.e.  $PL_L$  and  $\gamma$ ) with a more common industrial parameter,  $\sigma_{y(L)}$ , it also would reduce the number of variables from seven to six. As the new variable should also be non-dimensional, the longitudinal yield stress ought to be divided by a material parameter with a similar dimension.

The best option for this purpose is the transverse yield stress, as the resulting non-dimensional variable will be  $\sigma_{y(L)}/\sigma_{y(T)}$ . This new non-dimensional parameter is a good indicator of the material anisotropy which is the major interest point of this study.

The results of the screening study depicted in Figure 4-7 and Figure 4-8 also show that when  $\pi_2$  and  $\pi_3$  vary individually in their assigned range, the magnitude of the CBS variation is not as large as that in other variables. Therefore, since they both have an inverse relationship with the CBS, combining these parameters into one parameter magnifies the effects of anisotropy on the CBS to a level comparable to that of the other affecting parameters.

The  $PL_L/\sigma_{y(T)}$  ratio ranged between 0.4 and 0.6, and  $\gamma$  ranged between 350 and 550 in the parametric study. In order to see the relationship between  $\sigma_{y(L)}/\sigma_{y(T)}$  and the CBS, a process similar to the screening study was repeated. In this process  $\pi_1$ ,  $\pi_4$ ,  $\pi_5$ ,  $\pi_6$ , and  $\pi_7$  were set to their intermediate assigned values. Then, different values within the variation ranges of  $\pi_2$  and  $\pi_3$  were considered for these two parameters to form different combinations of  $PL_L/\sigma_{y(T)}$  and  $\gamma$  (which define different values for  $\sigma_{y(L)}/\sigma_{y(T)}$ ). Since  $\pi_1$  and  $\pi_4$  were fixed to the intermediate values, the variation of  $\sigma_{y(L)}/\sigma_{y(T)}$  was only a function of the variation in  $\pi_2$  and  $\pi_3$ . Five levels were considered for  $PL_L/\sigma_{y(T)}$  and  $\gamma$  in their corresponding variation ranges with uniform distribution. Each combination of  $PL_L/\sigma_{y(T)}$  and  $\gamma$  values resulted in a unique value of  $\sigma_{y(L)}/\sigma_{y(T)}$ . Table 4-4 shows the variation matrix of  $PL_L/\sigma_{y(T)}$  and  $\gamma$  and the corresponding ratio of  $\sigma_{y(L)}/\sigma_{y(T)}$ . Figure 4-20 shows the considered distribution of  $PL_L/\sigma_{y(T)}$  and  $\gamma$  as well as the distribution of these two variables in the available material database introduced in Chapter 2. In this figure, the assumed combinations of  $PL_L/\sigma_{y(T)}$  and  $\gamma$  are shown with dark dots, and the distribution of these parameters in the available database in Chapter 2 are shown in crosses. As this figure shows, no noticeable pattern existed in the distribution of  $(PL_L/\sigma_{y(T)}, \gamma)$  pairs.

Table 4-4 shows 25 combinations of  $PL_L/\sigma_{y(T)}$  and  $\gamma$ , and essentially 25 values of  $\sigma_{y(L)}/\sigma_{y(T)}$ . Twenty-five finite element models were built, each with one combination of  $\pi_2$  and  $\pi_3$  depicted in Table 4-4. Figure 4-21 shows all stress-strain curves for 25 material properties used in these finite element models. In these curves, the modulus of elasticity, transverse yield stress, and strain hardening modulus were set at 207000MPa, 690MPa, and 2760MPa, respectively. The longitudinal proportional limit and  $\gamma$  for each curve come from one out of 25 combinations shown in Table 4-4. As the transverse yield stress was 690MPa, the stress-strain curves in Figure 4-21 fall in five categories with five different values of  $PL_L$ : 276, 311, 345, 380, and 414. Within each category of constant  $PL_L$ , the kinematic hardening parameter,  $\gamma$ , has five different values of 350, 450, 550, 650, and 750.

Since  $PL_L/\sigma_{y(T)}$  and  $\gamma$  were combined into  $\sigma_{y(L)}/\sigma_{y(T)}$ , the only variation in these 25 finite element models was driven from variations in  $\sigma_{y(L)}/\sigma_{y(T)}$ . These models were analyzed and the corresponding CBS values are extracted from the buckling analyses. Figure 4-22 shows the variation of the CBS versus  $\sigma_{y(L)}/\sigma_{y(T)}$  as well as the corresponding regression line. The  $R^2$  factor of the linear regression is 0.96, indicating that the relationship between the CBS and the longitudinal-to-transverse yield stress is almost linear in the assumed domain of the affecting variables in the screening study. Nevertheless, as discussed in the previous section, it was not rational to extend this linear response to the parametric study's entire domain.

Both  $PL_L/\sigma_{y(T)}$  and  $\gamma$  have a direct effect on  $\sigma_{y(L)}/\sigma_{y(T)}$ ; therefore, the minimum value of  $PL_L/\sigma_{y(T)}$  and  $\gamma$  in their corresponding variation ranges was used to make the lower bound for  $\sigma_{y(L)}/\sigma_{y(T)}$ . In addition, the maximum value of  $PL_L/\sigma_{y(T)}$  and  $\gamma$  in their corresponding variation ranges made the upper bound for  $\sigma_{y(L)}/\sigma_{y(T)}$ . As Table 4-4 shows, using  $PL_L/\sigma_{y(T)}=0.4$  and  $\gamma=350$  results in  $\sigma_{y(L)}/\sigma_{y(T)}=0.71$ , and using  $PL_L/\sigma_{y(T)}=0.6$  and  $\gamma=750$  results in  $\sigma_{y(L)}/\sigma_{y(T)}=0.91$ . The assigned range of

variation for  $\sigma_{y(L)}/\sigma_{y(T)}$  between 0.71 and 0.91 covers the value of  $\sigma_{y(L)}/\sigma_{y(T)}$  in the available database; as in Chapter 2, the value of  $\sigma_{y(L)}/\sigma_{y(T)}$  ranges between 0.76 and 0.89.

Figure 4-23 shows the design centre point, and the longitudinal and transverse material stress-strain curves corresponding to the upper and lower bounds of  $\sigma_{y(L)}/\sigma_{y(T)}$ . The response in the transverse direction of these materials is exactly the same because the other material variables,  $\sigma_{y(T)}/E$  and  $E_{st}/E$  are the same.

Figure 4-24 shows the buckling analysis results of the models with maximum and minimum values of  $\sigma_{y(L)}/\sigma_{y(T)}$  in terms of the global moment versus the  $2D$  compressive strain in the buckling area. This figure also shows the results of the model with an intermediate value of  $\sigma_{y(L)}/\sigma_{y(T)}$  (i.e., the design centre point). As expected, higher values of  $\sigma_{y(L)}/\sigma_{y(T)}$  result in a lower CBS and vice versa. As apparent in this figure, even though the material anisotropy affects the CBS, it does not change the post-buckling response and all the curves with different levels of anisotropy rapidly converge after the onset of buckling and become identical in the post-buckling region.

Figure 4-25 shows the CBS from the design centre point along with the results of the assigned lower and upper levels of  $\sigma_{y(L)}/\sigma_{y(T)}$ . As was expected, the relationship between the CBS and the ratio of longitudinal to transverse yield stress is linear in this graph.

#### **4.3.4 Cases Analyzed**

The screening study showed that due to the linear response of the CBS and  $E_{st}/E$ , the number of variation levels assigned to this variable could be reduced to two levels (i.e., upper and lower limit of this parameter's variation). Furthermore, two material variables previously defined to address anisotropy (i.e.,  $PLI/\sigma_{y(T)}$  and  $\gamma$ )

were combined into another non-dimensional variable,  $\sigma_{y(L)}/\sigma_{y(T)}$ , to incorporate the effects of material anisotropy. Therefore, the number of non-dimensional variables was reduced to six.

Although, the screening study also showed that the relationship between the CBS and  $\sigma_{y(L)}/\sigma_{y(T)}$  was linear, it was decided to use three levels of variations for this parameter, as extending the linear response to the entire parametric study was not reasonable for this variable.

The updated non-dimensional variables (written with the capital  $\pi$  from the Greek alphabet) and their considered levels are as follow

$$\Pi_1 = \frac{\sigma_{y(T)}}{E} : \quad 0.00266, 0.00333 \text{ and } 0.00399$$

$$\Pi_2 = \frac{\sigma_{y(L)}}{\sigma_{y(T)}} : \quad 0.706, 0.836 \text{ and } 0.912$$

$$\Pi_3 = \frac{E_{sh}}{E} : \quad 0.0067 \text{ and } 0.02$$

$$\Pi_4 = \frac{D}{t} : \quad 50, 70 \text{ and } 90$$

$$\Pi_5 = \frac{\sigma_h}{\sigma_{y(T)}} : \quad 0.0\%, 40.0\% \text{ and } 80.0\%$$

$$\Pi_6 = \frac{H_{\max}}{D} : \quad 0.05\%, 0.25\% \text{ and } 0.50\%$$

Based on the above description, the parametric study was eventually performed on  $3^5 \times 2$  (i.e. 486) combinations of non-dimensional variables.

## 4.4 Results of the Parametric Study

The focus of this study was to see how the material anisotropy of HSS pipes changes their buckling response; therefore, the best way to illustrate the parametric study's results is to present them in series of graphs showing the CBS of HSS pipes with different degrees of material anisotropy. In graphs depicted in Figure 4-26 through Figure 4-52, the variation of the CBS is shown for HSS pipes with certain characteristics of all parameters (affecting the CBS) but with different ratios of  $\sigma_{y(L)}/\sigma_{y(T)}$  as an indicator of anisotropy. For each case, the average compressive strain in  $2D$  gauge length centered at the buckled zone was measured for each load increment during the analyses. The average compressive strain associated with the maximum moment carried by the pipe was reported as the CBS of that case.

These graphs also show how the alteration in anisotropic material properties changes HSS's buckling resistance with a specific  $D/t$  ratio, internal pressure, and initial imperfection. Each graph covers alterations in the material properties considered in the parametric study (i.e., material grade, strain hardening modulus, and the level of anisotropy). The following sections discuss the detailed effects of the material anisotropy on the buckling resistance of HSS pipes with different conditions.

Appendix A includes a complete list of input and output data.

### 4.4.1 Effects of Anisotropy on CBS of HSS Pipes with $D/t=50$

#### 4.4.1.1 Unpressurized HSS Pipes with $D/t=50$

The results of this group of HSS pipes are shown in Figure 4-26 to Figure 4-28 for three magnitudes of imperfections. Anisotropy's effects have an almost similar linear pattern in all pipes in this category. The CBS of HSS pipes made of all

three grades of steel linearly decreases when the  $\sigma_{y(L)}/\sigma_{y(T)}$  increases. In all of the above figures, the curves that belong to the steel material with lower strain hardening rates have slopes that are larger compared to those with higher strain hardening rates. For all three steel grades with low strain hardening rates, when the  $\sigma_{y(L)}/\sigma_{y(T)}$  changes from 0.706 to 0.912 the average and standard deviation of the CBS reductions are 23.6% and 2.1%, respectively. These values equal 11.6% and 2.8%, respectively, for steel grades with high strain hardening rates. In conclusion, the inverse association between the HSS pipes' material anisotropy and longitudinal compressive capacity becomes stronger for HSS materials in the group of lower strain hardening rates (i.e., lower  $\sigma_y/\sigma_u$ ).

Comparing these three figures, it is also apparent that although the responses of HSS pipes with different material properties become closer when the magnitude of initial imperfection increases, the response pattern belonging to each material property is independent of the initial imperfection magnitude.

#### **4.4.1.2 Moderately Pressurized HSS Pipes with $D/t=50$**

Figure 4-29 to Figure 4-31 show the results of this group of HSS pipes with different material properties and three magnitudes of initial imperfection. Similar to the first categories of HSS pipes, the CBS of these pipes has a linear and inverse association with  $\sigma_{y(L)}/\sigma_{y(T)}$ . Again, the magnitude of the initial imperfection has no effect on the pattern of anisotropy effects on the CBS but higher imperfection magnitudes reduce the CBS.

For all three steel grades with low strain hardening rates, the average and standard deviations of CBS reductions are 18.9% and 2.9%, respectively, when the  $\sigma_{y(L)}/\sigma_{y(T)}$  changes from 0.706 to 0.912. For the steel grades with high strain hardening rates, the same values are equal to 14.1% and 1.7%, respectively.

Another point from these results is that while the material grade has minor effects on the CBS of HSS pipes with low strain hardening, higher strain hardening rates accentuate the inverse association between the material grade and the CBS.

#### **4.4.1.3 Highly Pressurized HSS Pipes with $D/t=50$**

The results of highly pressurized HSS pipes with  $D/t=50$  are illustrated in Figure 4-32 to Figure 4-34. Regardless of the magnitude of the initial imperfection, the HSS pipes with similar material properties (steel grade and strain hardening rate) share analogous patterns of relationships between the CBS and the level of anisotropy. As these figures show, the effects of anisotropy on the CBS of highly pressurized HSS pipes is less consistent among different material properties compared to same HSS pipes with no or moderate internal pressure. While the  $\sigma_{y(L)}/\sigma_{y(T)}$  has no significant effect on the HSS pipes with low strain hardening rates, it shows little but inconsistent effects for HSS pipes with high strain hardening rates and different grades. In other words, when the  $\sigma_{y(L)}/\sigma_{y(T)}$  increases in pipes with high strain hardening rates, the CBS slightly decreases, doesn't change, and slightly increases for HSS pipes made of grades X80, X100, and X120, respectively.

For all three steel grades with low strain hardening rates, the average variation in the CBS equals 7.7% with a standard deviation of 1.1%, when the  $\sigma_{y(L)}/\sigma_{y(T)}$  changes from 0.706 to 0.912. For steel grades with high strain hardening rates, the average and standard deviations of the CBS changes are 1.9% and 5.3%, respectively.

Chapter 5 shows that the buckling resistance of highly pressurized pipes is mostly dominated by the tensile material response in the transverse direction. Here, the variation of material anisotropy was defined by the variation of the material's longitudinal behaviour, while the material response in the transverse direction was fixed. As a result, since the changes in anisotropy came from the changes in the

longitudinal response, there was no major effect on either the moment-curvature or the moment-compressive strain responses.

#### **4.4.2 Effects of Anisotropy on the CBS of HSS Pipes with $D/t=70$**

##### **4.4.2.1 Unpressurized HSS Pipes with $D/t=70$**

The results of this group of HSS pipes for three magnitudes of imperfections are shown in Figure 4-35 to Figure 4-37. The effects of anisotropy on the CBS has a similar linear pattern among all pipes in this category; i.e., the CBS of HSS pipes made of all three steel grades decreases linearly when the  $\sigma_{y(L)}/\sigma_{y(T)}$  increases.

In the above figures, the slope of the curves belonging to the steel materials with lower strain hardening rates is similar to the slope of HSS materials with higher strain hardening rates (unlike the unpressurized pipes with  $D/t=50$ ). For all three steel grades with low strain hardening rates, the average and standard deviation of CBS reductions are 25.9% and 1.7%, respectively, when the  $\sigma_{y(L)}/\sigma_{y(T)}$  changes from 0.706 to 0.912. For steel grades with high strain hardening rates, these values equal to 20.8% and 2.3%, respectively.

Similar to other cases, the observed response pattern of each material property is independent of the initial imperfection magnitude. Nevertheless, when the magnitude of initial imperfection increases, the CBS decreases and the responses of the HSS pipe with different material properties become closer. This means that an increase in the initial imperfections magnitude decreases the effects of the material grade.

##### **4.4.2.2 Moderately Pressurized HSS Pipes with $D/t=70$**

Figure 4-38 to Figure 4-40 show the results of this group of HSS pipes with different material properties and three magnitudes of initial imperfection. The

result of this category of HSS pipes is very similar to the same pipes with  $D/t=50$ ; i.e. the CBS has a linear and inverse association with  $\sigma_{y(L)}/\sigma_{y(T)}$ . Comparing these figures, the magnitude of the initial imperfection has no effect on the pattern of anisotropy effects on the CBS; however, a higher imperfection magnitude reduces the CBS.

For all three steel grades with low strain hardening rates, when the  $\sigma_{y(L)}/\sigma_{y(T)}$  changes from 0.706 to 0.912, there is a reduction in the CBS with an average and standard deviation of 23.1% and 3.3%, respectively. Similar values equal 16.4% and 2.1%, respectively, for steel grades with high strain hardening rates.

The material grade has minor effects on the CBS of HSS pipes with low strain hardening; however, higher strain hardening rates intensify the inverse relationship of material grade and the CBS.

#### **4.4.2.3 Highly Pressurized HSS Pipes with $D/t=70$**

The results of highly pressurized HSS pipes with  $D/t=70$  are illustrated in Figure 4-41 to Figure 4-43. Similar to the results of highly pressurized HSS pipes with  $D/t=50$ , the effects of  $\sigma_{y(L)}/\sigma_{y(T)}$  on the CBS of highly pressurized HSS pipes is less significant (and less consistent) compared to same HSS pipes with no or moderate internal pressure. It can be said that, in general, the material anisotropy has no significant effect on this category of pipes.

For all three steel grades with low strain hardening rates, the average and standard deviations of CBS variations are 5.5% and 4.7%, respectively, with an increase in the  $\sigma_{y(L)}/\sigma_{y(T)}$  from 0.706 to 0.912. For steel grades with high strain hardening rates, the average and standard deviations of CBS variations are 0.8% and 3.7%, respectively.

### 4.4.3 Effects of Anisotropy on CBS of HSS Pipes with $D/t=90$

#### 4.4.3.1 Unpressurized HSS Pipes with $D/t=90$

The results of this group of HSS pipes are shown in Figure 4-44 to Figure 4-46 for three magnitudes of imperfections. The effects of material anisotropy on the CBS follow a similar pattern in all pipes of this category. The CBS of HSS pipes made of all three grades of steel decreases linearly when the  $\sigma_{y(L)}/\sigma_{y(T)}$  increases, although the linearity seems to be weaker compared to HSS pipes with  $D/t=70$  and  $D/t=50$ .

In above figures, the slope of the curves belonging to the steel material with lower strain hardening rates is similar to the curves of HSS materials with higher strain hardening rates. The average and standard deviations of CBS reductions are 23.1% and 1.4%, respectively for steel grades with low strain hardening rates; and 22.4% and 1.2%, respectively, for steel grades with high strain hardening rates when the  $\sigma_{y(L)}/\sigma_{y(T)}$  changes from 0.706 to 0.912.

These figures also show that the material grade has a very limited effect on the CBS (the response curves of pipes with different material properties bound together).

In this category of HSS pipes, the initial imperfection magnitude not only changes the CBS value, but also (unlike other cases with  $D/t=70$  and  $D/t=50$ ) slightly changes each material property's response pattern. The reason behind this phenomenon could be the susceptibility of the buckling response to the pipe's geometry (including initial imperfection) due to the high  $D/t$  ratio. Therefore, different magnitudes of imperfections might have more significant effects on the buckling response and thus change the pattern in the relationship between the anisotropy and the CBS.

#### 4.4.3.2 Moderately Pressurized HSS Pipes with $D/t=90$

Figure 4-47 to Figure 4-49 show the results of this group of HSS pipes with different material properties and three magnitudes of initial imperfection. The relationship between the CBS and the material anisotropy of this category is still analogous to the same HSS pipes with  $D/t=50$  and  $D/t=70$ , though the linearity in the pattern is somehow weaker.

For all three steel grades with low strain hardening rates, the average and standard deviation of the CBS reduction are 23.5% and 5.5%, respectively, when the  $\sigma_{y(L)}/\sigma_{y(T)}$  changes from 0.706 to 0.912. For steel grades with high strain hardening rates, the average and standard deviations of the CBS reduction are 23.4% and 2.7%, respectively.

Similar to the unpressurized HSS pipes with  $D/t=90$ , the susceptibility to initial imperfections somehow disturbs the consistency between the association patterns of material anisotropy and buckling resistance.

#### 4.4.3.3 Highly Pressurized HSS Pipes with $D/t=90$

The results of highly pressurized HSS pipes with  $D/t=90$  are illustrated in Figure 4-50 to Figure 4-52. Similar to the other groups of highly pressurized HSS pipes, the effects of  $\sigma_{y(L)}/\sigma_{y(T)}$  on the CBS of this group is less significant compared to same HSS pipes with no or moderate internal pressures.

Increasing  $\sigma_{y(L)}/\sigma_{y(T)}$  from 0.706 to 0.912, the average and standard deviations of the CBS reduction are 2.7% and 4.8% for steel grades with low hardening ratios, and 2.3% and 2.0% for steel grades with high strain hardening rates, respectively.

Based on the results of all highly pressurized pipes, it is quite evident that the  $\sigma_{y(L)}/\sigma_{y(T)}$  has no significant effect on highly pressurized pipes. Chapter 5 investigates this phenomenon in more detail.

## 4.5 Summary

In this chapter, a parametric study presents the effects of six non-dimensional parameters (including material anisotropy) on the CBS of HSS pipes. These parameters include diameter to thickness ratio, internal pressure, initial imperfection's magnitude, material grade, strain hardening rate, and material anisotropy. Finite element models with different values of  $D/t$ ,  $\sigma_h/\sigma_{y(T)}$ ,  $H_{\max}/D$ ,  $\sigma_{y(T)}/E$ ,  $E_{sh}/E$ , and  $\sigma_{y(L)}/\sigma_{y(T)}$  were developed and analyzed to calculate the CBS.

The results of this parametric study not only provide a complete picture of the buckling mechanism of HSS pipes, they also show the interactive effects of these parameters on the CBS. Therefore, these results can be used to investigate how material anisotropy changes the buckling response in different conditions.

One parameter's pattern of effects on the HSS pipes' buckling response might change as a result of the magnitude of other parameters. For example, the effects of the material grade and strain hardening rate on the pipes' buckling resistance become more significant when magnitude of the initial imperfection is lower.

Likewise, based on the parametric study results, the significance of anisotropy effects on the CBS is different from one case to another. Internal pressure significantly influences the effect pattern of anisotropy on the CBS. While there is a strong association between the CBS and the material anisotropy among unpressurized and moderately pressurized pipes, this association is quite weak in the case of pressurized pipes. The average correlation factor ( $R$ ) between the CBS and the  $\sigma_{y(L)}/\sigma_{y(T)}$  ratio is 99.7% and 99.7% among all cases of unpressurized and moderately pressurized pipes. For the variation range of  $\sigma_{y(L)}/\sigma_{y(T)}$ , considered in the parametric study, the average change in the CBS is 21.2% and 19.9%, respectively, with a 5.0% standard deviation in both of the above cases. In pressurized pipes, however, the correlation factor between the CBS and the  $\sigma_{y(L)}/\sigma_{y(T)}$  ratio is 26.0% among all cases of highly pressurized pipes. For the

variation range of  $\sigma_{y(L)}/\sigma_{y(T)}$ , considered in the parametric study, the average change in the CBS is 1.9% with a 5.3% standard deviation.

## References

Box G.R.P., Hunter W.G. and Hunter J.S., (1978), "Statistics for Experimenters", John Wiley and Sons, New York, New York.

Canadian Standard Association, (2007), "Z662-07 Oil and Gas Pipeline Systems", Canadian Standard Association, Etobicoke, Ontario.

DiBatista J.D., Cheng J.J.R. and Murray D.W., (2000), "Behaviour of Sleeper Supported Line Pipe", Structural Engineering Report No. 230, Department of Civil and Environmental Engineering, University of Alberta, Edmonton, Alberta, 213 pages.

Dorey A.B., Cheng J.J.R. and Murray D.W., (2001), "Critical Buckling Strain in Energy Pipelines", Structural Engineering Report No. 237, Department of Civil and Environmental Engineering, University of Alberta, Edmonton, Alberta, 346 pages.

Langhaar H.L., (1951), "Dimensional Analysis and Theory of Models", John Wiley and Sons, New York, New York.

Shitamoto H., Hamada M., Okaguchi S., Takahashi N. and Takeuchi I., (2010), "Evaluation of Compressive Strain Limit Of X80 Saw Pipes with Girth Welding By FE Analysis", Proceeding of the International Pipeline Conference, American Society of Mechanical Engineers, Calgary, Alberta, v4, pp 213-219.

Taylor E.S., (1974), "Dimensional Analysis for Engineers", Oxford University Press, London, UK.

## Tables

Table 4-1 Distribution of non-dimensional material variables in the available (HSS pipe) material database

Material Type	$\sigma_{y(T)}/E$	$PL_L/\sigma_{y(T)}$	$\gamma$	$E_{st}/\sigma_{y(T)}$
A	0.00296	0.460	394	0.0135
B	0.00337	0.576	709	0.0078
C	0.00307	0.440	421	0.0123
D	0.00441	0.477	465	0.0141
E	0.00398	0.450	479	0.0142
F	0.00390	0.466	581	0.0102
H	0.00402	0.495	582	0.0117
G	0.00380	0.488	522	0.0142
Minimum	0.00296	0.440	394	0.0078
Average	0.00369	0.481	519	0.0123
Maximum	0.00441	0.576	709	0.0142

Table 4-2 Parameters' values used in the finite element models of the screening study

Item	Model Name	$\sigma_{y(T)}/E$	$PL_L/\sigma_{y(T)}$	$\gamma$	$E_{st}/E$	$D/t$	$\sigma_t/\sigma_{y(T)}$	$H/D$
1	0.00267-0.5-550-0.01333-70-0.4-.0025	0.00226	0.5	550	0.0133	70	0.4	0.25%
2	0.00333-0.4-550-0.01333-70-0.4-.0025	0.00333	0.4	550	0.0133	70	0.4	0.25%
3	0.00333-0.5-350-0.01333-70-0.4-.0025	0.00333	0.5	350	0.0133	70	0.4	0.25%
4	0.00333-0.5-550-0.00667-70-0.4-.0025	0.00333	0.5	550	0.0067	70	0.4	0.25%
5	0.00333-0.5-550-0.01333-50-0.4-.0025	0.00333	0.5	550	0.0133	50	0.4	0.25%
6	0.00333-0.5-550-0.01333-70-0.0-.0025	0.00333	0.5	550	0.0133	70	0.0	0.25%
7	0.00333-0.5-550-0.01333-70-0.4-.0005	0.00333	0.5	550	0.0133	70	0.4	0.05%
8	0.00333-0.5-550-0.01333-70-0.4-.0025	0.00333	0.5	550	0.0133	70	0.4	0.25%
9	0.00333-0.5-550-0.01333-70-0.4-.0050	0.00333	0.5	550	0.0133	70	0.4	0.50%
10	0.00333-0.5-550-0.01333-70-0.8-.0025	0.00333	0.5	550	0.0133	70	0.8	0.25%
11	0.00333-0.5-550-0.01333-90-0.4-.0025	0.00333	0.5	550	0.0133	90	0.4	0.25%
12	0.00333-0.5-550-0.02000-70-0.4-.0025	0.00333	0.5	550	0.0200	70	0.4	0.25%
13	0.00333-0.5-750-0.01333-70-0.4-.0025	0.00333	0.5	750	0.0133	70	0.4	0.25%
14	0.00333-0.6-550-0.01333-70-0.4-.0025	0.00333	0.6	550	0.0133	70	0.4	0.25%
15	0.00399-0.5-550-0.01333-70-0.4-.0025	0.00399	0.5	550	0.0133	70	0.4	0.25%

Table 4-3 CBS corresponding to different levels of each variable in the screening study

$\pi$ Parameter	Lower Limit	Intermediate Value	Upper Limit
$\sigma_{y(T)}/E$	-0.96%	-0.85%	-0.81%
$PL_L/\sigma_{y(T)}$	-0.87%		-0.80%
$\gamma$	-0.90%		-0.82%
$E_{sh}/\sigma_{y(T)}$	-0.71%		-1.05%
$D/t$	-1.49%		-0.60%
$\sigma_H/\sigma_{y(T)}$	-0.83%		-1.34%
$H_{max}/D$	-1.02%		-0.77%

Table 4-4 Combination matrix of  $PL_L/\sigma_{y(T)}$  and  $\gamma$  and the resultant  $\sigma_{y(L)}/\sigma_{y(T)}$  ratio

	$\gamma=350$	$\gamma=450$	$\gamma=550$	$\gamma=650$	$\gamma=750$
$PL_L/\sigma_{y(T)}=0.40$	0.71	0.76	0.80	0.84	0.87
$PL_L/\sigma_{y(T)}=0.45$	0.73	0.78	0.82	0.85	0.88
$PL_L/\sigma_{y(T)}=0.50$	0.76	0.80	0.84	0.87	0.89
$PL_L/\sigma_{y(T)}=0.55$	0.78	0.82	0.85	0.88	0.90
$PL_L/\sigma_{y(T)}=0.60$	0.81	0.84	0.87	0.89	0.91

## Figures

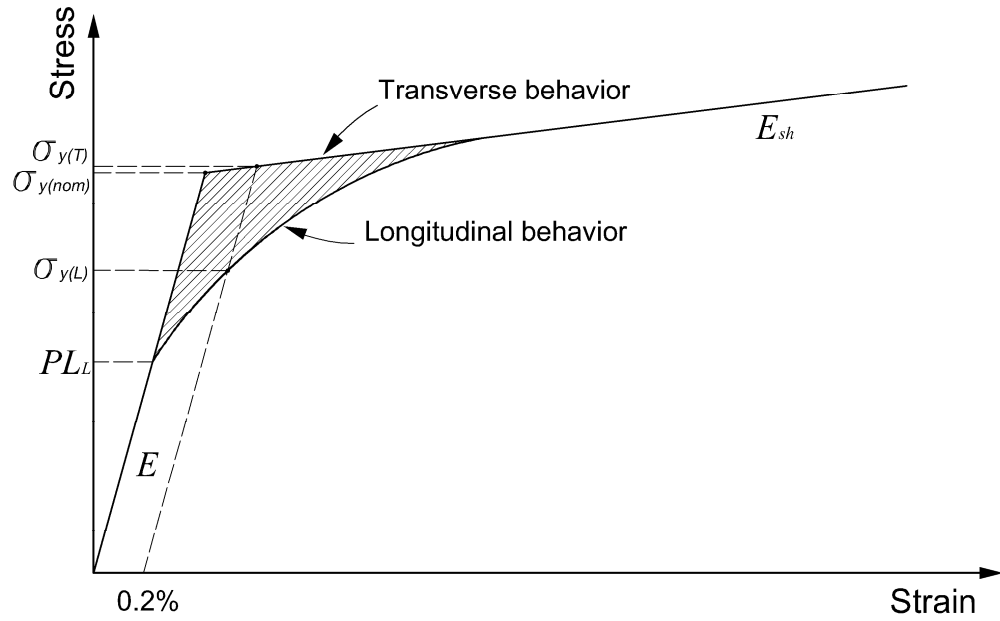


Figure 4-1 General format of longitudinal and transverse material (tension) responses of the proposed combined hardening model

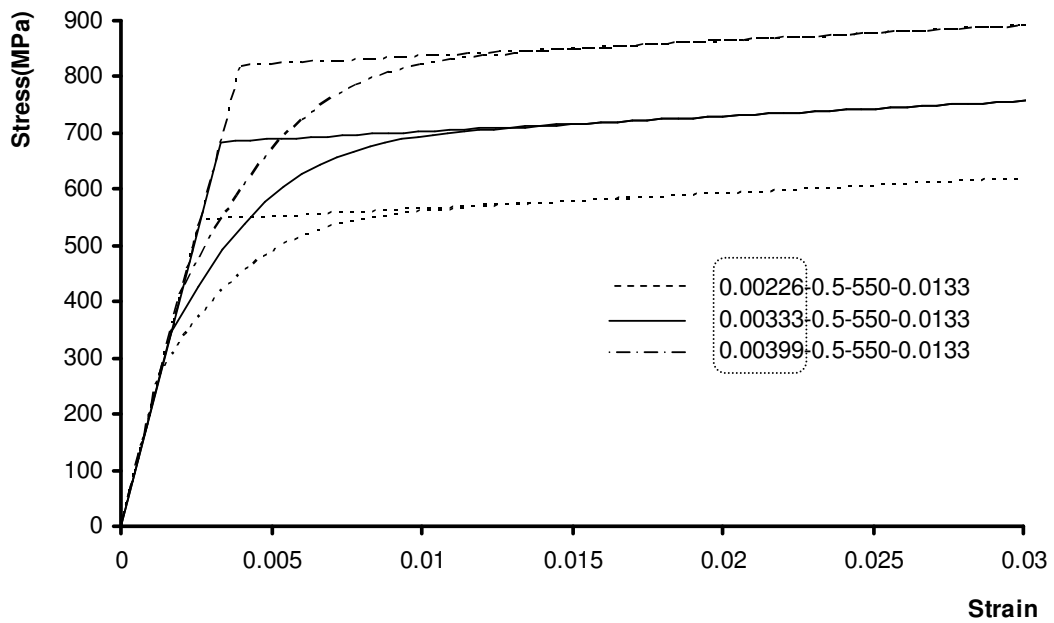


Figure 4-2 Different levels of  $\sigma_{y(T)}/E$  considered for the screening study

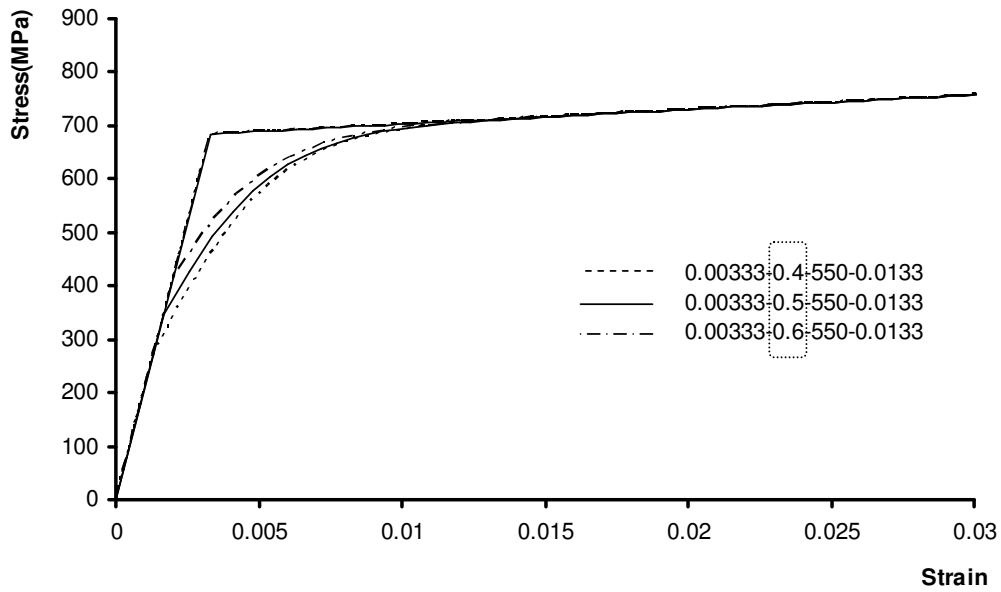


Figure 4-3 Different levels of  $PL_L/\sigma_{y(T)}$  considered for the screening study

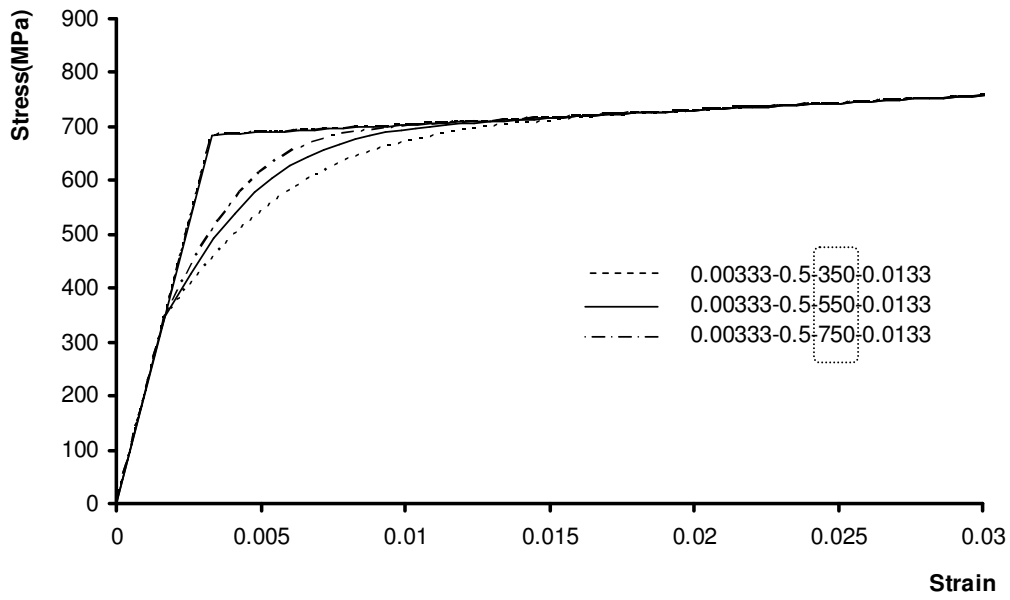


Figure 4-4 Different levels of  $\gamma$  considered for the screening study

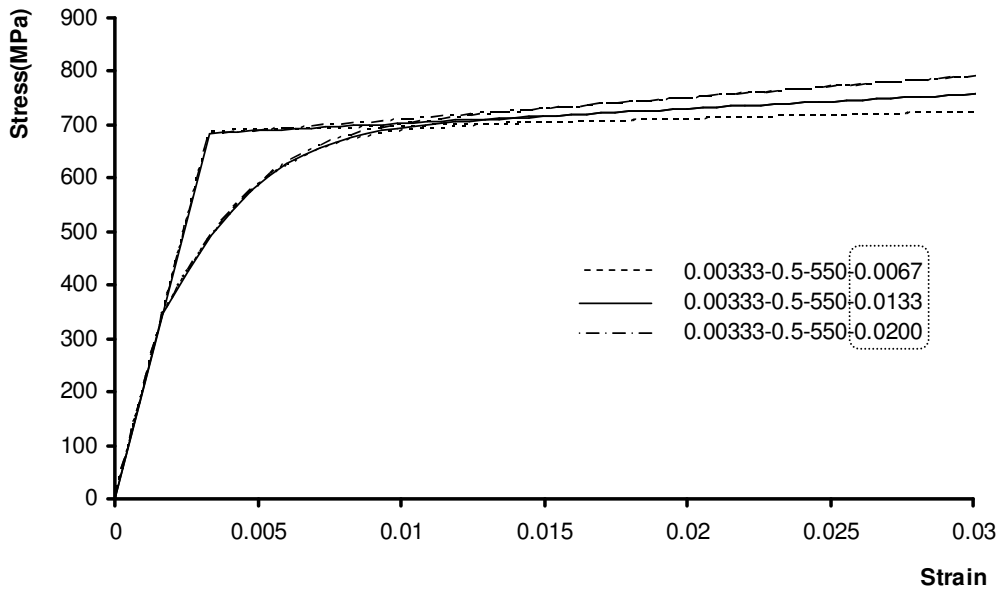


Figure 4-5 Different levels of  $E_{st}/E$  considered for the screening study

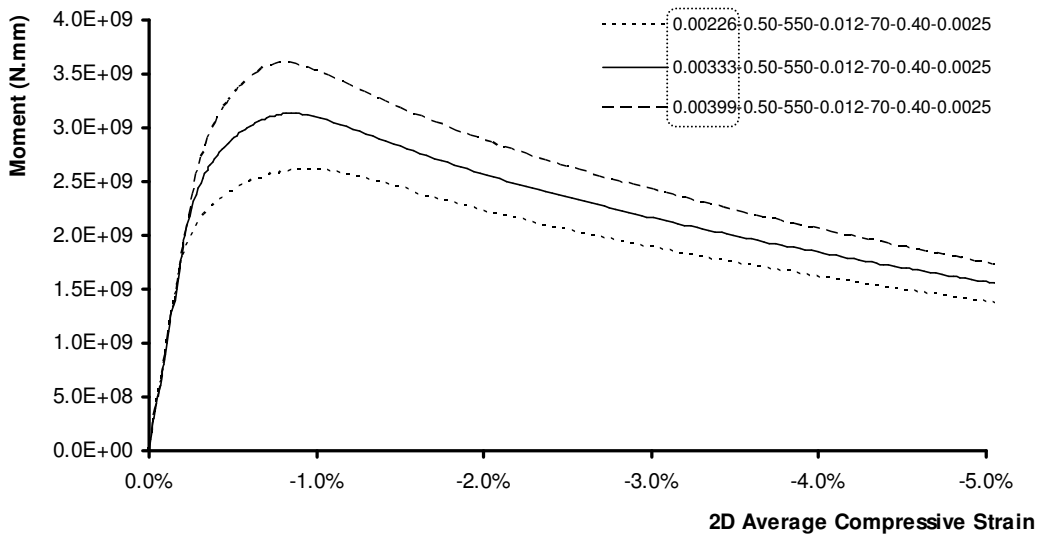


Figure 4-6 Effects of  $\sigma_{y(T)}/E$  on the buckling response of the finite element used in the screening study

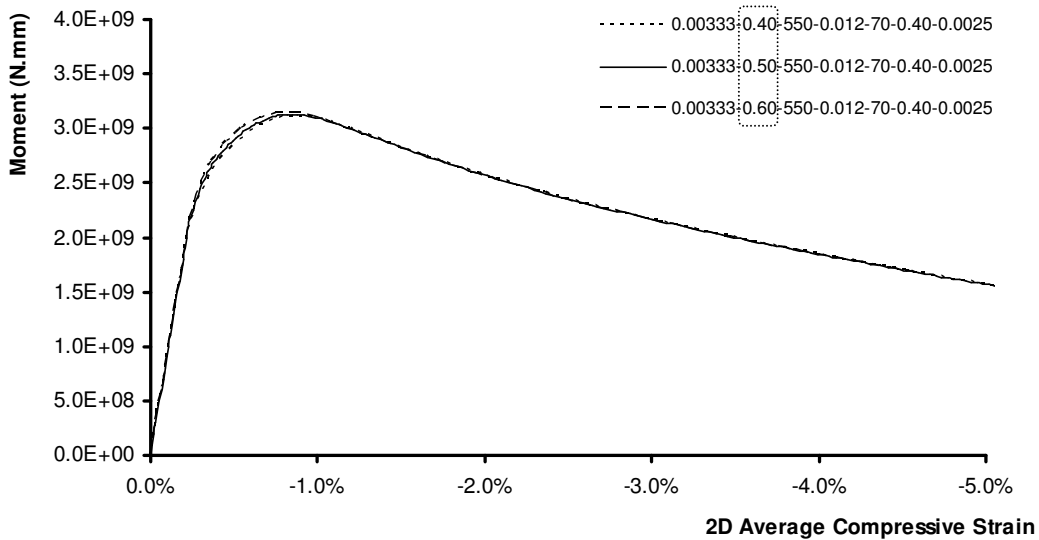


Figure 4-7 Effects of  $PL_I/\sigma_{y(T)}$  on the buckling response of the finite element used in the screening study

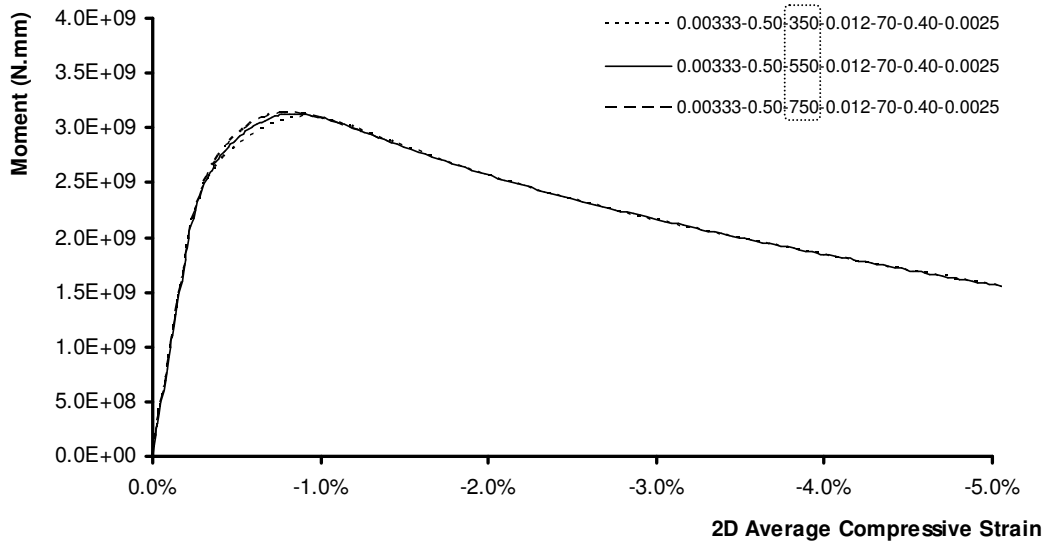


Figure 4-8 Effects of  $\gamma$  on the buckling response of the finite element used in the screening study

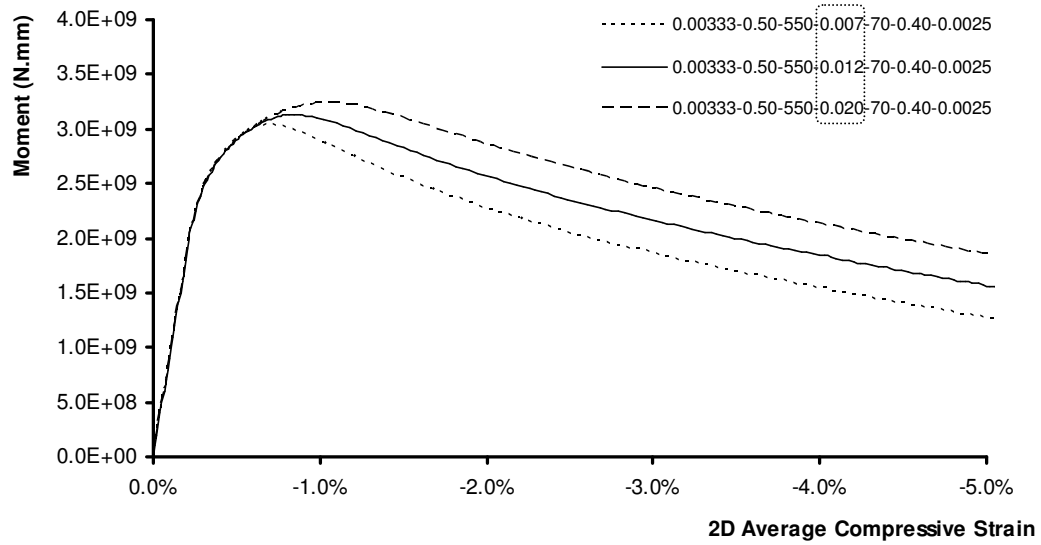


Figure 4-9 Effects of  $E_{sh}/E$  on the buckling response of the finite element used in the screening study

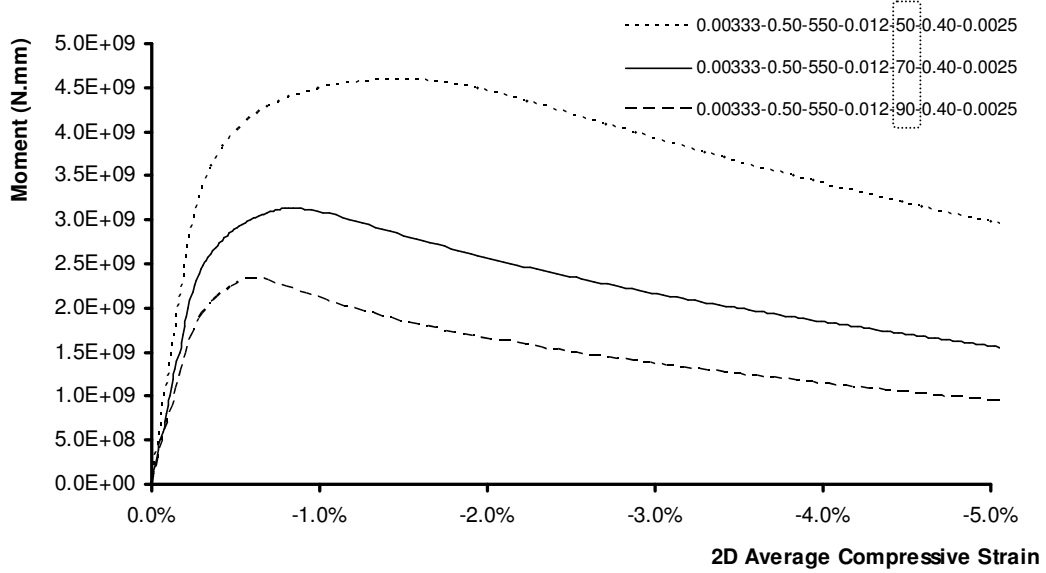


Figure 4-10 Effects of  $D/t$  on the buckling response of the finite element used in the screening study

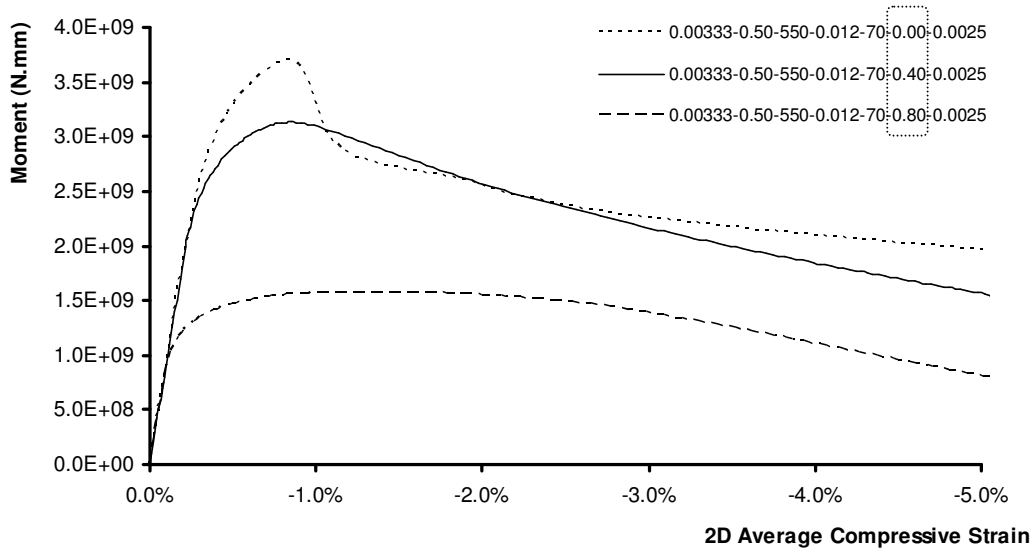


Figure 4-11 Effects of  $\sigma_h/\sigma_{y(T)}$  on the buckling response of the finite element used in the screening study

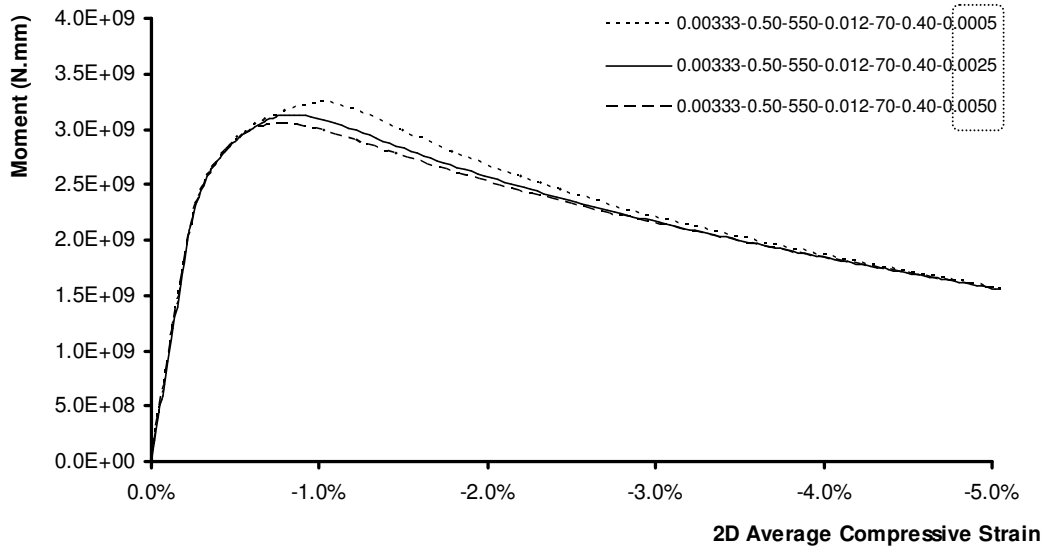


Figure 4-12 Effects of  $II_{max}/D$  on the buckling response of the finite element used in the screening study

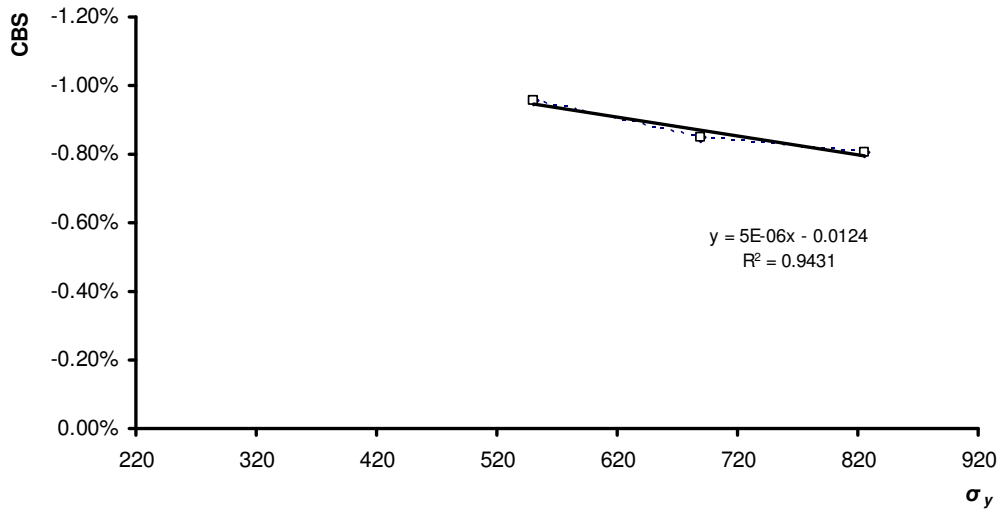


Figure 4-13 Effects of the variation of  $\sigma_{y(T)}$

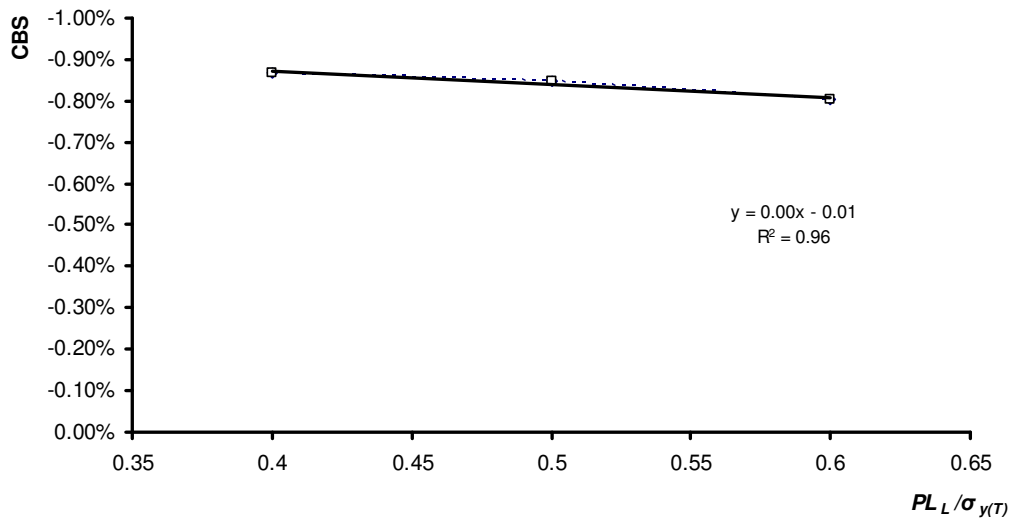


Figure 4-14 Effects of the variation of  $PL_L / \sigma_{y(T)}$

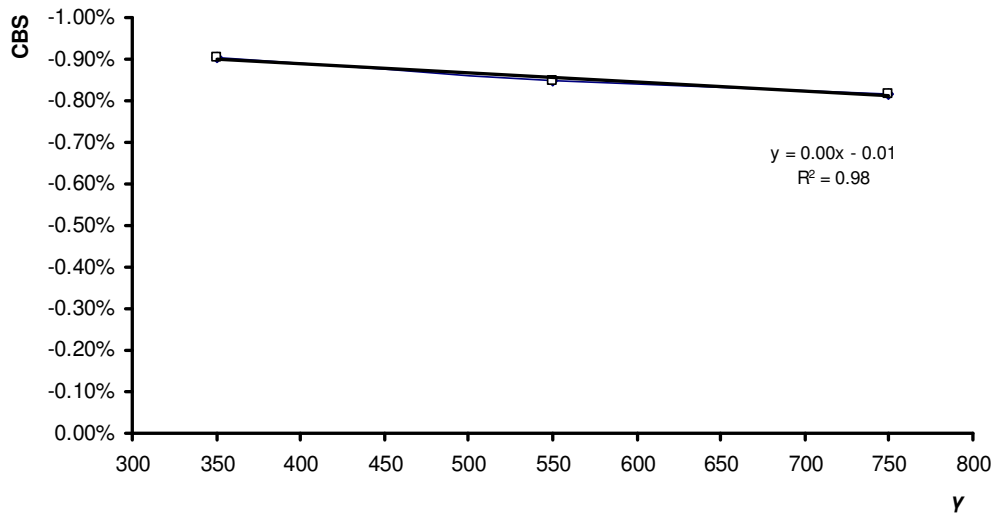


Figure 4-15 Effects of the variation of  $\gamma$

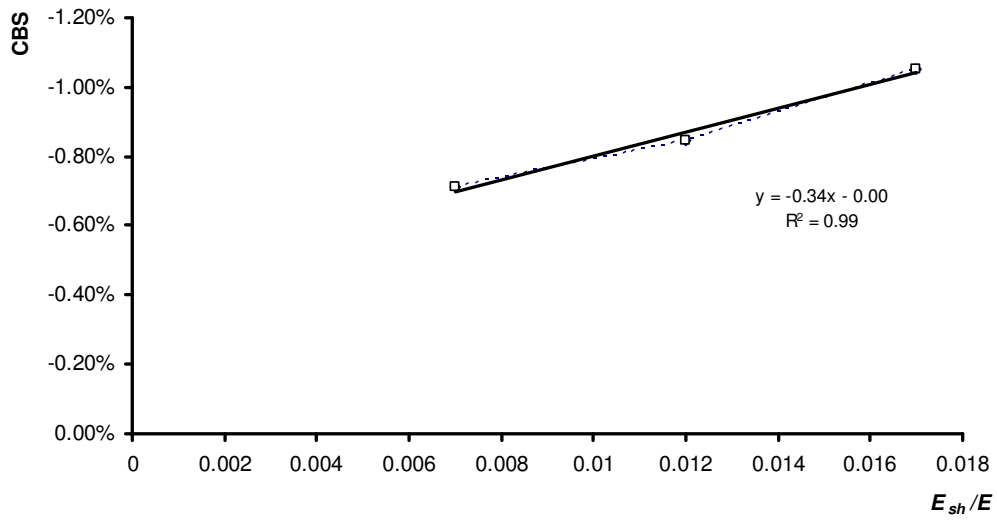


Figure 4-16 Effects of the variation of  $E_{sh}/E$

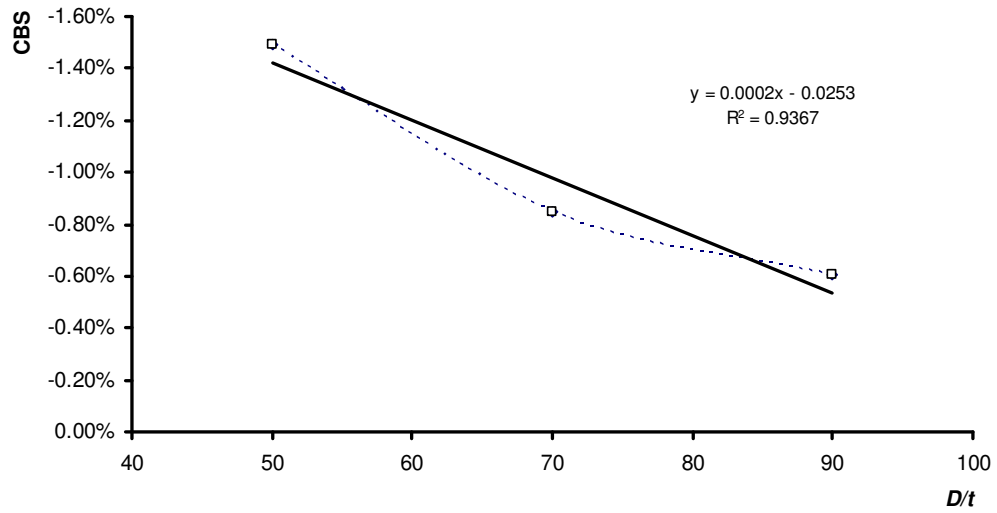


Figure 4-17 Effects of the variation of  $D/t$

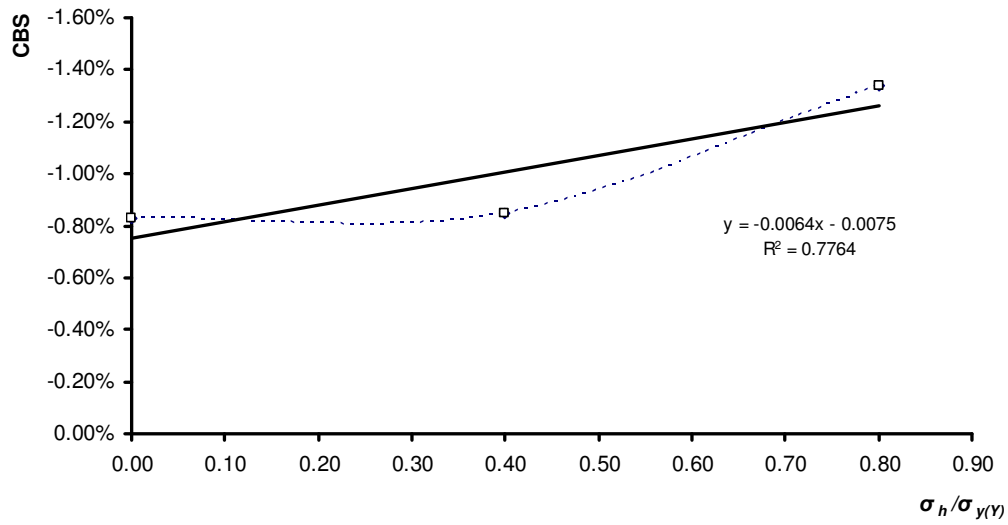


Figure 4-18 Effects of the variation of  $\sigma_h/\sigma_{y(T)}$

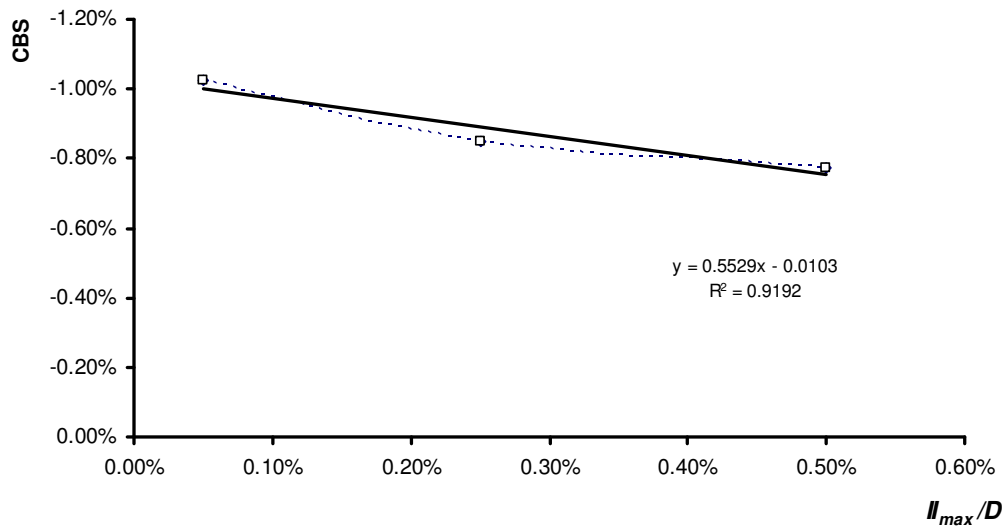


Figure 4-19 Effects of the variation of  $II_{max}/D$

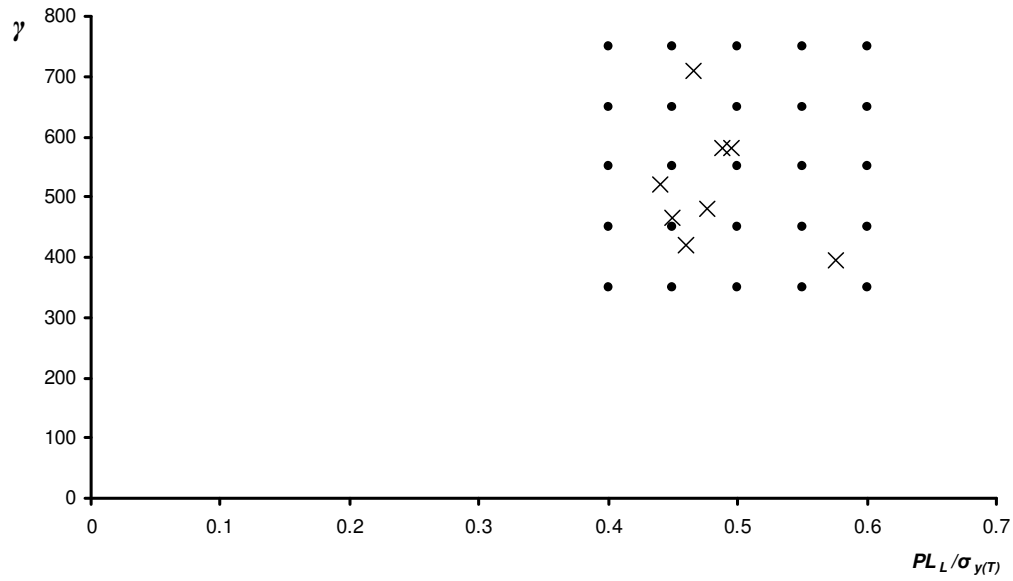


Figure 4-20 Distribution of  $\gamma$  versus  $PL_L/\sigma_{y(T)}$  in the experimental database compared to 25 combinations used in the screening study

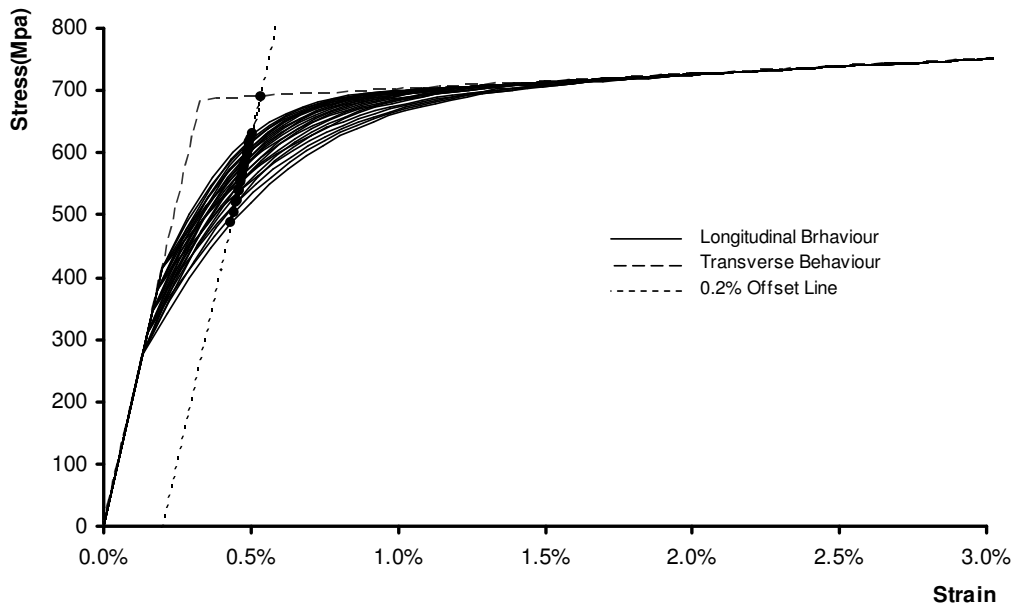


Figure 4-21 Stress-strain curves for 25 combinations of  $PL_L/\sigma_{y(T)}$  and  $\gamma$

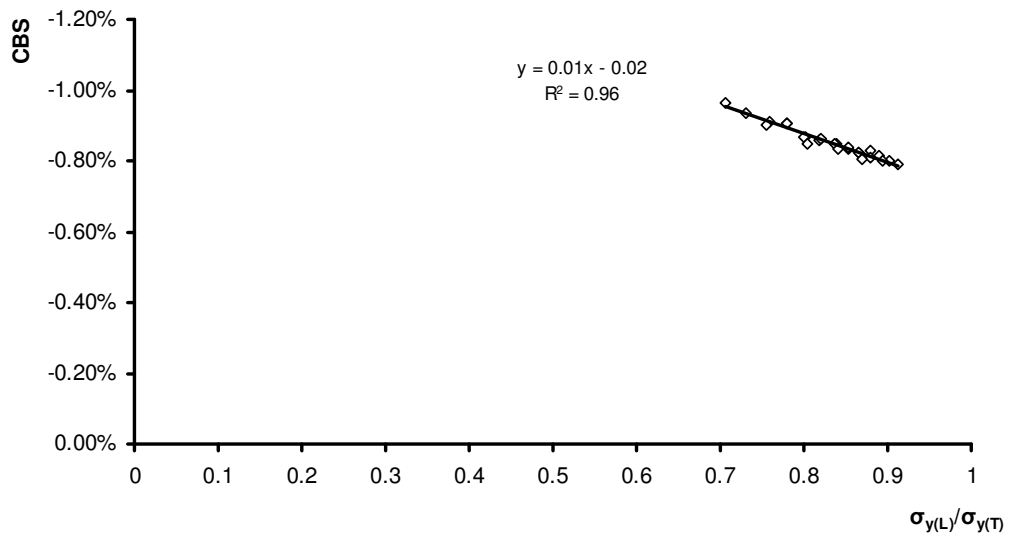


Figure 4-22 Variation of the CBS with  $\sigma_{y(L)}/\sigma_{y(T)}$

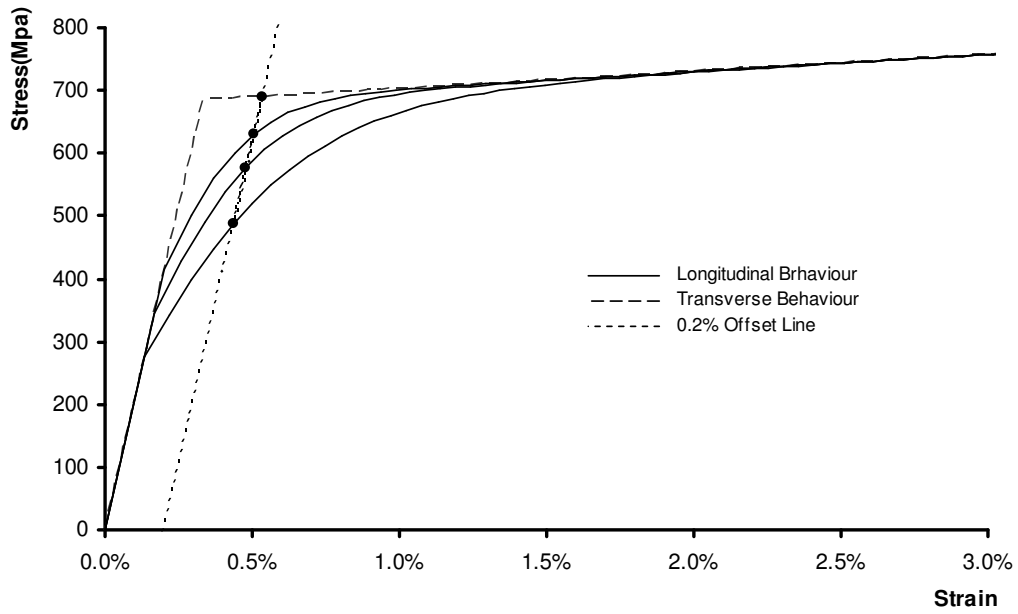


Figure 4-23 Stress-strain curves for minimum, intermediate, and maximum  $\sigma_{y(L)}/\sigma_{y(T)}$

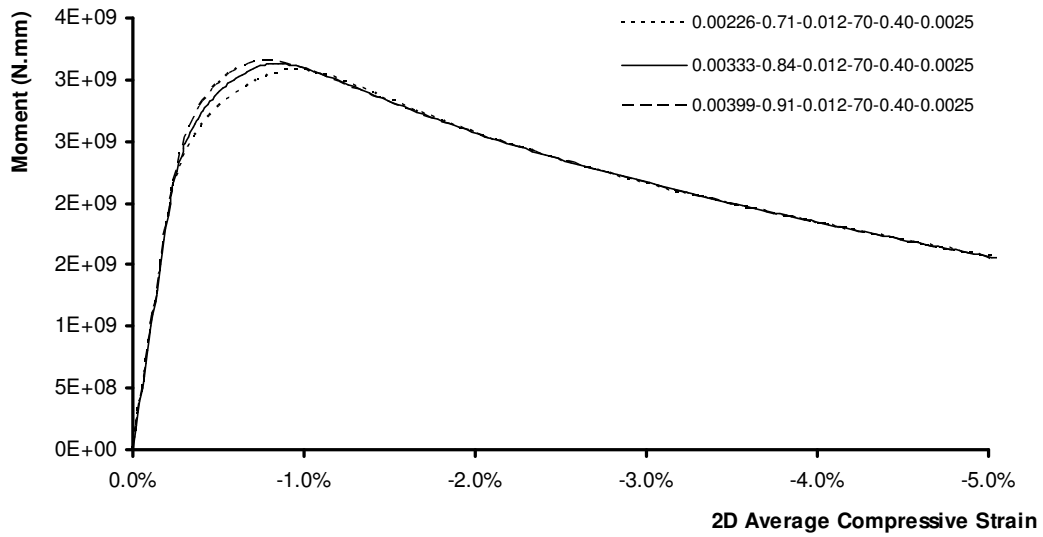


Figure 4-24 Effects of  $\sigma_{y(L)}/\sigma_{y(T)}$  on the buckling response of the finite element used in the screening study

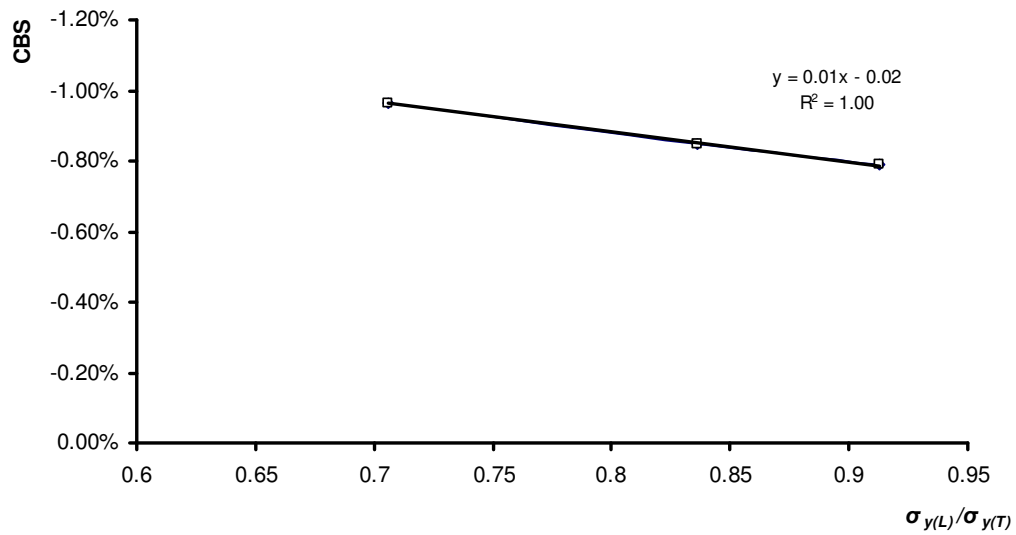


Figure 4-25 Effects of the variation of  $\sigma_{y(L)}/\sigma_{y(T)}$

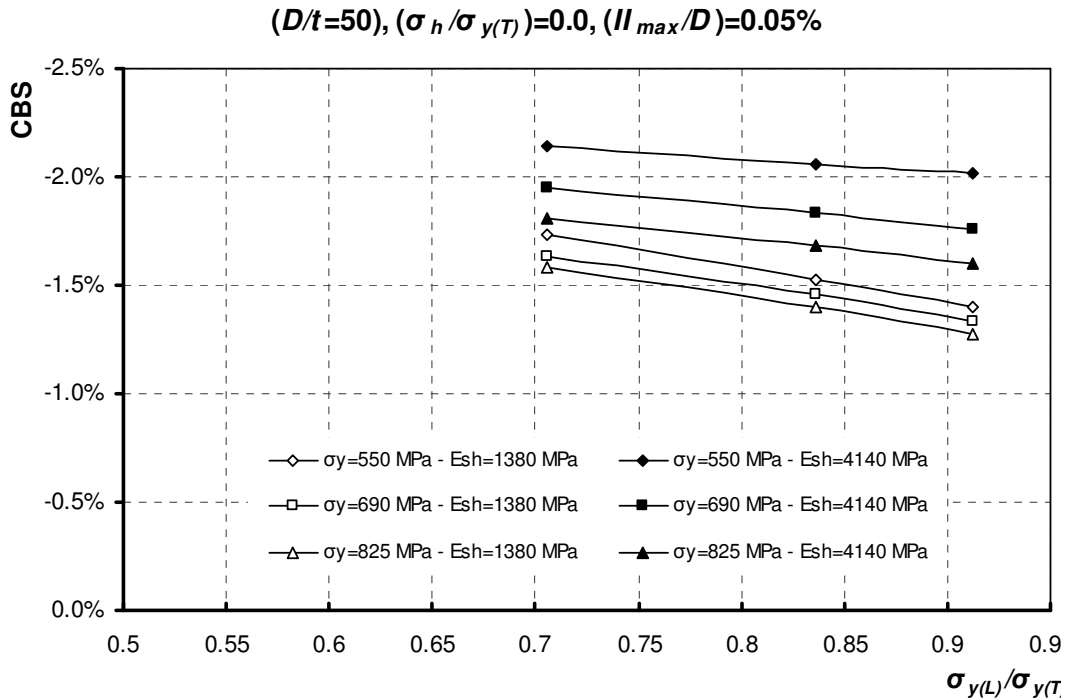


Figure 4-26 Variation of the CBS versus  $\sigma_{y(L)}/\sigma_{y(T)}$  for  $D/t=50, \sigma_h/\sigma_{y(T)}=0.0, I_{max}/D=0.05\%$

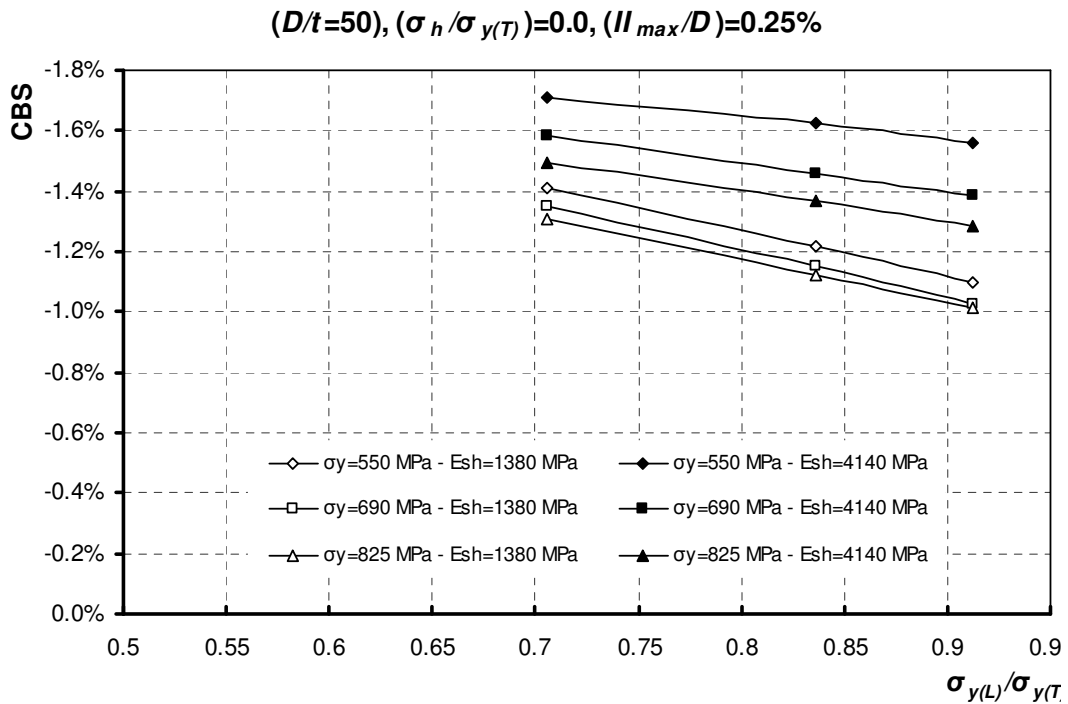


Figure 4-27 Variation of the CBS versus  $\sigma_{y(L)}/\sigma_{y(T)}$  for  $D/t=50, \sigma_h/\sigma_{y(T)}=0.0, I_{max}/D=0.25\%$

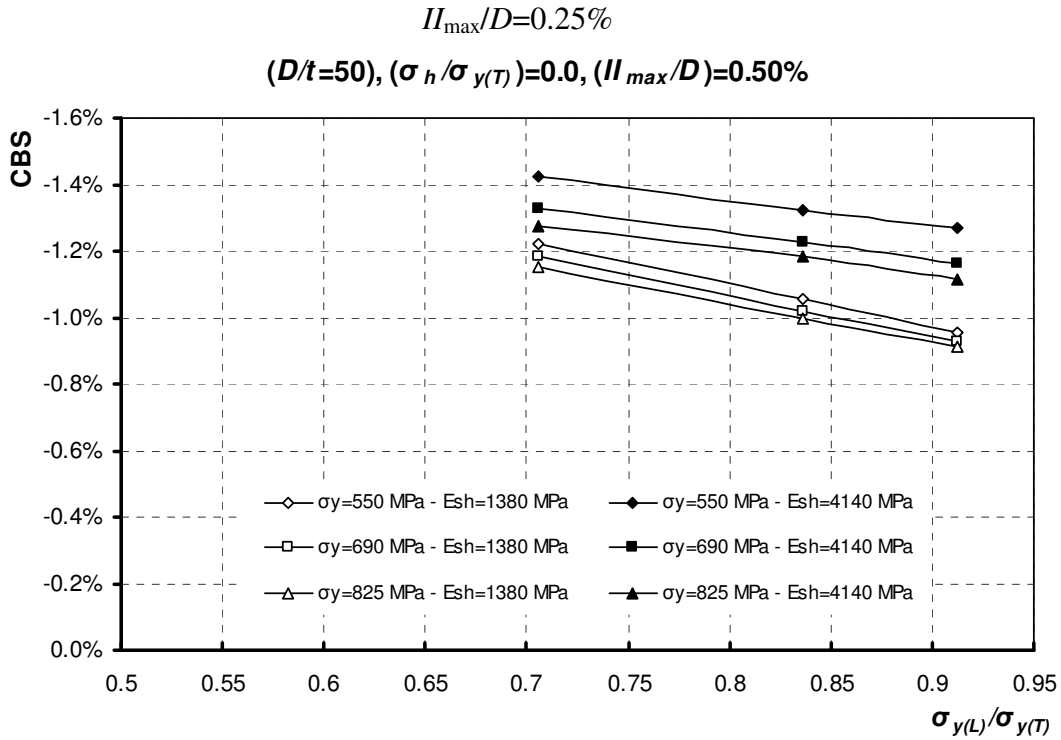


Figure 4-28 Variation of the CBS versus  $\sigma_{y(L)}/\sigma_{y(T)}$  for  $D/t=50$ ,  $\sigma_h/\sigma_{y(T)}=0.0$ ,  $I_{max}/D=0.50\%$

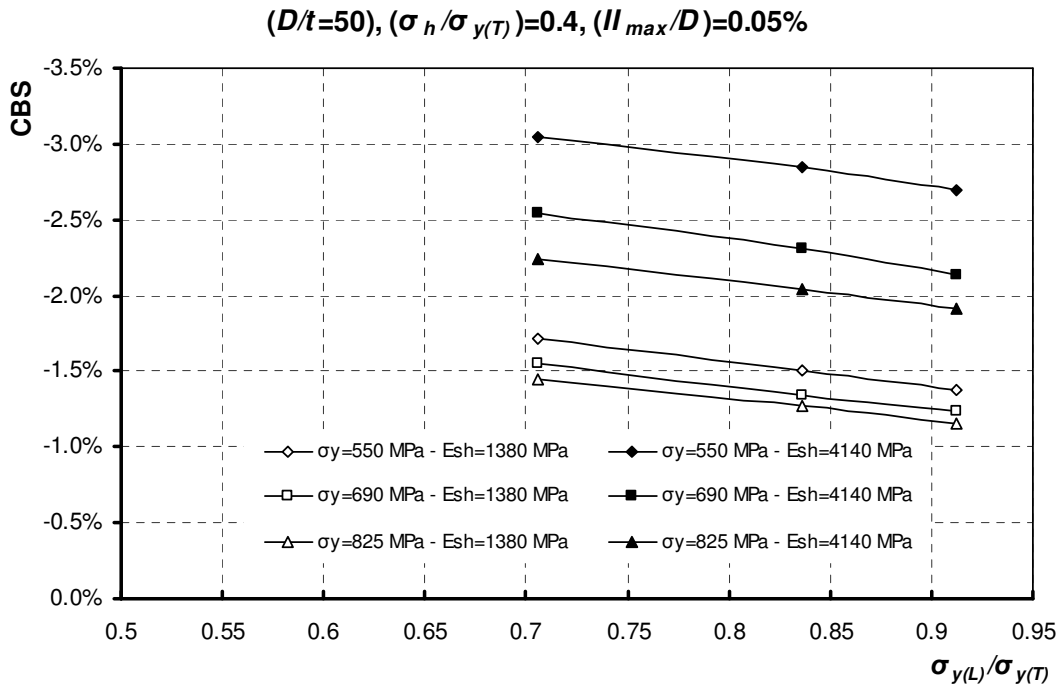


Figure 4-29 Variation of the CBS versus  $\sigma_{y(L)}/\sigma_{y(T)}$  for  $D/t=50$ ,  $\sigma_h/\sigma_{y(T)}=0.4$ ,  $I_{max}/D=0.05\%$

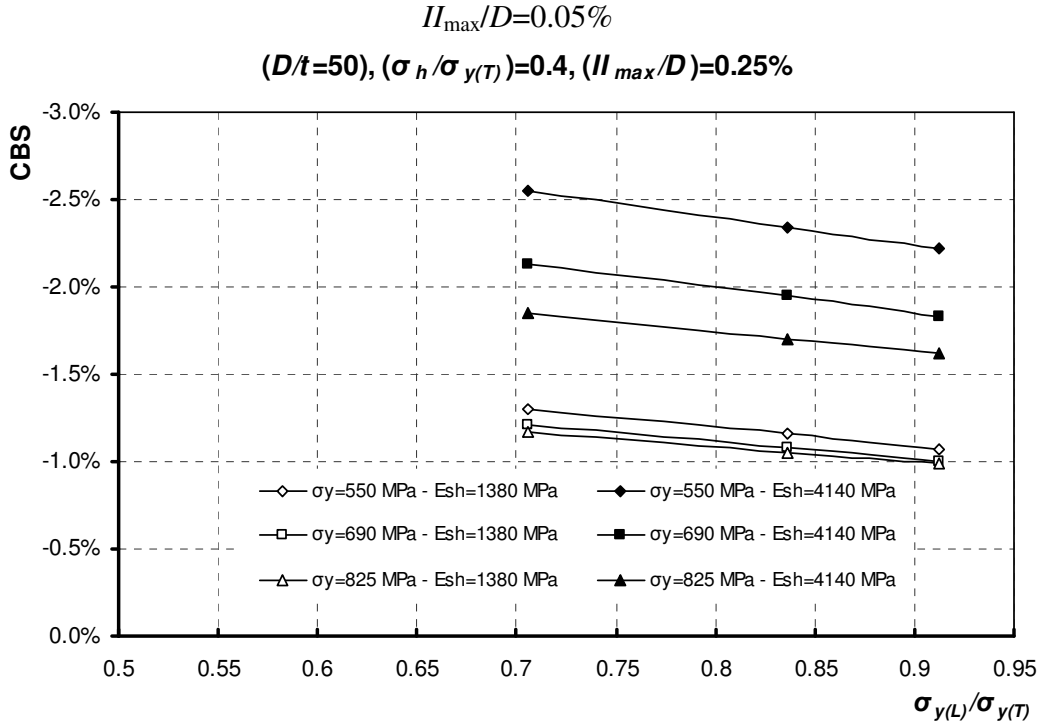


Figure 4-30 Variation of the CBS versus  $\sigma_{y(L)}/\sigma_{y(T)}$  for  $D/t=50, \sigma_h/\sigma_{y(T)}=0.4, I_{max}/D=0.25\%$

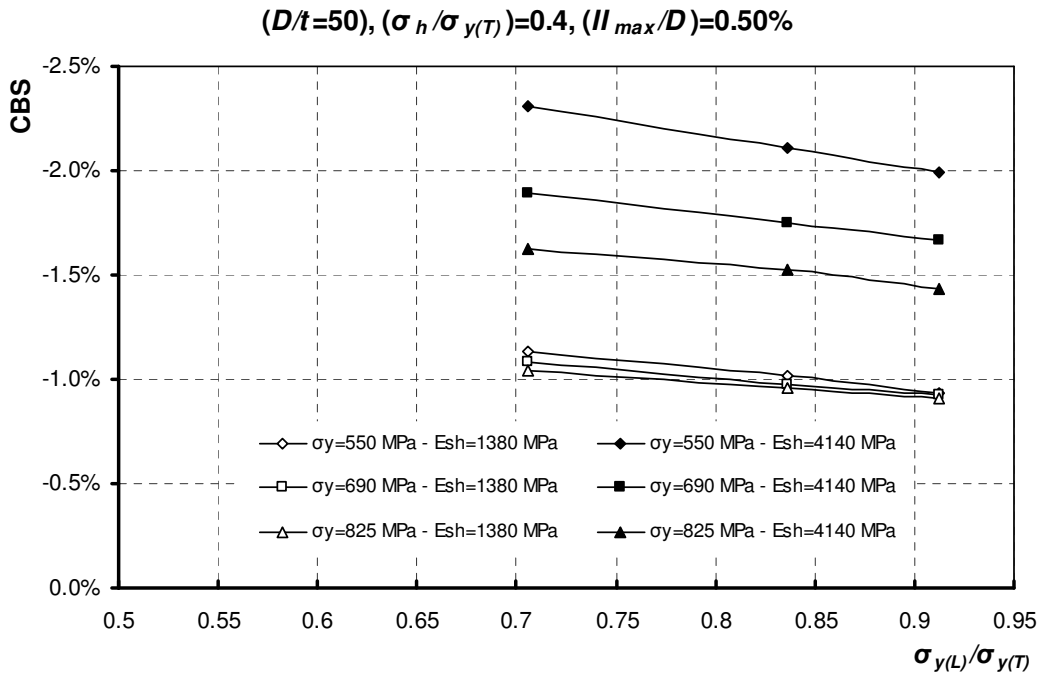


Figure 4-31 Variation of the CBS versus  $\sigma_{y(L)}/\sigma_{y(T)}$  for  $D/t=50, \sigma_h/\sigma_{y(T)}=0.4, I_{max}/D=0.50\%$

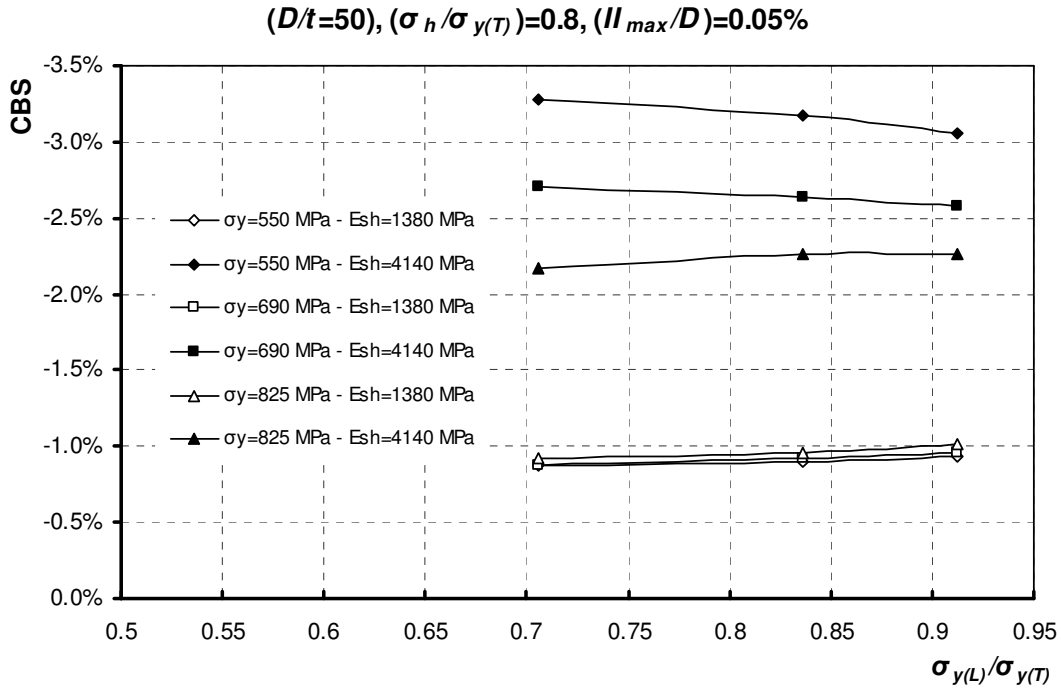


Figure 4-32 Variation of the CBS versus  $\sigma_{y(L)}/\sigma_{y(T)}$  for  $D/t=50, \sigma_h/\sigma_{y(T)}=0.8, I_{max}/D=0.05\%$

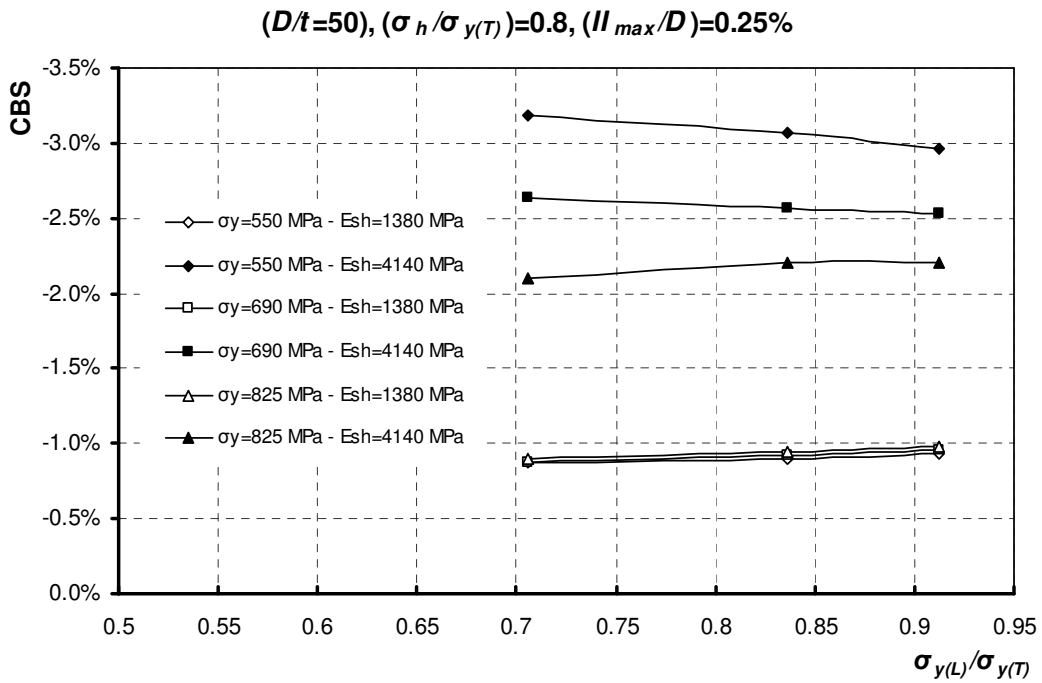


Figure 4-33 Variation of the CBS versus  $\sigma_{y(L)}/\sigma_{y(T)}$  for  $D/t=50, \sigma_h/\sigma_{y(T)}=0.8, I_{max}/D=0.25\%$

$(D/t=50), (\sigma_h/\sigma_{y(T)})=0.8, (I_{max}/D)=0.50\%$

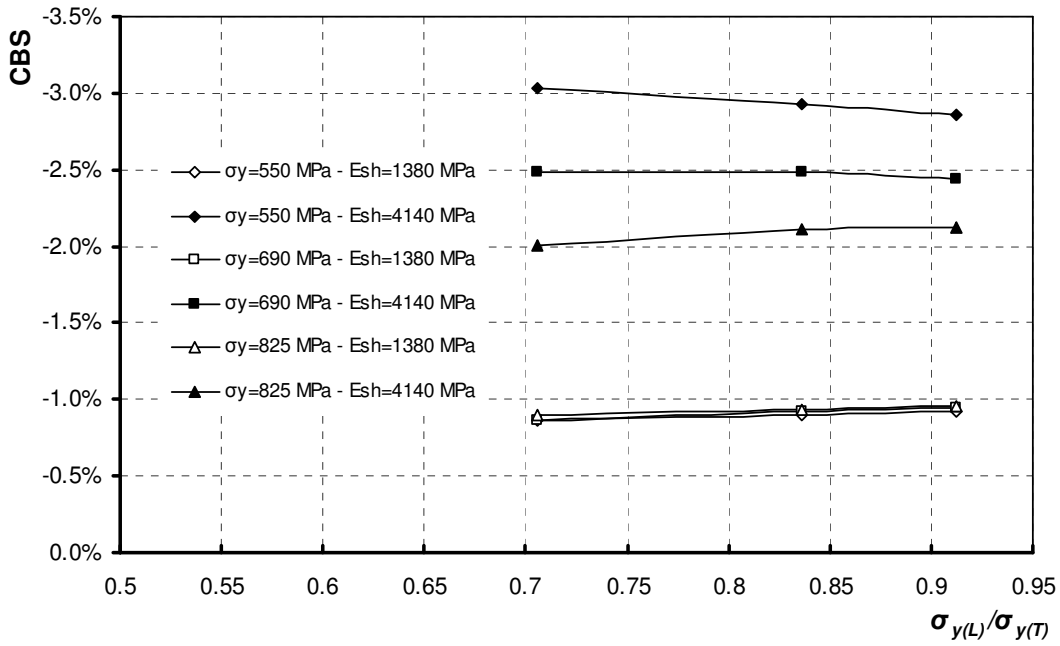


Figure 4-34 Variation of the CBS versus  $\sigma_{y(L)}/\sigma_{y(T)}$  for  $D/t=50$ ,  $\sigma_h/\sigma_{y(T)}=0.8$ ,  $I_{max}/D=0.50\%$

$(D/t=70), (\sigma_h/\sigma_{y(T)})=0.0, (I_{max}/D)=0.05\%$

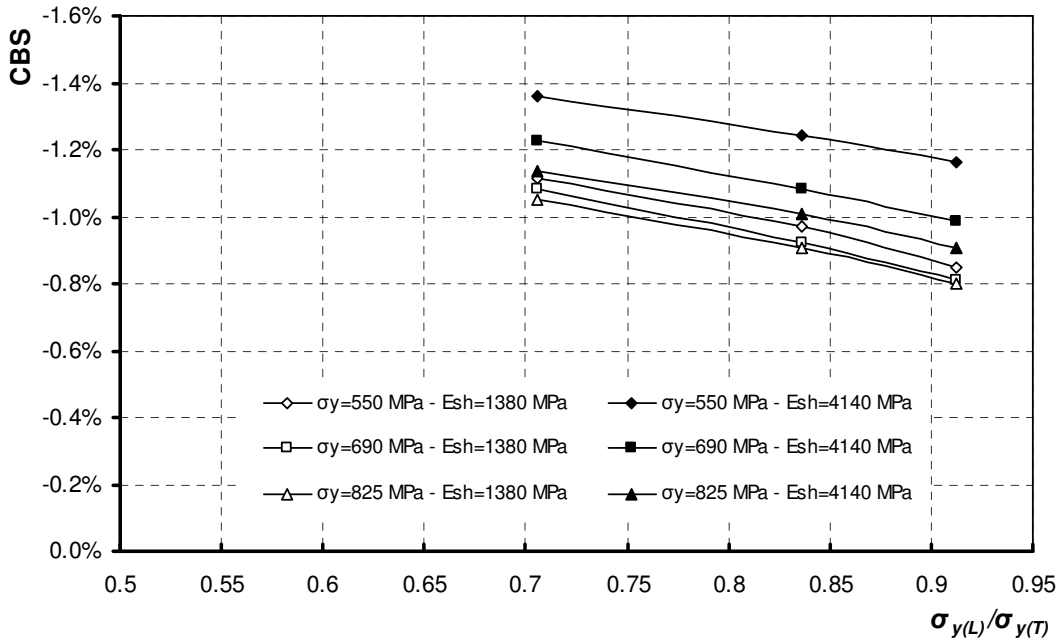


Figure 4-35 Variation of the CBS versus  $\sigma_{y(L)}/\sigma_{y(T)}$  for  $D/t=70$ ,  $\sigma_h/\sigma_{y(T)}=0.0$ ,  $I_{max}/D=0.05\%$

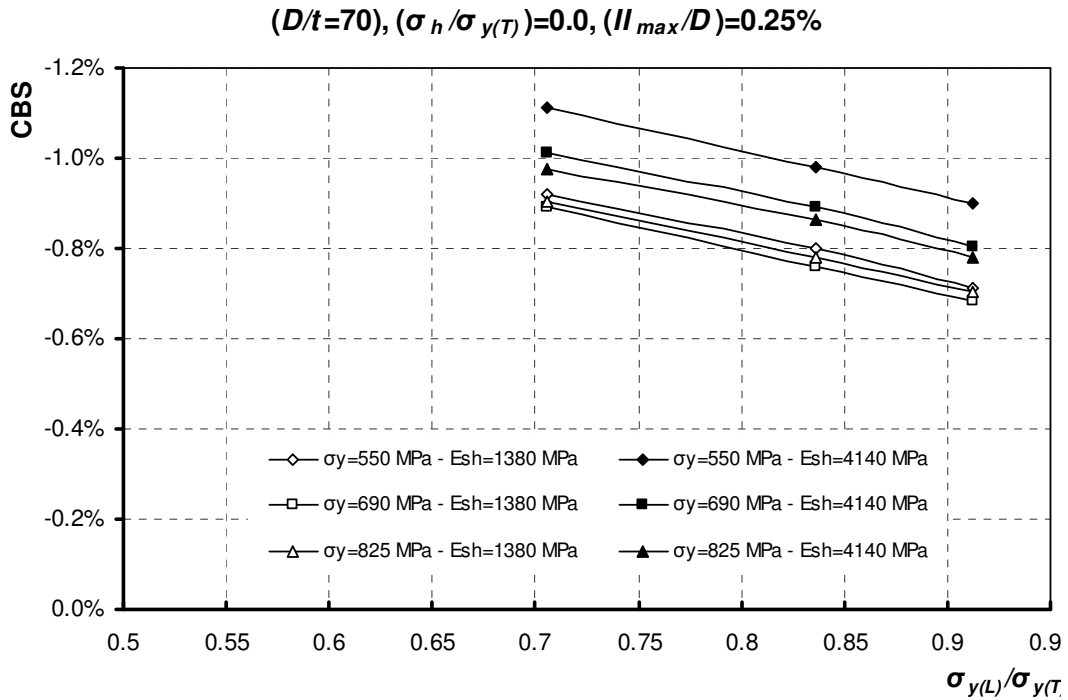


Figure 4-36 Variation of the CBS versus  $\sigma_{y(L)}/\sigma_{y(T)}$  for  $D/t=70, \sigma_h/\sigma_{y(T)}=0.0, I_{max}/D=0.25\%$

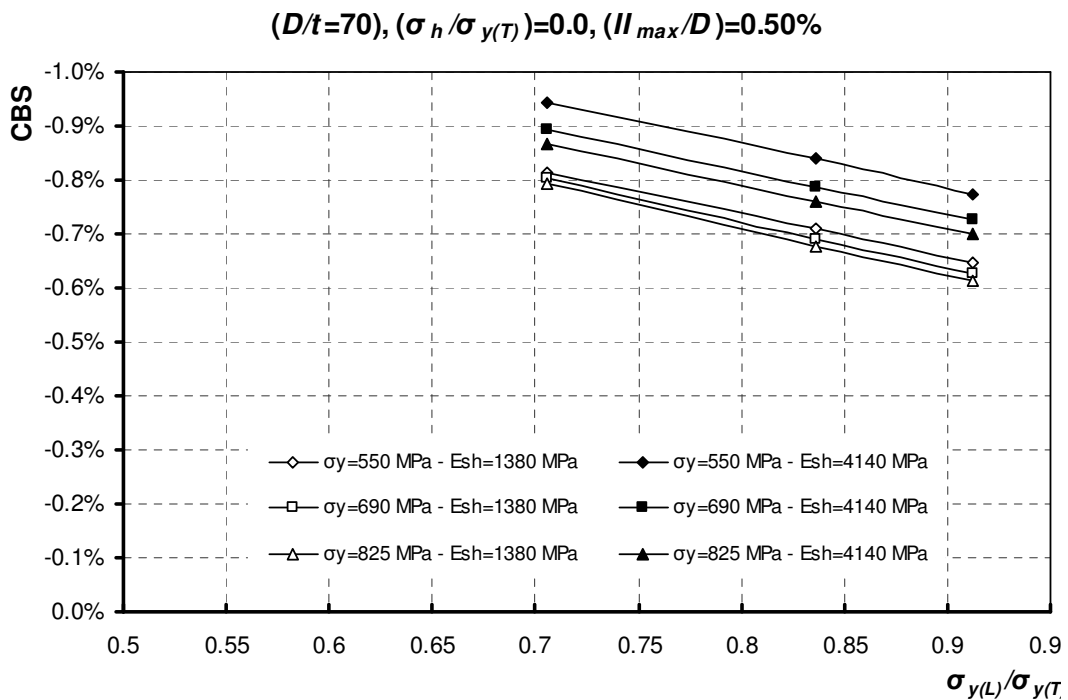


Figure 4-37 Variation of the CBS versus  $\sigma_{y(L)}/\sigma_{y(T)}$  for  $D/t=70, \sigma_h/\sigma_{y(T)}=0.0, I_{max}/D=0.50\%$

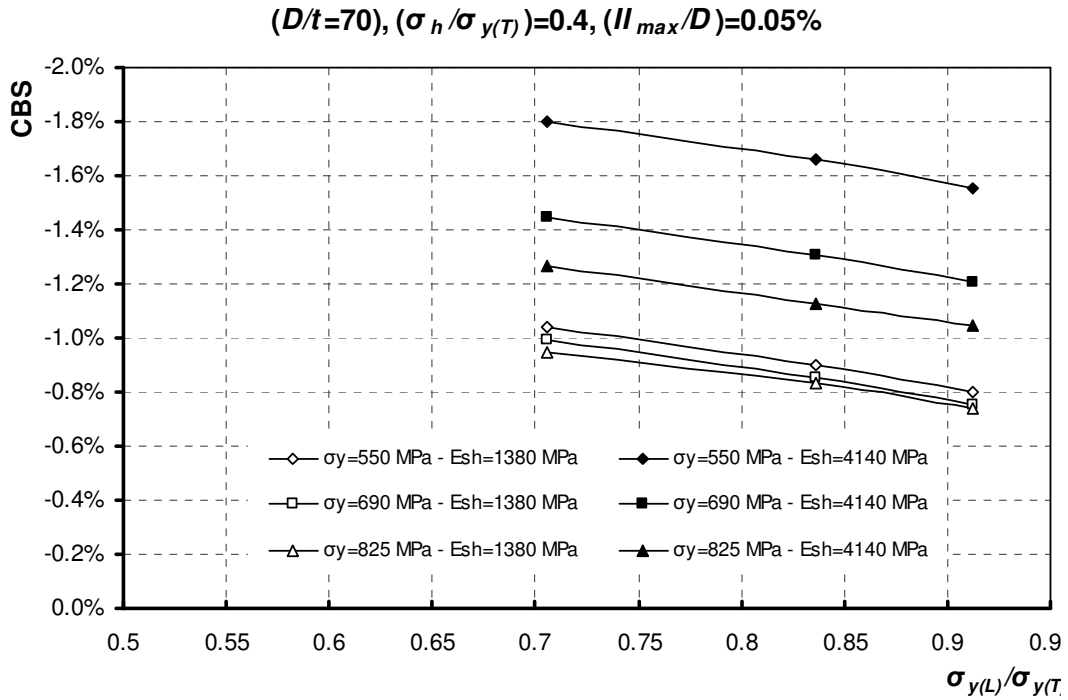


Figure 4-38 Variation of the CBS versus  $\sigma_{y(L)}/\sigma_{y(T)}$  for  $D/t=70$ ,  $\sigma_h/\sigma_{y(T)}=0.4$ ,  $I_{max}/D=0.05\%$

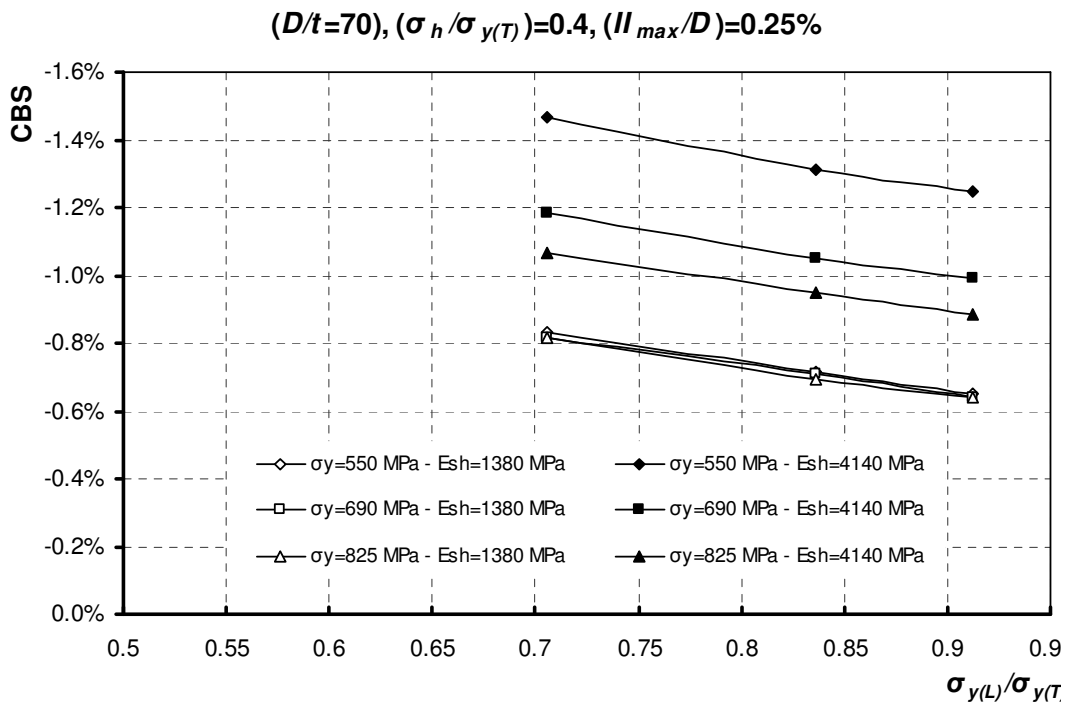


Figure 4-39 Variation of the CBS versus  $\sigma_{y(L)}/\sigma_{y(T)}$  for  $D/t=70$ ,  $\sigma_h/\sigma_{y(T)}=0.4$ ,  $I_{max}/D=0.25\%$

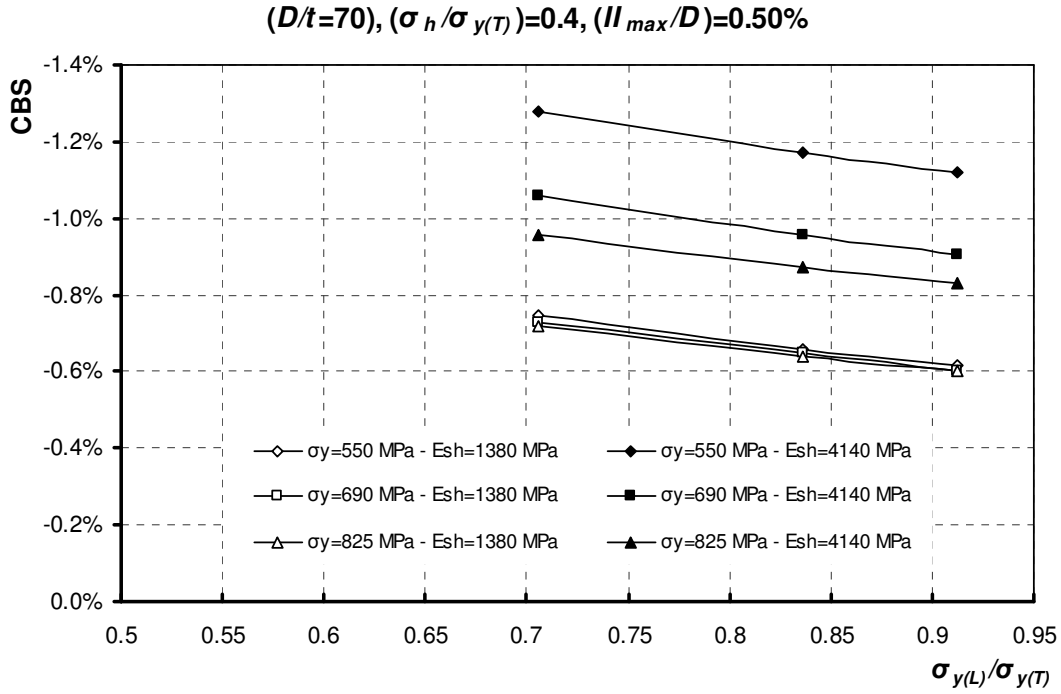


Figure 4-40 Variation of the CBS versus  $\sigma_{y(L)}/\sigma_{y(T)}$  for  $D/t=70$ ,  $\sigma_h/\sigma_{y(T)}=0.4$ ,  $I_{max}/D=0.50\%$

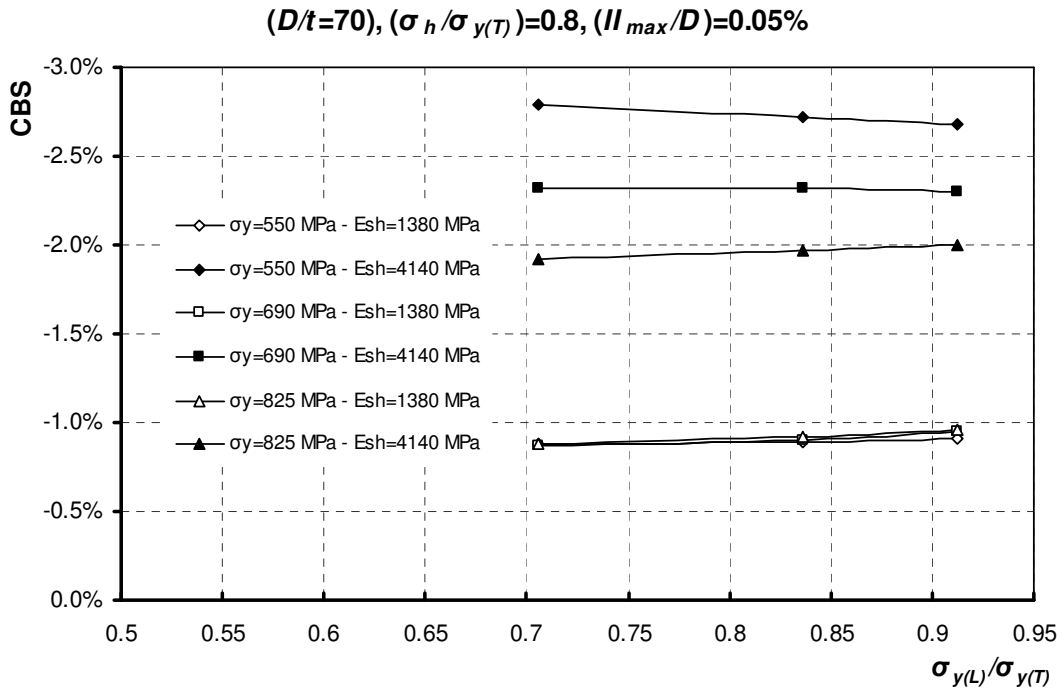


Figure 4-41 Variation of the CBS versus  $\sigma_{y(L)}/\sigma_{y(T)}$  for  $D/t=70$ ,  $\sigma_h/\sigma_{y(T)}=0.8$ ,  $I_{max}/D=0.05\%$

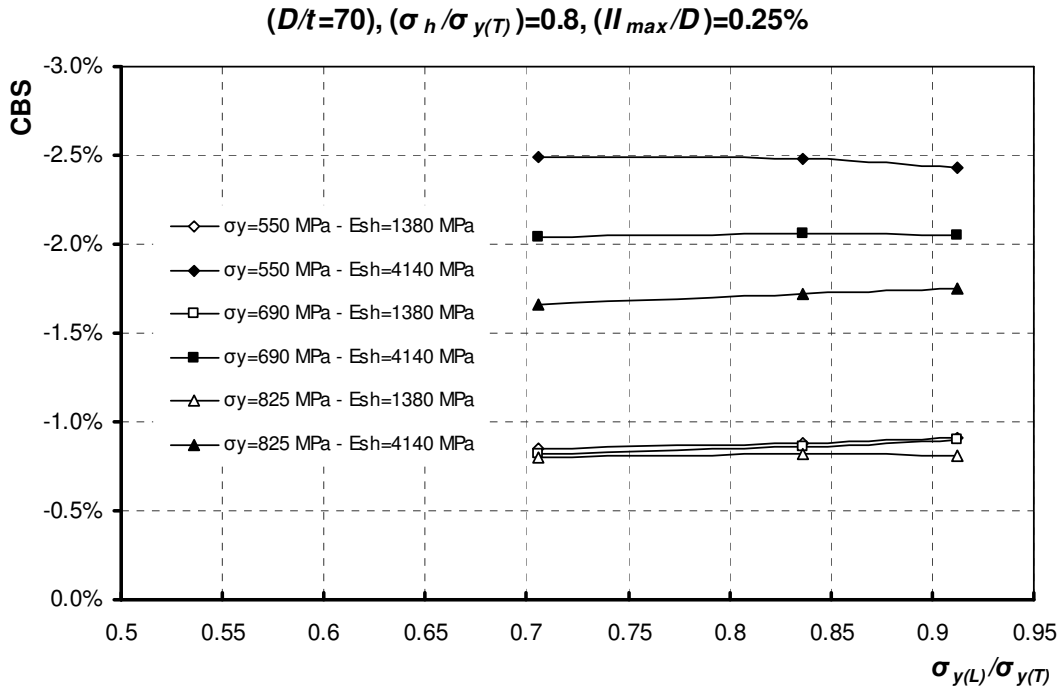


Figure 4-42 Variation of the CBS versus  $\sigma_{y(L)}/\sigma_{y(T)}$  for  $D/t=70$ ,  $\sigma_h/\sigma_{y(T)}=0.8$ ,  $I_{max}/D=0.25\%$

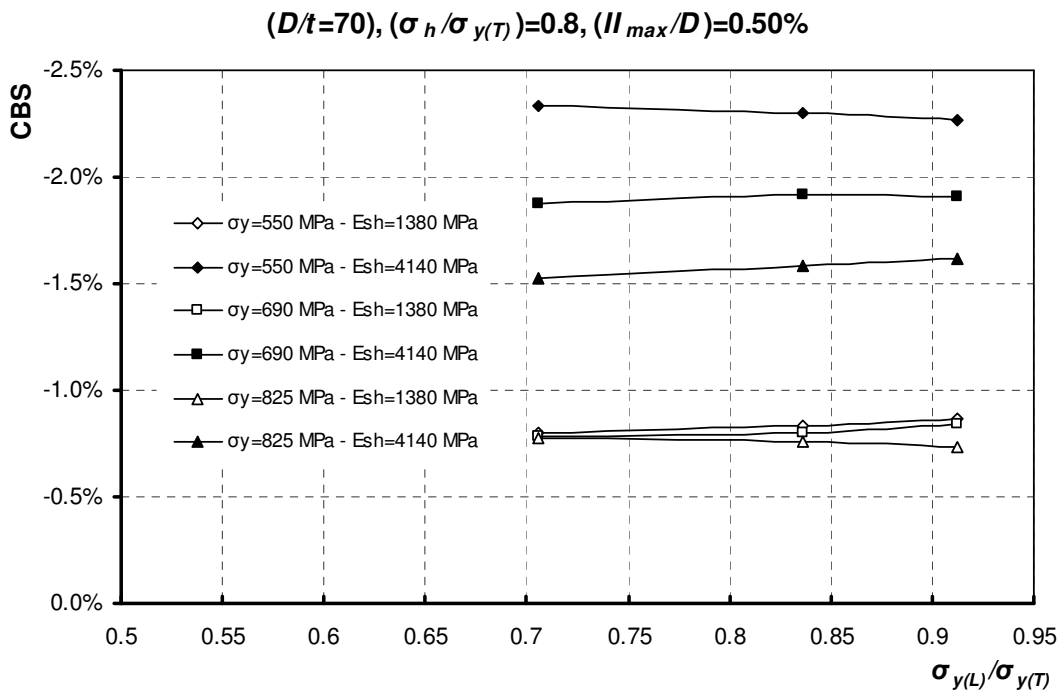


Figure 4-43 Variation of the CBS versus  $\sigma_{y(L)}/\sigma_{y(T)}$  for  $D/t=70$ ,  $\sigma_h/\sigma_{y(T)}=0.8$ ,  $I_{max}/D=0.50\%$

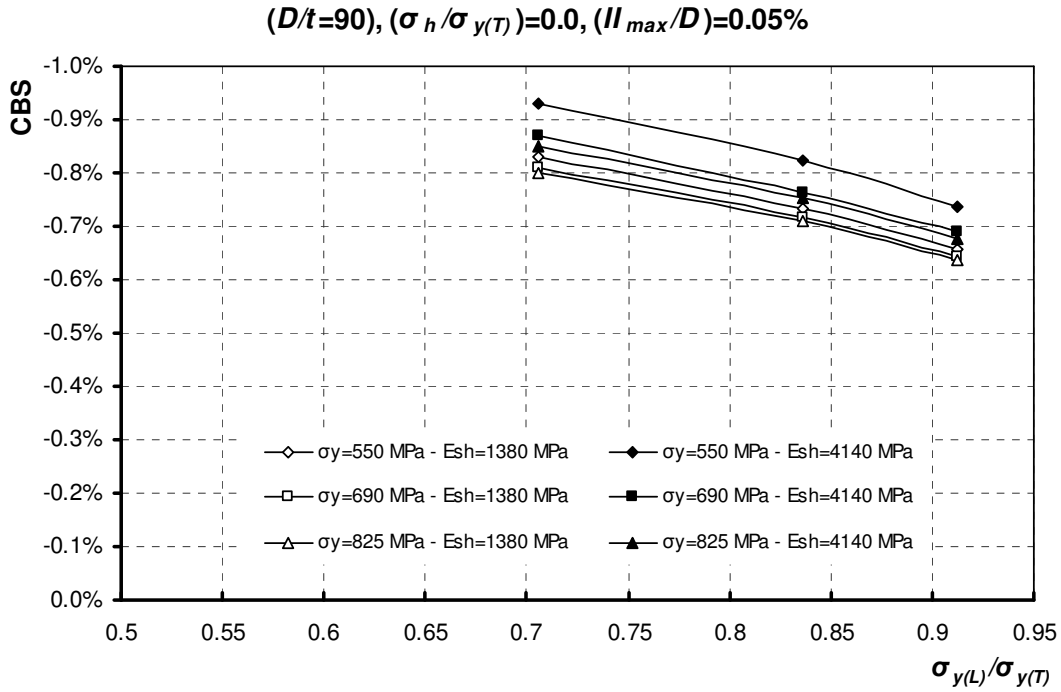


Figure 4-44 Variation of the CBS versus  $\sigma_{y(L)}/\sigma_{y(T)}$  for  $D/t=90, \sigma_h/\sigma_{y(T)}=0.0, I_{max}/D=0.05\%$

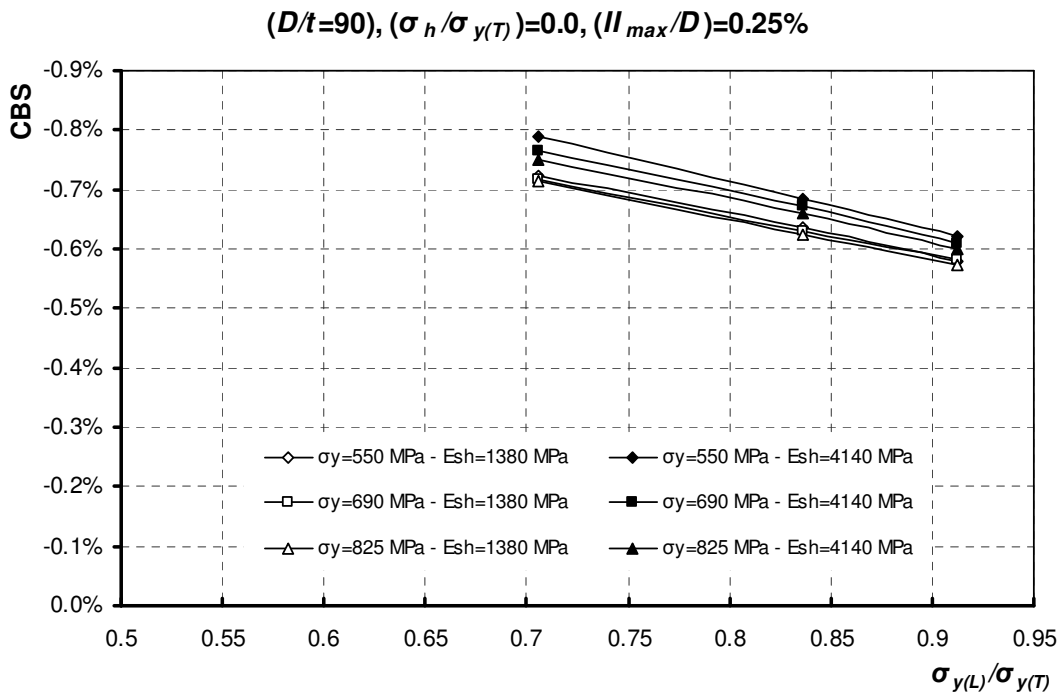


Figure 4-45 Variation of the CBS versus  $\sigma_{y(L)}/\sigma_{y(T)}$  for  $D/t=90, \sigma_h/\sigma_{y(T)}=0.0, I_{max}/D=0.25\%$

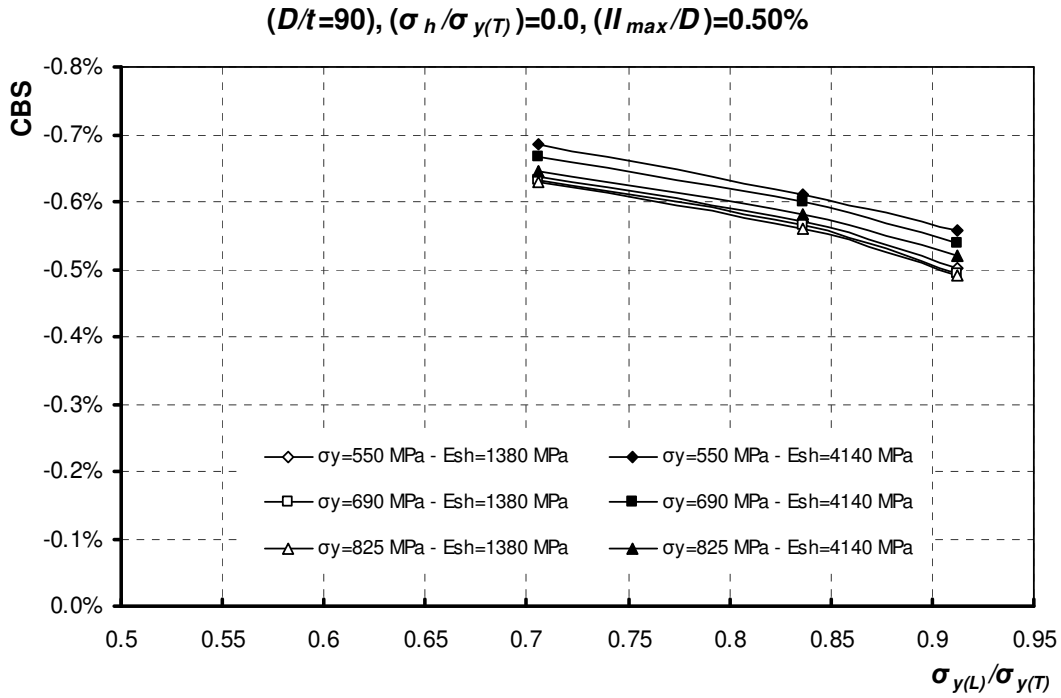


Figure 4-46 Variation of the CBS versus  $\sigma_{y(L)}/\sigma_{y(T)}$  for  $D/t=90, \sigma_h/\sigma_{y(T)}=0.0, I_{max}/D=0.50\%$

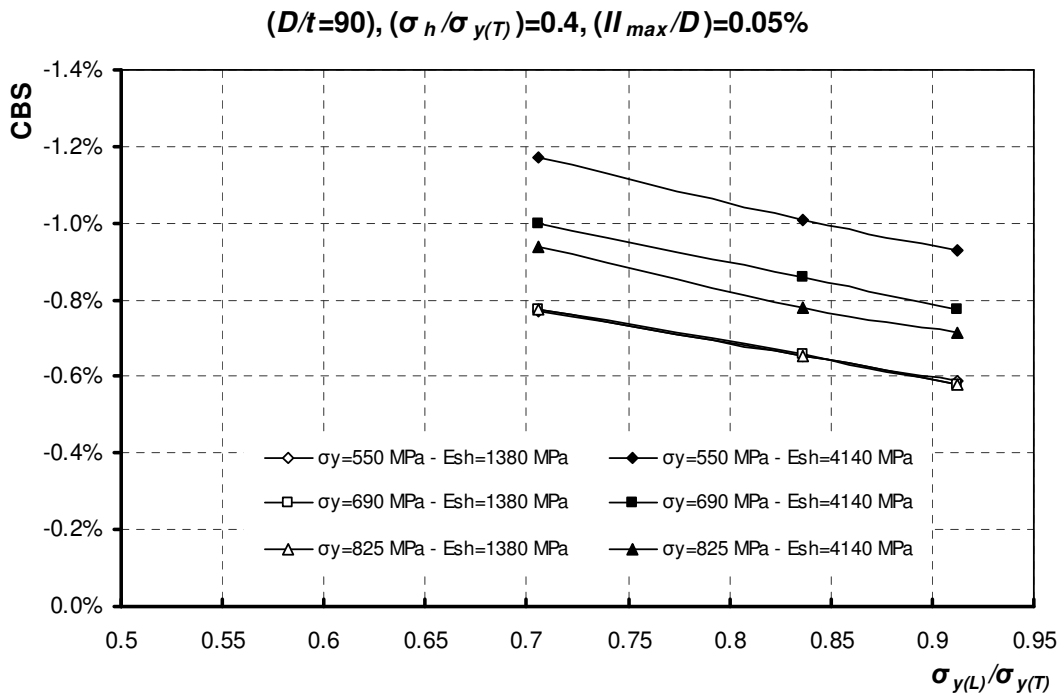


Figure 4-47 Variation of the CBS versus  $\sigma_{y(L)}/\sigma_{y(T)}$  for  $D/t=90, \sigma_h/\sigma_{y(T)}=0.4, I_{max}/D=0.05\%$

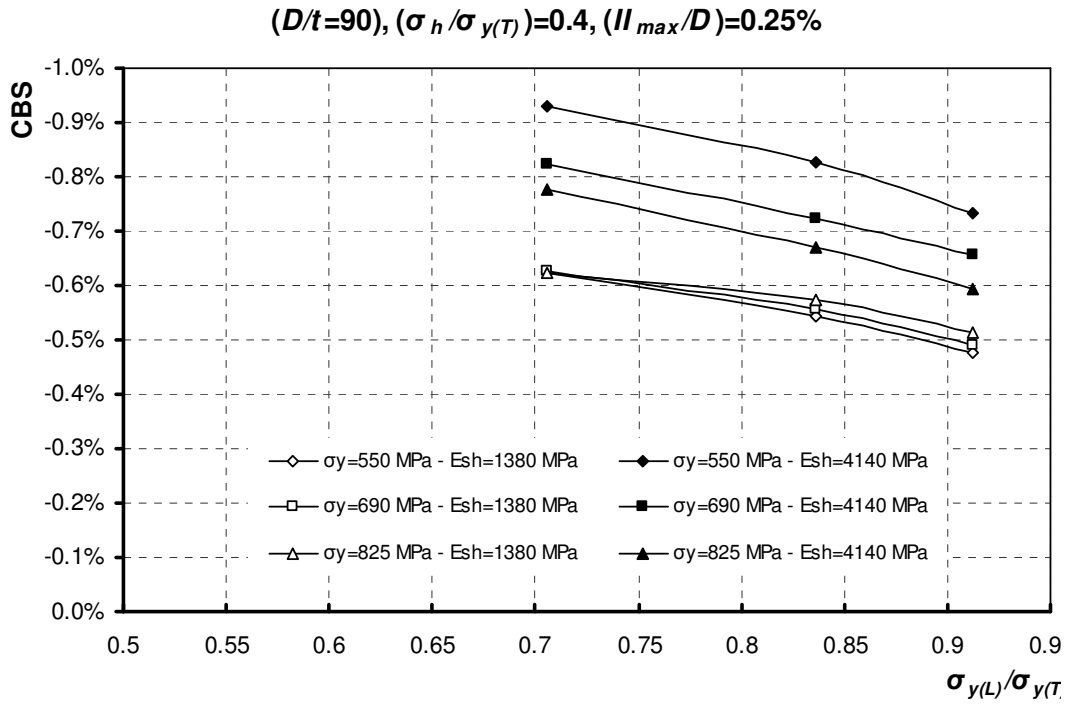


Figure 4-48 Variation of the CBS versus  $\sigma_{y(L)}/\sigma_{y(T)}$  for  $D/t=90$ ,  $\sigma_h/\sigma_{y(T)}=0.4$ ,  $I_{max}/D=0.25\%$

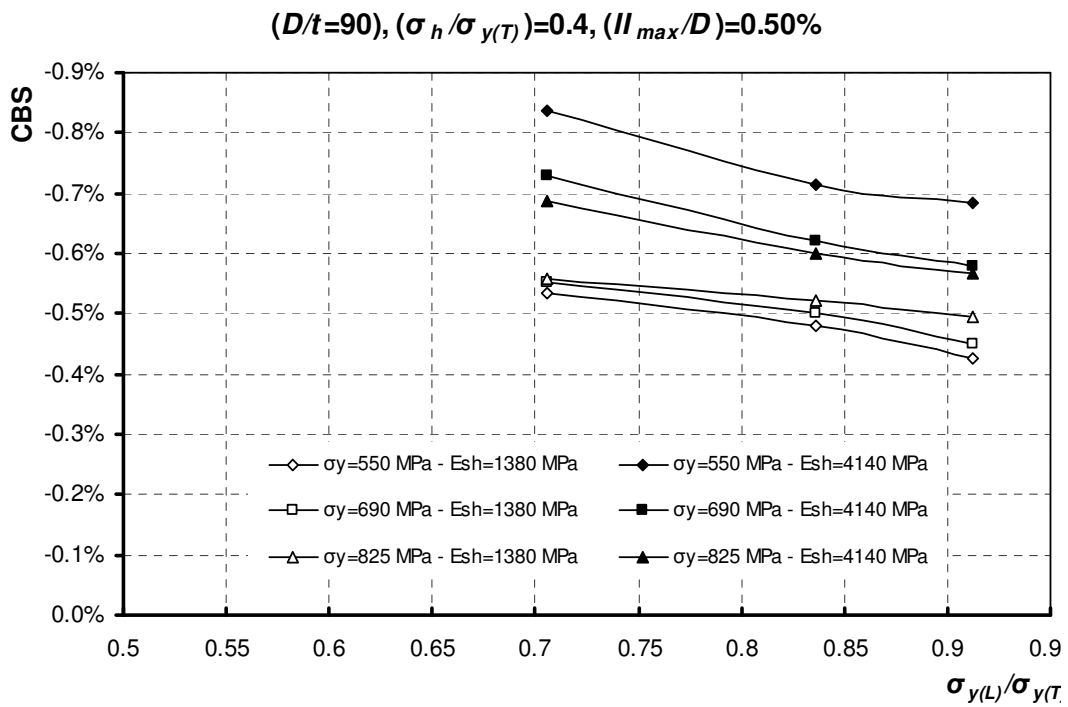


Figure 4-49 Variation of the CBS versus  $\sigma_{y(L)}/\sigma_{y(T)}$  for  $D/t=90$ ,  $\sigma_h/\sigma_{y(T)}=0.4$ ,  $I_{max}/D=0.50\%$

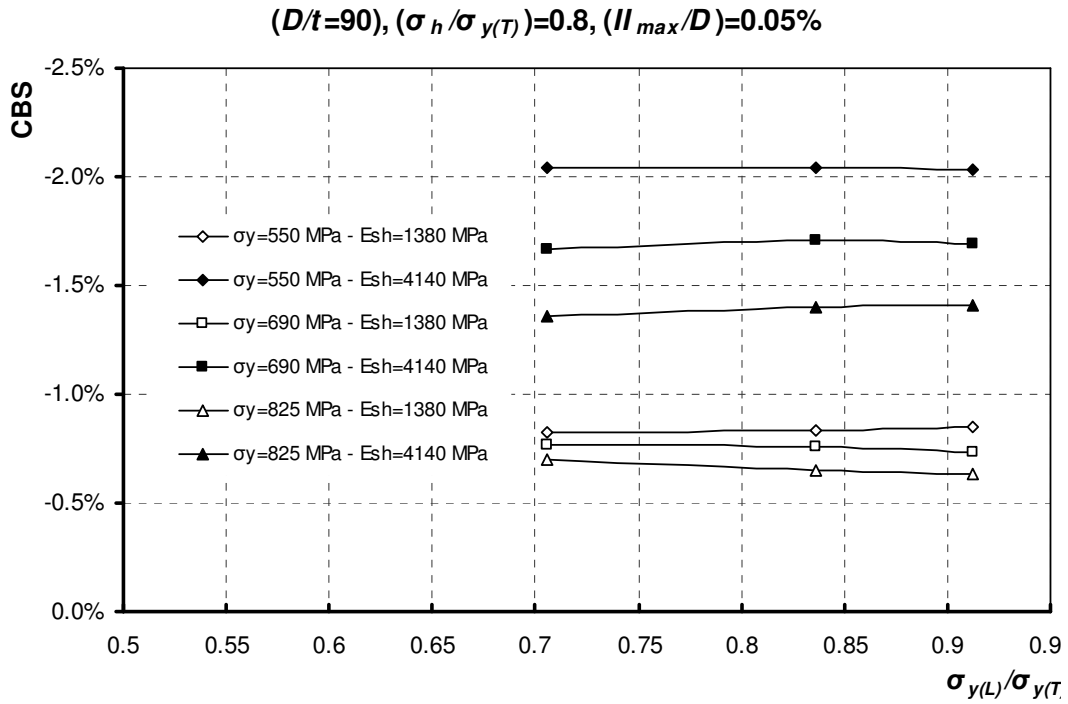


Figure 4-50 Variation of the CBS versus  $\sigma_{y(L)}/\sigma_{y(T)}$  for  $D/t=90$ ,  $\sigma_h/\sigma_{y(T)}=0.8$ ,  $I_{max}/D=0.05\%$

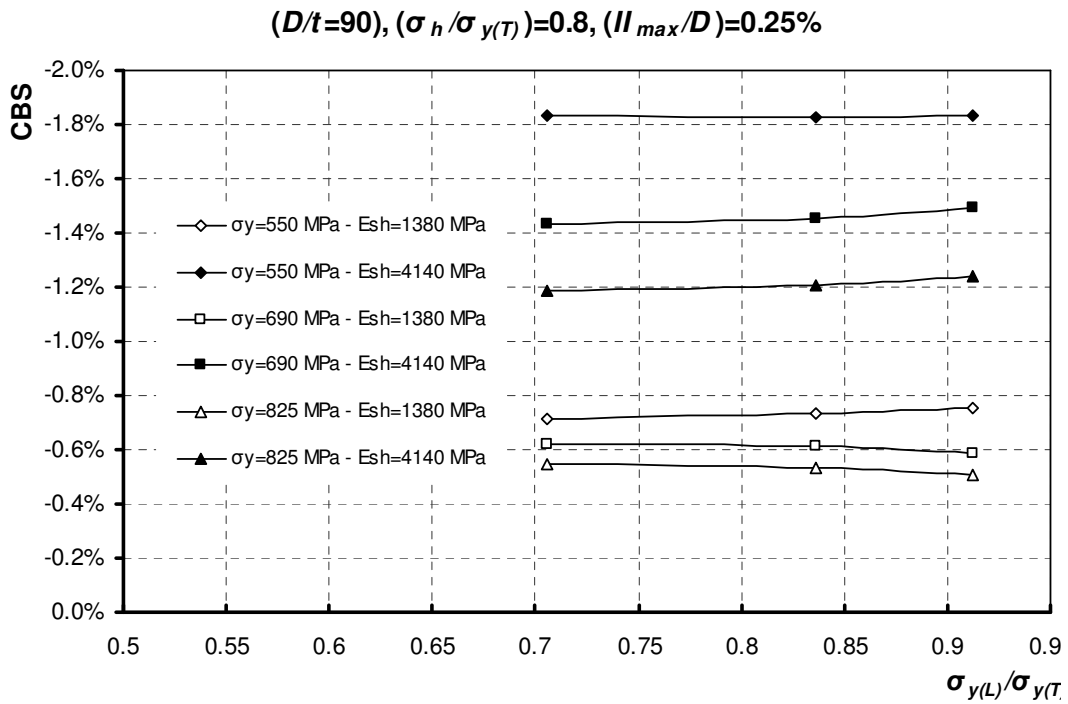


Figure 4-51 Variation of the CBS versus  $\sigma_{y(L)}/\sigma_{y(T)}$  for  $D/t=90$ ,  $\sigma_h/\sigma_{y(T)}=0.8$ ,  $I_{max}/D=0.25\%$

$(D/t=90), (\sigma_h/\sigma_{y(T)})=0.8, (I_{max}/D)=0.50\%$

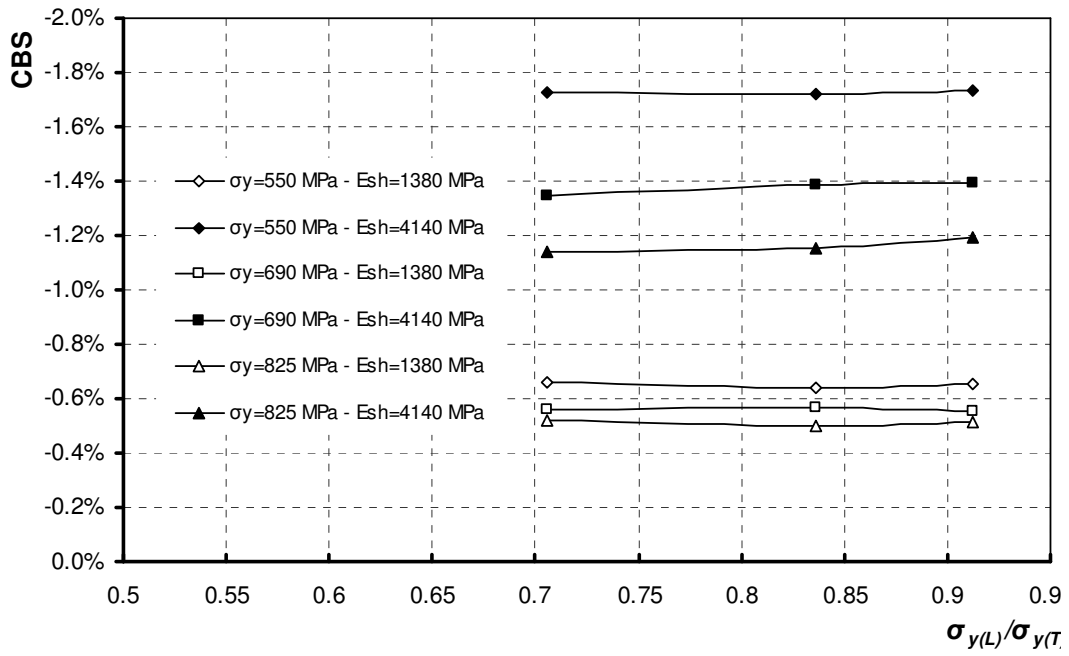


Figure 4-52 Variation of the CBS versus  $\sigma_{y(L)}/\sigma_{y(T)}$  for  $D/t=90, \sigma_h/\sigma_{y(T)}=0.8, I_{max}/D=0.50\%$

## **5 BUCKLING SENSITIVITY OF HSS TO PIPES DIFFERENT MATERIAL RESPONSES**

Previous studies have established empirical insight on the association between the material response and longitudinal strain capacity of normal-strength steel pipelines. It is well known that if the stress-strain response shows higher degrees of ductility, the pipeline will have higher deformability in terms of longitudinal strain capacity before buckling. Although the main factors influencing the deformability of pipeline steel material are not fully defined, it is generally known that they are closely related to the yield-to-tensile strength ratio, the amount of uniform elongation, the strain hardening exponent, and the shape of the stress-strain curve. This empirical perception can help pipeline designers to select the material class (considering desired longitudinal strain capacity). Moreover, it can help pipe producers to target the desired material properties of their products (considering different demands on the steel pipes in pipeline projects).

As discussed in Chapter 2 and Chapter 3, three types of normal stress are usually developed in on-shore energy pipelines: longitudinal tension (LT), longitudinal compression (LC), and transverse tension (TT). In high strength steel (HSS) pipes, the material responses to all these types of stress are different due to the anisotropy. Taking into consideration complex loadings, along with the material anisotropy of HSS pipelines, it is rather difficult to establish an empirical association between specific features of material responses to the final product's buckling behaviour.

For a complex phenomenon such as local buckling under a pure bending moment or a combination of a bending moment and axial load (that engages all three LT, LC, and TT responses), an accurate simulation of material responses is necessary. Isotropic material models can use only one stress-strain curve for the material

behaviour. This is the major drawback when an isotropic material model is used for HSS pipes, because it results in unrealistic material responses and eventually incorrect predictions of the behaviour. For example, if LT stress-strain data are used in an isotropic material model, the material response in LC and TT would not be similar to real responses.

The combined hardening material model proposed in Chapter 2 shows excellent capability in modeling all three above-mentioned behaviours at the same time. Therefore, the results of this model are more reliable than isotropic modeling. Using the combined hardening model is more advantageous in simulating structural phenomena involving material responses in more than one direction and/or under both tension and compression stresses.

The combined hardening material model makes it possible to better investigate the process of buckling under more general conditions. This chapter looks into how different material responses of HSS pipe (LT, TC, and TT) dominate the buckling process under generalized conditions similar to the field conditions.

The primary goal of this chapter is to provide a better understanding of the importance and contribution of each material response of HSS pipes in the buckling resistance under generalized imposed compressive deformations. The secondary objective of this chapter is to investigate the effects of compressive longitudinal strain distribution (due to different load combinations) on the buckling resistance of HSS pipes.

## **5.1 Tested Cases Studied**

Among 15 HSS pipes used to verify the combined hardening material model in Chapter 3, five pipes (i.e. HSSP#11 to HSSP#15) have material test results for LT, LC, and TT. These pipes were made of three different types of HSS

materials: types B, F, and G. The detailed material behaviour and the results of the combined hardening material modeling of these material types are discussed in Chapter 2. The buckling analyses results of HSSP#11 to HSSP#15 with combined hardening material properties and isotropic material properties (using longitudinal tension data) are shown in Chapter 3.

The first step was to repeat the buckling analyses on the finite element models of HSSP#11 to HSSP#15 with isotropic material properties using average LC and TT data. Comparing the results of these three isotropic pipes (i.e. LT, LC and TT) with the results of the combined hardening models as well as the test results, provides a good understanding of the mechanism and the effects of different material responses on the buckling process of HSS pipes. The next section describes different material models considered for the finite element analyses in this chapter.

### **5.1.1 Different Material Models**

Four different material modeling methods were considered for each finite element model:

- The combined hardening material model (CH)
- The isotropic material model using longitudinal stress-strain data of the tension test (LT model)
- The isotropic material model using longitudinal stress-strain data of the compression test (LC model)
- The isotropic material model using transverse stress-strain data of the tension test (TT model).

The average errors of the combined hardening technique in the longitudinal and transverse directions for material type F were the closest to the average error in

entire material database among all the HSS pipe material types. The longitudinal tension data from one strip test and four round-bar tests are shown in Figure 5-1 along with the average curve of these four stress-strain data between 0.0-3.0% total strain. Figure 5-2 shows the transverse tension data from four round-bar coupon tests and the average curve between 0.0-3.0% total strain. These average curves of longitudinal and transverse tension tests were used to define the isotropic elastic and plastic stress-strain relationship for the LT and TT models. These average curves were also used to calibrate the combined hardening material model for the reference material model (CH).

Figure 5-3 shows the compression stress-strain data from three round-bar tests on material type F. As this figure shows, the range of compressive data in the longitudinal direction is significantly smaller than the tension data due to the limitations associated with compression tests. The average of three compressive stress-strain data was also shown in Figure 5-3. This average curve is linearly extended to 3.0% total strain. The curve's slope was considered equal to the slope of the linear strain hardening region of the combined hardening model (i.e., the average slope of the linear strain hardening regions of longitudinal and transverse tension responses). A similar approach was used to extend the compressive stress-strain data of material types B and G.

These LC average curves were used to define the elastic and plastic regions of material responses of isotropic (LC) models. For the elastic region of each isotropic material model (i.e., LT, TT, and LC), the modulus of elasticity was equated to the slope of the linear-elastic part of the model's corresponding average curve. Poisson's ratio equal to 0.3 was used for all material models. Data pairs of the stress-plastic strain were extracted from each average curve using their corresponding modulus of elasticity. These pairs of stress-plastic strain data were used in ABAQUS to define the plastic hardening of each isotropic material

model. For the combined hardening material model, however, the details of model calibration were similar to what is described in Chapter 2.

The initial imperfection pattern used to trigger the buckling was similar to the pattern used in Chapter 3 for finite element models (i.e., smooth half-ring imperfection pattern on the compression side having the point of maximum out-of-roundness one element away from the middle cross-section of the pipe). The length of the imperfect zone and the maximum initial out-of-roundness were also similar to the values used in Chapter 3 for the finite element models of these pipes.

For the pressurized pipes, the internal pressure was applied as a distributed load on the internal surface of the shell elements forming the pipe, collars, and end plates, before applying the end rotations. A concentrated compressive force was applied at the top pivot point to cancel out the axial resultant force due to the internal pressure. Similar to the test conditions, analyses were performed by applying equal rotations at both pivot points to generate pure bending throughout the pipe's length. The arc-length control technique (modified Riks method) was used to carry out the buckling analyses.

The variation of global moment with respect to the average compressive strain was extracted from the analysis results and compared with the experimental measurements in Figure 5-4 to Figure 5-8 for HSSP#11 to HSSP#15, respectively.

As anticipated, the buckling results from the combined hardening models are in better agreement with the actual experiments among all different material modeling methods. Among the isotropic models, the isotropic LT model resulted in the lowest maximum global moment and the highest critical buckling strain (CBS), while the TT model delivered the highest maximum global moment and the lowest CBS. The maximum global moment and its corresponding compressive

strain values of the isotropic LC model are between the LT and TT models' values.

Another observation is that for HSSP#11, which is an unpressurized pipe, the LC model gives the closest response to the experimental results (and the CH model results) among all three isotropic models. For HSSP#12 to HSSP#15 (pressurized pipes), however, the result closest to the experimental result belongs to the TT models. This phenomenon is discussed further in Section 5.3, this chapter's results and discussion section.

The above-mentioned models simulate actual test conditions and their results are comparable to experimental measurements. These results provide a valuable tool for studying the effects of different material responses on the buckling of HSS pipes (see section 5.3.1). However, the load combination used in these models covers a limited range compared to the loads on a real pipeline. In order to expand the load combinations, extensions were applied to one unpressurized and one pressurized pipe. This extension was designed to investigate the effects of different material responses of HSS pipes under the conditions expected in the field. The details of these extensions are described in the next section.

### **5.1.2 Extensions to the Selected Models**

For the defined objectives of this chapter, it was decided to expand this study on the finite element models of one unpressurized and one pressurized pipe which were already validated with experimental results in Chapter 3. The best candidates for the expansion were HSSP#11 and HSSP#14 because they were the only pair of unpressurized and pressurized pipe segments in the database made from similar material (material type F) of which all three material test results (LT, LC and TT) were available.

The main objective of the model extensions was to make the buckling conditions of the pipe models more similar to the real field conditions. These extensions provide a broader range of different factors that might influence the study. Three types of extensions were applied to the finite element models. These extensions were applied in the models' length, loading scheme, and pattern of initial imperfection.

Since considering variations in all affecting variables (important for pipe buckling) increases the number of required analyses exponentially, it was decided to limit the study to one unpressurized and one pressurized pipe made of same type of material with a constant magnitude of  $D/t$  ratio and maximum imperfection magnitude.

#### **5.1.2.1 Model Length**

The first extension applied to the models was increasing the model's length to reduce the end effects. The length of HSSP#11 and HSSP#14 models were 3.5 times their outside diameter. As recommended in the literature, the lengths of the models were increased to five times their diameters to minimize end effects on the buckling process (Dorey et al., 2001; and Del Col et al., 1998).

The number of elements used in 180° of the models' circumference remained at 40. The number of element rows in the pipe length was increased from 104 to 130 elements, keeping the aspect ratio of the pipe elements close to one. The first and last six rows of elements were assigned to collars with wall thicknesses two times the pipe's wall thickness with the same material properties as the pipe elements. The end plates were modeled with fully elastic behaviour with the same modulus of elasticity as the pipe material.

The boundary conditions of the pivot points and nodes on the longitudinal symmetry plane of the modeled pipe were also exactly similar to the models used in Chapter 3.

### **5.1.2.2 Loading Schemes**

The local buckling of actual pipelines happens due to the localization of excessive compressive deformations in the critical cross section. Compressive strain can be caused by axial compression and bending deformations. The buckling tests on HSSP#11 and HSSP#14 were carried out under a monotonically increasing curvature which results in developing an internal pure bending moment in the entire pipe's length. In a real pipeline, environmentally imposed deformations usually cause a combination of axial compression and bending moment in the pipe. Based on the nature of imposed deformations, the contribution rate of bending and axial compressive deformations can vary quite significantly. Consequently, the component of either one of the compressive deformations might be considerably larger than the other.

Different load combinations cause different strain distributions in the critical cross section of the pipe that might change the way that each material property affects the buckling resistance and eventually the CBS. To see the effects of different material properties on the buckling response of HSS pipes in a generalized loading condition, it was decided to extend the loading pattern applied to the pipes' models. The extended loading pattern covers a wider range of deformation that might be imposed to energy pipelines, and provides a wider range of strain distributions on the pipe's critical cross-section.

Four different combinations of axial compressive load and bending moment were considered. While the bending moment was applied on the top and bottom pivot points, compressive axial forces were applied on the centre of the top end plate. Four different magnitudes of axial force were used, resulting in four different

ratio of the axial compressive force-to-the bending moment. These ratios were kept constant during the buckling analyses which makes the scenario equivalent to buckling under eccentric (axial) compressive force causing internal (axial) compressive force plus bending moment. The bending moment in these cases is proportional to the magnitude of the compressive force and the ratio of the force to the moment depends on the distance between the pipe longitudinal axis and the line of action of the force.

The combinations of axial compressive force and bending moment were selected as such the initial (linear-elastic) distances of the neutral axes to the pipe's longitudinal axes  $y$ , were  $0.0D$ ,  $0.5D$ ,  $1.5D$ , and  $5.0D$ . Although the strain distributions and the actual neutral axis locations change after the first yield in the pipe's body (and also due to the second order effects), the initial (linear-elastic)  $y/D$  is still a suitable indicator of the ratio of bending to compression deformations. Figure 5-9 shows all initial (linear-elastic) cross-sectional strain distributions as indicators of the ratio of compressive axial force-to-the bending moment applied to the pipe models.

### **5.1.2.3 Initial Imperfections Patterns**

The last extension considered for the pipe models was the applied imperfection pattern. As discussed in previous chapters, initial imperfection magnitude, location and pattern have significant effects on the pipe buckling response and the CBS. Researchers have introduced idealized imperfection patterns for use in finite element simulations of pipes for which no initial imperfection data are available. Employing idealized imperfection patterns is also indispensable in numerical studies of a pipe's buckling behaviour when the models simulate hypothetical pipes.

The idealized imperfection pattern used for finite element models of tested pipes in Chapter 3 are similar to the so-called half-ring imperfection patterns introduced

by Dorey et al. (2006). This pattern applies out-of-roundness in a certain gauge length around 180° of the pipe's circumference.

Dorey et al. (2006) also introduced two more idealized imperfection patterns for buckling analyses of plain pipes, i.e., blister and full-ring types. The blister-type imperfection applies the out-of-roundness in 90° of a pipe's circumference centred at the extreme compression fibre. In the full-ring imperfection, the pipe's radius changes uniformly in the entire circumference of the cross-sections located in the imperfect zone. Looking at the cross-sections of these imperfection patterns, the blister and half-ring types are asymmetric in the cross-section, the blister type is more skewed than the half-ring type, and the full-ring type is symmetric. Dorey et al. (2006) recommended the blister and half-ring patterns for pipes under loadings dominated by bending moments. They also recommended using a full-ring imperfection type for pipes under loadings dominated by compression force. Their logic was to use the imperfection type that has a cross-sectional distribution compatible with the distribution of compressive strain in the cross-section.

As in this study, the loading scheme varies from pure bending to nearly pure compression, using one type of the above-mentioned imperfection patterns that might have resulted in a subjective CBS and, eventually, biased conclusions. Hence, it was decided to repeat the buckling analyses with all three aforementioned imperfection patterns. Figure 5-10 exaggeratedly shows these imperfection patterns applied to the finite element models.

A magnitude of maximum imperfection equal to 20% of the pipe's wall thickness with a gauge length equal to the pipe's diameter (similar to the imperfection gauge length used in finite element models' validations in Chapter 3) was used for all pipe models. The imperfection patterns were applied in a way that the point of the maximum imperfection placed one element off the pipe's mid-span. Figure 5-10 shows the maximum imperfection,  $I_{\max}$ , and the gauge length of the

imperfect zone,  $L_{II}$ . The pipe's original radius is shown as  $R^o$  and the distance of the imperfect wall to the pipe's axes is shown as  $R$ . In Figure 5-10, the imperfections vary from a very skewed ( $90^\circ$ , blister) to a symmetric ( $360^\circ$ , ring) pattern in any cross-section of the imperfect zone.

## 5.2 Cases Analyzed

Having four material modeling methods, four load combinations, and three types of imperfection patterns, the unpressurized and pressurized pipe models were analyzed with 48 different combinations. The summary of different cases considered for all 96 (i.e.  $3 \times 4 \times 4 \times 2$ ) combinations analyzed in this case study is described below.

- Internal pressure: 2 cases of internal pressure;  $\sigma_h=0.0$  and  $\sigma_h=77.0\%$  of SMYS
- Material models: Anisotropic (CH); 3 isotropic (LT, LC and TT) models
- Load combinations: 4 cross sectional strain distributions;  $y/D=0.0, 0.5, 1.5$  and  $5.0$
- Imperfection type: 3 patterns; blister (BL), half ring (HR) and full ring (FR)

The same analysis method (modified Riks method) as previous analyses was used to carry out the buckling analyses. The results of the buckling analyses are discussed in the next section.

## 5.3 Results and Discussion

The method of the CBS calculation described in Chapter 3 is valid in any linear cross-sectional strain distribution. A similar equation was used to extract the CBS from finite element models. Figure 5-11 to Figure 5-13 show the variation of the CBS with the  $y/D$  ratio for unpressurized models with blister, half-ring, and full-ring imperfections, respectively. Similar results of the pressurized pipe models are shown in Figure 5-14 to Figure 5-16.

As these figures show, for all combinations of  $y/D$  and imperfection types, the isotropic models using longitudinal tension data provided the upper bound of the CBS. The isotropic models that use transverse tension data gave the lower bound response. The anisotropic models and isotropic models with longitudinal compression data resulted in a CBS between these limits.

The response patterns of all pipes with similar internal pressure are uniform, regardless of imperfection types. However, different imperfection patterns resulted in slightly different CBS responses (e.g., the CBS from models having full-ring imperfections generally were the lowest and the CBS from the models having blister-type imperfections were the highest among the pipes with similar material property and internal pressure). Nevertheless, it can be concluded that the distribution of imperfections in a pipe's cross-section does not have a significant effect on the buckling response pattern under any combination of axial load and bending moment.

### 5.3.1 Effects of Directional Material Responses on HSS Pipes Buckling

The primary goal of this part of the study was to see the effects of each material response (i.e., LT, LC, and TT) on the buckling behaviour of HSS pipes. In general, the combined hardening material model gives the most accurate results in

the buckling analysis of HSS pipes because it is able to simulate the material responses both in longitudinal and transverse directions under tension and compression, simultaneously. Therefore, the significance of the effects of each material response on the buckling process appears by comparing the buckling response of isotropic pipe models with the same pipe that has the combined hardening material properties.

Looking at Figure 5-11 to Figure 5-13, it is evident that the CBS of unpressurized pipe models with combined hardening material properties is closer to that of isotropic models using longitudinal compression data. In pressurized pipes, however (as shown in Figure 5-14 to Figure 5-16), the CBS of pipe models with combined hardening material properties is closer to that of the isotropic models using transverse tension data. These phenomena are independent of the employed imperfection pattern and the magnitude of the  $y/D$  ratio (i.e., different combinations of axial load and bending moment).

Pipe buckling is a complicated process affected by several factors, including material response. The CBS used in strain-based design defines the amount of compressive deformation a pipe segment can accommodate before buckling. Since the buckling usually occurs in an inelastic range, the CBS is affected by both material strength and stiffness. Under different loading scenarios that cause buckling, the critical area of the pipe body undergoes different stress paths. If a material model can predict material's strength and stiffness under that specific stress path, it can give the best results under that specific loading condition, and govern the buckling process.

The best way to observe the mechanism of each material response affecting the buckling process is to look at the stress paths of pipe elements in the stress space. Figure 5-17 shows the stress paths of unpressurized pipe elements under longitudinal tension and compression. The yield surfaces of four material models

(i.e., combined hardening, LT, LC, and TT isotropic hardening models) are shown in this figure for material type F. As discussed in Chapter 2, the combined hardening output for longitudinal tension and compression, as well as for transverse tension, was adequately close to the real responses. Therefore, to ease the comparisons, the isotropic yield surfaces were drawn based on the combined hardening outputs instead of real responses. The combined hardening model crosses the longitudinal axis at longitudinal tensile and compressive proportional limits and the transverse axis at nominal yield stress. For isotropic models, however, the yield surface is centered at the centre of the coordination system resulting in similar material responses in all directions under tension and compression.

In order to accurately estimate the CBS, the evolution of the longitudinal compressive strain should be accurately monitored under the load combinations that cause buckling. As Figure 5-17 shows, for an unpressurized pipe under a combination of bending moment and axial force, the isotropic LC model can simulate the stress evolution for elements above the neutral axis that have longitudinal compressive stress. Therefore, among three isotropic models, the LC material model that simulates the compressive stress evolution accurately, provides a better estimation of the compressive strain before buckling. It can be concluded that the material response in longitudinal compression is the most dominating material property that controls the buckling of unpressurized pipes.

During the buckling of pressurized pipes, elements under longitudinal tensile and compressive stresses have a biaxial stress state due to the tensile hoop stress caused by internal pressure. This condition creates a stress path similar to what is shown in Figure 5-18. Under the internal pressure, all elements have tensile hoop stress,  $\sigma_h$ . As discussed in Chapter 3 for isotropic LT models, if the internal pressure is high enough to cause hoop stress larger than the tensile longitudinal proportional limit, the yield surface expands to the  $\sigma_h$  symmetrically in all

directions. For the combined hardening material model as well as for the isotropic LC and TT models, the part of the stress path corresponding to the hoop stress is located inside the yield surface. This is because, in these models, the elastic range in the transverse direction is usually higher than the hoop stress caused by the internal pressure.

When the axial force and bending moment generate longitudinal compressive stress in pressurized pipes, the stress path continues in the stress space from  $\sigma_h$  (on the transverse axis), parallel to the longitudinal axis. For CBS calculations, the evolution of the longitudinal compressive strain should be estimated accurately. Therefore, the projection of the material compressive stress-strain response in the longitudinal direction determines the evolution of longitudinal compressive strain. Hence, each isotropic material model that gives a material response closer to the combined hardening model (in the fraction of the stress path parallel to the longitudinal axis), gives more accurate CBS results. On the part of the compressive stress path which is parallel to the longitudinal axis in Figure 5-18, the isotropic TT yield surface is closer to the combined hardening model. Therefore, its simulation of compressive strain evolution is closer to the combined hardening material method. In conclusion, the evolution of compressive strain for highly pressurized pipes is dominated by the material tension response in the transverse direction.

### **5.3.2 Effects of Cross-sectional Distribution of Normal Strain on HSS Pipes Buckling**

Another result that can be extracted from Figure 5-11 to Figure 5-16 is that in both unpressurized and pressurized pipe models, the CBS is reduced by increasing the axial compression force. Reducing the CBS is independent of the pipe's initial imperfections and material properties. A major drop in CBS value for both unpressurized and pressurized pipes occurs between pure bending and  $y/D=0.5$

(i.e., when the compressive strain occupies the entire cross section of the pipe). The CBS variations among different cross-sectional strain distributions indicate that the CBS is a function of the applied load. This contradicts with the philosophy behind most of CBC criteria that assumes the CBS independent from the axial load and bending moment combination. Different design criteria predict the CBS without taking the applied load combination (of axial load and bending moment) into account. The key justification for disregarding the effects of the applied load combination is that “buckling of a structural member is a stability phenomenon and the buckling load and its corresponding strain are the function of member’s geometry and not the applied load” (Dorey et al., 2001). The validity of this statement for individual structural elements can be easily justified by examining the buckling strain associated with a column’s elastic buckling (Euler’s) load.

$$\epsilon_{cr} = \frac{\pi^2}{\left(\frac{L_e}{r}\right)^2} \quad (5-1)$$

where

$L_e$ : effective length of the column;

$r$ : radius of gyration.

However, local buckling in energy pipelines is different from the elastic buckling of an individual member, as it occurs in a part of a continuum shell structure and involves plastic deformations. CBS’s sensitivity to the cross-sectional strain distribution shows that during local buckling of pipes, the buckled zone interacts with the adjacent area in the critical cross-section.

In pipelines, the local buckling occurs when the longitudinal strain localizes in a critical zone. This zone surrounds the pipe’s extreme compression fiber. As the pipes are continuum shell structures, buckling requires deformation of not only

the critical zone but also the adjacent area in the cross-section. Therefore, the area engaged in the buckling process is larger than the buckling zone, which is concentrated around the extreme compression fiber.

The buckling zone is the first area of the cross-section that becomes destabilized under compressive strain. The rest of the cross-section provides constrains for this area. Although it is impossible to identify the exact distinction between the buckling and the constraining areas in a buckled pipeline, a schematic illustration can be made, as shown in Figure 5-19.

The constraining action depends on the degree of lateral stiffness that the constraining area can provide against the buckling deformation. The pipe's local buckling usually occurs in the inelastic range. The constraining area's stiffness depends on whether the area is elastic or has already yielded. Looking back at Figure 5-9, with a specific plastic strain of the extreme compressive fiber, the higher  $y/D$  ratio results in larger yielded zone of the cross-section. Hence, the provided constrain is a function of the stress that is applied to the constraining area. The higher the stress on the constraining area, the lower the stiffness it can provide to support the buckling zone. For load combinations with larger compressive axial loads compared to the bending moment, the constraining area becomes smaller and will carry higher compressive stress. Therefore, it can provide smaller constrains for the buckling zone.

Figure 5-11 to Figure 5-16 also show that the cross-sectional strain distribution has different effects on the CBS in unpressurized and pressurized models. By increasing the  $y/D$ , the reduction of CBS is more significant in the pressurized model compared to the unpressurized pipe. The CBS in the unpressurized pipe reduces around 25% compared to 50% in the pressurized pipe for  $0.0 < y/D < 5.00$ . This dissimilarity can be explained by the difference between buckling modes in unpressurized and pressurized pipes.

Under all combinations of axial load and bending moments in this study, unpressurized buckled pipes have an inward diamond shape in the buckling zone, while pressurized buckled pipes have a bulged shape. Typical buckled unpressurized and pressurized pipe models with the same end rotations are shown in Figure 5-20a and Figure 5-20b, respectively.

In both unpressurized and pressurized pipes, the buckling deformation initiates at the extreme compression fiber. As Figure 5-20 shows, the bulge penetrates to the other side of the pipe and occupies a larger part of the cross-section because it better agrees with the pipe's circular cross-section. But the inward diamond dent does not propagate as much as the bulge does, and it remains in the same side as the critical zone. In other words, the buckling in a pressurized pipe engages a larger portion of the cross-section compared to the buckling in a unpressurized pipe. Hence, due to the buckling mode, the buckling zone in the pressurized pipe has a stronger interaction with the rest of the critical cross-section and more sensitivity to the cross-sectional strain distribution compared to the unpressurized pipes.

## **5.4 Summary**

The results of this chapter show that the buckling response of unpressurized HSS pipes is highly affected by a pipe's material behaviour under longitudinal compression. The results also show that the buckling responses of highly pressurized HSS pipes are dominated by the material response under transverse tension. Although the material response under longitudinal tension has been the most common material test for steel pipes, it does not directly affect the buckling behaviour of either pressurized or unpressurized HSS pipes. The above conclusions are valid under any combination of axial compressive load and

bending moment and any distribution of imperfection within the pipe's cross-section.

In addition, energy pipelines may show a lower longitudinal strain capacity against operational or environmental sources of imposed displacements, which cause more axial than bending compressive deformations. The CBS prediction criteria developed by pure bending condition may result in un-conservative estimations for real situations with axial compression components.

## References

Del Col P.R., Grondin G.Y., Cheng J.J.R. and Murray D.W., (1998), “Behaviour of Large Diameter Line Pipes Under Combined Loads”, Structural Engineering Report No. 224, Department of Civil and Environmental Engineering, University of Alberta, Edmonton, Alberta, 174 pages.

Dorey A.B., Cheng J.J.R. and Murray D.W., (2001), “Critical Buckling Strain in Energy Pipelines”, Structural Engineering Report No. 237, Department of Civil and Environmental Engineering, University of Alberta, Edmonton, Alberta, 346 pages.

Dorey A.B., Murray D.W. and Cheng J.J.R., (2006), “Initial Imperfection Models for Segments of Line Pipe” *Journal of Offshore Mechanics and Arctic Engineering*, 128(4) pp. 322-329.

Tsuru E., Agata J. and Nagata Y., (2010), “Analytical Approach for Buckling Resistance of UOE Linepipe with Orthogonal Anisotropy under Combined Loading”, *Proceedings of the 8th International Pipeline Conference*, American Society of Mechanical Engineering, Calgary, Alberta, v4, pp 67-75.

**Figures**

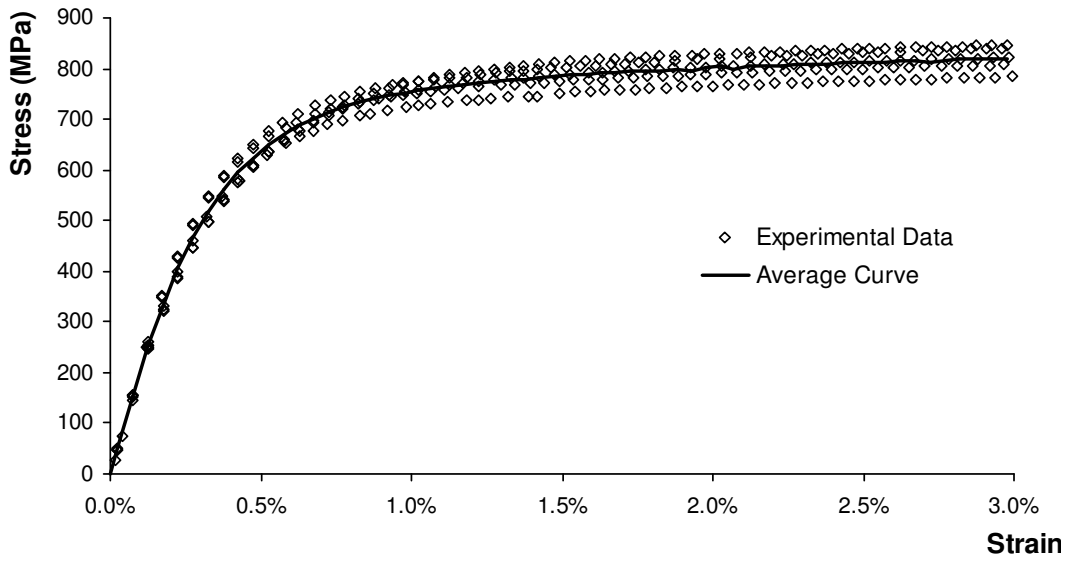


Figure 5-1 Longitudinal stress-strain data from the material tension test and the average curve used in the LT isotropic models

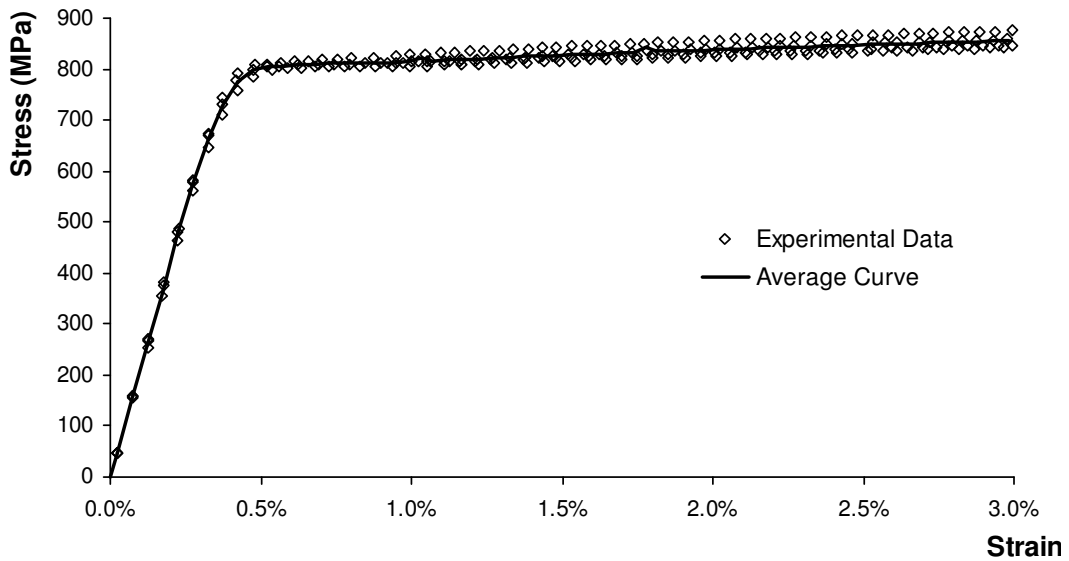


Figure 5-2 Transverse stress-strain data from the material tension test and the average curve used in the TT isotropic models

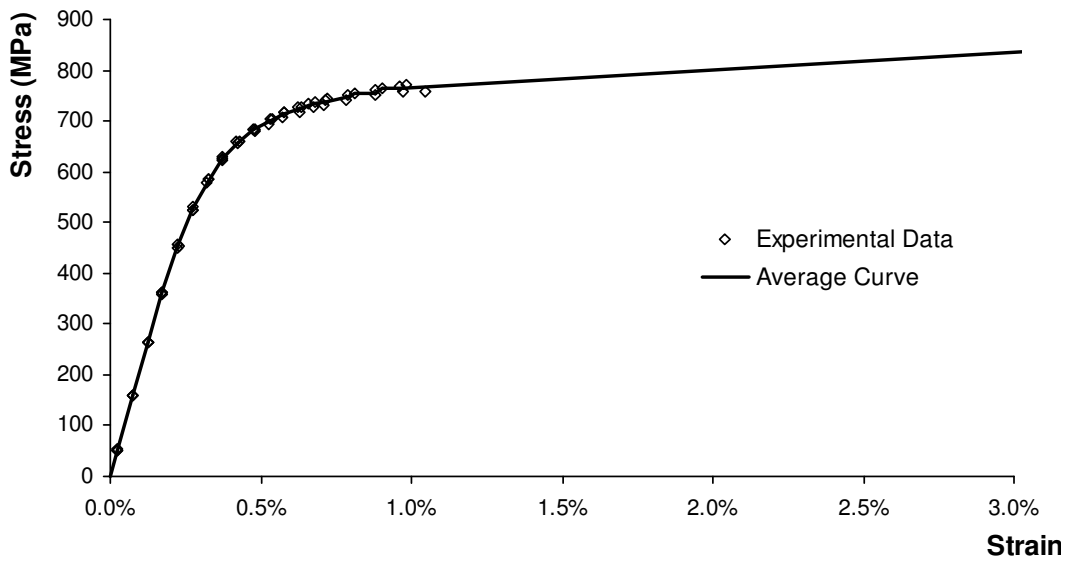


Figure 5-3 Longitudinal stress-strain data from the material compression test and the extended average curve used in the LC isotropic models

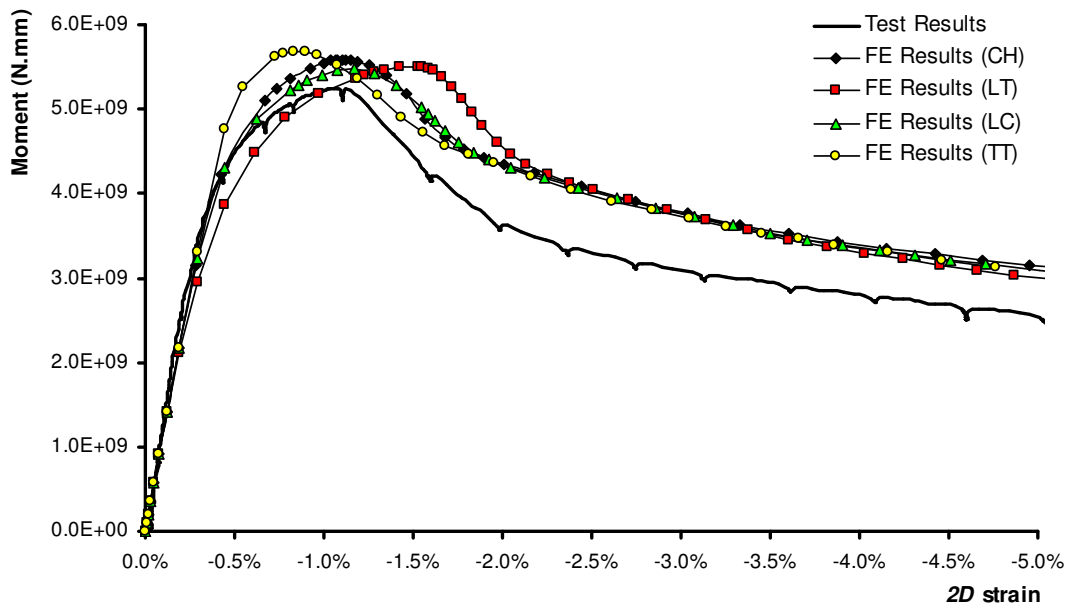


Figure 5-4 Buckling responses from finite element models with different material models compared with the experimental result for HSSP#11

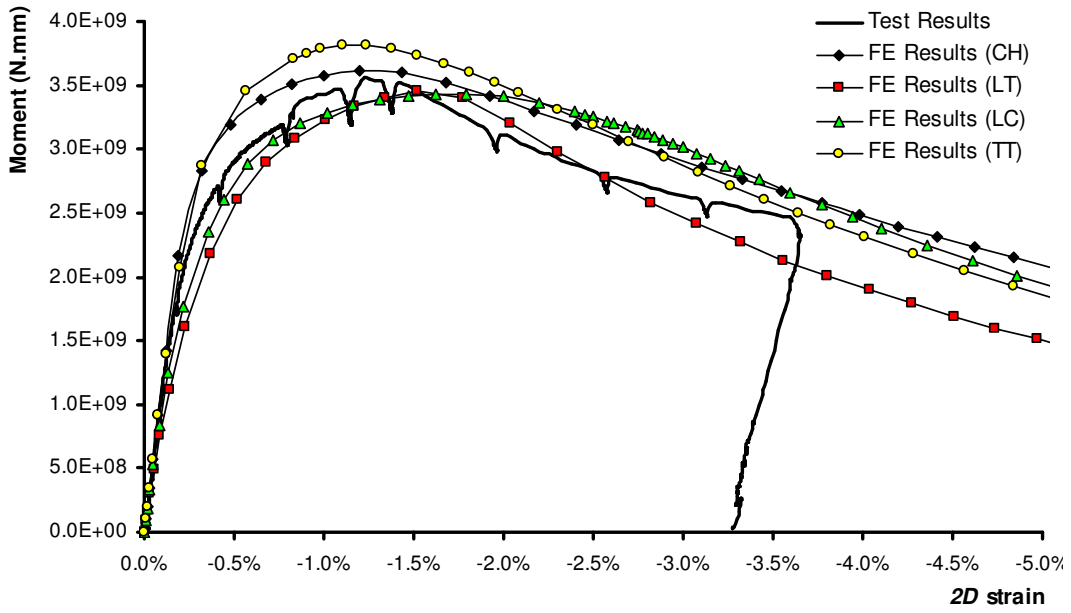


Figure 5-5 Buckling responses from finite element models with different material models compared with the experimental result for HSSP#12

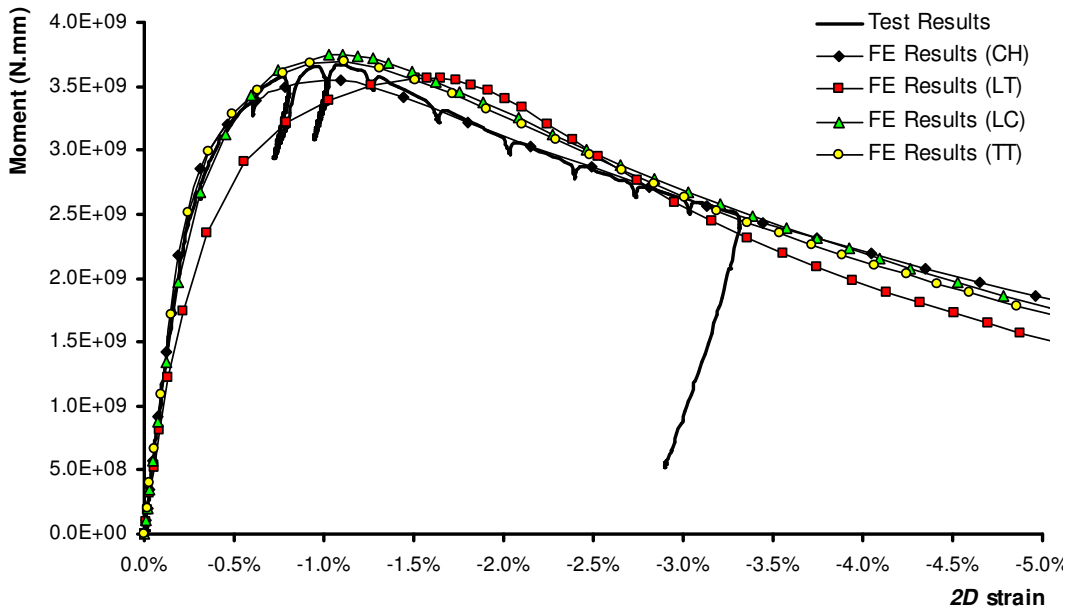


Figure 5-6 Buckling responses from finite element models with different material models compared with the experimental result for HSSP#13

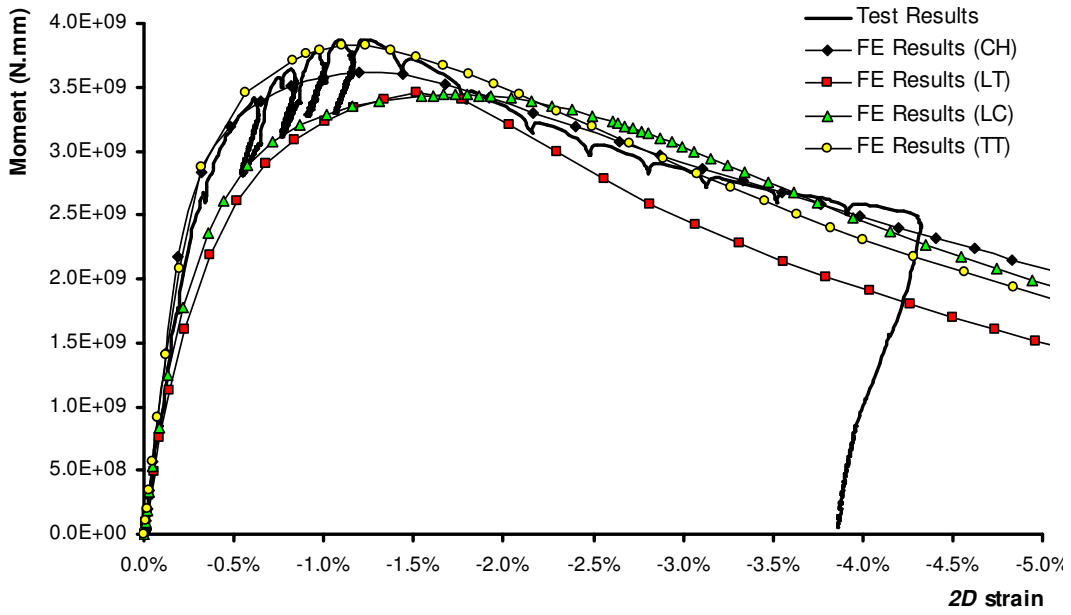


Figure 5-7 Buckling responses from finite element models with different material models compared with the experimental result for HSSP#14

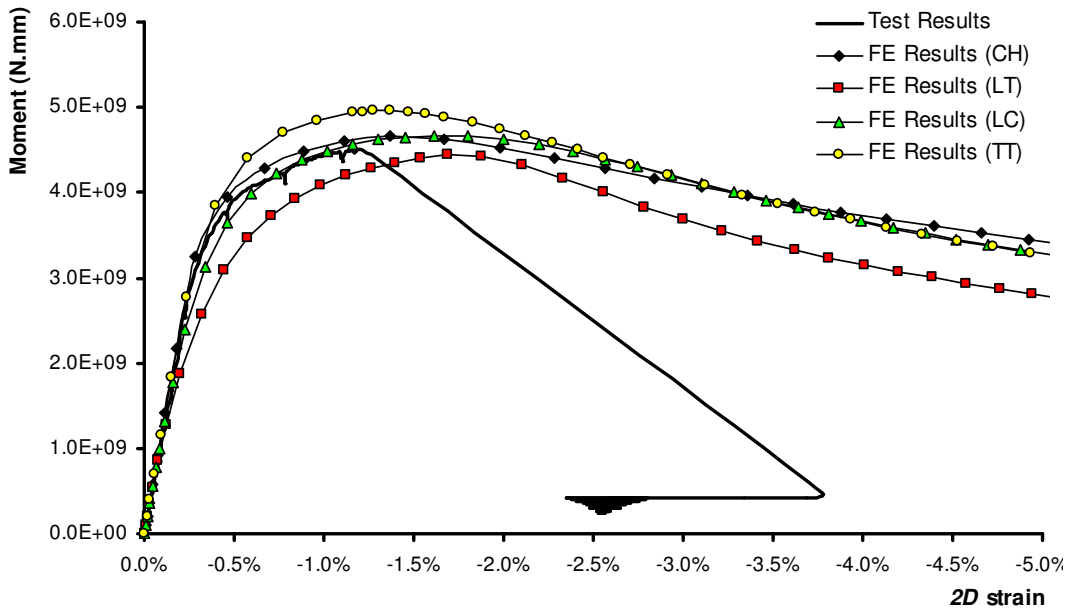


Figure 5-8 Buckling responses from finite element models with different material models compared with the experimental result for HSSP#15

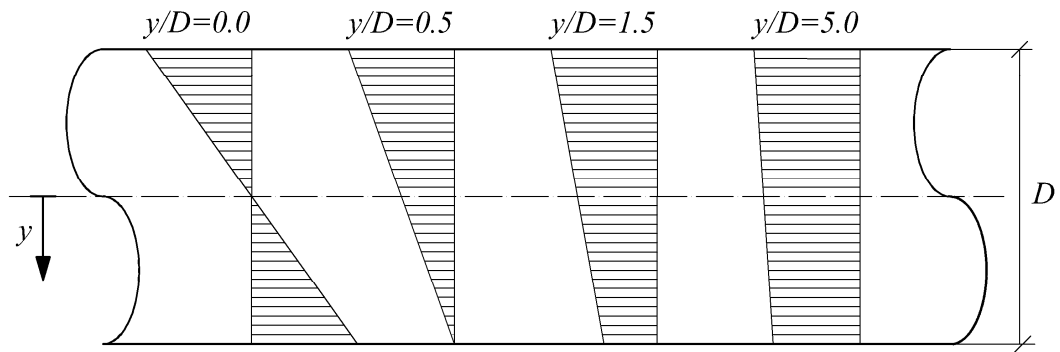


Figure 5-9 Different initial (linear-elastic) strain distributions as indicators of different ratio of applied axial compressive force-to-bending moments

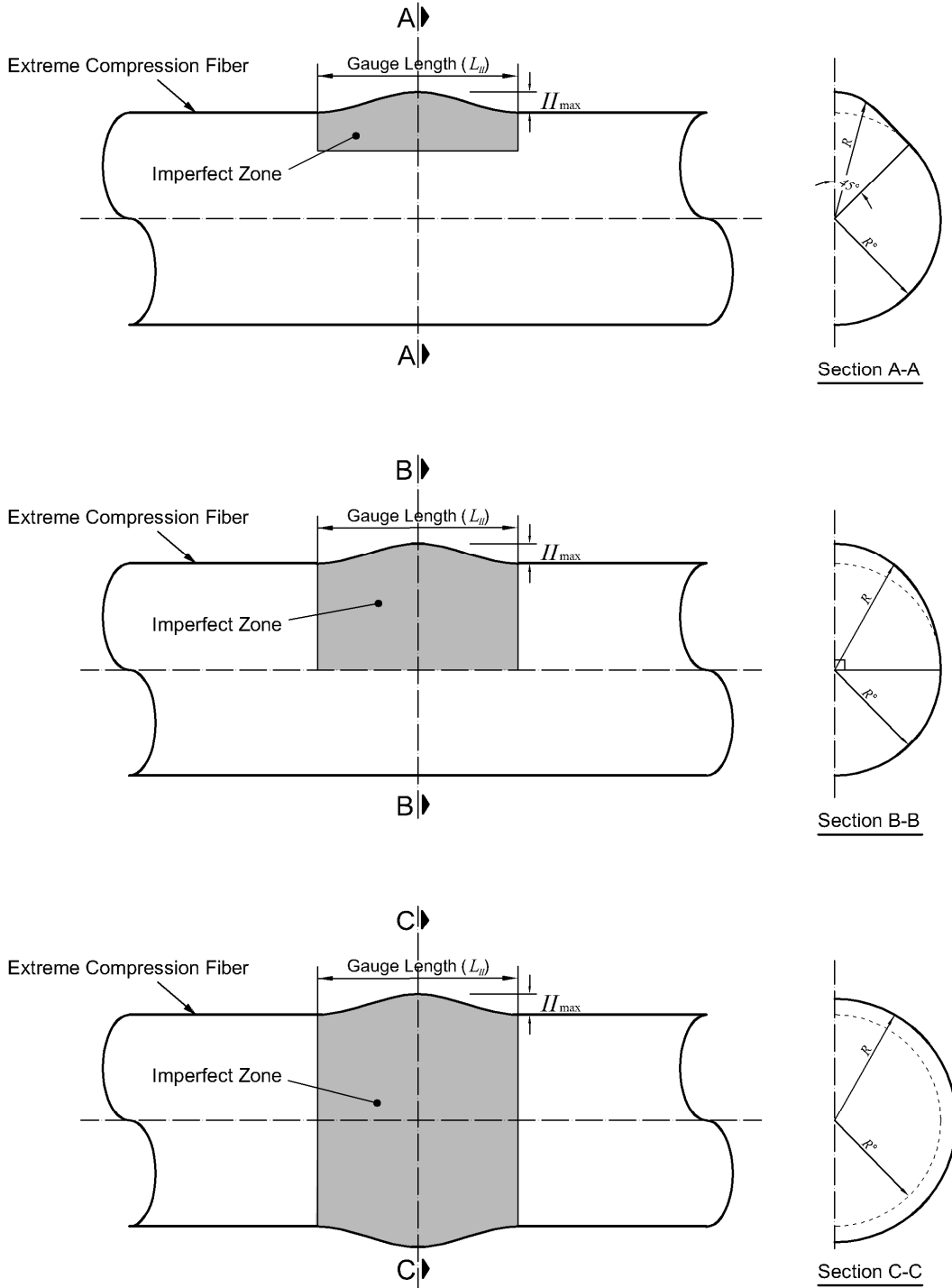


Figure 5-10 Different imperfection patterns used in pipe models

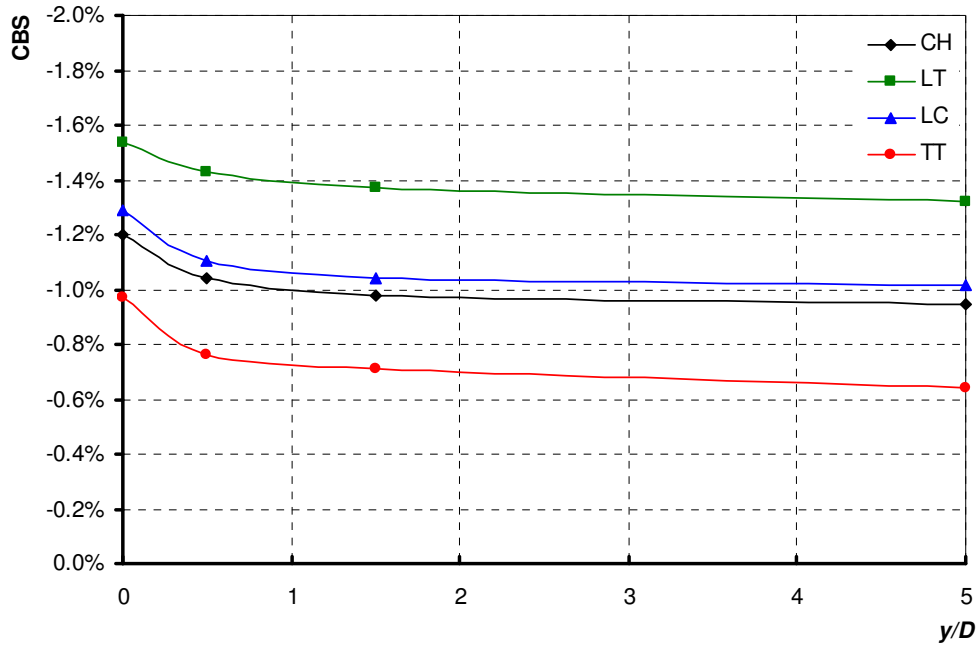


Figure 5-11 Variation of the CBS with the  $y/D$  ratio for the unpressurized pipe with a blister-type imperfection pattern and different material modeling methods

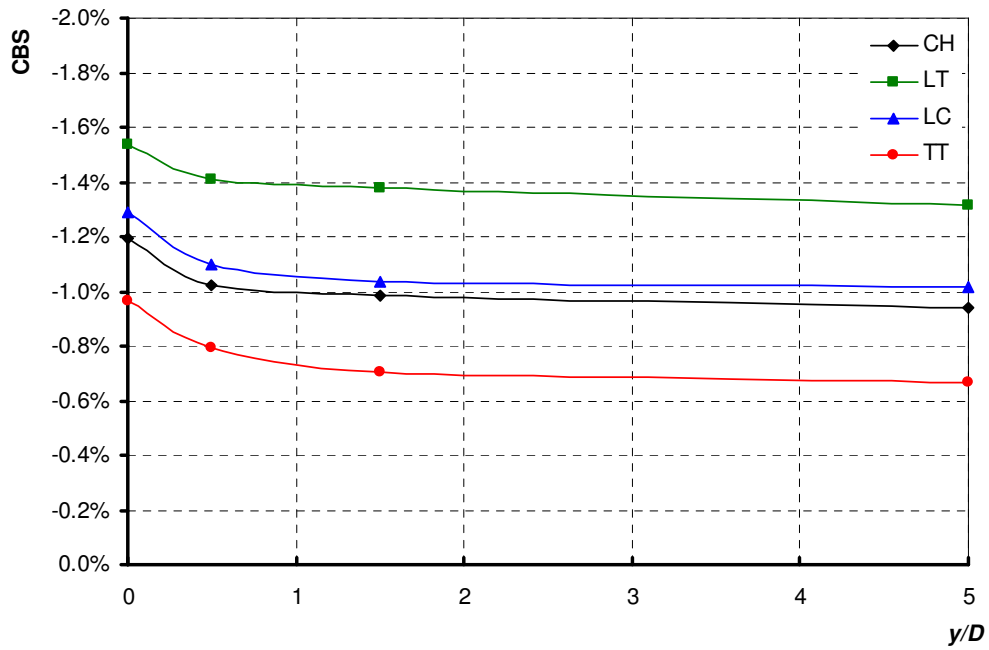


Figure 5-12 Variation of the CBS with the  $y/D$  ratio for the unpressurized pipe with a half-ring type imperfection pattern and different material modeling methods

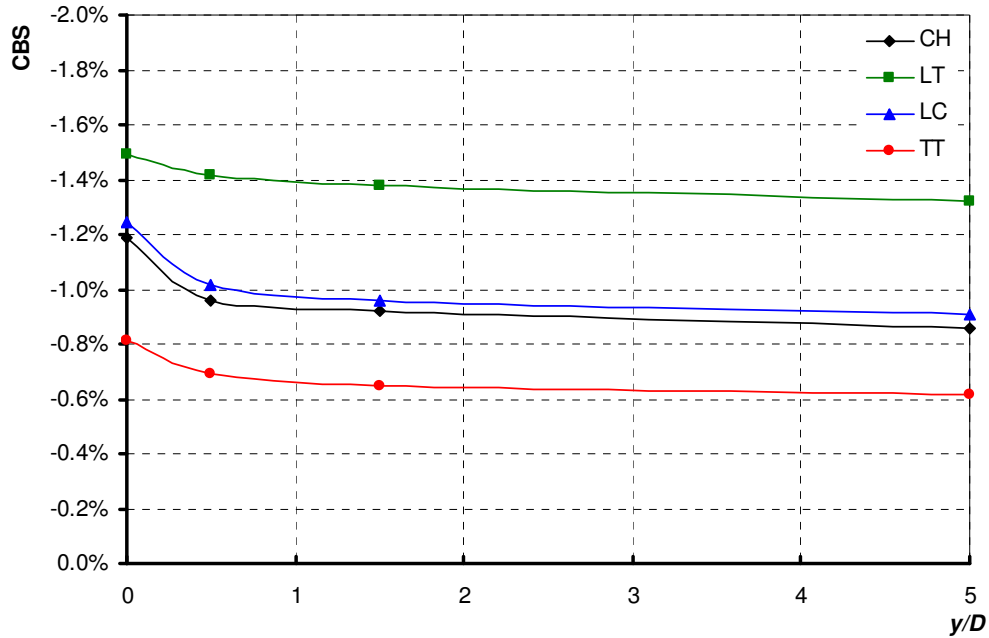


Figure 5-13 Variation of the CBS with the  $y/D$  ratio for the unpressurized pipe with a full-ring type imperfection pattern and different material modeling methods

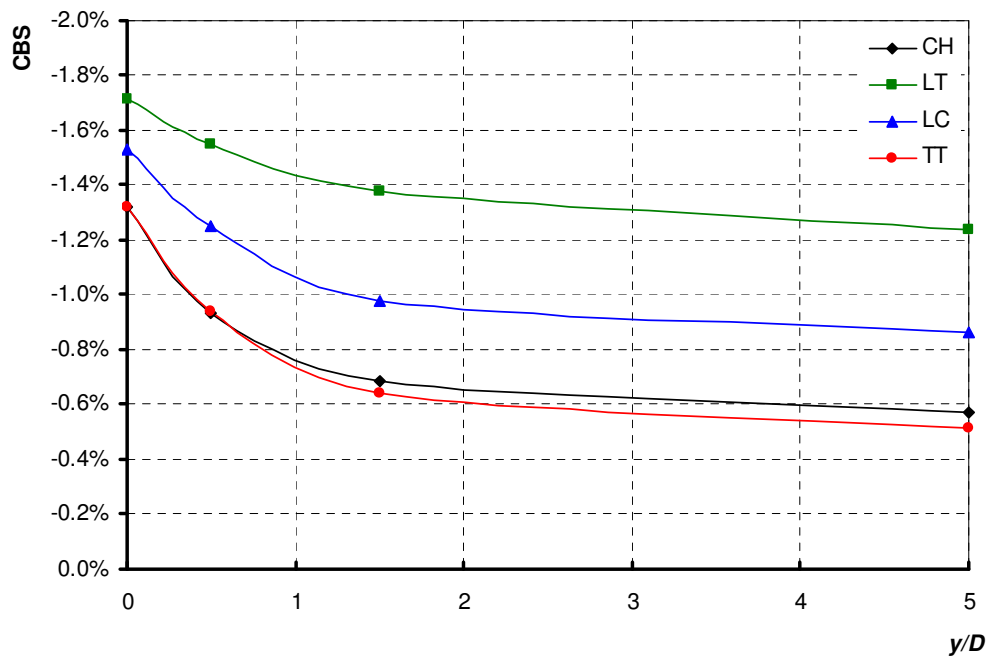


Figure 5-14 Variation of the CBS with the  $y/D$  ratio for the pressurized pipe with a blister-type imperfection pattern and different material modeling methods

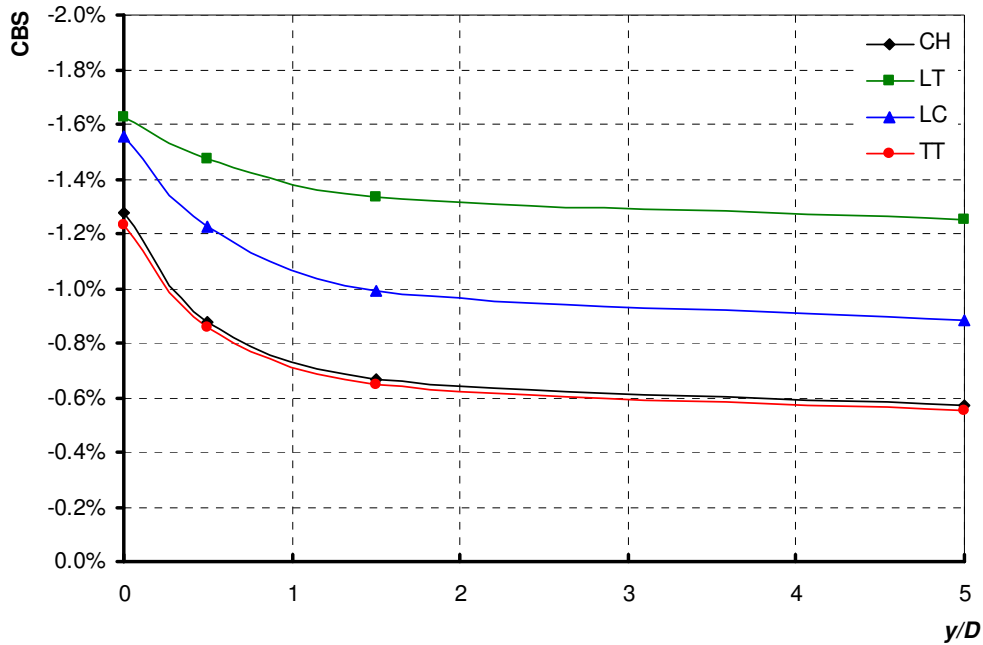


Figure 5-15 Variation of the CBS with the  $y/D$  ratio for the pressurized pipe with a half-ring type imperfection pattern and different material modeling methods

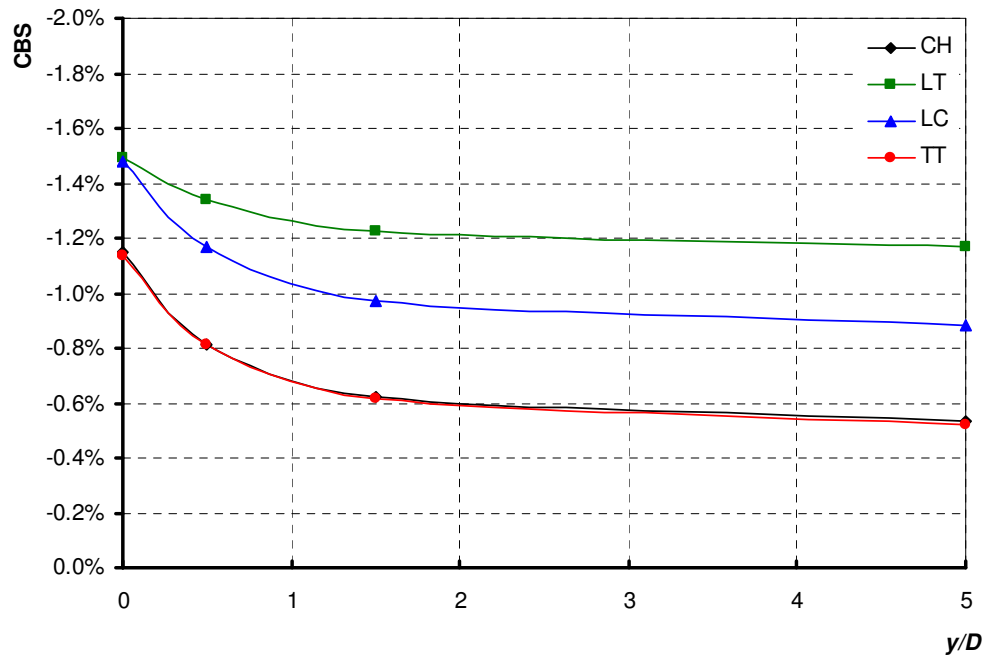


Figure 5-16 Variation of the CBS with the  $y/D$  ratio for the pressurized pipe with a full-ring type imperfection pattern and different material modeling methods

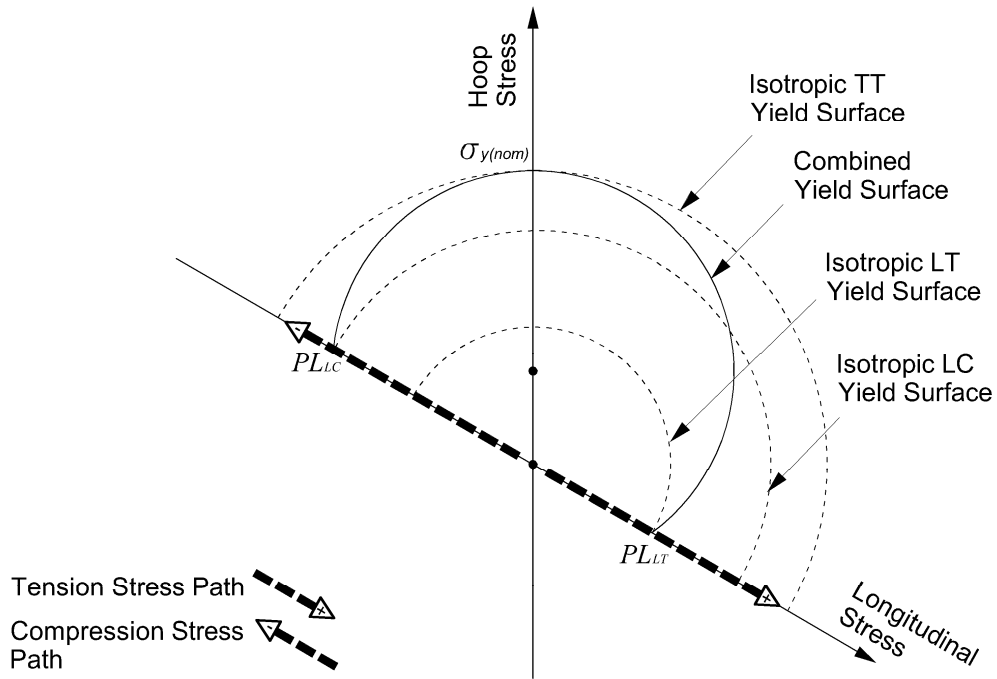


Figure 5-17 Stress path of unpressurized pipe elements under longitudinal compression

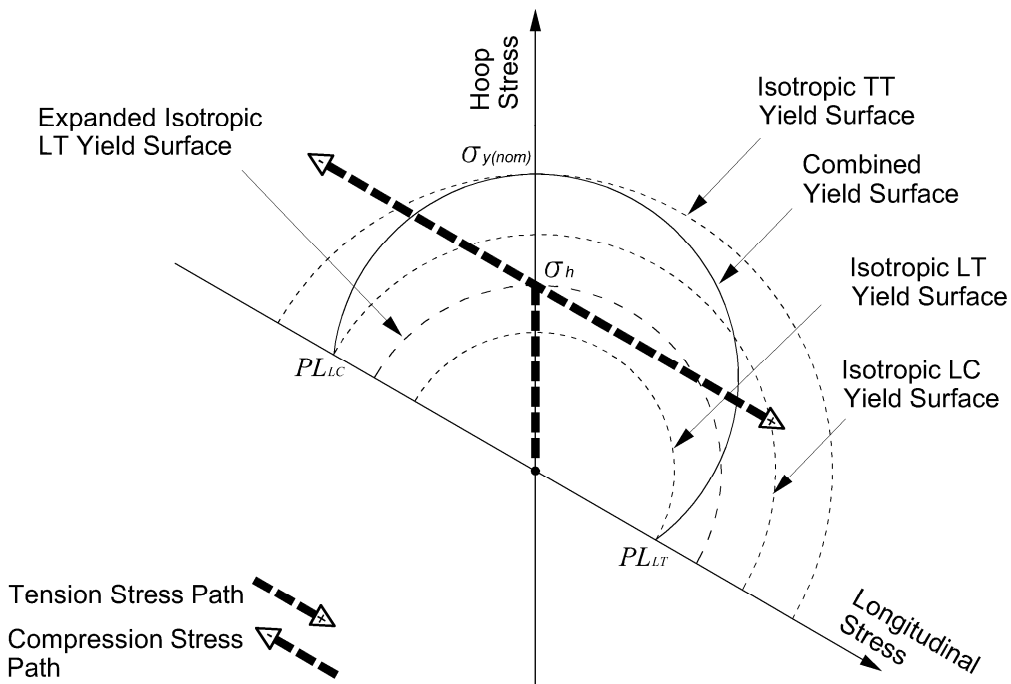


Figure 5-18 Stress path of pressurized pipe elements under longitudinal compression

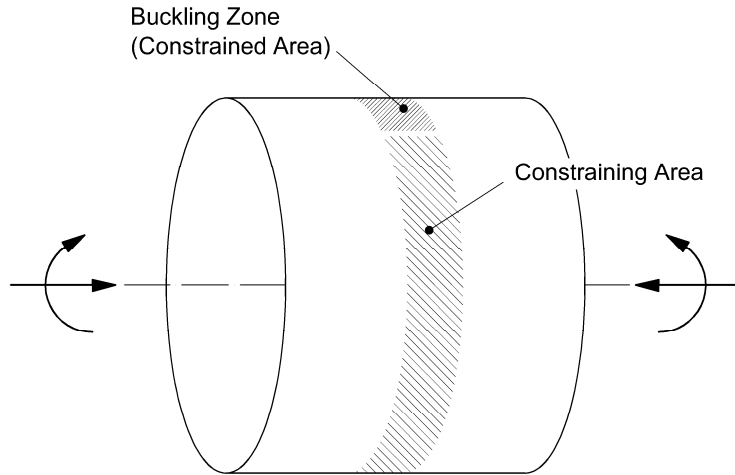


Figure 5-19 E Constrained and constraining area in the critical cross-section of a pipe under compression and bending

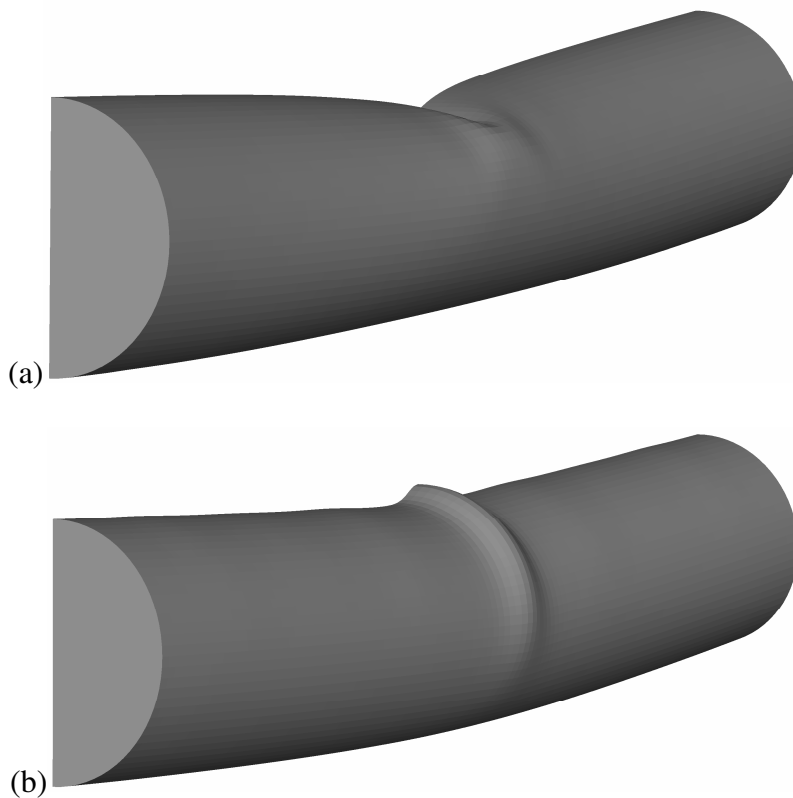


Figure 5-20 Typical buckling modes of unpressurized (a) and pressurized (b) models under compression and bending

## **6 MODELING THE ANISOTROPIC MATERIAL RESPONSE OF THERMALLY COATED HSS PIPES**

The material database used in Chapter 2 belonged to high strength steel (HSS) pipes that had been formed from flat plates through the UOE pipe-making process. The material anisotropy of these pipes is the result of plastic deformations applied in the transverse direction during the expansion stage. The combined hardening model introduced in Chapter 2 showed excellent capability for simulating material responses in different directions under tension and compression. This model can be used for HSS pipes made through a similar production procedure and that have essentially similar material response patterns in longitudinal and transverse directions.

Thermal coating is an additional stage in the production of linepipes that are intended to be used in corrosive environments or transport corrosive products. Exposure to high temperature during thermal coating affects the material response in both directions and eventually changes the material anisotropy pattern from what was observed in Chapter 2. Since the thermal coating changes the material response and anisotropy pattern of HSS pipes, the introduced combined hardening model might provide better results in coated HSS pipes after modifying the calibration method.

The effects of thermal coating on the material response and anisotropy features of HSS pipes are discussed in this chapter. Subsequently, the capability of the combined hardening material modeling method developed in Chapter 2 is tested for these pipes.

The material data and full-scale bending test results of two HSS pipes, one unpressurized and one pressurized, were used to study the buckling resistance of

thermally coated HSS pipes. Based on the results of chapters 4 and 5, some changes were applied to the calibration process of the combined hardening model to minimize the simulation error of the material and buckling tests.

## **6.1 Effects of Thermal Coating on the HSS Pipes' Material**

Anti-corrosion coating is usually added to pipes after the pipe-making, by applying fusion-bond epoxy coating. This process usually requires exposing the pipes to temperatures of 200 to 250°C for five to 10 minutes. The strain accumulated during the pipe-making process, combined with the heat exposure during thermal coating, affects the pipe material's mechanical properties in a process called thermal aging (Seo et al., 2009). The common effect of thermal aging on pipelines' behaviour is degradation of deformability in field application due to reduction of the material ductility (see Shitamoto et al., 2007; and Tsuru et al., 2005).

The common change in the material response due to thermal aging is that the yield stress is increased while the tensile strength remains unchanged, or increases to less of an extent compared to the yield stress. These changes result in lower ductility and work hardening of the coated pipe material compared to the as-expanded pipes. Loss of material work hardening, as well as the pipe deformability due to the thermal coating, is a function of thermal aging effects.

It is believed that the interaction between carbon atoms and dislocations plays the main role in thermal aging. At the coating temperatures, diffusion of free interstitial carbon and nitrogen atoms is activated and these atoms tend to move into dislocation cores. The dislocations become pinned and their mobility becomes more limited. As a result, the stress-strain response of the pipe body is changed (Bian et al., 2010).

The effects of thermal aging can range from a minor reduction in the material work hardening capacity by increasing the yield stress (while maintaining the continuous yielding), to a major loss of ductility with discontinuous yielding (small uniform elongation and appearance of Lüders plateau). The magnitude of thermal aging effects is a function of three major factors: aging time, aging temperature, and the plastic strain applied to the material prior to the aging process. Generally, a higher aging temperature, longer exposure to heat, and larger pre-applied plastic strain generally increase the thermal aging effects (Li et al., 2010).

Seo et al. (2009) showed that thermal aging behaviour is also different through the thickness of pipes because of the different plastic strain induced by UOE pipe forming<sup>2</sup> and the different thermal history of anti-corrosion coating. However, they concluded that the whole pipe wall's thermal aging behavior corresponds to that of the pipe's wall centre position.

In HSS pipes, the material experiences different pre-straining in longitudinal and transverse directions. Therefore, plastic deformation in the transverse direction during pipe forming makes the material less resistant to thermal aging and, as such, the increase of yield stress tends to be more prominent in the transverse direction than in the longitudinal direction (Liessem et al., 2009).

Although thermal aging also increases the longitudinal yield stress, the longitudinal stress-strain curves maintain the continuous round shape and the ability of uniform elongation, even after an aging temperature of 240°C. Thermal

---

<sup>2</sup> During the pipe forming, the inner side of pipe deforms in the compressive mode in U bending and then in the tensile mode during the expansion process. On the other hand, the outer side deforms in the tensile mode in U bending followed by an additional tensile strain after expansion.

aging also increases the proportional limit in the longitudinal direction compared to the as-expanded condition. However, the yielding region in the longitudinal direction remains continuous and curvilinear.

In the transverse direction, the increase in yield stress is followed by the formation of Lüders plateau at 210°C and higher (Nagal et al., 2010). Liessem et al. (2009) showed that the Lüders plateau is much less expressed in the ring expansion test (compared to the coupon tensile test) due to the larger constraint present in the bigger test specimen. However, the effect of thermal aging is significant in both tensile and ring expansion tests. Figure 6-1 shows typical effects of strain aging (due to the HSS pipes' thermal coating) on the transverse stress-strain curves. For both as-expanded and as-coated conditions, tensile test results of round specimens are depicted along with the corresponding ring expansion test curves.

Different effects of thermal aging on the longitudinal and transverse behaviour of HSS pipes result in an anisotropy pattern slightly different from that in the as-expanded HSS pipes (Nagal et al., 2010). The changes in the material properties due to thermal aging deteriorate pipelines' deformability in the field. In order to minimize the adverse outcome of thermal coating on the buckling resistance, pipeline producers try to come up with steel products that are more resistant to the aging effects (Ishikawa et al., 2008) and also try to invent thermal coating methods that require less temperature during heat treatment (Bian et al., 2010). Nevertheless, there is no systematic procedure to incorporate the material changes due to thermal coating in longitudinal and transverse directions in the buckling analysis.

## 6.2 Experimental Data

The anisotropy of thermally coated HSS pipes was studied using a full-scale buckling test, and material test results of two pipes. These data are from the same test project used in chapters 2 and 3, conducted by Transcanada Pipeline Ltd. in collaboration with the JFE Corporation (JFE R&D) and carried out by C-FER Technologies. Two thermally coated HSS pipes were also tested in that project.

The nominal outside diameter and wall thickness of these two pipes were 914 and 13.8 mm, respectively, and they had similar material types from grade X100 (with SMYS equal to 690MPa). Hereafter, the material type of these pipes is called material type “T”. Table 6-1 shows the specimens’ grade, dimensions, and the internal pressure applied to the pipes during the test.

Similar to the HSS pipes discussed in Chapter 3, initial imperfection measurements were not performed systematically on the pipe specimens before running the buckling tests. Instead, ovality and average diameter measurements were carried out in three stations X, Y, and Z, equally spaced along the pipe; where station Y was located in the middle and stations X and Z were the distance of one pipe’s diameter from station Y. The wall thickness is the average of 16 measurements distributed in eight locations at stations X and Z.

Table 3-2 shows the range of variation in wall thickness, outside diameter, and ovality for each pipe (the measured imperfections are expressed as the percentage of each pipe’s wall thicknesses in this table).

### 6.2.1 Material Tests

Tension coupon tests were performed on three longitudinal and three transverse round-bar coupons. These coupons were cut from three different positions in the pipe’s circumference. If the longitudinal seam weld position is considered as 12

o'clock, these specimens were cut from the 6, 7, and 9 o'clock positions. Compression coupon tests were also performed on two round-bar specimens located at the 7 and 9 o'clock locations.

Figure 6-2 shows the stress-strain curves from longitudinal and transverse tension coupon tests for the full range of the material response before rupture. As this figure shows, the material has similar elastic stiffness in both directions but the plastic responses are quite different. In the longitudinal direction, the material curvilinear yielding region is followed by continuous plastic deformation up to around 10% total strain, in which the material reaches its ultimate strength. In the transverse direction, the material shows a discontinuous yield region and comparatively high yield strength. The plastic response in the transverse direction reaches its ultimate strength around the 3% strain and then starts to soften. These differences indicate major differences in the material ductility in the longitudinal and transverse directions.

### **6.2.2 Full-scale Buckling Tests**

The test set-up and data acquisition system used for these pipes was exactly the same as what was used for HSS pipes in Chapter 3. These two pipes were tested under a monotonically increasing curvature (pure bending moment) for buckling. HSSP#16 had no internal pressure and HSSP#17 was pressurized during the test. HSSP#16 buckled in the middle length but HSSP#17 buckled near to the top collar.

## 6.3 Anisotropic Material Modeling

### 6.3.1 Material Anisotropy Features of Thermally Coated HSSP

As discussed in chapters 2 and 3, the critical buckling strain (CBS) in HSS pipes hardly exceeds 3.0%; therefore the pipe's longitudinal strain capacity is not affected by the entire range of material response. Rather, it is affected by the material response's elastic, yielding, and early plastic regions. Hence, in the material modeling of HSS pipes, the material responses between 0.0% to 3.0% total strain require special care.

Figure 6-3 shows the tensile stress-strain curves of material type "I" in longitudinal and transverse directions up to 3.0% total strain. This figure better illustrates the anisotropy features important for the buckling response of HSSP#16 and HSSP#17. Due to the thermal aging effects, the anisotropy pattern of material type "I" has some similarities to, as well as differences from, the HSS pipes' material types discussed in Chapter 2. The yield stress of material type "I" (defined as the true stress corresponding to 0.2% plastic stress) in longitudinal and transverse directions was 717Mpa and 813Mpa, respectively. This indicates a 13% difference in the yield stress in two directions, whereas the average difference between longitudinal and transverse yield stresses in the material types A to H was 25%.

Although the modulus of elasticity in the transverse direction was slightly higher than that in the longitudinal direction, elastic stiffness was very close in both directions. The difference between the modulus of elasticity in both directions of material type "I" was 8%, while the average of this difference in the material database of as-expanded HSS pipes in Chapter 2 was 5%.

In the transverse direction, the material shows an upper yield stress at which the elastic response ends; afterwards, the strength drops to the lower yield stress. The

yielding region in the transverse direction is relatively small and the material continues to have plastic deformation with an almost linear pattern with a small slope. The small yielding region, which is followed by linear strain hardening, makes it possible to approximate the transverse stress-strain response with a bilinear curve.

In the longitudinal direction, the elastic response ends at the longitudinal proportional limit that is significantly smaller compared to the transverse direction. The plastic response starts with a curvilinear shape up to 1.5% total strain; subsequently, the plastic deformation takes on a linear strain hardening pattern. The slope of the linear strain hardening region of the longitudinal response is bigger than that of the same region in the transverse direction. In the HSS pipes' material in Chapter 2, the longitudinal and transverse stress-strain curve converged around 1.5% total strain and continued with an almost similar slope. In the material type "I", however, the convergence happens relatively later, at 3.0% total strain. The reason for this phenomenon is the different effects of the thermal aging on the longitudinal and transverse directions. Increasing the yield stress in the transverse direction due to thermal aging results in higher nominal yield stress,  $\sigma_{y(nom)}$ , and a lower strain hardening modulus,  $E_{sh}$ , compared to the longitudinal direction. As Table 6-3 shows, the longitudinal and transversal nominal yield stresses for material type "I" were 772 and 843, respectively, which shows a 10% difference, while the difference between the longitudinal and transverse nominal stresses in material types A to H was 5%.

The difference between  $E_{sh}$  values in both directions of material type "I" was more significant compared to that of other HSS pipes in Chapter 2. The linear strain hardening modulus,  $E_{sh}$ , in the longitudinal and transverse directions, was 2582MPa and 408MPa, respectively. The ratio of  $E_{sh(T)}/E_{sh(L)}$  equals 16% in material type "I" while the average of this value for material types A to H was 83%.

Due to minor differences between  $E_{sh}$  and  $\sigma_{y(nom)}$  in the longitudinal and transverse directions of material types A to H, the average of these values was used to calibrate the combined hardening model in Chapter 2. In this case, using the same calibration method might result in poor material response simulations and, consequently, poor buckling simulations. Therefore, some modifications might be necessary for the combined hardening model in order to make it useful for thermally coated HSS pipes.

### 6.3.2 Modified Combined Hardening Material Models

In this section, the performance of the combined hardening material model introduced in Chapter 2 is tested for thermally coated HSS pipes. Subsequently, some modifications are introduced to the calibration method to improve the results of the combined hardening model in thermally coated HSS pipes.

The combined hardening model needs five material parameters for calibration:  $E$ ,  $\sigma_{y(nom)}$ ,  $PL_L$ ,  $E_{sh}$ , and  $\gamma$ . In Chapter 2, the elastic response was defined by the average value of longitudinal and transverse moduli of elasticity along with Poisson's ratio,  $\nu$  equal to 0.3. The longitudinal proportional limit and average value of longitudinal and transverse nominal yield stress were used to define the size and location of the yield surface in the stress state. The average longitudinal and transverse strain hardening moduli were used to define the isotropic hardening rate. The kinematic hardening parameter,  $\gamma$  (which defines the hardening rate of the kinematic component), was defined by trial-and-error to give the best fit to the longitudinal stress-plastic strain data.

Figure 6-4 shows the results of the combined hardening material model for material type "I" calibrated by the above-mentioned method, along with the average experimental data for longitudinal and transverse tension responses. In the range of the 0.0% to 3.0% total strain, the mean absolute errors of the model's

simulation in tension responses were 1.1% for longitudinal and 2.2% for transverse directions. The result of the combined hardening material model for the longitudinal compression response of material type “I” is shown in Figure 6-5 along with the average experimental stress-strain data of the longitudinal compression response. The average experimental tension responses in both directions are also depicted in this figure to emphasize the advantages of the combined hardening model over the isotropic material model. The mean absolute error of the model’s simulation in longitudinal compression responses was 2.2% in the present range.

Although Chapter 5 shows that the material responses in longitudinal compression and transverse tension are the most important material responses for pipe buckling analyses, in this case the model was calibrated by the longitudinal and transverse tension stress-strain data because tension coupon tests are more common for material testing. Nevertheless, the combined hardening material model results in a longitudinal compression response with acceptable accuracy. Therefore, it is reasonable to use the tension test results in longitudinal and transverse directions for the model calibration. It is worth mentioning that the model’s accuracy in simulating the longitudinal compression responses indicates that the material follows the von Mises yield criterion.

The major difference between the material type “I” and as-expanded HSS pipes’ material used in this study is its limited ductility in the transverse tension response. Accurate simulation of this low ductility is very important for pressurized HSS pipes because, as discussed in Chapter 5, the CBS of these pipes is strongly affected by the transverse material response.

The difference between the  $\sigma_{y(nom)}$  and  $E_{sh}$  values in longitudinal and transverse directions of material type “I” is more significant compared to material types A to H. Therefore, using the average values of these parameters in the combined

hardening model results in a lower yield strength and higher strain hardening modulus in transverse direction. These differences eventually result in a higher ductility level compared to the real transversal material response. Consequently, using this material model in the buckling analysis might overestimate the actual longitudinal compressive strain resistance of coated HSS pipes.

The simulation results of the combined hardening model were improved by making a slight change in the calibration process. The values of  $\sigma_{y(nom)}$  and  $E_{sh}$  in the transverse direction were used as substitutes of average (of longitudinal and transverse) values of these parameters. As a result, the model became more accurate in the transverse direction. The rest of the calibration process remained intact but the values of material parameters changed slightly. Since different value was used for  $\sigma_{y(nom)}$ , the size of the original yield surface and the initial back-stress changed. Furthermore, different  $\gamma$  value was obtained from the buckling process due to the different value of  $E_{sh}$  in the new model. Table 6-4 shows the parameters used to calibrate this model and the previous combined hardening model using average longitudinal and transversal  $\sigma_{y(nom)}$  and  $E_{sh}$ .

The results of this anisotropic model (hereafter called the “modified combined hardening model”) are shown in Figure 6-6 and Figure 6-7 for tension and compression responses, respectively. As seen in these figures, the simulation of the transverse tension is improved using the new method compared to the combined hardening model with average  $\sigma_{y(nom)}$  and  $E_{sh}$ . However, the longitudinal tension and compression results show almost similar accuracy in both models.

In order to have better comparisons, the mean absolute error of these two models for longitudinal and transverse tension responses and longitudinal compression responses are illustrated in Table 6-5. As this table shows, the above-mentioned change in material model calibration reduced the error in the transversal tension

response from 2.2% to 0.6%, while the accuracy of longitudinal tension and compression simulations remains almost constant.

As the above-mentioned combined hardening models simulate the longitudinal responses of material type “T” with almost similar accuracy, it is expected that their results would be similar in the buckling analyses of HSSP#16. This is because HSSP#16 was unpressurized during the test. Based on the results of Chapter 5, the compressive strain evolution is highly dominated by the material longitudinal compression response. For the HSSP#17, however, the modified material model’s improvement in the transversal stress strain response should result in a better simulation of the buckling response. The next section describes the buckling analysis of HSSP#16 and HSSP#17.

## **6.4 Buckling Analyses**

The test procedures and set-up for HSSP#16 and HSSP#17 were similar to HSSP#1 to HSSP#15, as described in Chapter 3. Therefore, their finite element models were developed in ABAQUS in similar conditions of geometry, meshing, element types, and boundary conditions.

The cross-sectional measurements shown in Table 6-2 were not used for imperfection modeling because they provide limited imperfection data for only a few locations and cannot present any pattern for each type of imperfection. Therefore, the idealized half-ring initial imperfection patterns were used to trigger the buckling of pipe segments in the absence of actual initial imperfection data.

HSSP#16 had buckled in the middle length during the buckling test. Therefore, the half-ring dent-type imperfection pattern was applied to the same area of finite element model of HSSP#16. The point of maximum out-of-roundness was placed on the extreme compression fiber one element away from the pipe’s middle

length. As HSSP#17 had buckled close to the top collar during the buckling test, the half-ring bulge was applied as such that the point of maximum out-of-roundness was placed close to the top collar. This arrangement of predefined imperfections resulted in a final buckled shape similar to that in the tested pipes. A similar magnitude for maximum out-of-roundness was used for both HSS pipes, making ovality equal to 12.5% of their wall thicknesses.

Regarding the material modeling, three isotropic models were developed for HSSP#16 and HSSP#17, each of which had stress-strain data based on longitudinal tension (LT), transversal tension (TT), and longitudinal compression (LC) responses. The intention behind the analyses of these isotropic models was to learn which material response dominates the buckling of pressurized and unpressurized (thermally coated) HSS pipes.

The isotropic data for defining the stress-plastic strain curve were defined as the average data for each group of coupon tests: i.e., LT, TT, and LC. For TT data, the resulting average curve was not a smooth curve around the yielding zone (because of the upper yield stress). In order to achieve convergence in the isotropic TT model, the zigzag part of the yielding zone of the TT curve was replaced by a smooth curve representing the average strength of the material in that area. This replacement is shown in Figure 6-8.

The available range of compressive data for material type “T” in the longitudinal direction was significantly smaller than that for the tension data, due to the limitations associated with compression tests. For the isotropic LC models, this average longitudinal compressive data linearly extended with a slope of average longitudinal and transversal strain hardening moduli of tension curves.

Based on the discussions in the previous section (about anisotropic material modeling), two anisotropic models were also built for HSSP#16 and HSSP#17. The first model (hereafter called the “average anisotropic model”) used the

average value of  $\sigma_{y(nom)}$  and  $E_{sh}$  in longitudinal and transverse directions. The second model (the “modified anisotropic model”) used the values of  $\sigma_{y(nom)}$  and  $E_{sh}$  in the transverse direction.

Similar to the test conditions, the buckling analyses were performed by applying equal rotations at both pivot points to generate pure bending throughout the pipe’s length. For HSSP#17, the internal pressure was applied as a distributed load on the internal surface of the shell elements forming the pipe, collars, and end plates. Before applying the end rotations, axial compressive force was applied on the top pivot point of HSSP#17 to counteract the axial tensile force due to the internal pressure. The arc-length control technique (modified Riks method) was used to carry out the buckling analyses.

## 6.5 Results and Discussions

Figure 6-9 shows the buckling analyses results of isotropic models along with the experimental measurements for HSSP#16. This figure shows the global moment versus the average compressive strain measured in  $2D$  gauge length (in the buckling zone). The variations of the global moment with respect to the average compressive strain from isotropic models of HSSP#17 are compared with the experimental measurements in Figure 6-10. As this pipe had buckled close to the top collar, due to the instrumentation arrangements, the average compressive strain was measured in  $2.25D$  gauge length. The analyses results are also shown for the same gauge length.

For both pipes, HSSP#16 and HSSP#17, the isotropic models with longitudinal tension data provide the upper bound of CBS, and the isotropic models with transverse tension data give the lower bound response. Although none of the isotropic models could accurately simulate the response of HSSP#16, the isotropic model of HSSP#17 with transversal tension data provided the closest

results up to the onset of buckling. Nevertheless, none of the isotropic models can be used for both unpressurized and pressurized cases, and more precise methods of material modeling are needed for these pipes.

As discussed in section 6.3, the combined hardening material model is able to simultaneously simulate the material responses in longitudinal and transverse directions under tension and compression. Therefore, the combined hardening material modeling was expected to give more accurate results compared to the isotropic models in the buckling analysis of thermally coated HSS pipes. Figure 6-11 and Figure 6-12 show the buckling analyses results compared to test results of HSSP#16 and HSSP#17, respectively. As Figure 6-11 shows, both anisotropic models (with average combined hardening material and modified combined hardening material models) were able to accurately simulate the moment versus average compressive strain, and eventually the CBS of HSSP#16. It is also apparent in this figure that both anisotropic models provided almost similar results. This phenomenon was expected since HSSP#16 was unpressurized during the buckling test and the buckling response is highly affected by the material's longitudinal compressive response (Chapter 5). Also, the longitudinal responses predicted by both anisotropic models had similar accuracy.

Figure 6-12 shows that the finite element model with modified anisotropic material resulted in more accurate simulations of the bending response of HSSP#17, as well as the buckling strength and the CBS. This phenomenon can be explained by the results of Chapter 5. In other words, when the longitudinal compressive deformation accumulates on a highly pressurized pipe, the surface traction vector has a large component in the transverse direction because of the tensile hoop stress. This large transversal component increases the influence of the transversal material behaviour on the compressive deformation before buckling. Thermal coating results in degradation of the material ductility and enlargement of the elastic range in the transverse direction. These alterations of

the material response eventually reduce the compressive deformation before buckling and the CBS of pressurized pipes. The modified anisotropic material model accurately acknowledges the lack of ductility caused by the thermal coating in the transverse direction.

## **6.6 Summary**

Strain aging due to thermal coating reduces the material ductility of HSS pipes, especially in the transverse direction. The primary goal of this chapter was to investigate the application of the combined hardening material modeling method in buckling analyses of thermally coated HSS pipes. The secondary goal was to study the effects of material property changes due to strain aging on the buckling resistance of HSS pipes.

The results showed that the combined hardening material model introduced in this research can also be used for thermally coated HSS pipes. However, it needs some modifications before being used for buckling analyses of pressurized-coated HSS pipes. These modifications enhance the material model's capability to simulate the degradation of the transversal material ductility due to the thermal coating. The modified model also gives very good results for the unpressurized pipe.

The results of this chapter also showed that the detrimental effects of thermal coating on the longitudinal compressive strain capacity of HSS pipes are more significant in highly pressurized pipe compared to unpressurized pipes. This is because the thermal coating results in more significant loss of ductility in the transverse direction than in the longitudinal direction.

## References

Bian Y., Penniston C., Collins L. and Mackenzie R., (2010), "Evaluation of UOE and Spiral-Welded Line Pipe for Strain Based Designs", Proceeding of the International Pipeline Conference, American Society of Mechanical Engineers, Calgary, Alberta, v4, pp 139-148.

Ishikawa N., Okatsu M., Shimamura J., Endo S. Shikanai, N. Muraoka, R. Kondo, J. and Suzuki, N, (2009). "Material development and strain capacity of grade X100 high strain linepipe produced by heat treatment online process", 2008 ASME International Pipeline Conference, IPC 2008, September 29, 2008 - October 3, American Society of Mechanical Engineers, Calgary, AB, Canada, v3, pp 713-720.

Li Y., Zhang W., Gong S., Ji L., Huo C. and Feng, Y., (2010), "Study on Tensile Property and Strain Ageing Behaviour of X100 Linepipe", Proceeding of the International Pipeline Conference, American Society of Mechanical Engineers, Calgary, Alberta, v2, pp 351-357.

Liessem A., Schroder J., Pant M., Knauf G., Zimmermann S., Stallybrass C. and Erdelen-Peppler, M., (2009), "Investigation of the stress-strain behaviour of large-diameter X100 linepipe in view of strain-based design requirements", 2008 ASME International Pipeline Conference, IPC 2008, September 29, 2008 - October 3, American Society of Mechanical Engineers, Calgary, AB, Canada, v3, pp 755-762.

Nagal K., Shinohara Y., Sakamoto S., Tsuru E., Asahi H. and Hara T., (2010), "Anisotropy of the Stress-Strain Curves for Line Pipe Steels", Proceeding of the International Pipeline Conference, American Society of Mechanical Engineers, Calgary, Alberta, v4, pp 59-65.

Seo D., Yoo J., Song W. and Kang, K. (2009), "Development of X100 linepipe steel with high deformation capacity", 2008 ASME International Pipeline Conference, IPC 2008, September 29, 2008 - October 3, American Society of Mechanical Engineers, Calgary, AB, Canada, v3, pp 585-592.

Shitamoto H., Makino H., Okaguchi S., Hamada M., Takahashi N., Yamamoto A. and Takeuchi, I. (2007), "Evaluation of strain limit of compressive buckling by FE analysis", 17th 2007 International Offshore and Polar Engineering Conference, ISOPE 2007, July 1, 2007 - July 6, International Society of Offshore and Polar Engineers, Lisbon, Portugal, pp 3261-3268.

Tsuru E., Shinohara Y., Asahi H. and Terada Y., (2005), "Strain capacity of line pipe with yield point elongation", 15th International Offshore and Polar Engineering Conference, ISOPE-2005, June 19, 2005 - June 24, International Society of Offshore and Polar Engineers, Seoul, Korea, v3 2005, pp 177-184.

## Tables

Table 6-1 Specimens' grade, dimensions, and testing conditions

Specimen ID	Steel Grade	Diameter (D)	Wall Thickness (t)	D/t	Length (L)	L/D	Internal Pressure
		(mm)	(mm)		(mm)		(Mpa)
HSSP#16	X100	913.88	13.81	66.2	3201	3.5	0
HSSP#17	X100	914.36	13.72	66.6	3195	3.5	15.9

Table 6-2 Specimens' initial imperfections

Specimen ID	Measured Imperfection Range (%WT)		
	Wall Thickness Variation	Radius Variation	Ovality
HSSP#16	1.3%	4.9%	4.4%
HSSP#17	1.3%	6.1%	3.5%

Table 6-3 Material properties in both directions from tensions tests

Major Directions	Material Properties (MPa)			
	$E$	$PL$	$E_{sh}$	$\sigma_{y(nom)}$
Longitudinal Direction	206694	675	2582	772
Transverse Direction	222839	-	408	843

Table 6-4 Material properties used in anisotropic models

Anisotropic Models	Material Properties Used for Calibration					Size and Location of the Yield Surface	
	$E$ (MPa)	$PL$ (MPa)	$E_{sh}$ (MPa)	$\sigma_{y(nom)}$ (MPa)	$\gamma$	$\sigma_o^o$ (MPa)	$c/\gamma$ (MPa)
Old Model	214767*	675	1495*	808*	148	722	86
Modified Model	214767*	675	408	843	105	735	108

\* The average values in longitudinal and transverse directions were used for these parameters

Table 6-5 Material simulation error by combined hardening models

Combined Hardening Models	Longitudinal Tension	Transverse Tension	Longitudinal Compression
Old Model (with average $\sigma_{y(nom)}$ and $E_{sh}$ )	1.1%	2.2%	2.2%
Modified Model	1.2%	0.6%	2.0%

## Figures

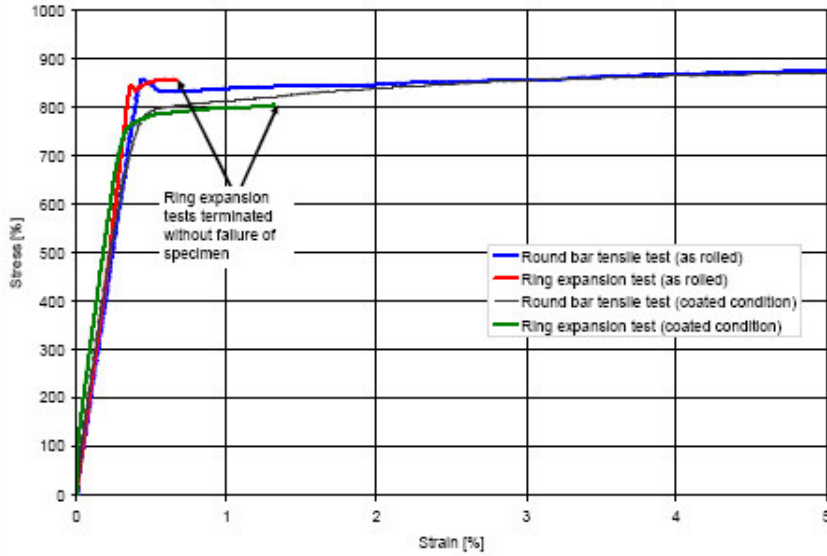


Figure 6-1 Effects of thermal coating on the tension stress-strain response of HSSP (grade X100) - transverse tension coupon and ring expansion test results

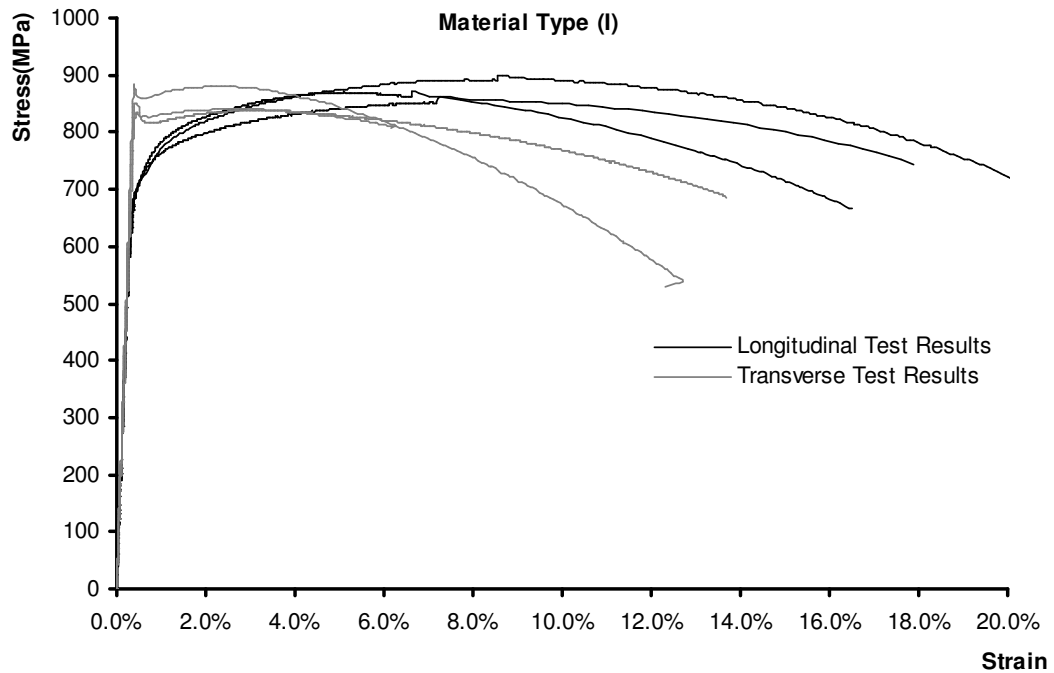


Figure 6-2 Longitudinal and transverse stress-strain data from the material tension test for material type "T" – entire range

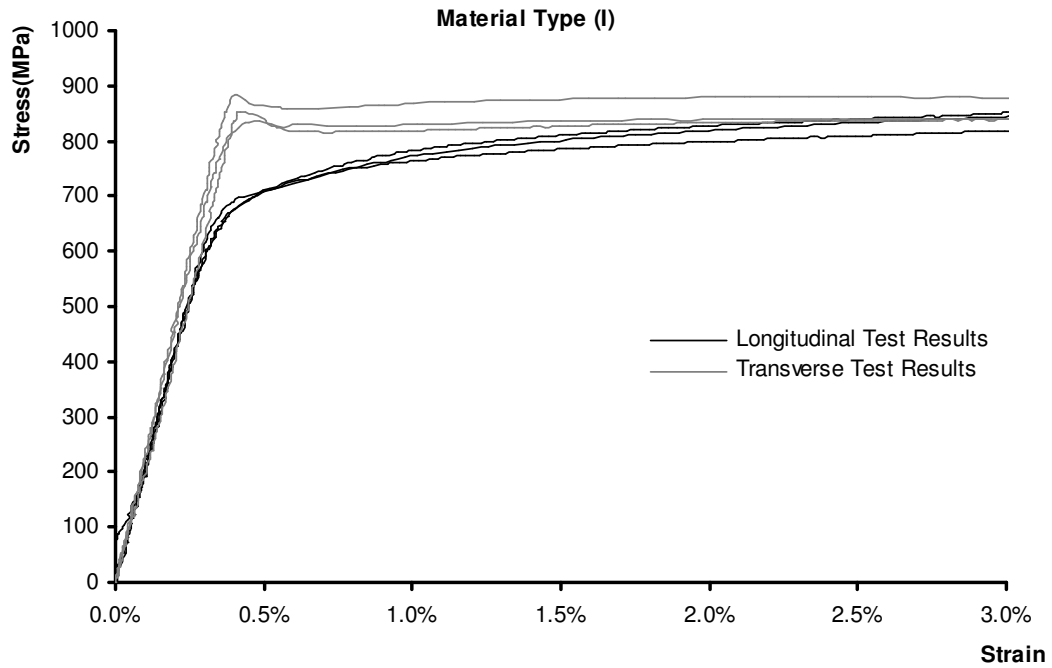


Figure 6-3 Longitudinal and transverse stress-strain data from the material tension test for material type “I” – elastic and early plastic response

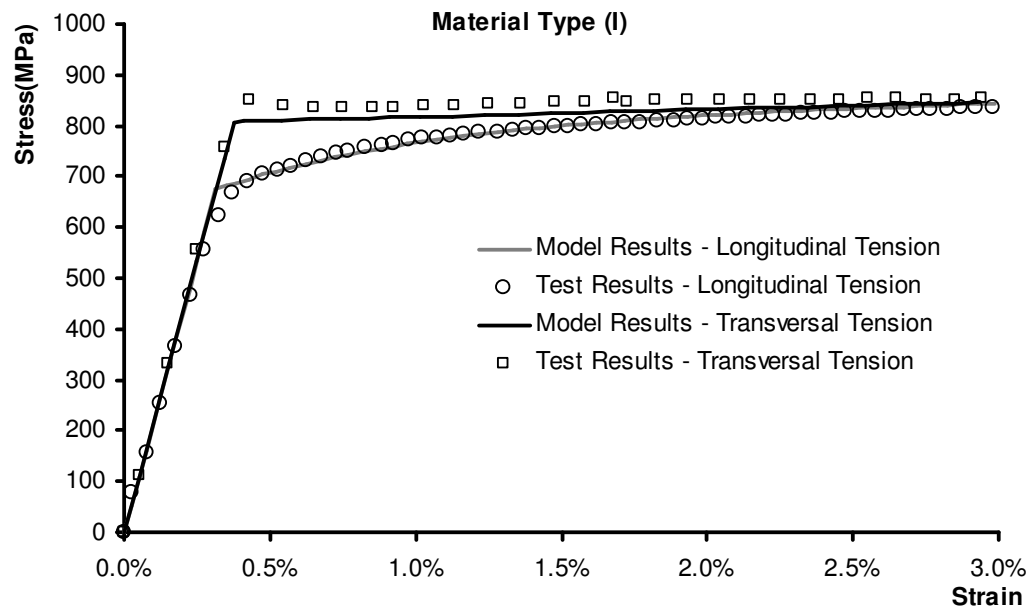


Figure 6-4 Average experimental and combined hardening material model results for material type “I” – longitudinal and transverse tension responses

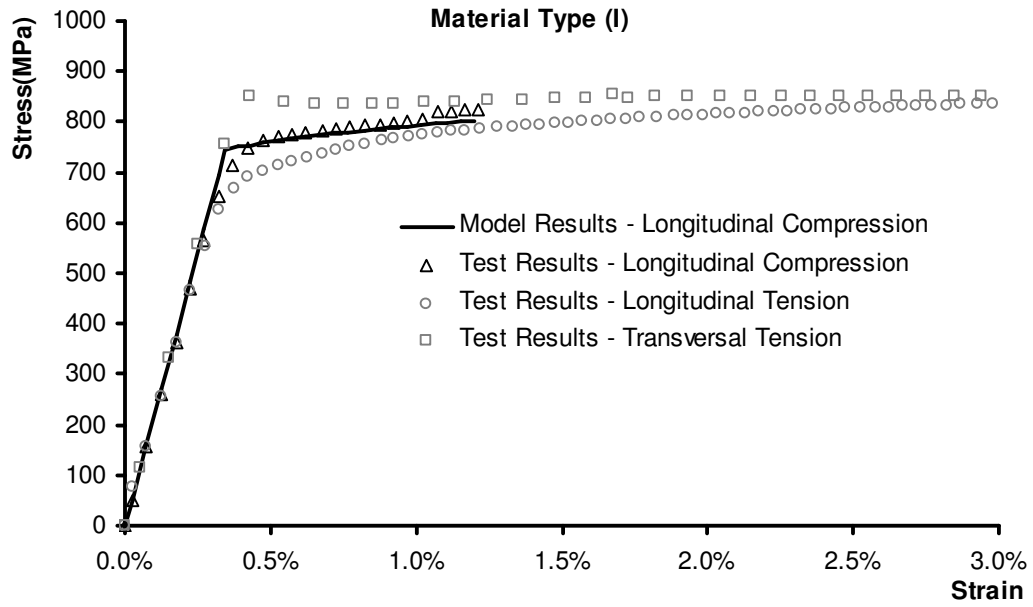


Figure 6-5 Average experimental and combined hardening material model results for material type “I” – longitudinal compression responses

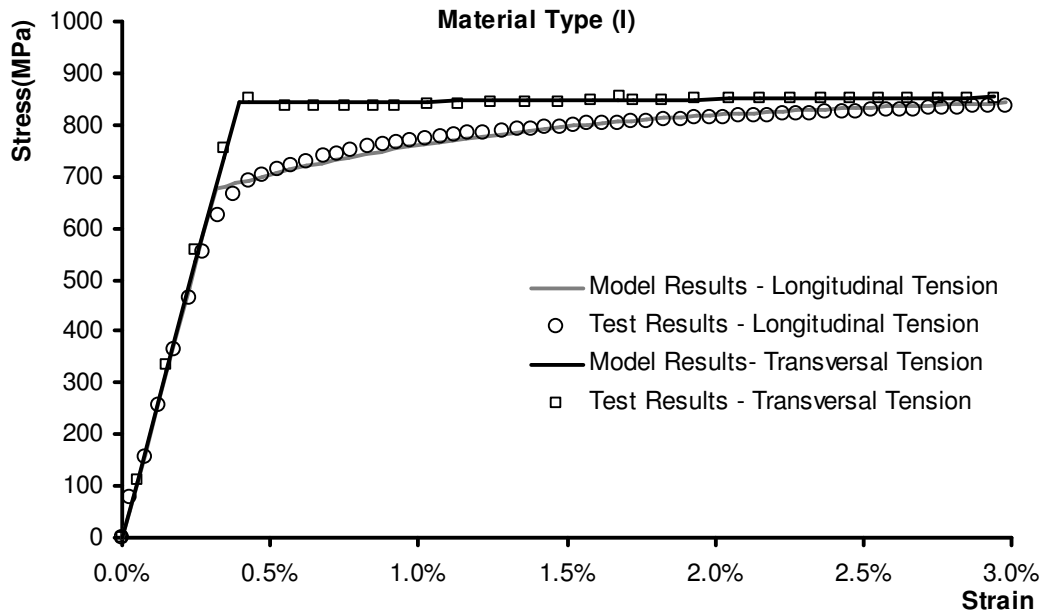


Figure 6-6 Average experimental and modified combined hardening material model results for material type “I” – longitudinal and transverse tension responses

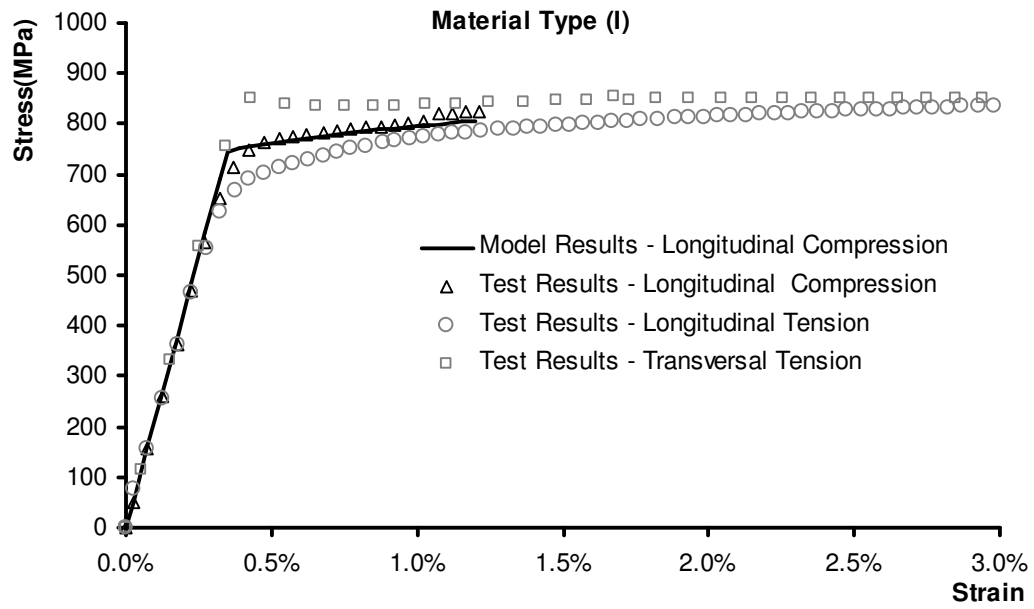


Figure 6-7 Average experimental and modified combined hardening material model results for material type “I” – longitudinal compression responses

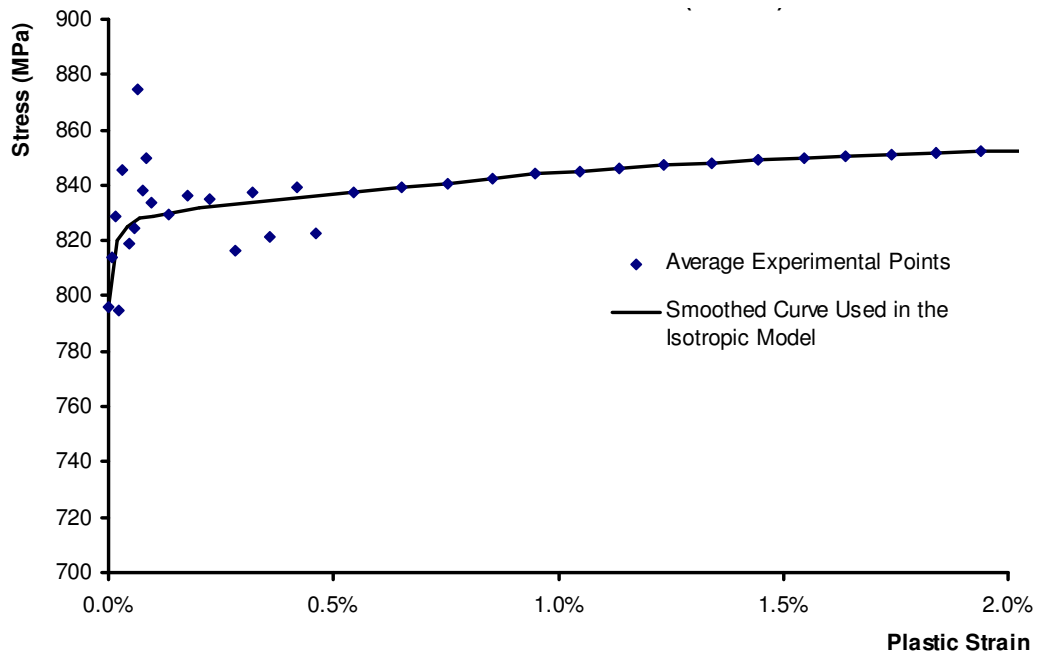


Figure 6-8 Average experimental stress-plastic strain points and the smoothed curve used in the isotropic TT pipe model - transverse tension response

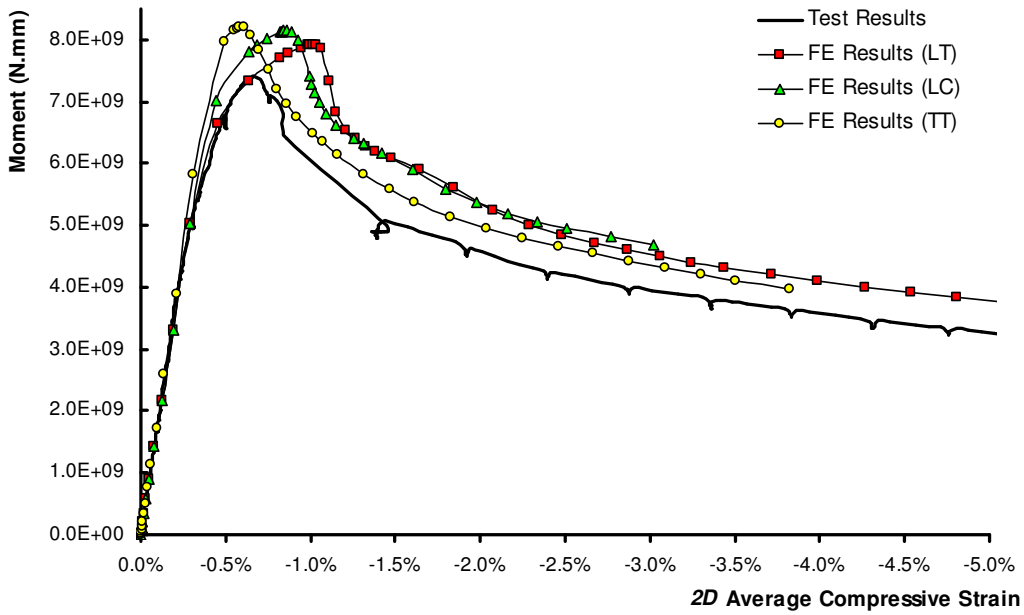


Figure 6-9 Variation of global moment versus *2D* compressive strain from isotropic FE models and experimental result of HSSP#16

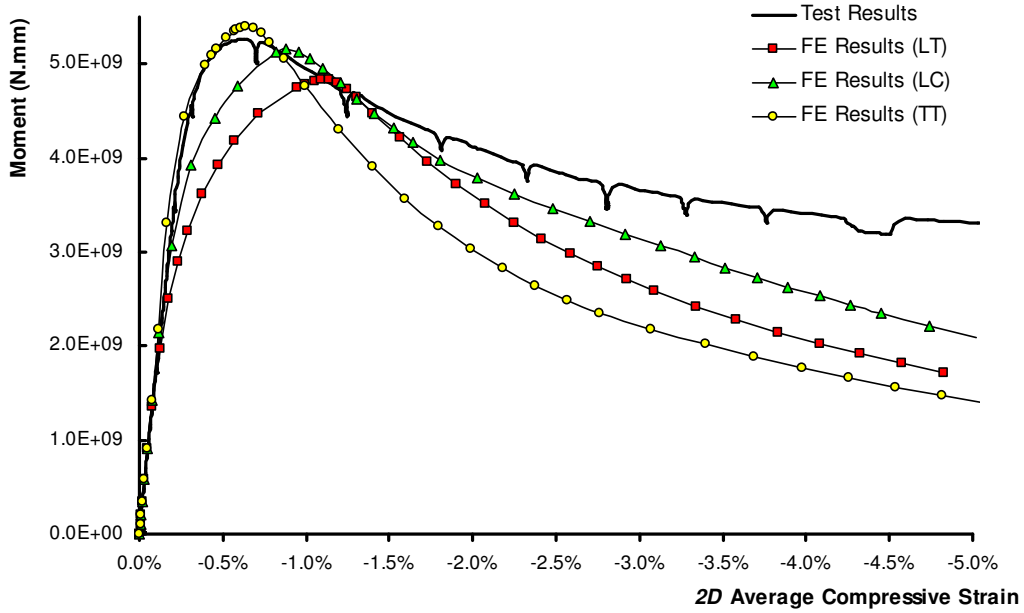


Figure 6-10 Variation of global moment versus *2.25D* compressive strain from isotropic FE models and experimental result of HSSP#17

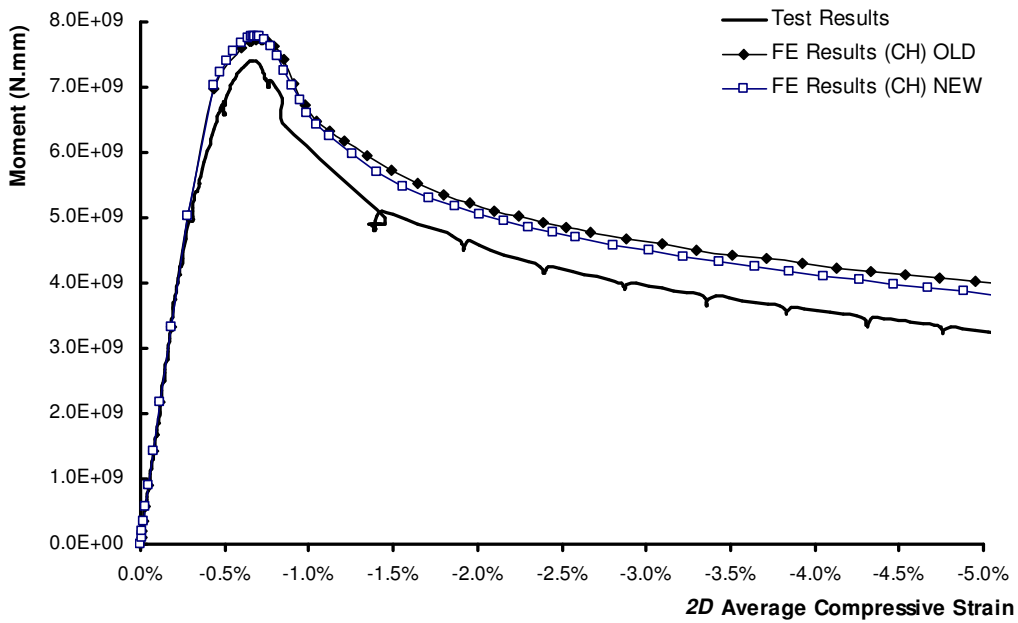


Figure 6-11 Variation of global moment versus  $2D$  compressive strain from anisotropic FE models and experimental result of HSSP#16

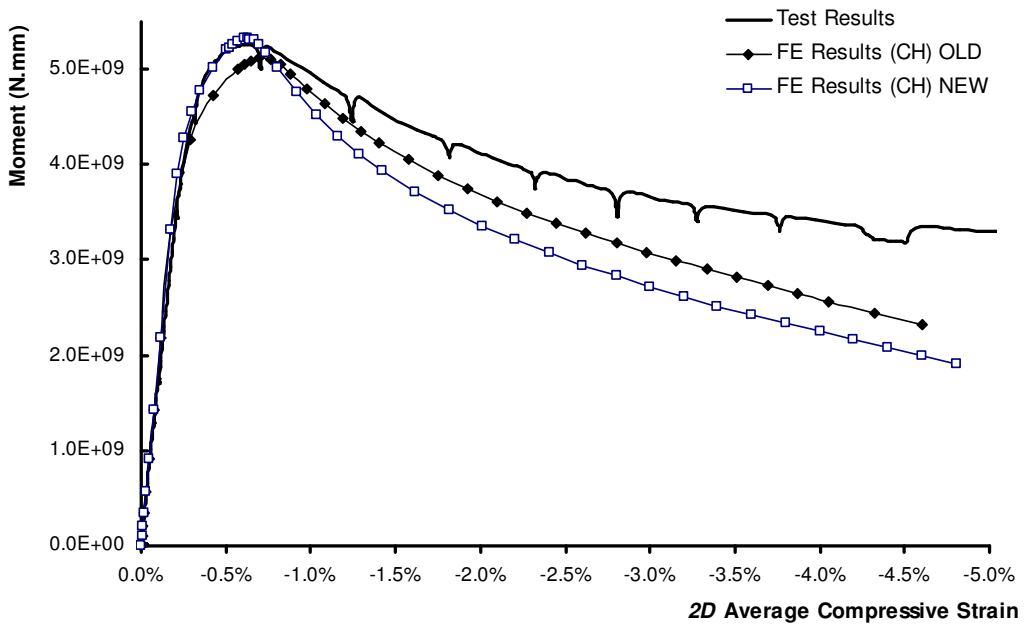


Figure 6-12 Variation of global moment versus  $2.25D$  compressive strain from anisotropic FE models and experimental result of HSSP#17

## **7 SUMMARY, CONCLUSION, AND RECOMMENDATIONS**

### **7.1 Summary**

This research was designed and implemented with the intent of understanding the buckling response of high strength steel (HSS) pipes which are considered the best option for highly pressurized pipelines transporting natural gas across environmentally harsh areas. Specifically, this project was developed to expand the current knowledge of finite element modeling of pipelines with anisotropic material properties. An additional objective of this study was to investigate the effects of pipes' material properties on the longitudinal compressive resistance of HSS pipes when anisotropy is present.

In order to develop an accurate and practical anisotropic material model for HSS pipes, 152 longitudinal and transversal stress-strain curves from HSS pipes' material tests were studied. This database contained stress-strain responses of eight different material types of grades X80 and X100 steel pipes. The first stage examined general patterns of material responses in longitudinal and transverse directions of HSS pipes. The study was focused on the elastic, yielding and early plastic regions that are important for the pipes' behaviour up to the onset of buckling. Based on the observed hardening patterns in longitudinal and transverse directions, a combined hardening material model was introduced with linear isotropic and Armstrong-Frederick kinematic hardening rules. A simple calibration method was also introduced for this model, based on tensile stress-strain data from longitudinal and transverse directions. A comparison between the results of this model and the experimental measurements confirmed that the model results adequately agreed with the actual behaviour of HSS pipes' material both in longitudinal and transverse directions. Although the model was calibrated

with tensile stress-strain data, it also simulated the longitudinal compressive response with an acceptable level of accuracy. All these validations indicated appropriate selection of the isotropic and kinematic hardening rules, as well as the yield criterion.

The anisotropic material model was used to improve the accuracy of finite element buckling analyses of HSS pipes, in order to better understand the effects of material anisotropy on the structural behaviour of HSS pipes. Fifteen finite element models were developed for HSS pipes that had been tested for buckling under different load combinations. Two types of material modeling methods were used for the finite element models, the isotropic model (with longitudinal stress-strain data) and the anisotropic model (developed and introduced in this research). The results of the buckling analyses of both models were compared with the experimental measurements. These comparisons showed that the isotropic models did not provide accurate results, while the anisotropic models showed excellent agreement with the real behaviour of HSS pipes.

Subsequently, the finite element model validated with anisotropic material was used in a parametric study on the buckling response of HSS pipes. The effect of material anisotropy on the critical buckling strain (CBS) was studied along with five other parameters (diameter to thickness ratio, internal pressure, initial imperfection's magnitude, material grade, and strain hardening rate). The Buckingham-Pi Theorem was used to develop a set of non-dimensional parameters to study the effects of all factors on the CBS of HSS pipes. Finite element models with different values of  $D/t$ ,  $\sigma_h/\sigma_{y(T)}$ ,  $II_{\max}/D$ ,  $\sigma_{y(T)}/E$ ,  $E_{sh}/E$ , and  $\sigma_{y(L)}/\sigma_{y(T)}$  were developed and analyzed to calculate the CBS. The CBS of HSS pipes (with different geometry, material, and operational conditions) was presented versus the level of material anisotropy. These results provided a qualitative insight into the effects of material properties on the buckling resistance of HSS pipes, especially when anisotropy is present.

Afterwards, extended buckling conditions were applied to the anisotropic model to explore the effects of mechanical material properties on the buckling resistance, and discover the ones with a governing role in the buckling of HSS pipes. A finite element study was performed on one unpressurized and one pressurized pipe under different combinations of bending moment and compressive axial force. Four material modeling methods were used in these finite element models: the anisotropic material model, and three isotropic models using material responses for longitudinal tension, longitudinal compression, and transverse tension. The results were used to understand which aspect of the material response controls the compressive strain limit in the strain-based design of HSS pipes.

Finally, a case study was performed on the anisotropic material properties and buckling responses of thermally coated HSS pipes. A literature review was completed about the effects of thermal coating on the material properties and the common anisotropy attributes of thermally coated HSS pipes. Then, finite element models were developed to simulate one unpressurized and one pressurized HSS pipe that had been tested for buckling after being thermally coating. After minor modifications, the combined hardening material modeling method was successfully employed for the buckling analyses of these pipes. The model's modifications were based on the parametric study results and findings on the association between anisotropic material features and the buckling response of HSS pipes established in earlier sections of this study. The results showed that how the deterioration of material ductility (especially in the transverse direction) due to the strain aging affects the buckling response of HSS pipes.

## **7.2 Conclusion**

The following conclusions can be drawn from the analytical study on the material and buckling responses of HSS pipes carried out in this research project:

1. Transversal plastic deformations during the expansion stage (in the UOE pipe-making process) result in significant Bauschinger's effects in HSS pipes' material. As a result, the HSS pipes' final products usually show material anisotropy.
2. The major difference between the longitudinal and transversal material responses under tensile deformations is in the yielding and early plastic regions. In addition, the yielding and early plastic responses are different under tension and compression in the same (either longitudinal or transverse) direction of HSS pipes.
3. Since the local buckling of energy pipelines is an inelastic stability phenomenon, it is highly affected by material plasticization. A precise study of HSS pipes' structural behaviour and accurate predictions of the CBS require appropriate simulations of material responses under all possible stress paths involved in the buckling.
4. Material anisotropy highly affects the plastic stiffness of HSS pipes under different stress paths. As a result, conventional isotropic material modeling is unable to predict the amount of plastic deformation a HSS pipe can accommodate before buckling.
5. The anisotropic (combined hardening) material model introduced in this research project is well capable of mimicking the actual material responses of HSS pipes. The model's results show excellent agreement with the experimental stress-strain data from transversal tension, and longitudinal tension and compression material tests.
6. Since the model is calibrated by tension coupon test results (which are more common and convenient for material testing), good agreement between the model outputs and experimental data from longitudinal compressive tests confirm that the combined hardening components and

their hardening patterns, as well as the yield criterion (von Mises), were properly selected.

7. While the material model and the calibration process were designed to generate accurate material simulation results, it was considered that the proposed model and its calibration process are uncomplicated and straightforward. Good final results proved that the assumptions and simplifications made to develop the material model and the calibration process did not adversely affect the model's performance.
8. Finite element modeling of HSS pipe buckling tests showed that using the proposed anisotropic material model results in better behavioural simulations compared to conventional isotropic modeling. Using the anisotropic material model provides accurate predictions of how much load and deformation a HSS pipe can resist before buckling.
9. Although the predicted buckling loads by both anisotropic and isotropic models were fairly close to the experimental measurements, the anisotropic model was able to provide significantly more accurate predictions of the compressive deformations before the buckling. This is because the anisotropic material model better simulates the bending stiffness of the HSS pipe due to its capability for capturing the material responses under different stress paths.
10. Due to the absence of experimentally measured imperfections, idealized initial imperfection patterns were used in this study to trigger the buckling in the finite element analyses. The results of buckling analyses with different initial imperfection magnitudes showed that the adequacy of the proposed material model was not affected by the initial imperfections of pipes. In fact, regardless of the magnitude of the imperfection, the

anisotropic model accurately followed the experimental curve before the onset of buckling.

11. Since the proposed anisotropic material model is competent, it is a good candidate to use for studying the HSS pipes' buckling behaviour and estimating the CBS under different conditions of operation, cross-sectional size, material grade, etc. Therefore, this material model was used to study the variation of the CBS of HSS pipes under different combinations of six non-dimensional parameters (including material anisotropy).
12. The results of the parametric study provided a complete picture of the buckling mechanism of HSS pipes when anisotropy is present. In addition, these results showed the interactive effects of all affecting parameters on the buckling response of HSS pipes.
13. Based on the parametric study results, if the ratio of longitudinal-to-transversal yield strength is considered as the level of material anisotropy, the CBS of HSS pipes has an almost linear relationship with the anisotropy level. Nevertheless, the correlation between the anisotropy level and the CBS varies from one case to another.
14. Among all parameters involved in the buckling of HSS pipes, internal pressure has a larger impact on the correlation between the material anisotropy and the CBS. Higher internal pressures significantly decrease the effects of material anisotropy on the CBS of HSS pipes. While there is a strong association between the CBS and the material anisotropy among unpressurized and moderately pressurized pipes, this association is weak in cases of highly pressurized pipes.
15. The average correlation factor (R) between the CBS and  $\sigma_{y(L)}/\sigma_{y(T)}$  ratio was 99.7% among both unpressurized and moderately pressurized pipes. For  $\sigma_{y(L)}/\sigma_{y(T)}$  variations between 0.706 and 0.912, the average change in

the CBS was 21.2% and 19.9% for unpressurized and moderately pressurized pipes, respectively. In highly pressurized pipes, however, the average change in the CBS was 1.9% and the correlation factor between the CBS and  $\sigma_{y(L)}/\sigma_{y(T)}$  ratio was 26.0% for a similar variation range of  $\sigma_{y(L)}/\sigma_{y(T)}$ .

16. The lower material grades and higher strain hardening moduli generally result in a higher CBS. However, when the strain hardening modulus is low, the effects of the material grade on the CBS become less significant. Yet, for unpressurized and moderately pressurized pipes, the effects of these parameters become even less significant when the magnitude of the initial imperfection is high.
17. The combined hardening model was employed in an extended range of combined axial load and bending moment to study the effects of each individual material response (i.e., longitudinal tension and compression, and transverse tension) on the buckling behavior of HSS pipes. The results showed that the buckling of unpressurized HSS pipes is highly affected by the pipe's material response under longitudinal compression. In addition, the material response under transverse tension has a greater effect on the buckling of highly pressurized HSS pipes. These conclusions are valid under any combination of axial compressive load and bending moment, and any distribution of imperfections within the pipe's critical cross-section.
18. Although the material response under longitudinal tension has been the most common material test for steel pipes, it does not directly affect the buckling behaviour of either pressurized or unpressurized pipes.
19. It is also observed that energy pipelines may show a lower longitudinal strain capacity against operational or environmental sources of imposed

displacements, causing more axial rather than bending compressive deformations. The CBS criteria developed by pure bending may result in unconservative estimations for real conditions with large axial compression loads. Nevertheless, this subject needs further numerical and experimental investigations.

20. Strain aging, due to the thermal coating process, changes the material response as well as the anisotropy pattern of HSS pipes. Specifically, it reduces the material ductility in the transverse direction under tensile loads. The combined hardening material model is applicable to accurately simulate the buckling response of thermally coated HSS pipes, with minor modifications. These modifications make the material model capable of simulating the degradation of the transversal material ductility due to the thermal coating.
21. Thermal coating's detrimental effects on the longitudinal compressive strain capacity of HSS pipes are more significant in highly pressurized pipes than in unpressurized pipes. This is because the thermal coating results in a more significant loss of ductility in the transverse direction than in the longitudinal direction.

### **7.3 Recommendations**

The combined hardening material model developed in this research project provides excellent results when used for finite element buckling simulations of HSS pipes. Therefore, this method of material modeling is highly recommended for further studies of HSS pipes buckling when anisotropy is present. The results of this research project also provide a number of substantial enhancements to the current state of the art for the effects of anisotropic material properties on the buckling response of HSS pipes, and especially the amount of deformation the

pipes can accommodate before buckling. However, some other areas are identified for further investigation:

1. This study showed that both longitudinal and transversal material responses affect the CBS of HSS pipes. It is recommended that for any quantitative study of the CBS (intended to develop design equations for HSS pipes), the material anisotropy level should be incorporated along with other affecting parameters.
2. The CBS is highly affected by the type, magnitude, and distribution pattern of the initial imperfections. Development of any design criteria for predicting the CBS of HSS pipes requires a realistically conservative incorporation of the initial imperfection effects. A comprehensive study is required to identify the distribution of the magnitude and pattern of each type of initial imperfections (out-of-roundness, radius and thickness variations). This experimental study should be followed by finite element sensitivity analyses examining the response of HSS pipes to different patterns. Using the results of the two above-mentioned studies, it is possible to identify an idealized pattern that can be used in the parametric studies for developing design equations for the CBS of HSS pipes.
3. If an isotropic material model is used for HSS pipes with anisotropic material properties, it is recommended to use stress-strain data from a material test with a stress path closest to the path of the problem under consideration. For example, for tensile and compressive limit states of unpressurized pipes, the longitudinal tensile and compressive stress-strain data would provide the best results, respectively, while for tensile and compressive limit states of highly pressurized pipes, the transverse tensile stress-strain data gives the best results. However, using the combined hardening material model remains the best method to capture the material response.

4. Investigating the effects of cross-sectional strain distribution on the CBS of pipelines showed that energy pipelines may show a lower longitudinal strain capacity under axial forces compared to bending moments. Therefore, the CBS criteria developed by the pure bending condition may result in unconservative estimations for actual cases with axial compressive components. It is recommended to perform a detailed (experimental and analytical) study on the effects of cross-sectional strain distribution on the buckling resistance of HSS pipes. It is also advisable to be cautious in using available criteria (especially criteria that originated from buckling under bending) to predict the CBS of pipe segments under buckling conditions dominated by axial compressive forces.
5. Although HSS pipes show high ductility in longitudinal coupon tests, high strength and low ductility of the transversal material response may adversely affect the pipes' longitudinal strain capacity. This study showed that these effects are common for compressive strain limits. Tensile strain limits and girth weld overmatching strength are other topics in which the material anisotropy effects might play a significant role. Therefore, it is recommended to consider the material anisotropy in the process of HSS material selection for pipe projects.
6. The anisotropic material model introduced in this research is capable of capturing an anisotropic response of HSS pipes material in the yielding and early plastic regions. This material model is also recommended for other limit states which are sensitive to the same range of material response. Specifically, using this material model will be quite valuable for studying the tensile strain limit of HSS pipes when internal pressure is high. Since under these conditions, the main component of the von Mises stress is the transversal component, the amount of deformation the material can take before reaching a certain stress level drops due to the

larger elastic domain (lack of ductility) in the transverse direction. The combined hardening material model reflects a more realistic level of ductility and gives more accurate simulations (compared to isotropic models) of the material stiffness under any stress paths.

7. Based on the results of this study, when the internal pressure is high, HSS pipes with anisotropic material properties show higher tensile and compressive strength in the longitudinal direction. Therefore, the overmatch of the girth weld should be examined using the longitudinal strength under the highest allowable internal pressure. If the girth weld overmatch is examined with the longitudinal coupon test results, there is a possibility of strain accumulation in the weld material instead of the base material. This is because due to the anisotropy, the material strength in the longitudinal direction is higher than the coupon test strength when the internal pressure is high.
8. The material tests as well as the pipe buckling tests used in this research for validation of the combined hardening model were performed in monotonic conditions. Additional material and buckling tests of HSS pipes will support further validation/improvement of the material model and better understanding of the HSS pipes buckling behaviour. The material test program should include more longitudinal compression tests to enrich the available anisotropic material database of HSS pipes. The material test program should also include cyclic material tests which can be used to define the isotropic and kinematic hardening components of the material model more accurately. The buckling tests of HSS pipes should include cyclic loading patterns to verify the models robustness under strain reversal conditions. The buckling test program should also include different combinations of axial compressive force and bending moments.

More detail measurements of local compressive strain are recommended for these tests.

# **APPENDIX A**

## **Results of Parametric Study**

$\sigma_{(T)}$ (MPa)	$\frac{\sigma_{y(L)}}{\sigma_{y(T)}}$	$\frac{E_{sh}}{E}$	$\frac{D}{t}$	$\frac{\sigma_h}{\sigma_{y(T)}}$	$\frac{II_{max}}{D}$	CBS (%)
550	0.706	0.0067	50	0.0	0.0005	-1.73
550	0.706	0.02	50	0.0	0.0005	-2.14
550	0.836	0.0067	50	0.0	0.0005	-1.53
550	0.836	0.02	50	0.0	0.0005	-2.06
550	0.912	0.0067	50	0.0	0.0005	-1.40
550	0.912	0.02	50	0.0	0.0005	-2.01
690	0.706	0.0067	50	0.0	0.0005	-1.63
690	0.706	0.02	50	0.0	0.0005	-1.95
690	0.836	0.0067	50	0.0	0.0005	-1.45
690	0.836	0.02	50	0.0	0.0005	-1.84
690	0.912	0.0067	50	0.0	0.0005	-1.33
690	0.912	0.02	50	0.0	0.0005	-1.76
825	0.706	0.0067	50	0.0	0.0005	-1.59
825	0.706	0.02	50	0.0	0.0005	-1.81
825	0.836	0.0067	50	0.0	0.0005	-1.40
825	0.836	0.02	50	0.0	0.0005	-1.68
825	0.912	0.0067	50	0.0	0.0005	-1.28
825	0.912	0.02	50	0.0	0.0005	-1.60
550	0.706	0.0067	50	0.0	0.0025	-1.41
550	0.706	0.02	50	0.0	0.0025	-1.71
550	0.836	0.0067	50	0.0	0.0025	-1.22
550	0.836	0.02	50	0.0	0.0025	-1.62
550	0.912	0.0067	50	0.0	0.0025	-1.10
550	0.912	0.02	50	0.0	0.0025	-1.56
690	0.706	0.0067	50	0.0	0.0025	-1.35
690	0.706	0.02	50	0.0	0.0025	-1.58
690	0.836	0.0067	50	0.0	0.0025	-1.15
690	0.836	0.02	50	0.0	0.0025	-1.46
690	0.912	0.0067	50	0.0	0.0025	-1.03
690	0.912	0.02	50	0.0	0.0025	-1.39
825	0.706	0.0067	50	0.0	0.0025	-1.31
825	0.706	0.02	50	0.0	0.0025	-1.49
825	0.836	0.0067	50	0.0	0.0025	-1.12
825	0.836	0.02	50	0.0	0.0025	-1.37
825	0.912	0.0067	50	0.0	0.0025	-1.01
825	0.912	0.02	50	0.0	0.0025	-1.28

$\sigma_{(T)}$ (MPa)	$\frac{\sigma_{y(L)}}{\sigma_{y(T)}}$	$\frac{E_{sh}}{E}$	$\frac{D}{t}$	$\frac{\sigma_h}{\sigma_{y(T)}}$	$\frac{II_{max}}{D}$	CBS (%)
550	0.706	0.0067	50	0.0	0.005	-1.22
550	0.706	0.02	50	0.0	0.005	-1.43
550	0.836	0.0067	50	0.0	0.005	-1.05
550	0.836	0.02	50	0.0	0.005	-1.33
550	0.912	0.0067	50	0.0	0.005	-0.95
550	0.912	0.02	50	0.0	0.005	-1.27
690	0.706	0.0067	50	0.0	0.005	-1.18
690	0.706	0.02	50	0.0	0.005	-1.33
690	0.836	0.0067	50	0.0	0.005	-1.02
690	0.836	0.02	50	0.0	0.005	-1.23
690	0.912	0.0067	50	0.0	0.005	-0.93
690	0.912	0.02	50	0.0	0.005	-1.16
825	0.706	0.0067	50	0.0	0.005	-1.15
825	0.706	0.02	50	0.0	0.005	-1.27
825	0.836	0.0067	50	0.0	0.005	-1.00
825	0.836	0.02	50	0.0	0.005	-1.18
825	0.912	0.0067	50	0.0	0.005	-0.91
825	0.912	0.02	50	0.0	0.005	-1.11
550	71	0.0067	50	0.4	0.0005	-1.71
550	71	0.02	50	0.4	0.0005	-3.05
550	84	0.0067	50	0.4	0.0005	-1.51
550	84	0.02	50	0.4	0.0005	-2.84
550	91	0.0067	50	0.4	0.0005	-1.38
550	91	0.02	50	0.4	0.0005	-2.70
690	71	0.0067	50	0.4	0.0005	-1.55
690	71	0.02	50	0.4	0.0005	-2.54
690	84	0.0067	50	0.4	0.0005	-1.34
690	84	0.02	50	0.4	0.0005	-2.31
690	91	0.0067	50	0.4	0.0005	-1.24
690	91	0.02	50	0.4	0.0005	-2.14
825	71	0.0067	50	0.4	0.0005	-1.44
825	71	0.02	50	0.4	0.0005	-2.24
825	84	0.0067	50	0.4	0.0005	-1.27
825	84	0.02	50	0.4	0.0005	-2.04
825	91	0.0067	50	0.4	0.0005	-1.16
825	91	0.02	50	0.4	0.0005	-1.92

$\sigma_{(T)}$ (MPa)	$\frac{\sigma_{y(L)}}{\sigma_{y(T)}}$	$\frac{E_{sh}}{E}$	$\frac{D}{t}$	$\frac{\sigma_h}{\sigma_{y(T)}}$	$\frac{II_{max}}{D}$	CBS (%)
550	0.706	0.0067	50	0.4	0.0025	-1.30
550	0.706	0.02	50	0.4	0.0025	-2.55
550	0.836	0.0067	50	0.4	0.0025	-1.16
550	0.836	0.02	50	0.4	0.0025	-2.34
550	0.912	0.0067	50	0.4	0.0025	-1.07
550	0.912	0.02	50	0.4	0.0025	-2.22
690	0.706	0.0067	50	0.4	0.0025	-1.21
690	0.706	0.02	50	0.4	0.0025	-2.13
690	0.836	0.0067	50	0.4	0.0025	-1.08
690	0.836	0.02	50	0.4	0.0025	-1.95
690	0.912	0.0067	50	0.4	0.0025	-1.00
690	0.912	0.02	50	0.4	0.0025	-1.83
825	0.706	0.0067	50	0.4	0.0025	-1.17
825	0.706	0.02	50	0.4	0.0025	-1.85
825	0.836	0.0067	50	0.4	0.0025	-1.05
825	0.836	0.02	50	0.4	0.0025	-1.70
825	0.912	0.0067	50	0.4	0.0025	-0.99
825	0.912	0.02	50	0.4	0.0025	-1.62
550	0.706	0.0067	50	0.4	0.005	-1.14
550	0.706	0.02	50	0.4	0.005	-2.30
550	0.836	0.0067	50	0.4	0.005	-1.02
550	0.836	0.02	50	0.4	0.005	-2.10
550	0.912	0.0067	50	0.4	0.005	-0.94
550	0.912	0.02	50	0.4	0.005	-1.99
690	0.706	0.0067	50	0.4	0.005	-1.08
690	0.706	0.02	50	0.4	0.005	-1.89
690	0.836	0.0067	50	0.4	0.005	-0.97
690	0.836	0.02	50	0.4	0.005	-1.75
690	0.912	0.0067	50	0.4	0.005	-0.92
690	0.912	0.02	50	0.4	0.005	-1.67
825	0.706	0.0067	50	0.4	0.005	-1.04
825	0.706	0.02	50	0.4	0.005	-1.63
825	0.836	0.0067	50	0.4	0.005	-0.96
825	0.836	0.02	50	0.4	0.005	-1.53
825	0.912	0.0067	50	0.4	0.005	-0.91
825	0.912	0.02	50	0.4	0.005	-1.44

$\sigma_{(T)}$ (MPa)	$\frac{\sigma_{y(L)}}{\sigma_{y(T)}}$	$\frac{E_{sh}}{E}$	$\frac{D}{t}$	$\frac{\sigma_h}{\sigma_{y(T)}}$	$\frac{II_{max}}{D}$	CBS (%)
550	0.706	0.0067	50	0.8	0.0005	-0.87
550	0.706	0.02	50	0.8	0.0005	-3.28
550	0.836	0.0067	50	0.8	0.0005	-0.90
550	0.836	0.02	50	0.8	0.0005	-3.17
550	0.912	0.0067	50	0.8	0.0005	-0.94
550	0.912	0.02	50	0.8	0.0005	-3.05
690	0.706	0.0067	50	0.8	0.0005	-0.88
690	0.706	0.02	50	0.8	0.0005	-2.70
690	0.836	0.0067	50	0.8	0.0005	-0.92
690	0.836	0.02	50	0.8	0.0005	-2.64
690	0.912	0.0067	50	0.8	0.0005	-0.95
690	0.912	0.02	50	0.8	0.0005	-2.58
825	0.706	0.0067	50	0.8	0.0005	-0.92
825	0.706	0.02	50	0.8	0.0005	-2.17
825	0.836	0.0067	50	0.8	0.0005	-0.96
825	0.836	0.02	50	0.8	0.0005	-2.26
825	0.912	0.0067	50	0.8	0.0005	-1.01
825	0.912	0.02	50	0.8	0.0005	-2.26
550	0.706	0.0067	50	0.8	0.0025	-0.87
550	0.706	0.02	50	0.8	0.0025	-3.18
550	0.836	0.0067	50	0.8	0.0025	-0.90
550	0.836	0.02	50	0.8	0.0025	-3.07
550	0.912	0.0067	50	0.8	0.0025	-0.93
550	0.912	0.02	50	0.8	0.0025	-2.96
690	0.706	0.0067	50	0.8	0.0025	-0.88
690	0.706	0.02	50	0.8	0.0025	-2.64
690	0.836	0.0067	50	0.8	0.0025	-0.92
690	0.836	0.02	50	0.8	0.0025	-2.57
690	0.912	0.0067	50	0.8	0.0025	-0.95
690	0.912	0.02	50	0.8	0.0025	-2.53
825	0.706	0.0067	50	0.8	0.0025	-0.90
825	0.706	0.02	50	0.8	0.0025	-2.10
825	0.836	0.0067	50	0.8	0.0025	-0.94
825	0.836	0.02	50	0.8	0.0025	-2.21
825	0.912	0.0067	50	0.8	0.0025	-0.98
825	0.912	0.02	50	0.8	0.0025	-2.21

$\sigma_{(T)}$ (MPa)	$\frac{\sigma_{y(L)}}{\sigma_{y(T)}}$	$\frac{E_{sh}}{E}$	$\frac{D}{t}$	$\frac{\sigma_h}{\sigma_{y(T)}}$	$\frac{II_{max}}{D}$	CBS (%)
550	0.706	0.0067	50	0.8	0.005	-0.86
550	0.706	0.02	50	0.8	0.005	-3.03
550	0.836	0.0067	50	0.8	0.005	-0.90
550	0.836	0.02	50	0.8	0.005	-2.92
550	0.912	0.0067	50	0.8	0.005	-0.92
550	0.912	0.02	50	0.8	0.005	-2.86
690	0.706	0.0067	50	0.8	0.005	-0.87
690	0.706	0.02	50	0.8	0.005	-2.49
690	0.836	0.0067	50	0.8	0.005	-0.93
690	0.836	0.02	50	0.8	0.005	-2.48
690	0.912	0.0067	50	0.8	0.005	-0.94
690	0.912	0.02	50	0.8	0.005	-2.44
825	0.706	0.0067	50	0.8	0.005	-0.90
825	0.706	0.02	50	0.8	0.005	-2.01
825	0.836	0.0067	50	0.8	0.005	-0.94
825	0.836	0.02	50	0.8	0.005	-2.11
825	0.912	0.0067	50	0.8	0.005	-0.96
825	0.912	0.02	50	0.8	0.005	-2.12
550	0.706	0.0067	70	0.0	0.0005	-1.11
550	0.706	0.02	70	0.0	0.0005	-1.36
550	0.836	0.0067	70	0.0	0.0005	-0.97
550	0.836	0.02	70	0.0	0.0005	-1.24
550	0.912	0.0067	70	0.0	0.0005	-0.85
550	0.912	0.02	70	0.0	0.0005	-1.17
690	0.706	0.0067	70	0.0	0.0005	-1.08
690	0.706	0.02	70	0.0	0.0005	-1.23
690	0.836	0.0067	70	0.0	0.0005	-0.92
690	0.836	0.02	70	0.0	0.0005	-1.08
690	0.912	0.0067	70	0.0	0.0005	-0.81
690	0.912	0.02	70	0.0	0.0005	-0.99
825	0.706	0.0067	70	0.0	0.0005	-1.05
825	0.706	0.02	70	0.0	0.0005	-1.13
825	0.836	0.0067	70	0.0	0.0005	-0.91
825	0.836	0.02	70	0.0	0.0005	-1.01
825	0.912	0.0067	70	0.0	0.0005	-0.80
825	0.912	0.02	70	0.0	0.0005	-0.91

$\sigma_{(T)}$ (MPa)	$\frac{\sigma_{y(L)}}{\sigma_{y(T)}}$	$\frac{E_{sh}}{E}$	$\frac{D}{t}$	$\frac{\sigma_h}{\sigma_{y(T)}}$	$\frac{II_{max}}{D}$	CBS (%)
550	0.706	0.0067	70	0.0	0.0025	-0.92
550	0.706	0.02	70	0.0	0.0025	-1.11
550	0.836	0.0067	70	0.0	0.0025	-0.80
550	0.836	0.02	70	0.0	0.0025	-0.98
550	0.912	0.0067	70	0.0	0.0025	-0.71
550	0.912	0.02	70	0.0	0.0025	-0.90
690	0.706	0.0067	70	0.0	0.0025	-0.89
690	0.706	0.02	70	0.0	0.0025	-1.01
690	0.836	0.0067	70	0.0	0.0025	-0.76
690	0.836	0.02	70	0.0	0.0025	-0.89
690	0.912	0.0067	70	0.0	0.0025	-0.69
690	0.912	0.02	70	0.0	0.0025	-0.80
825	0.706	0.0067	70	0.0	0.0025	-0.90
825	0.706	0.02	70	0.0	0.0025	-0.98
825	0.836	0.0067	70	0.0	0.0025	-0.78
825	0.836	0.02	70	0.0	0.0025	-0.86
825	0.912	0.0067	70	0.0	0.0025	-0.70
825	0.912	0.02	70	0.0	0.0025	-0.78
550	0.706	0.0067	70	0.0	0.005	-0.81
550	0.706	0.02	70	0.0	0.005	-0.94
550	0.836	0.0067	70	0.0	0.005	-0.71
550	0.836	0.02	70	0.0	0.005	-0.84
550	0.912	0.0067	70	0.0	0.005	-0.65
550	0.912	0.02	70	0.0	0.005	-0.77
690	0.706	0.0067	70	0.0	0.005	-0.80
690	0.706	0.02	70	0.0	0.005	-0.89
690	0.836	0.0067	70	0.0	0.005	-0.69
690	0.836	0.02	70	0.0	0.005	-0.79
690	0.912	0.0067	70	0.0	0.005	-0.63
690	0.912	0.02	70	0.0	0.005	-0.73
825	0.706	0.0067	70	0.0	0.005	-0.79
825	0.706	0.02	70	0.0	0.005	-0.87
825	0.836	0.0067	70	0.0	0.005	-0.68
825	0.836	0.02	70	0.0	0.005	-0.76
825	0.912	0.0067	70	0.0	0.005	-0.61
825	0.912	0.02	70	0.0	0.005	-0.70

$\sigma_{(T)}$ (MPa)	$\frac{\sigma_{y(L)}}{\sigma_{y(T)}}$	$\frac{E_{sh}}{E}$	$\frac{D}{t}$	$\frac{\sigma_h}{\sigma_{y(T)}}$	$\frac{II_{max}}{D}$	CBS (%)
550	71	0.0067	70	0.4	0.0005	-1.04
550	71	0.02	70	0.4	0.0005	-1.80
550	84	0.0067	70	0.4	0.0005	-0.90
550	84	0.02	70	0.4	0.0005	-1.66
550	91	0.0067	70	0.4	0.0005	-0.80
550	91	0.02	70	0.4	0.0005	-1.56
690	71	0.0067	70	0.4	0.0005	-0.99
690	71	0.02	70	0.4	0.0005	-1.45
690	84	0.0067	70	0.4	0.0005	-0.85
690	84	0.02	70	0.4	0.0005	-1.31
690	91	0.0067	70	0.4	0.0005	-0.76
690	91	0.02	70	0.4	0.0005	-1.21
825	71	0.0067	70	0.4	0.0005	-0.95
825	71	0.02	70	0.4	0.0005	-1.27
825	84	0.0067	70	0.4	0.0005	-0.83
825	84	0.02	70	0.4	0.0005	-1.12
825	91	0.0067	70	0.4	0.0005	-0.74
825	91	0.02	70	0.4	0.0005	-1.05
550	71	0.0067	70	0.4	0.0025	-0.83
550	71	0.02	70	0.4	0.0025	-1.46
550	84	0.0067	70	0.4	0.0025	-0.71
550	84	0.02	70	0.4	0.0025	-1.31
550	91	0.0067	70	0.4	0.0025	-0.65
550	91	0.02	70	0.4	0.0025	-1.25
690	71	0.0067	70	0.4	0.0025	-0.82
690	71	0.02	70	0.4	0.0025	-1.18
690	84	0.0067	70	0.4	0.0025	-0.71
690	84	0.02	70	0.4	0.0025	-1.05
690	91	0.0067	70	0.4	0.0025	-0.64
690	91	0.02	70	0.4	0.0025	-0.99
825	71	0.0067	70	0.4	0.0025	-0.81
825	71	0.02	70	0.4	0.0025	-1.07
825	84	0.0067	70	0.4	0.0025	-0.70
825	84	0.02	70	0.4	0.0025	-0.95
825	91	0.0067	70	0.4	0.0025	-0.64
825	91	0.02	70	0.4	0.0025	-0.89

$\sigma_{(T)}$ (MPa)	$\frac{\sigma_{y(L)}}{\sigma_{y(T)}}$	$\frac{E_{sh}}{E}$	$\frac{D}{t}$	$\frac{\sigma_h}{\sigma_{y(T)}}$	$\frac{H_{max}}{D}$	CBS (%)
550	71	0.0067	70	0.4	0.005	-0.74
550	71	0.02	70	0.4	0.005	-1.28
550	84	0.0067	70	0.4	0.005	-0.66
550	84	0.02	70	0.4	0.005	-1.17
550	91	0.0067	70	0.4	0.005	-0.61
550	91	0.02	70	0.4	0.005	-1.12
690	71	0.0067	70	0.4	0.005	-0.73
690	71	0.02	70	0.4	0.005	-1.06
690	84	0.0067	70	0.4	0.005	-0.65
690	84	0.02	70	0.4	0.005	-0.96
690	91	0.0067	70	0.4	0.005	-0.60
690	91	0.02	70	0.4	0.005	-0.90
825	71	0.0067	70	0.4	0.005	-0.72
825	71	0.02	70	0.4	0.005	-0.96
825	84	0.0067	70	0.4	0.005	-0.64
825	84	0.02	70	0.4	0.005	-0.87
825	91	0.0067	70	0.4	0.005	-0.60
825	91	0.02	70	0.4	0.005	-0.83
550	0.706	0.0067	70	0.8	0.0005	-0.88
550	0.706	0.02	70	0.8	0.0005	-2.79
550	0.836	0.0067	70	0.8	0.0005	-0.89
550	0.836	0.02	70	0.8	0.0005	-2.72
550	0.912	0.0067	70	0.8	0.0005	-0.91
550	0.912	0.02	70	0.8	0.0005	-2.68
690	0.706	0.0067	70	0.8	0.0005	-0.87
690	0.706	0.02	70	0.8	0.0005	-2.32
690	0.836	0.0067	70	0.8	0.0005	-0.90
690	0.836	0.02	70	0.8	0.0005	-2.32
690	0.912	0.0067	70	0.8	0.0005	-0.95
690	0.912	0.02	70	0.8	0.0005	-2.30
825	0.706	0.0067	70	0.8	0.0005	-0.88
825	0.706	0.02	70	0.8	0.0005	-1.92
825	0.836	0.0067	70	0.8	0.0005	-0.92
825	0.836	0.02	70	0.8	0.0005	-1.97
825	0.912	0.0067	70	0.8	0.0005	-0.96
825	0.912	0.02	70	0.8	0.0005	-2.00

$\sigma_{(T)}$ (MPa)	$\frac{\sigma_{y(L)}}{\sigma_{y(T)}}$	$\frac{E_{sh}}{E}$	$\frac{D}{t}$	$\frac{\sigma_h}{\sigma_{y(T)}}$	$\frac{H_{max}}{D}$	CBS (%)
550	0.706	0.0067	70	0.8	0.0025	-0.85
550	0.706	0.02	70	0.8	0.0025	-2.49
550	0.836	0.0067	70	0.8	0.0025	-0.88
550	0.836	0.02	70	0.8	0.0025	-2.48
550	0.912	0.0067	70	0.8	0.0025	-0.91
550	0.912	0.02	70	0.8	0.0025	-2.43
690	0.706	0.0067	70	0.8	0.0025	-0.82
690	0.706	0.02	70	0.8	0.0025	-2.04
690	0.836	0.0067	70	0.8	0.0025	-0.86
690	0.836	0.02	70	0.8	0.0025	-2.06
690	0.912	0.0067	70	0.8	0.0025	-0.90
690	0.912	0.02	70	0.8	0.0025	-2.05
825	0.706	0.0067	70	0.8	0.0025	-0.80
825	0.706	0.02	70	0.8	0.0025	-1.66
825	0.836	0.0067	70	0.8	0.0025	-0.82
825	0.836	0.02	70	0.8	0.0025	-1.72
825	0.912	0.0067	70	0.8	0.0025	-0.81
825	0.912	0.02	70	0.8	0.0025	-1.75
550	0.706	0.0067	70	0.8	0.005	-0.80
550	0.706	0.02	70	0.8	0.005	-2.34
550	0.836	0.0067	70	0.8	0.005	-0.84
550	0.836	0.02	70	0.8	0.005	-2.30
550	0.912	0.0067	70	0.8	0.005	-0.87
550	0.912	0.02	70	0.8	0.005	-2.27
690	0.706	0.0067	70	0.8	0.005	-0.78
690	0.706	0.02	70	0.8	0.005	-1.87
690	0.836	0.0067	70	0.8	0.005	-0.80
690	0.836	0.02	70	0.8	0.005	-1.92
690	0.912	0.0067	70	0.8	0.005	-0.84
690	0.912	0.02	70	0.8	0.005	-1.90
825	0.706	0.0067	70	0.8	0.005	-0.77
825	0.706	0.02	70	0.8	0.005	-1.52
825	0.836	0.0067	70	0.8	0.005	-0.76
825	0.836	0.02	70	0.8	0.005	-1.59
825	0.912	0.0067	70	0.8	0.005	-0.74
825	0.912	0.02	70	0.8	0.005	-1.62

$\sigma_{(T)}$ (MPa)	$\frac{\sigma_{y(L)}}{\sigma_{y(T)}}$	$\frac{E_{sh}}{E}$	$\frac{D}{t}$	$\frac{\sigma_h}{\sigma_{y(T)}}$	$\frac{H_{max}}{D}$	CBS (%)
550	0.706	0.0067	90	0.0	0.0005	-0.83
550	0.706	0.02	90	0.0	0.0005	-0.93
550	0.836	0.0067	90	0.0	0.0005	-0.73
550	0.836	0.02	90	0.0	0.0005	-0.82
550	0.912	0.0067	90	0.0	0.0005	-0.66
550	0.912	0.02	90	0.0	0.0005	-0.74
690	0.706	0.0067	90	0.0	0.0005	-0.81
690	0.706	0.02	90	0.0	0.0005	-0.87
690	0.836	0.0067	90	0.0	0.0005	-0.72
690	0.836	0.02	90	0.0	0.0005	-0.76
690	0.912	0.0067	90	0.0	0.0005	-0.64
690	0.912	0.02	90	0.0	0.0005	-0.69
825	0.706	0.0067	90	0.0	0.0005	-0.80
825	0.706	0.02	90	0.0	0.0005	-0.85
825	0.836	0.0067	90	0.0	0.0005	-0.71
825	0.836	0.02	90	0.0	0.0005	-0.75
825	0.912	0.0067	90	0.0	0.0005	-0.64
825	0.912	0.02	90	0.0	0.0005	-0.68
550	0.706	0.0067	90	0.0	0.0025	-0.72
550	0.706	0.02	90	0.0	0.0025	-0.79
550	0.836	0.0067	90	0.0	0.0025	-0.64
550	0.836	0.02	90	0.0	0.0025	-0.68
550	0.912	0.0067	90	0.0	0.0025	-0.58
550	0.912	0.02	90	0.0	0.0025	-0.62
690	0.706	0.0067	90	0.0	0.0025	-0.72
690	0.706	0.02	90	0.0	0.0025	-0.76
690	0.836	0.0067	90	0.0	0.0025	-0.63
690	0.836	0.02	90	0.0	0.0025	-0.67
690	0.912	0.0067	90	0.0	0.0025	-0.58
690	0.912	0.02	90	0.0	0.0025	-0.61
825	0.706	0.0067	90	0.0	0.0025	-0.71
825	0.706	0.02	90	0.0	0.0025	-0.75
825	0.836	0.0067	90	0.0	0.0025	-0.62
825	0.836	0.02	90	0.0	0.0025	-0.66
825	0.912	0.0067	90	0.0	0.0025	-0.57
825	0.912	0.02	90	0.0	0.0025	-0.60

$\sigma_{(T)}$ (MPa)	$\frac{\sigma_{y(L)}}{\sigma_{y(T)}}$	$\frac{E_{sh}}{E}$	$\frac{D}{t}$	$\frac{\sigma_h}{\sigma_{y(T)}}$	$\frac{H_{max}}{D}$	CBS (%)
550	0.706	0.0067	90	0.0	0.005	-0.64
550	0.706	0.02	90	0.0	0.005	-0.69
550	0.836	0.0067	90	0.0	0.005	-0.57
550	0.836	0.02	90	0.0	0.005	-0.61
550	0.912	0.0067	90	0.0	0.005	-0.50
550	0.912	0.02	90	0.0	0.005	-0.56
690	0.706	0.0067	90	0.0	0.005	-0.63
690	0.706	0.02	90	0.0	0.005	-0.67
690	0.836	0.0067	90	0.0	0.005	-0.57
690	0.836	0.02	90	0.0	0.005	-0.60
690	0.912	0.0067	90	0.0	0.005	-0.49
690	0.912	0.02	90	0.0	0.005	-0.54
825	0.706	0.0067	90	0.0	0.005	-0.63
825	0.706	0.02	90	0.0	0.005	-0.64
825	0.836	0.0067	90	0.0	0.005	-0.56
825	0.836	0.02	90	0.0	0.005	-0.58
825	0.912	0.0067	90	0.0	0.005	-0.49
825	0.912	0.02	90	0.0	0.005	-0.52
550	0.706	0.0067	90	0.4	0.0005	-0.77
550	0.706	0.02	90	0.4	0.0005	-1.17
550	0.836	0.0067	90	0.4	0.0005	-0.65
550	0.836	0.02	90	0.4	0.0005	-1.01
550	0.912	0.0067	90	0.4	0.0005	-0.59
550	0.912	0.02	90	0.4	0.0005	-0.93
690	0.706	0.0067	90	0.4	0.0005	-0.78
690	0.706	0.02	90	0.4	0.0005	-1.00
690	0.836	0.0067	90	0.4	0.0005	-0.66
690	0.836	0.02	90	0.4	0.0005	-0.86
690	0.912	0.0067	90	0.4	0.0005	-0.58
690	0.912	0.02	90	0.4	0.0005	-0.78
825	0.706	0.0067	90	0.4	0.0005	-0.78
825	0.706	0.02	90	0.4	0.0005	-0.94
825	0.836	0.0067	90	0.4	0.0005	-0.66
825	0.836	0.02	90	0.4	0.0005	-0.78
825	0.912	0.0067	90	0.4	0.0005	-0.58
825	0.912	0.02	90	0.4	0.0005	-0.71

$\sigma_{(T)}$ (MPa)	$\frac{\sigma_{y(L)}}{\sigma_{y(T)}}$	$\frac{E_{sh}}{E}$	$\frac{D}{t}$	$\frac{\sigma_h}{\sigma_{y(T)}}$	$\frac{H_{max}}{D}$	CBS (%)
550	0.706	0.0067	90	0.4	0.0025	-0.62
550	0.706	0.02	90	0.4	0.0025	-0.93
550	0.836	0.0067	90	0.4	0.0025	-0.54
550	0.836	0.02	90	0.4	0.0025	-0.83
550	0.912	0.0067	90	0.4	0.0025	-0.48
550	0.912	0.02	90	0.4	0.0025	-0.73
690	0.706	0.0067	90	0.4	0.0025	-0.63
690	0.706	0.02	90	0.4	0.0025	-0.82
690	0.836	0.0067	90	0.4	0.0025	-0.56
690	0.836	0.02	90	0.4	0.0025	-0.72
690	0.912	0.0067	90	0.4	0.0025	-0.49
690	0.912	0.02	90	0.4	0.0025	-0.66
825	0.706	0.0067	90	0.4	0.0025	-0.62
825	0.706	0.02	90	0.4	0.0025	-0.78
825	0.836	0.0067	90	0.4	0.0025	-0.57
825	0.836	0.02	90	0.4	0.0025	-0.67
825	0.912	0.0067	90	0.4	0.0025	-0.51
825	0.912	0.02	90	0.4	0.0025	-0.59
550	0.706	0.0067	90	0.4	0.005	-0.53
550	0.706	0.02	90	0.4	0.005	-0.84
550	0.836	0.0067	90	0.4	0.005	-0.48
550	0.836	0.02	90	0.4	0.005	-0.71
550	0.912	0.0067	90	0.4	0.005	-0.42
550	0.912	0.02	90	0.4	0.005	-0.69
690	0.706	0.0067	90	0.4	0.005	-0.55
690	0.706	0.02	90	0.4	0.005	-0.73
690	0.836	0.0067	90	0.4	0.005	-0.50
690	0.836	0.02	90	0.4	0.005	-0.62
690	0.912	0.0067	90	0.4	0.005	-0.45
690	0.912	0.02	90	0.4	0.005	-0.58
825	0.706	0.0067	90	0.4	0.005	-0.56
825	0.706	0.02	90	0.4	0.005	-0.69
825	0.836	0.0067	90	0.4	0.005	-0.52
825	0.836	0.02	90	0.4	0.005	-0.60
825	0.912	0.0067	90	0.4	0.005	-0.50
825	0.912	0.02	90	0.4	0.005	-0.57

$\sigma_{(T)}$ (MPa)	$\frac{\sigma_{y(L)}}{\sigma_{y(T)}}$	$\frac{E_{sh}}{E}$	$\frac{D}{t}$	$\frac{\sigma_h}{\sigma_{y(T)}}$	$\frac{H_{max}}{D}$	CBS (%)
550	0.706	0.0067	90	0.8	0.0005	-0.83
550	0.706	0.02	90	0.8	0.0005	-2.05
550	0.836	0.0067	90	0.8	0.0005	-0.84
550	0.836	0.02	90	0.8	0.0005	-2.04
550	0.912	0.0067	90	0.8	0.0005	-0.85
550	0.912	0.02	90	0.8	0.0005	-2.03
690	0.706	0.0067	90	0.8	0.0005	-0.77
690	0.706	0.02	90	0.8	0.0005	-1.67
690	0.836	0.0067	90	0.8	0.0005	-0.76
690	0.836	0.02	90	0.8	0.0005	-1.71
690	0.912	0.0067	90	0.8	0.0005	-0.73
690	0.912	0.02	90	0.8	0.0005	-1.69
825	0.706	0.0067	90	0.8	0.0005	-0.70
825	0.706	0.02	90	0.8	0.0005	-1.36
825	0.836	0.0067	90	0.8	0.0005	-0.65
825	0.836	0.02	90	0.8	0.0005	-1.40
825	0.912	0.0067	90	0.8	0.0005	-0.64
825	0.912	0.02	90	0.8	0.0005	-1.41
550	0.706	0.0067	90	0.8	0.0025	-0.72
550	0.706	0.02	90	0.8	0.0025	-1.83
550	0.836	0.0067	90	0.8	0.0025	-0.74
550	0.836	0.02	90	0.8	0.0025	-1.83
550	0.912	0.0067	90	0.8	0.0025	-0.75
550	0.912	0.02	90	0.8	0.0025	-1.83
690	0.706	0.0067	90	0.8	0.0025	-0.62
690	0.706	0.02	90	0.8	0.0025	-1.44
690	0.836	0.0067	90	0.8	0.0025	-0.61
690	0.836	0.02	90	0.8	0.0025	-1.45
690	0.912	0.0067	90	0.8	0.0025	-0.59
690	0.912	0.02	90	0.8	0.0025	-1.49
825	0.706	0.0067	90	0.8	0.0025	-0.55
825	0.706	0.02	90	0.8	0.0025	-1.19
825	0.836	0.0067	90	0.8	0.0025	-0.54
825	0.836	0.02	90	0.8	0.0025	-1.21
825	0.912	0.0067	90	0.8	0.0025	-0.51
825	0.912	0.02	90	0.8	0.0025	-1.24

$\sigma_{(T)}$ (MPa)	$\frac{\sigma_{y(L)}}{\sigma_{y(T)}}$	$\frac{E_{sh}}{E}$	$\frac{D}{t}$	$\frac{\sigma_h}{\sigma_{y(T)}}$	$\frac{H_{max}}{D}$	CBS (%)
550	0.706	0.0067	90	0.8	0.005	-0.66
550	0.706	0.02	90	0.8	0.005	-1.73
550	0.836	0.0067	90	0.8	0.005	-0.64
550	0.836	0.02	90	0.8	0.005	-1.72
550	0.912	0.0067	90	0.8	0.005	-0.65
550	0.912	0.02	90	0.8	0.005	-1.74
690	0.706	0.0067	90	0.8	0.005	-0.56
690	0.706	0.02	90	0.8	0.005	-1.34
690	0.836	0.0067	90	0.8	0.005	-0.57
690	0.836	0.02	90	0.8	0.005	-1.39
690	0.912	0.0067	90	0.8	0.005	-0.56
690	0.912	0.02	90	0.8	0.005	-1.39
825	0.706	0.0067	90	0.8	0.005	-0.52
825	0.706	0.02	90	0.8	0.005	-1.14
825	0.836	0.0067	90	0.8	0.005	-0.50
825	0.836	0.02	90	0.8	0.005	-1.15
825	0.912	0.0067	90	0.8	0.005	-0.51
825	0.912	0.02	90	0.8	0.005	-1.19